Waves in Shallow Water Magnetohydrodynamics

Samuel Hunter

Submitted in accordance with the requirements for the degree of Doctor of Philosophy

The University of Leeds
Department of Applied Mathematics

August 2015

Abstract

The dynamics of planetary and stellar objects are dominated by the fluid motions of electrically conducting media. Often, such fluid is confined to a shallow layer, perhaps in an atmosphere or bounded by stratification. One such layer is the solar tachocline (Spiegel and Zahn 1992): a thin layer of high velocity shear in the Sun, which is permeated by strong magnetic fields.

The discovery of the solar tachocline by Schou et al. (1997) has inspired the derivation of the equations of shallow water magnetohydrodynamics (SWMHD) by Gilman (2000), in which the small aspect ratio of vertical to horizontal length scales is used to simplify the governing equations. This thesis takes these equations as a base, and aims to build on knowledge of the wave-like dynamics supported in the shallow water system.

It will be shown that the analogy between the shallow water and 2D compressible hydrodynamic systems is broken with the introduction of magnetic field, and the differences between the two systems discussed. An energy conservation law will be derived and be used to infer stability properties of the SWMHD system. We will then construct a multi-layer system, and consider linear wave-like perturbations to a motionless basic state with a uniform magnetic field. Particular focus will be on the 2- and 3-layer models, and the effect of magnetic field strength on wave properties.

A weakly nonlinear analysis reveals that the single layer and 2-layer rigid lid weakly non-hydrostatic models support solitary and cnoidal waves. The effect of magnetic field in the single layer case translates to a long-time rescaling, but has much more of an effect on the supported modes in the 2-layer model. The phenomenon of three-wave resonance is also supported in the single layer system, and magnetic influence is discussed.

In rotating SWMHD, we find that resonant triad interactions are supported only in the presence of magnetic field. Weakly nonlinear predictions are found to be accurate at low disturbance amplitudes, when compared to the results from a fully nonlinear numerical scheme. Exact nonlinear solutions are derived and categorised, and their stability addressed using numerics.

To Jill Hunter

who taught me that if something’s worth doing, it’s worth doing right.

Acknowledgements

First and foremost I would like to thank my supervisors, David Hughes and Stephen Griffiths, for their support and direction in the production of this work. Their knowledge and expertise has been an invaluable asset, opening my eyes to such a rich and interesting subject.

I would also like to thank Steve Tobias and Chris Jones for their questions and discussions, and their clear explanations. I am grateful to Julian Mak, who was like a mentor to me when I started my research; our frequent discussions helped me find my feet quickly. Thanks also to Laura Currie, for guidance when I started working with MATLAB, and my friends and colleagues who have created a pleasant working environment at Leeds.

Thanks to my family for their continued encouragement and interest during my studies, and finally to my wife, Kim. Your support has helped me more than you know.

Contents

List of figures

List of tables

General nomenclature

α	fractional density jump	-
β	fractional layer depth	-
ρ	density	kg/m^3
η	free surface height	m
η_j	fluid/fluid interface height	m
f	rotation rate	rads s^{-1}
g	gravitational acceleration	m s^{-2}
g^r	reduced gravity, αg	m s^{-2}
H	undisturbed fluid height	m
p	pressure	N m^{-2}
P	pressure exerted by rigid lid	N m^{-2}

Wave properties

ω	frequency	s^{-1}
k	wavenumber	m^{-1}
$\mathbf{k}$	wavevector	m^{-1}
v_A	Alfvén speed	m s^{-1}
v_S	sound speed	m s^{-1}
v_G	gravity wave speed, $\sqrt{gH}$	m s^{-1}

Operators and vectors

∇	$\left(\frac{\partial}{\partial x}, \frac{\partial}{\partial y}\right)$
$\mathbf{u}$	horizontal velocity, (u, v)
$\mathbf{B}$	horizontal magnetic field

Chapter 1

Introduction

1.1 Waves

Waves are a fundamental property of nearly all fluid systems. They have long been a phenomenon of great scientific interest (see, for example, Stokes, 1849; Rayleigh, 1876, 1877; Gill, 1982; Stix, 1992), responsible for the waves we see in the Earth's ocean and atmosphere, and in astrophysical bodies such as the Sun. They are ubiquitous in the universe, present in the interior of the Earth, the solar wind, the atmospheres of gaseous giant planets, accretion discs, galactic structures and stars, to name but a few examples. Waves are not only a curiosity for us; they play a great many roles in fluid systems. They transfer energy from one place to another, and play a key role in mixing in the Earth's atmosphere and deep oceans (Garrett and Munk, 1972; Turner, 1973); these are important factors that will affect, for example, weather systems, the distribution of nutrients or plankton in the ocean or how a pollutant will spread through the atmosphere. Waves have enabled us to infer the structure of the Earth through seismology, and later the Sun, through helioseismology, as documented by Schou et al. (1997). They may also help explain the relative paucity of lithium observed in the atmosphere of the Sun (Melendez et al., 1968) or the heating of the solar corona (reviewed, for example, by McLellan and Winterberg, 1968). Waves have also been observed in the Sun; see, for example, Erdélyi and Mendoza-Briceño (2008).

Wave-like motion in fluids is manifest through oscillatory motion of fluid particles. The physical mechanism typically employed to visualise this is one with small parcels of fluid that have been displaced from a starting equilibrium position. A 'restoring force' then pulls the parcel back towards its original position, but there is nothing to stop it when it gets there; it overshoots and is subsequently displaced in the opposite direction. The restoring force pulls it back again, and so on. This mechanism has been well understood for many years; see, for example, Rayleigh (1876); Lighthill (1978); Gill (1982).

Waves are categorised by the restoring force that drives them. This force can be induced by fluid pressure, in which case the waves propagate as regions of compression and rarefaction known as sound waves, first studied in this way by Rayleigh (1877). These are examples of longitudinal waves, as the particle movement is in the direction of wave travel (or the wavevector), with an initial disturbance creating an area of high pressure. Particles are then forced out of this region, only to 'bump' into more particles, creating another high pressure area further from the initial perturbation, and so on. They propagate through the Earth's atmosphere very quickly compared to other atmospheric effects such as the wind (at around 350m s^{-1}) and through the ocean quicker still (around 1500m s^{-1}, according to MacKenzie 1981), owing to the higher density of the water. They are also relatively small scale, compared with, say the familiar waves on a beach; the wavelength of the sound of a typical human voice is around 3cm.

The restoring force can also be gravity, in a fluid with a stable density stratification profile. A displaced fluid parcel is forced back towards equilibrium through gravitational buoyancy, leading to so-called gravity waves. Reports of gravity waves date as far back as Halley (1686, pp.165), and are often categorised into surface and internal waves. Surface gravity waves can be observed on the surface of the sea, gravity playing a dominant role in the driving of the waves. In 1844, Scott Russell observed a solitary wave propagating down a canal, maintaining its shape for extended periods of time. These waves propagate at much slower speeds than sound waves, typically at around 1-200m s^{-1} compared to the 1500m s^{-1} sound speed in water.

The second category is internal gravity waves, which occur within a fluid. These have also been observed in the ocean, with tracers or detectors suspended in the fluid, or by using satellites such as the Earth Resources Technology Satellite (Apel et al., 1975). Internal waves can also be found in the atmosphere. For example, the so-called Morning Glory waves that are observed around 150m above the Australian coast, first documented in the Royal Australian air force in 1942, travel at around 10m s^{-1}. As well as travelling slower than sound waves, internal gravity waves also occur on much larger spatial scales: a crest of a wave in the Morning Glory wavetrain will have a wavelength of approximately 10km, as documented by Clarke (1971), compared to the 3cm wavelength of sound waves. More recent observations of atmospheric internal gravity waves are reviewed in Hocke and Schlegel (1996).

The first internal waves were documented in 1792 by Benjamin Franklin, who conducted an experiment with oil on water. Later, in 1898, Bjerknes attempted to explain the 'dead water' phenomenon using internal waves, which were subsequently investigated experimentally by Ekman in 1904. Since then, two-layer hydrodynamic models have been used to describe the ocean (see, for example, Gill (1982)), with a well-mixed upper layer (with buoyancy frequency close to zero) overlaying a deeper lower layer.

There are many other examples of forces that give rise to waves; inertial waves, for example, arise from the Coriolis force arising from the Earth's rotation. Surface tension can also contribute to the restoring force of waves. Of course, when we say 'the restoring force', we really mean the *dominating* restoring force; in reality this is not the only force present on any system.

1.1.1 Magnetically influenced waves

In this thesis we are particularly interested in the nature of waves in electrically conducting fluids, possibly influenced by rotation and gravity. When a fluid (typically gaseous hydrogen) has enough thermal energy, or when it is under enough pressure, the electrons break free from the atoms comprising the gas in a process known as ionisation, and are able to move freely in the fluid. Under such conditions, the fluid conducts electricity and becomes a plasma, the fourth state of matter (see explanations by Priest, 1982; Goldston and Rutherford, 1995; Goedbloed and Poedts, 2004, for a more in-depth insight). Since electric charges are able to move about freely, the particles comprising the fluid are affected by magnetic fields, and can move in response to an imposed field.

Movement of the ions in the fluid can also *generate* magnetic fields by magnetic induction; this interplay between the flow velocity and magnetic fields is described by the equations of magnetohydrodynamics (MHD). The equations of MHD are an extension of the standard hydrodynamic fluid equations of motion; they contain an extra force in the Navier-Stokes equation (the Lorentz force) and the addition of an equation for magnetic induction, which describes the evolution of magnetic field (see, for example, Goedbloed and Poedts (2004)). Standard MHD is non-relativistic; the induction equation is derived from Maxwell's equations (which are exact) and Ohm's law for a moving conductor (which is not). This constraint on fluid velocity, however, is not such a huge restriction for flows inside the Sun, where typical speeds are modest, as documented by Priest (1982); Hughes et al. (2007).

Electromagnetism was founded by Maxwell (1861), furthering the work by Faraday (1821) and Ampère (1827), but it was over a hundred years later when Alfvén (1942) was the first to propose waves with magnetic tension as the restoring force. These Alfvén waves propagate by disturbing magnetic field lines, which are carried by the fluid. Magnetic tension resists the bending of field lines, and provides the force that returns the magnetic field and the accompanying fluid back to its unperturbed state. Alfvén waves, then, can travel along the field lines rather like waves travel down a guitar string when it is plucked, with a speed increasing with magnetic field strength. Since their discovery in 1942, magnetically influenced waves have been proposed in heating mechanisms in the solar atmosphere by Alfvén (1947), attributed to oscillations in the Earth's magnetic field by Dungey (1954), and proposed as a method of energy transport in the interstellar medium by Parker (1955). The role of rotation on magnetic waves has been studied, both in MHD by Lehnert (1955), for example, and in shallow water magnetohydrodynamics (SWMHD) by Zaqarashvili et al. (2008). Figure 1.2 is a timeline of some of the advances in the study of magnetically modified waves.

Often, magnetic tension is not the only restoring force; it can conspire with gravitational forces to generate magneto-gravity waves in plasmas (see, for example, Priest 1982; Goedbloed and Poedts 2004); these will feature prominently in this work.

1.2 Astrophysical objects and stellar dynamics

The universe is almost entirely ionised. We are in constant contact with the few bits that are not, such as the Earth's atmosphere and oceans, but electrically charged fluids are ubiquitous throughout the cosmos. Many, if not all, of these fluids will support magnetically influenced waves: the outer core of the Earth, the solar wind, and galactic discs are all examples of electrically conducting fluids.

The atmosphere of Jupiter is composed mainly of hydrogen in a gaseous state, at least near the surface. In this regime, where weather phenomena such as the Great Red Spot occur, the gas is wrapped around the planet in a thin atmospheric layer which is not electrically conducting (featured in the works of Dowling and Ingersoll 1989; Showman 2007; Warneford and Dellar 2014). Deeper in the Jovian atmosphere, the hydrogen becomes ionised owing to the high temperatures and pressures, and the fluid becomes known as metallic hydrogen, which is electrically conducting.

Other examples of astrophysical phenomena that involve ionised fluid include accretion discs (see, for example, Weizsacker (1948); Balbus and Hawley (1998); Umurhan (2008)). These are thin layers of gas and dust orbiting a central body, which very slowly accretes (gathers) onto the central mass. One could model this as a Keplerian disc, with centrifugal forces balancing the pull of gravity towards the centre, and weak gravity acting towards the meridional plane of symmetry, as outlined by Kepler in the seminal Astronomia Nova in 1609. Of course, one would have to include the differences in orbital velocity in this model, for example using a shearing box (see, for example, Blaes 2003); the velocity shear would have to be taken into account when considering basic states to perturb.

Stars too consist of plasma, held in an almost spherical shape by gravitational forces. Recent advances in helioseismology by Christensen-Dalsgaard et al. (1996); Schou et al. (1997); Charbonneau et al. (1999) have revealed the structure of the interior of the Sun, by observing vertical oscillations of fluid on the solar surface as very slight Doppler shifts in the spectrum of light omitted. The paths of these helioseismic waves through the interior of the Sun are then inferred from surface observations. These techniques have led to the discovery of the tachocline, a thin layer of velocity shear located at around $0.7R_{\odot}$, or $200,000$km below the solar surface, radially.

The tachocline, first coined by Spiegel and Zahn (1992), is a layer of electrically conducting fluid in the Sun, which bridges the transition region between the outer convective region and the inner radiative region of the Sun. Its defining property is its velocity shear. The lower boundary of the tachocline contains the inner two-thirds of the Sun (by radius), which exhibits approximate solid body rotation, perhaps due to a relic magnetic field. The upper boundary meets the convective region of the Sun, which is differentially rotating; the velocity difference between these two bounding regions is reconciled by shear flows in the shallow tachocline. The shear flow stretches out magnetic fields in the direction of flow, since magnetic diffusion is so low in the Sun, and magnetic field lines are ‘frozen in’ to the fluid. This conversion of poloidal to toroidal field, the ω-effect, is one half of the story of solar dynamo models, which attempt to explain how huge astrophysical bodies maintain their large-scale magnetic fields (see, for example, Jones et al.,

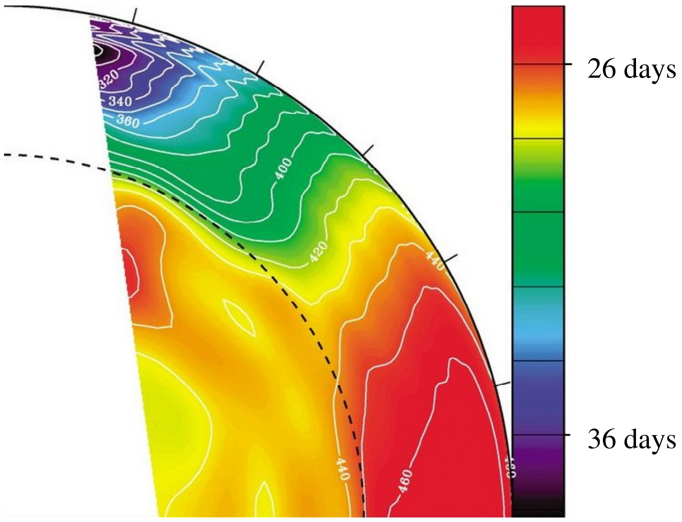

Figure 1.1 – Internal rotation of the Sun as inferred using helioseismology. Rotation rate is colour-coded so that on the surface, fluid at the equator takes around 25 days for one rotation around the Sun; fluid towards the equator takes around 36 days. This differential rotation ends rather abruptly at the tachocline (dotted line). Image courtesy of the High Altitude Observatory.

2010). Since the field is predominantly toroidal in the tachocline, one may choose to model this in a Cartesian system with a locally horizontal magnetic field. Although the horizontal geometry of the magnetic field in the tachocline is widely accepted, the strength of the field remains a point of contention. Buoyancy arguments with flux tubes give a value of 10T, or 10^5G (e.g. Schecter et al., 2001), but other studies that take into account extra MHD effects suggest a much lower value of 0.2T, or 2000G (e.g. Gough, 2007).

In the turbulent convection zone, where heat transfer is achieved by overturning of the fluid, convective plumes are able to penetrate the tachocline. Bounding the layer from below is the stably stratified radiative zone, where heat is transferred primarily by radiation. This has led to a further partition of the tachocline into an overshoot sublayer, which contains the 'overshooting' convective flows, and a radiative sublayer (adjacent to the radiative zone).The radiative sublayer is thought to be stably stratified, with gravitational buoyancy balancing pressure gradients in the vertical. This vertical balance of forces is known as magnetohydrostatic balance.

This thesis will be concerned with stratification, magnetic field configurations and rotation; we will not consider the role of shear flows (see Mak, 2013, for a discussion of SWMHD shear flows). See Hughes et al. (2007) for a range of articles on different aspects of the tachocline for the interested

Quantity	Meaning	Value	Units
ρ_{top}	density at top	178	$\text{kg}\,\text{m}^{-3}$
ρ_{bottom}	density at bottom	208	$\text{kg}\,\text{m}^{-3}$
g	gravitational acceleration	54	$\text{m}\,\text{s}^{-2}$
N	buoyancy frequency	8×10^{-5}	s^{-1}
$0.02R_\odot$	depth	1.392×10^{7}	m
$\lvert\mathbf{B}\rvert$	magnetic field strength	0.2	T
v_G	gravity wave speed	19	$\text{m}\,\text{s}^{-1}$
v_A	Alfvén wave speed	13	$\text{m}\,\text{s}^{-1}$
v_S	sound speed	2.25×10^{5}	$\text{m}\,\text{s}^{-1}$
Rm	magnetic Reynolds number	10^{8}	-

Table 1.1 – Parameter values for the radiative layer of the tachocline used in this work, taken from Gough (2007), and Christensen-Dalsgaard et al. (1996). The 'top' of this sublayer has been taken to be situated at $0.72R_\odot$ and the 'bottom' at $0.7R_\odot$. Values for Alfvén speed and sound speed have been calculated with median values at $0.71R_\odot$.

reader.

1.3 The shallow water approximation

A common feature in some of the above examples of naturally occurring electrically conducting layers (such as accretion disks, planetary atmospheres, and the tachocline) is that they are, in some sense, *thin*; the height of one of these layers is much less than a typical horizontal length scale (a wavelength, for example). This is also true for many phenomena in Earth's atmosphere and oceans, and the ubiquitous thin property has prompted further study, as documented by Gill (1982); Vallis (2006).

Waves in shallow fluid layers have been studied for many years; Laplace used the shallow water equations as far back as 1776. The shallow water approximation, which takes advantage of the small aspect ratio of vertical to horizontal length scales in a thin layer of fluid, has since been used to model geophysical phenomena such as tsunamis in the ocean and flows in our stably stratified atmosphere (see, for example, Gill 1982; Vreugdenhil 1994). Its attraction is that it makes the full governing equations of motions mathematically simpler. Not only do the shallow water equations contain two (rather than three) components of velocity whilst retaining gravity, rotation and stratification, but also variables such as horizontal velocity are independent of vertical co-ordinate z, making significant mathematical savings.

The introduction of magnetic effects into the shallow water system was first proposed by Gilman (2000), who derived the equations of shallow water magnetohydrodynamics (SWMHD). This developed Gilman's earlier work on a quasi-geostrophic form of the SWMHD system (see Gilman, 1967a,b,c). The equations of SWMHD describe a stably stratified thin layer of ionised gas, or plasma, some examples of which we shall discuss later. They extend the hydrodynamic shallow water equations by introducing a Lorentz force in the momentum equation, and including a magnetic induction equation. The system was later shown to be hyperbolic and Hamiltonian by De Sterck (2001); Dellar (2002b,a). The equations contain fewer variables than the full 3D MHD equations, since the vertical components of both magnetic field and velocity are linear functions of height and do not appear in the equations. Furthermore, as in the hydrodynamic case, the variables used in the SWMHD system are independent of z.

Of course, there are limitations to what the shallow water equations can be used to describe. However, the simplicity and understanding gained makes this worthwhile. Physical applicability still holds: we have discussed many examples of shallow layers in astrophysics and well as geophysics. Indeed, Dowling and Ingersoll (1989) and Warneford and Dellar (2014) have applied the shallow water approximation to the Jovian atmosphere and Umurhan (2008) to accretion discs in the hydrodynamic case. Gilman (2000), Dikpati and Gilman (2001), Schecter et al. (2001), and Heng and Spitkovsky (2009) have applied the SWMHD model to the solar tachocline. Of course, this approximation means that our model deviates from the real physical scenario, but it is slight in the above examples. The ability to proceed with analysis on a much simpler mathematical model is a very worthwhile trade-off.

There are many interesting dynamics one could choose to study with the SWMHD system; for example, Mak (2013) looked for shear-flow instabilities. There have even been attempts to model aspects of the solar dynamo using the SWMHD equations by Lillo et al. (2005), although this is disputed. In this work, we will consider wave-like motion supported by these governing equations.

Studies on linear and nonlinear waves in the SWMHD system were first undertaken by Schecter et al. (2001), and London (2014) performed a weakly nonlinear analysis on the SWMHD system, and these have been applied to the tachocline, which almost certainly supports wakelike motion. Indeed, the SWMHD system developed by Gilman (2000) may have been created as a conceptual model of the then recently discovered tachocline, which was proposed by Spiegel and Zahn (1992) and confirmed by helioseismology by Schou et al. (1997). The exact properties of the supported waves, such as phase and group velocities and structure, are not well known because knowledge of the magnetic structure in the tachocline is uncertain. However, the roles they play in mixing and transfer of energy have interesting ramifications: for example, they could exert effects on the complicated magnetic field rearrangements necessary for the dynamo effect. It has even been proposed by Forgacs-Dajka and Petrovay (2001) that waves may play a role in the confinement of the tachocline itself, helping to explain why it remains so thin.

An extension to the single layer system is the multi-layer model, in which more than one layer are stacked immiscibly (see, for example, Zeitlin, 2013). In hydrodynamic applications, the advantages with having more than one layer is that it enables a greater control over the stratification of the system, and also more options for a basic state (different velocities in different layers, for example). In the multi-layer SWMHD system, one has all the advantages of the hydrodynamic multi-layer system, but also that the basic state magnetic field, too, can be different in each layer. This allows us to model the effects on waves of magnetic fields that vary with depth, and is the main focus of Chapter 4. By ensuring that the vertical structure of field is adjustable in our models, we allow for further helioseismic discoveries with the tachocline, or keep the models applicable to other astrophysical phenomena.

Another of the advantages of having a model with more than one layer, in the hydrodynamic regime, is that one can experiment with different stratification settings. Experiments and observations of waves in two-fluid shallow water systems go back many years, as documented by Gill (1982). Models with two immiscible shallow water layers have been the main focus, in works by Choi and Camassa (1999), Ovsyannikov (1979), and Benjamin (1966), for example, but extensions to more general n-layer systems have been undertaken in the hydrodynamic case by Stewart and Dellar (2010), Vallis (2006) and Liu and Wang (2012). Since then, magnetic fields have been introduced to multi-layer (thin layers, but non-shallow water) MHD models (e.g. Umurhan, 2013) and more recently SWMHD systems (e.g. Zeitlin, 2013, and this thesis; these seem to have been achieved simultaneously). One of the aims of this thesis is to further this work and consider wave dynamics in more detail.

Aims of the thesis

The hydrodynamic (non-magnetic) shallow water equations have been well-studied and used to describe fluid motion in planetary atmospheres and oceans; waves in such models with one or more layers are well understood. However, what is *not* well understood is the role that magnetic field plays when the fluid is electrically conducting. We will consider the changes in phase and group velocities brought about by the addition of magnetic fields, as well as the structural augmentations of the waves. In the linear hydrodynamic case, both phase and group velocity are known to be isotropic and equal in both horizontal directions. It is also known that magnetic fields introduce a restoring force in the direction of magnetic field lines; exactly how this is manifest in multi-layered shallow water systems is not yet known, and will be investigated in Chapters 3 and 4.

It has been shown that energy is conserved in the shallow water system, but a corresponding conservation law has not yet been derived in SWMHD. The magnetic energy flux in shallow water systems is hitherto unknown; these issues will be addressed in Chapter 3.

Nonlinear effects in hydrodynamic shallow water systems are also well understood. Solitons are ubiquitous in studies of nonlinear waves, as are cnoidal waves; it is interesting to see how these are manifest in the SWMHD model, and exactly what effect magnetic field has. The magnetic influence on any solitary waves will be discussed in Chapter 5, together with an analysis of the effect of magnetic field geometry on cnoidal waves.

The phenomenon of three-wave resonance is also a well-known interesting phenomenon, in which three separate waves exchange energy periodically (see, for example, Craik (1985)). It is of interest to find out if this is possible in the SWMHD system, and how the magnetic influence is manifest; such an analysis has not yet been undertaken in the SWMHD system. We will shed some light on these small-amplitude dynamics in Chapter 6.

There is little understanding of the nonlinear effects in magnetically influenced shallow water systems, and so one aim of this work is to investigate this. One aim of Chapter 6 is to relax the small-amplitude constraint and analyse the dynamics numerically. Well-known nonlinear dynamics such as wave steepening and the cascade of energy to smaller length scales will be examined for the first time in SWMHD.

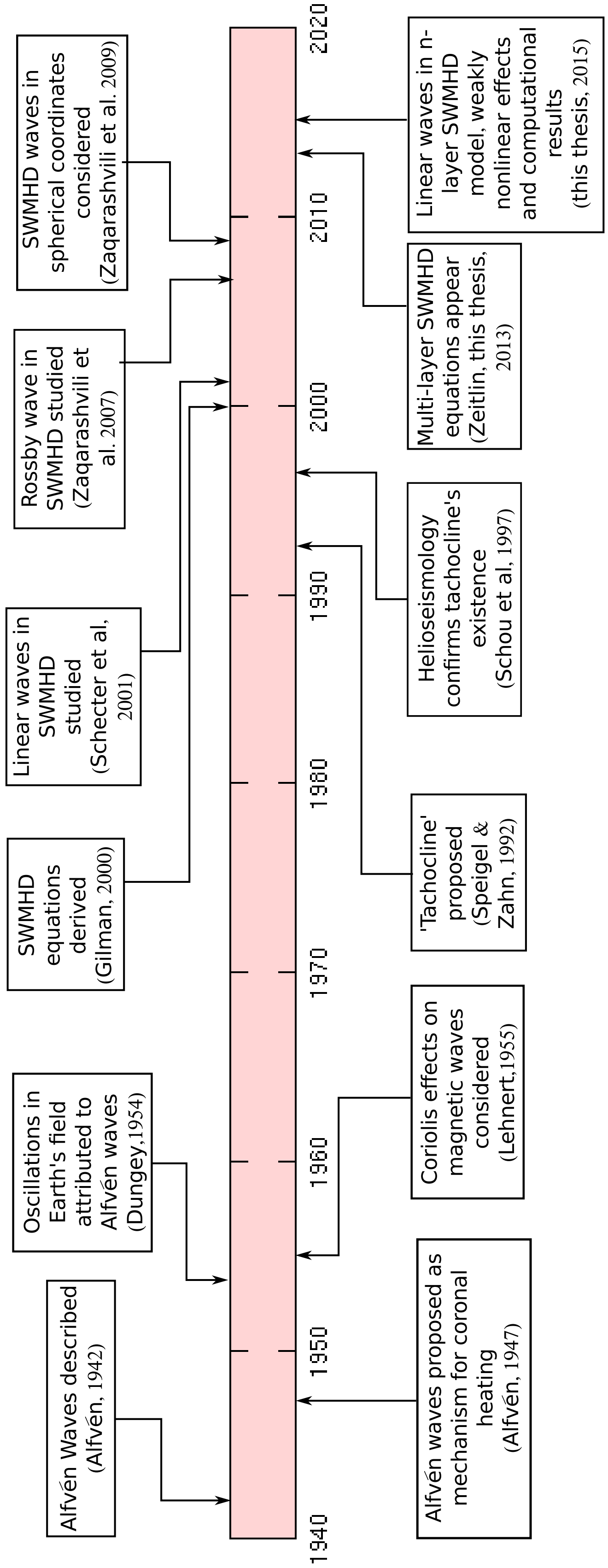

Figure 1.2 – Selected history of the study of magnetic systems, pertinent to this thesis.

1.4 Outline of the thesis

The thesis is split into two main sections: Chapters 2, 3, and 4 focus on linear wave analysis, including single- and multi-layer systems, and nonlinear wave dynamics are discussed in Chapters 5 and 6, including a weakly nonlinear analysis.

In Chapter 2, the single layer SWMHD equations will be derived, building on the work of Gilman (2000). The differences between these and the conventional two-dimensional compressible MHD equations will be discussed, and the analogy that exists between the two systems in the purely hydrodynamic case will be tested with the introduction of magnetic field. Linear waves shall then be sought in a similar manner to Schecter et al. (2001) and Heng and Spitkovsky (2009), and a dispersion relation bridging the two systems (SWMHD and compressible MHD) will be found and analysed, helping us to understand the differences between the wave-like dynamics of the well-studied MHD system and the relatively new SWMHD model.

The focus of Chapter 3 will be an n-layer model of SWMHD, a system of n immiscible fluid layers stacked atop one another. Particular attention will be paid to the energy in the system and the resulting conservation property, which will be used to determine the stability of a motionless basic state in the stably stratified model. Equations will be derived from which the dispersion relations and wave structure can be obtained. These will allow us to probe the influence of magnetic field on the structures and speeds of the modes present. Chapter 4 will contain a detailed study of the $n = 2$ and $n = 3$ examples, and comparisons to hydrodynamic cases will be made, with particular scrutiny on new wave dynamics. The rigid lid model, in which surface displacements are inhibited by a flat lid containing the fluid, has been used in geophysical applications in the absence of magnetic field (see, for example, Gill, 1982). The addition of a rigid lid filters out barotropic modes, and is sometimes favoured when the layer to be modelled is bounded above, by stratification, for example. For the derivations in Chapter 3 we shall also consider the rigid lid cases, and discuss these further in the linear wave analyses in Chapter 4.

In Chapter 5, the focus is on non-rotating weakly nonlinear waves in a shallow (but not shallow-water, since the layer is weakly non-hydrostatic) layer. Solitons (e.g. Lamb (1932)) and cnoidal waves are ubiquitous in nonlinear wave analysis. It would be interesting to see if such waves are supported in the SWMHD model and, if so, what their properties would be. A KdV equation will be derived for both the single layer free-surface and the 2-layer rigid lid models, with the effect of magnetic field geometry on the supported surface profiles considered. In order to investigate how interesting phenomena such as three-wave resonance, documented by Craik (1985), is manifest in the SWMHD model, we will derive weakly nonlinear equations for SWMHD (see, for example, London, 2014) in Chapter 5. The effect of magnetic field on the interchange of energy between modes via the nonlinear terms will be studied.

The aim of Chapter 6 will be to reintroduce rotation into the single layer one-dimensional model.The chapter will begin with an analysis of three-wave resonance in the (rotating) SWMHD model, and a comparison with numerical solutions of the full nonlinear governing equations carried out. [An outline of the computational code is discussed in appendix E, including choice of spatial derivatives and timestepping implementation.] This code will then allow us to probe the dynamics of the system when the surface disturbances are no longer required to be small, and enable study of wave-like motion that is more likely to represent physical systems. Exact nonlinear solutions will then be derived and classified, extending the work of Schecter et al. (2001). The stability of these solutions will be considered at the end of the chapter.

The thesis will end in Chapter 7 with conclusions, discussions, and possible further work.

.

Chapter 2

The single layer model

2.1 Introduction

In this chapter we derive the equations of motion for a single shallow layer of fluid under gravity. This will be based on the model first derived by Gilman (2000). Gilman's derivation was, however, rather brief. Here we shall add additional considerations and explanations to the derivation, and make the chapter (and thesis) self-contained; this model and its governing equations will provide the foundations for the whole thesis.

The hydrodynamic shallow water model (see Stokes, 1849) has been well-studied and applied to many physical stably stratified thin layers, such as the Earth's atmosphere and ocean (see, for example, Gill, 1982). It exploits the small aspect ratio of vertical to horizontal length scales, which leads to approximate hydrostatic balance in the vertical and a simplified set of governing equations. These involve vectors with only two components that depend on x, y and t only, and are therefore easier to analyse, whilst maintaining properties such as stratification. Here, this well-known model is adapted to include the effects of a magnetic field, to enable us to apply it to a shallow layer of electrically conducting fluid. This shallow water magnetohydrodynamic model can then be used to describe the fluid motions in stellar interiors (see Gilman, 2000; Schecter et al., 2001; Heng and Spitkovsky, 2009), accretion discs, planetary atmospheres and other stably stratified thin layers of plasma. The model will primarily be applied to the solar tachocline, a shear layer located inside the Sun at around $0.7R_{\odot}$, where $R\odot \approx 6.96 \times 10^8$m is the solar radius (the interested reader is directed to Hughes et al. 2007 for further information on the tachocline). It contains a stably stratified sub-layer, the radiative sublayer, which is around $0.02R\odot$ deep; this is the layer we aim to model in this thesis.

It is known that in the absence of magnetic field, there exists an analogy between the linear hydrodynamic shallow water and the 2D compressible systems; the equations contain the same terms and so the linear dynamics in each system are equivalent (see, for example, Vallis, 2006). After deriving the governing equations of shallow water magnetohydrodynamics (SWMHD), we will discover that the introduction of a magnetic field breaks this analogy, opening the door to possible new dynamics in the SWMHD system. The chapter will end with an analysis of linear waves in both the 2D compressible MHD and SWMHD systems, with a derivation of a dispersion relation bridging the two models.

2.2 Derivation of the equations of shallow-water MHD

We consider a single layer of fluid of constant density ρ_0, with a free surface at $z = \eta(x, y, t)$, as illustrated in figure 2.1. The fluid occupies a horizontally infinite expanse, with undisturbed depth H and disturbed depth $h = H + \eta$. The fluid is inviscid and perfectly electrically conducting. Figure 2.1 is a schematic of the model set-up.

Of course, fluid in the tachocline (or elsewhere) is not perfectly inviscid, nor perfectly conducting. We are constructing an idealised model and choosing parameters to reflect the physics in the solar tachocline, at all times aware of the attraction of mathematical simplicity. The high values of Rm given in table 1.1, and Re due to the long horizontal length scales, certainly indicate that the effects of viscosity and magnetic diffusion are very low; ignoring their effects completely is therefore a sensible simplification for our purposes. A more detailed model could include the effects of curvature or velocity shear on the wave motion. There are many factors that affect the dynamics in the solar interior, and we have chosen to investigate just two of these, namely stratification and magnetic field topology.

The equations that describe the fluid motion in the layer under these simplifications are then

$$\frac{D\mathbf{u}_3}{Dt} + f\hat{\mathbf{z}} \times \mathbf{u}_3 = -\frac{1}{\rho}\nabla_3 p - g\hat{\mathbf{z}} + \frac{1}{\mu_0 \rho}\mathbf{B}_3 \cdot \nabla_3 \mathbf{B}_3 \qquad \text{(cons. of momentum)} \qquad (2.1a)$$

$$\nabla_3 \cdot \mathbf{u}_3 = 0 \qquad \text{(cons. of mass)} \qquad (2.1b)$$

$$\frac{D\mathbf{B}_3}{Dt} = \mathbf{B}_3 \cdot \nabla_3 \mathbf{u}_3 \qquad \text{(magnetic induction),} \qquad (2.1c)$$

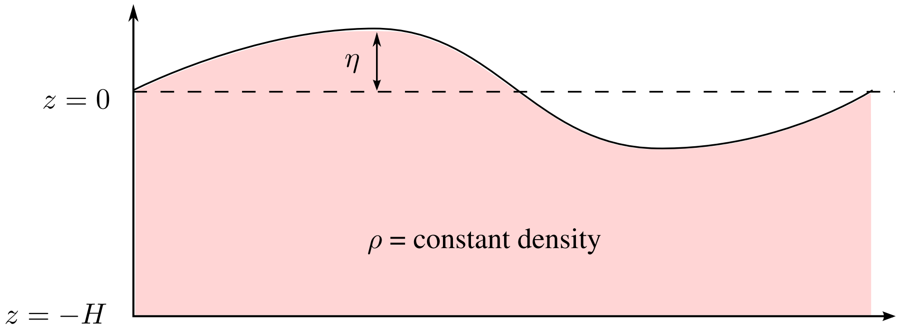

Figure 2.1 – Schematic of the single layer model.

where the vectors $\mathbf{u}_3$ and $\mathbf{B}_3$ are the three-dimensional velocity and magnetic field, respectively. The operator ∇_3 is the (usual) three dimensional grad operator, and $\frac{D}{Dt} \equiv \frac{\partial}{\partial t} + \mathbf{u}_3 \cdot \nabla_3$ the material derivative. The constant f is twice the rotation rate about the local vertical, with unit vector $\hat{\mathbf{z}}$. antiparallel to gravity. The Lorentz force acting on the fluid has also been decomposed into a magnetic tension term, shown on the far right of equation (2.1a), and a magnetic pressure term, which has been absorbed into the mechanical pressure gradient. Thus p in equation (2.1a) is the *total* pressure, i.e. the sum of the mechanical and magnetic pressures, $p = p_{mech} + |\mathbf{B}|^2/(2\mu_0)$.

Equations (2.1a-c) are the equations of ideal MHD. They are complemented by the solenoidal constraint on the magnetic field,

$$\nabla_3 \cdot \mathbf{B}_3 = 0, \tag{2.2}$$

which, if satisfied initially, holds for all future times according to equations (2.1b,c). Equations (2.1) form the basis upon which we shall apply the shallow water approximation in order to derive the equations of SWMHD.

2.2.1 The momentum equation

We should begin by defining exactly what it means for a layer to be shallow. We denote a typical horizontal length (a wavelength, say) by L, and a typical height (for example, the height of the undisturbed layer) by the layer depth H. If the ratio of the typical height to the length is small (smaller than 1/10, perhaps) then the layer is ‘shallow’; i.e., a shallow layer satisfies $\epsilon = H/L \ll 1$.

We shall now estimate the relative sizes of each term in the governing equation for conservation of momentum. Writing equation (2.1a) as two equations, the first a vector equation containing the horizontal components and the second a scalar equation for the third vertical component, we have

$$\underbrace{\frac{\partial \mathbf{u}}{\partial t}}_{\sim\frac{U}{T}} + \underbrace{\mathbf{u}_3 \cdot \nabla_3 \mathbf{u}}_{\sim\frac{U^2}{L}} + \underbrace{f\hat{\mathbf{z}} \times \mathbf{u}}_{\sim fU} = \underbrace{-\frac{1}{\rho}\nabla p}_{\sim\frac{P}{\rho L}} + \underbrace{\frac{1}{\mu_0 \rho}\mathbf{B}_3 \cdot \nabla_3 \mathbf{B}}_{\sim\frac{BB_z}{H}} \tag{2.3a}$$

$$\underbrace{\frac{\partial w}{\partial t}}_{\sim\frac{W}{T}} + \underbrace{\mathbf{u}_3 \cdot \nabla_3 w}_{\sim\frac{UW}{L}} = \underbrace{-\frac{1}{\rho}\frac{\partial p}{\partial z}}_{\sim\frac{P}{\rho H}} - g + \underbrace{\frac{1}{\mu_0 \rho}\mathbf{B}_3 \cdot \nabla_3 B_z}_{\sim\frac{BB_z}{L}}. \tag{2.3b}$$

Horizontal vectors (no subscripts) have been introduced, so that $\mathbf{u} = (u, v)$ represents the horizontal components of the full 3-D velocity field $\mathbf{u}_3 = (u, v, w)$ and $\mathbf{B} = (B_x, B_y)$ denotes the horizontal magnetic field. We also have $\nabla = (\partial_x, \partial_y)$ as the horizontal gradient operator. Typical magnitudes are shown underneath each term, given in terms of U, W, T, etc., where U is a typical horizontal velocity, W a vertical velocity, T a time scale, and so on. The solenoidal conditions on velocity (2.1b) and magnetic field (2.2) imply that $\frac{W}{H} \sim \frac{U}{L}$ and $\frac{B_z}{H} \sim \frac{B}{L}$, and these have also been implemented in the scalings of the equations above. Using the horizontal momentum equation (2.3a), one can determine the size of the horizontal pressure term:

$$\left|\frac{1}{\rho}\nabla p\right| \sim U \max\left\{\frac{1}{T}, \frac{U}{L}, f, \frac{BB_z}{\mu_0 \rho U H}\right\}. \tag{2.4}$$

The magnitude of the magnetic field is assumed to be such that the Lorentz force is the same order of magnitude as the horizontal pressure force in (2.3a). We will now show that the Lorentz force is negligible in the vertical. We can use (2.4) to compare the relative sizes of the terms in the vertical momentum equation, (2.3b). One can verify that

$$\frac{\left|\frac{Dw}{Dt}\right|}{\left|\frac{1}{\rho}\frac{\partial p}{\partial z}\right|} \sim \frac{WH}{UL} \frac{\max\left\{\frac{1}{T}, \frac{U}{L}\right\}}{\max\left\{\frac{1}{T}, \frac{U}{L}, f, \frac{BB_z}{\mu_0 \rho U H}\right\}} \ll 1,$$

$$\frac{\left|\mathbf{B}_3 \cdot \nabla_3 B_z\right|}{\left|\frac{1}{\rho}\frac{\partial p}{\partial z}\right|} \sim \frac{H^2}{L^2} \frac{\frac{1}{\mu_0 \rho} BB_z}{\max\left\{\frac{HU}{T}, \frac{HU^2}{L^2}, fUH, \frac{1}{\mu_0 \rho} BB_z\right\}} \ll 1.$$

Since the pressure term is much larger than the inertial and Lorentz terms under the shallow approximation $H/L \ll 1$, we can thus conclude that the main balance of forces in the vertical is between total pressure and gravity. The fluid is in magnetohydrostatic balance, and approximately satisfies

$$\frac{\partial p}{\partial z} = -\rho g. \tag{2.5}$$

Equation (2.5) can then be integrated to give $p = p_{atm} - \rho g(z - \eta)$, where p_{atm} is the pressure on the surface. This may then be substituted into the horizontal momentum equation, giving

$$\frac{\partial \mathbf{u}}{\partial t} + \mathbf{u}_3 \cdot \nabla_3 \mathbf{u} + f\hat{\mathbf{z}} \times \mathbf{u} = -g\nabla\eta + \frac{1}{\mu_0 \rho}\mathbf{B}_3 \cdot \nabla_3 \mathbf{B}. \tag{2.6}$$

Now, since the free surface height η is a function of x, y and t only, $\nabla\eta$ is independent of z. We can find a consistent solution of (2.6) with $\mathbf{u}$ and $\mathbf{B}$ also independent of z. This enables us to write $\mathbf{u}_3 \cdot \nabla_3 \equiv \mathbf{u} \cdot \nabla + w\partial_z = \mathbf{u} \cdot \nabla$ and $\mathbf{B}_3 \cdot \nabla_3 \equiv \mathbf{B} \cdot \nabla$, leading to the SWMHD momentum equation:

$$\frac{\partial \mathbf{u}}{\partial t} + \mathbf{u} \cdot \nabla \mathbf{u} + f\hat{\mathbf{z}} \times \mathbf{u} = -g\nabla\eta + \frac{1}{\mu_0 \rho}\mathbf{B} \cdot \nabla \mathbf{B}. \tag{2.7}$$

This does not look so dissimilar to the momentum equation in conventional ideal MHD; at first glance it appears that the pressure term has been replaced with a surface height term according to magnetohydrostatic balance (2.5). The crucial difference, however, is that all vectors and differential operators here are two-dimensional, lending a mathematical convenience to any further calculations.

2.2.2 The equation for conservation of mass

Equation (2.1b) is the equation for conservation of mass in a constant density (incompressible) fluid. We shall use this, in conjunction with boundary conditions for flow at the surface and floor, to obtain a shallow water counterpart.

On the surface of the layer, at $z = \eta(x, y, t)$, any velocity flux perpendicular to the surface must be balanced by a corresponding change in surface height, in order to maintain the physical kinematic condition that the fluid stays under the surface of the layer. That is, any nonzero $\mathbf{u}_3 \cdot \mathbf{n}_3$ must induce a change in η, or

$$\frac{\partial \eta}{\partial t} = \mathbf{u}_3 \cdot \mathbf{n}_3 \qquad \text{at} \quad z = \eta, \tag{2.8}$$

where $\mathbf{n}_3$ is the 3-dimensional normal to the surface. This normal can be written as the gradient of $z - \eta = 0$ for an outward pointing normal, giving

$$\mathbf{n}_3 = \left(-\frac{\partial \eta}{\partial x}, -\frac{\partial \eta}{\partial y}, 1 \right).$$

Equation (2.8), therefore, gives

$$w = \frac{\partial \eta}{\partial t} + u\frac{\partial \eta}{\partial x} + v\frac{\partial \eta}{\partial y}, \text{ on } z = \eta. \tag{2.9}$$

This is interpreted physically as vertical velocity following the material derivative of the surface motion. Complementing this surface boundary condition is a corresponding condition for the floor bounding the fluid from below at $z = -H$. Insisting that the floor is impermeable is equivalent to imposing

$$w = 0 \text{ on } z = -H. \tag{2.10}$$

We can now integrate the incompressibility condition (2.1b) over the layer depth, exploiting the fact that $\mathbf{u}$ is independent of z, to get

$$[w]_{z=-H}^{z=\eta} = -(\nabla \cdot \mathbf{u})h, \tag{2.11}$$

where $h = H + \eta$ is the total (perturbed) height of the layer. Applying the boundary conditions (2.9)-(2.10) leads to

$$\frac{\partial \eta}{\partial t} + \nabla \cdot (h\mathbf{u}) = 0. \tag{2.12}$$

Equation (2.12) is the shallow water equation for conservation of mass. A conservation property for surface height, it describes the evolution of the surface in terms of the horizontal mass flux of the fluid below it.

The above derivation assumes that the horizontal velocity is indepent of z. An alternative is to replace the z-dependent horizontal velocity by an average over z (see Wu, 1981), giving

$$\frac{\partial h}{\partial t} + \nabla \cdot (h\bar{\mathbf{u}}) = 0, \tag{2.13}$$

where the overbar denotes a depth average over the layer.

2.2.3 The induction equation

To complete the set of SWMHD equations, we require an equation for the evolution of horizontal magnetic field $\mathbf{B}$. As before, we start with the full three-dimensional induction equation (2.1c), the horizontal component of which can be written as

$$\frac{\partial \mathbf{B}}{\partial t} + \mathbf{u} \cdot \nabla \mathbf{B} + w\frac{\partial \mathbf{B}}{\partial z} = \mathbf{B} \cdot \nabla \mathbf{u} + B_z \frac{\partial \mathbf{u}}{\partial z}. \tag{2.14}$$

Since we are considering solutions of $\mathbf{u}$ and $\mathbf{B}$ that are functions only of x, y and t, the z-derivatives vanish and we are left with

$$\frac{\partial \mathbf{B}}{\partial t} = \mathbf{B} \cdot \nabla \mathbf{u} - \mathbf{u} \cdot \nabla \mathbf{B}. \tag{2.15}$$

Equation (2.15) above is the shallow water induction equation.

For completeness, we should verify that the z-component of (2.1c) is also satisfied:

$$\frac{\partial B_z}{\partial t} = \mathbf{B} \cdot \nabla w + B_z \frac{\partial w}{\partial z} - \mathbf{u} \cdot \nabla B_z - w\frac{\partial B_z}{\partial z}. \tag{2.16}$$

Integrating the solenoidal constraints on velocity (2.1b) and magnetic field (2.2), using the conditions $w = B_z = 0$ on $z = -H$, we find $w = -(z+H)\nabla \cdot \mathbf{u}$ and $B_z = -(z+H)\nabla \cdot \mathbf{B}$. When substituted into (2.16), these give

$$\begin{aligned} \nabla \cdot \left(\frac{\partial \mathbf{B}}{\partial t} \right) &= \mathbf{B} \cdot \nabla(\nabla \cdot \mathbf{u}) - \mathbf{u} \cdot \nabla(\nabla \cdot \mathbf{B}) \\ &= \nabla \cdot (\mathbf{u} \cdot \nabla \mathbf{B}) - \nabla \cdot (\mathbf{B} \cdot \nabla \mathbf{u}), \qquad (2.17) \end{aligned}$$

the latter equality of which can be verified with vector analysis. Equation (2.17) is satisfied by (2.15), and so all three components of the full induction equation (2.1c) hold.

2.2.4 The solenoidal constraint

Supplementing these equations is a constraint on the magnetic field analogous to the condition (2.2) for the 3-D case. In a manner similar to the derivation of (2.12), the derivation of a corresponding condition on magnetic field starts by considering boundary conditions. The conditions we choose for magnetic field are no normal component at the surface ($\mathbf{B}_3 \cdot \mathbf{n}_3 = 0$ at $z = \eta$), and no normal component at the floor ($B_z = 0$ at $z = -H$). This physically translates to the restriction that magnetic field lines do not penetrate the floor (i.e., the floor is perfectly conducting) or the surface (i.e., the material above the surface is perfectly electrically conducting too). Integrating (2.2) over the layer depth, as in the conservation of mass derivation, and applying these boundary conditions one obtains

$$\nabla \cdot (h\mathbf{B}) = 0. \qquad (2.18)$$

We should reiterate that $\nabla \cdot \mathbf{B}$ is not necessarily zero, because in our notation both ∇ and $\mathbf{B}$ are two-dimensional. It is still true, however, that $\nabla_3 \cdot \mathbf{B}_3 = 0$; in fact, if one wanted to calculate the B_z, one would use this solenoidal constraint, along with the horizontal magnetic field components. In a similar manner, the vertical velocity w is easily obtainable from (2.1b).

It is well known that if (2.2) is satisfied initially, then it holds true at all subsequent times; that is, equations (2.1a-c) maintain this constraint over time. In a similar manner, we need to check that the constraint (2.18) holds for all times if it holds initially. Using (2.12) and (2.15) one obtains

$$\begin{aligned}\frac{\partial}{\partial t}(h\mathbf{B}) &= h\frac{\partial \mathbf{B}}{\partial t} + \mathbf{B}\frac{\partial \eta}{\partial t}\\ &= h\mathbf{B}\cdot\nabla\mathbf{u} - h\mathbf{u}\cdot\nabla\mathbf{B} - \mathbf{B}\nabla\cdot(h\mathbf{u})\\ &= h\mathbf{B}\cdot\nabla\mathbf{u} - h\mathbf{u}\cdot\nabla\mathbf{B} - \mathbf{B}(\mathbf{u}\cdot\nabla h) - h\mathbf{B}(\nabla\cdot\mathbf{u})\\ &= h\mathbf{B}\cdot\nabla\mathbf{u} + \mathbf{u}\nabla\cdot(h\mathbf{B}) - \mathbf{u}\cdot\nabla(h\mathbf{B}) - h\mathbf{B}(\nabla\cdot\mathbf{u})\\ &= \nabla_3\times(\mathbf{u}\times(h\mathbf{B})),\end{aligned}$$

where the cross products are the usual three-dimensional cross products. The red term is zero if (2.18) holds. Taking the divergence of the above equation, one deduces that $\partial_t\nabla\cdot(h\mathbf{B}) = 0$, and so the constraint (2.18) is satisfied for all times.

2.2.5 Summary

The governing equations of SWMHD are then

$$\frac{\partial \mathbf{u}}{\partial t} + \mathbf{u}\cdot\nabla\mathbf{u} + f\hat{\mathbf{z}}\times\mathbf{u} = -g\nabla\eta + \frac{1}{\mu_0\rho}\mathbf{B}\cdot\nabla\mathbf{B}, \tag{2.7}$$

$$\frac{\partial \eta}{\partial t} + \nabla\cdot(h\mathbf{u}) = 0, \tag{2.12}$$

$$\frac{\partial \mathbf{B}}{\partial t} + \mathbf{u}\cdot\nabla\mathbf{B} = \mathbf{B}\cdot\nabla\mathbf{u}, \tag{2.15}$$

with

$$\nabla\cdot(h\mathbf{B}) = 0, \tag{2.18}$$

with the vertical components available as linear functions of height according to

$$w = -(z+H)\nabla\cdot\mathbf{u}, \tag{2.19}$$

$$B_z = -(z+H)\nabla\cdot\mathbf{B}. \tag{2.20}$$

Equations (2.7), (2.12) and (2.15) complete the SWMHD system. They comprise a set of five equations with five unknowns (u, v, η, B_x and B_y), and thus form a closed system.

2.3 Energy conservation

The single layer model can be shown to conserve energy (Mak, 2013). To establish this, we consider the three types of energy in the system: kinetic energy from movement of the fluid, magnetic energy and gravitational potential energy (since the fluid is incompressible, we do not need to worry about internal energy). How the sum of these three energies changes over time must be balanced by a divergence of some flux if energy is conserved. With this in mind, we will find an expression for each of these energies, and manipulate the time derivative of their sum into a divergence.

Kinetic energy is defined as $\rho|\mathbf{u}_3|^2/2$ for a blob of fluid of unit volume in the layer, but $w \ll |\mathbf{u}|$ in our simplifications. Integrating this over the layer depth will give the required layer-integrated kinetic energy, E_K. Since $\mathbf{u}$ is independent of z, we find

$$E_K = \frac{1}{2}\int_{-H}^{\eta} \rho|\mathbf{u}|^2\,dz = \frac{1}{2}\rho h|\mathbf{u}|^2, \tag{2.21}$$

where $h = H + \eta$ is the total height of the (disturbed) layer. Taking the time derivative, we have

$$\begin{aligned}\frac{\partial E_K}{\partial t} &= \frac{1}{2}\rho|\mathbf{u}|^2\frac{\partial h}{\partial t} + \rho h\mathbf{u}\cdot\frac{\partial \mathbf{u}}{\partial t}\\ &= -\frac{1}{2}\rho\nabla\cdot\big(h|\mathbf{u}|^2\mathbf{u}\big) - \rho g h\mathbf{u}\cdot\nabla\eta + \frac{1}{\mu_0}h\mathbf{u}\cdot(\mathbf{B}\cdot\nabla\mathbf{B}),\end{aligned} \tag{2.22}$$

using (2.7) and (2.12). Since ρ is a constant, the first term is already a divergence; it remains to manipulate the latter two terms. The second term on the right hand side can be manipulated as

$$\begin{aligned}-\rho g h\mathbf{u}\cdot\nabla\eta &= -\rho g\nabla\cdot(h\eta\mathbf{u}) + \rho g\eta\nabla\cdot(h\mathbf{u})\\ &= -\nabla\cdot(\rho g\eta h\mathbf{u}) - \rho g\eta\frac{\partial\eta}{\partial t},\end{aligned} \tag{2.23}$$

the latter equality making use of equation (2.12). Then the energy conservation law (2.22) becomes

$$\frac{\partial}{\partial t}\left(E_K + \frac{1}{2}\rho g\eta^2\right) = -\nabla\cdot\left(\frac{1}{2}\rho h|\mathbf{u}|^2\mathbf{u} + \rho g h\eta\mathbf{u}\right) + \frac{1}{\mu_0}h\mathbf{u}\cdot(\mathbf{B}\cdot\nabla\mathbf{B}). \tag{2.24}$$

This is almost in the form of a conservation law. The last term can be manipulated as follows:

$$\begin{aligned}\frac{1}{\mu_0}h\mathbf{u}\cdot(\mathbf{B}\cdot\nabla\mathbf{B}) &= \frac{1}{\mu_0}h\mathbf{B}\cdot\nabla(\mathbf{u}\cdot\mathbf{B}) - \frac{1}{\mu_0}h\mathbf{B}\cdot(\mathbf{B}\cdot\nabla\mathbf{u})\\ &= \frac{1}{\mu_0}\nabla\cdot\big(h(\mathbf{u}\cdot\mathbf{B})\mathbf{B}\big) - \frac{1}{\mu_0}h\mathbf{B}\frac{\partial\mathbf{B}}{\partial t} - \frac{1}{\mu_0}h\mathbf{B}\cdot(\mathbf{u}\cdot\nabla\mathbf{B}),\end{aligned} \tag{2.25}$$

the latter equality arising from (2.18) and (2.15). This can be further manipulated to give

$$\begin{aligned}\frac{1}{\mu_0}h\mathbf{u}\cdot(\mathbf{B}\cdot\nabla\mathbf{B}) &= \nabla\cdot\big(\frac{1}{\mu_0}h(\mathbf{u}\cdot\mathbf{B})\mathbf{B}\big) - \frac{1}{2\mu_0}h\frac{\partial}{\partial t}\left(|\mathbf{B}|^2\right) - \frac{1}{\mu_0}h\mathbf{B}\cdot(\mathbf{u}\cdot\nabla\mathbf{B}),\\ &= \nabla\cdot\big(\rho h(\mathbf{u}\cdot\mathbf{B})\mathbf{B}\big) - \frac{1}{2\mu_0}h\frac{\partial}{\partial t}\left(|\mathbf{B}|^2\right) - \frac{1}{2\mu_0}\nabla\cdot\big(h|\mathbf{B}|^2\mathbf{u}\big) - \frac{1}{2\mu_0}|\mathbf{B}|^2\frac{\partial h}{\partial t},\end{aligned} \tag{2.26}$$

making use of (2.12). The second and last terms on the right hand side combine into one time derivative, and (2.24) becomes

$$\frac{\partial}{\partial t}\left(\frac{1}{2}\rho h\left(|\mathbf{u}|^2+\frac{1}{\mu_0\rho}|\mathbf{B}|^2\right)+\frac{1}{2}\rho g\eta^2\right)+\nabla\cdot\left(\frac{1}{2}\rho h|\mathbf{u}|^2\mathbf{u}+\rho gh\eta\mathbf{u}+\mathbf{S}\right)=0, \tag{2.27}$$

where $\mathbf{S}$ is the shallow water Poynting vector, defined by

$$\mathbf{S}=\frac{1}{\mu_0}h\left(\frac{1}{2}|\mathbf{B}|^2\mathbf{u}-(\mathbf{u}\cdot\mathbf{B})\mathbf{B}\right). \tag{2.28}$$

Equation (2.27) is a conservation law satisfied by the governing equations of SWMHD; in the absence of gravity, it reduces to that found by Mak (2013) when velocity shear is neglected. The first term in the time derivative is the kinetic energy E_K we started with; there is an associated kinetic energy flux, $E_K\mathbf{u}$, which is the first term in the divergence. It states that kinetic energy is carried around with the fluid motions, as one might expect. In the absence of all other (non-kinetic energy) terms, the conservation law would indicate that the change in kinetic energy in a given volume over time is balanced by the amount of that energy entering (or leaving) that volume.

Alongside the kinetic energy in the time derivative, there is also a magnetic energy term of the form

$$E_M=\frac{1}{2\mu_0}h|\mathbf{B}|^2. \tag{2.29}$$

This is similar in form to the kinetic energy; in fact, if we compare it with the traditional kinetic energy formula used earlier, $\rho v^2/2$, using the Alfvén speed instead of fluid velocity $\mathbf{u}$, this is the result one would get. The magnetic flux that balances the change in magnetic energy over time is given by (2.28), a shallow-water Poynting vector.

The three-dimensional (non-shallow) Poynting flux is proportional to $\mathbf{E}_3\times\mathbf{B}_3$, the cross product of the electric and the magnetic fields (see Poynting 1884). Since the curl of $\mathbf{E}_3$ equals (minus) the time derivative of $\mathbf{B}_3$, the induction equation gives $\mathbf{E}_3=\mathbf{B}_3\times\mathbf{u}_3$. The traditional 3-D Poynting vector of MHD is then

$$\mathbf{S}_{\text{MHD}}=|\mathbf{B}_3|^2\mathbf{u}_3-(\mathbf{u}_3\cdot\mathbf{B}_3)\mathbf{B}_3, \tag{2.30}$$

which has been derived in the MHD case in previous works (see, for example, Priest 1982). Comparing this MHD Poynting flux with the shallow water analogue (2.28), we find two differences: the first is the factor $1/2$, which arises owing to the (necessary) absorption of the magnetic pressure into a total pressure in the governing momentum equation, and the second in the factor h, which arises through integration over the layer. This indicates that in the shallow water case, a lesser proportion of magnetic flux is attributed to the flow carrying around magnetic energy, and a greater fraction is in the direction of the field. The vector (2.28) can not be written as the vector product of the magnetic and electric fields, and so magnetic flux in the shallow water system is not necessarily perpendicular to these vectors.

The third term in the time derivative of (2.27) is interpreted as a potential energy. When the surface is perturbed, higher fluid has more gravitational potential energy, which is then converted into other forms of energy as is falls. The final term in the conservation law (2.27) is the second term in the divergence, which is the integral of the product of pressure and velocity.

2.4 The analogy with compressible flow

An analogy exists between the shallow water and 2-dimensional compressible systems, in the linear regime, in the absence of magnetic field. That is, the (small-amplitude) perturbation equations that govern the two systems are equivalent, and therefore share the same dynamics; it is therefore interesting to check whether this analogy still holds when a magnetic field is introduced. The existence of an analogy is of interest because one could use the plethora of results from compressible fluids in the study of the fluid dynamics of the shallow water system.

In order to linearise the equations of SWMHD, we first need to define a basic state. Taking a motionless unperturbed fluid, with a flat surface ($\eta = 0$) and uniform, unidirectional ambient magnetic field $\mathbf{B}_0$, we can write the variables η, $\mathbf{u}$ and $\mathbf{B}$ as a sum of their basic state values and their perturbed quantities, denoted with a dash. Substituting $\mathbf{u} = \mathbf{u}'$ and $\mathbf{B} = \mathbf{B}_0 + \mathbf{B}'$ into equations (2.7), (2.12) and (2.15) and neglecting any terms that are quadratic in small quantities, one obtains

$$\frac{\partial \mathbf{u}'}{\partial t} + f\hat{\mathbf{z}} \times \mathbf{u}' = -g\nabla\eta + \frac{1}{\mu_0\rho_0}\mathbf{B}_0 \cdot \nabla\mathbf{B}', \tag{2.31a}$$

$$\frac{\partial \eta}{\partial t} + H\nabla \cdot \mathbf{u}' = 0, \tag{2.31b}$$

$$\frac{\partial \mathbf{B}'}{\partial t} = \mathbf{B}_0 \cdot \nabla\mathbf{u}'. \tag{2.31c}$$

By neglecting small quantities, we are restricting our dynamics to small amplitudes. Note that η is also small.

These equations will now be compared with the (distinct) set of equations that govern the flow in two-dimensional compressible MHD. We shall now consider the equations that govern 2-D compressible systems, and later compare them with the linear SWMHD equations when looking for an analogy.

The 2-D compressible system we shall consider is a perfectly conducting inviscid fluid of constant density. The equations that govern fluid flow in such a system are the Euler equation (conservation of momentum), conservation of mass (not $\nabla \cdot \mathbf{u} = 0$ this time) and an induction equation. These can be linearised in much the same way as above. In MHD systems we need a thermodynamic equation of state linking mechanical pressure p_{mech} and density ρ. The simplest circumstances are when the layer is assumed either isothermal, or to be an adiabatic perfect gas. In both cases $p_{mech} = P(\rho)$, and then

$$p'_{mech} = v_S^2 \rho', \tag{2.32}$$

where v_S is either the isothermal sound speed, P/ρ, or the adiabatic sound speed $\gamma P/\rho$, where γ is the ratio of specific heats. Substituting this into the two-dimensional Euler equation and linearising, the equations governing this flow can be written as

$$\frac{\partial \mathbf{u}'}{\partial t} + f\hat{\mathbf{z}} \times \mathbf{u}' = -\frac{v_S^2}{\rho_0}\nabla\rho' + \frac{1}{\mu_0\rho_0}\mathbf{B}_0 \cdot \nabla\mathbf{B}' - \frac{1}{\mu_0\rho_0}\nabla(\mathbf{B}_0 \cdot \mathbf{B}'), \tag{2.33a}$$

$$\frac{\partial \rho'}{\partial t} + \rho_0 \nabla \cdot \mathbf{u}' = 0, \tag{2.33b}$$

$$\frac{\partial \mathbf{B}'}{\partial t} = \mathbf{B}_0 \cdot \nabla\mathbf{u}' - \mathbf{B}_0(\nabla \cdot \mathbf{u}'). \tag{2.33c}$$

With *no magnetic field*, equations (2.31a) and (2.33a) are equivalent with $g \to v_S^2/\rho_0$ and $\eta \to \rho'$. Also, equations (2.31b) and (2.33b) are equivalent with $H \to \rho_0$. This is the hydrodynamic analogy alluded to previously. If we compare the two sets of equations when a magnetic field is introduced, one can see the presence of two extra terms in the 2-D compressible case. The first of these terms arises from the Lorentz force. It is not possible to combine mechanical and magnetic pressure in this system (as we did in the SWMHD case) because the equation of state applies only to the fluid mechanical pressure (without magnetic influence). The magnetic pressure term is then kept separate, and appears as an extra term in equation (2.33a). The second of these extra terms is in the 2-D induction equation (2.33c), and arises because $\nabla \cdot \mathbf{u} \neq 0$ in this case; it was not present in the shallow water induction equation because in that system $\nabla_3 \cdot \mathbf{u}_3 = 0$.

It appears that the analogy is broken by the presence of a magnetic field. To further explore this, we can write down a set of equations that bridge the gap between the two systems, and look for linear waves. These ‘bridging’ equations artificially link 2-D compressible MHD and SWMHD, and are given by

$$\frac{\partial \mathbf{u}'}{\partial t} + f\hat{\mathbf{z}} \times \mathbf{u}' = -\frac{v_S^2}{\rho_0}\nabla\rho' + \frac{1}{\mu_0\rho_0}\mathbf{B}_0 \cdot \nabla\mathbf{B}' - \frac{1}{\mu_0\rho_0}\delta\nabla(\mathbf{B}_0 \cdot \mathbf{B}') \tag{2.34a}$$

$$\frac{\partial \rho'}{\partial t} + \rho_0\nabla \cdot \mathbf{u}' = 0 \tag{2.34b}$$

$$\frac{\partial \mathbf{B}'}{\partial t} = \mathbf{B}_0 \cdot \nabla\mathbf{u}' - \delta\mathbf{B}_0(\nabla \cdot \mathbf{u}'), \tag{2.34c}$$

where the extra terms (highlighted in red) have been tagged with a δ, so that if $\delta = 0$, the equations describe the SWMHD system, and if $\delta = 1$, they describe the two-dimensional compressible MHD system. Note that using the equivalencies $g \to v_S^2/\rho_0$ and $H \to \rho_0$, the square of the sound speed v_S^2 can be interchanged with the square of the gravity wave speed gH depending on the value of δ. When $\delta = 1$, we are in the compressible MHD regime, and we keep the equations as they are, including the v_S^2. If $\delta = 0$, we are in the shallow water regime, and we should really replace v_S^2 with gH, according to the equivalencies, to remain consistent.

2.4.1 Linear waves

We will now look for linear waves in this model. We can seek solutions to equations (2.34) that are sinusoidal in nature. These waves would represent small amplitude modes with long wavelengths (at least in the shallow water limit $\delta = 0$), which are wave-like both in space and time. Our aim will be to derive an equation relating frequency to wavevector, the dispersion relation. Finding this is very important in wave analysis; it enables one to find the speed of propagation of waves (the phase speed) and the direction and speed of energy transfer (group velocity), as well as well as structural properties.

We seek solutions of the form

$$\mathbf{u}' = \tilde{\mathbf{u}}e^{i(\mathbf{k}\cdot\mathbf{x}-\omega t)}, \tag{2.35}$$

real part understood, where $\tilde{\mathbf{u}}$ is a constant, $\mathbf{k}$ is the wavevector, with magnitude equal to the number of waves per unit length and argument the direction of phase propagation, and ω is the frequency, or number of waves per unit time. The spatial differential operator ∇ is then equivalent to $i\mathbf{k}$, and time derivatives ∂_t are equivalent to multiplying by the factor $-i\omega$. Substituting (2.35) (and similar for ρ' and $\mathbf{B}'$) into the equations of motion (2.34), and combining (2.34a) and (2.34b) to eliminate ρ', one arrives at

$$\omega^2\tilde{\mathbf{u}} + fi\omega\hat{\mathbf{z}} \times \tilde{\mathbf{u}} = v_S^2(\mathbf{k}\cdot\tilde{\mathbf{u}})\mathbf{k} - \frac{1}{\mu_0\rho_0}(\mathbf{B}_0\cdot\mathbf{k})\omega\tilde{\mathbf{B}} + \frac{1}{\mu_0\rho_0}\delta(\mathbf{B}_0\cdot\tilde{\mathbf{B}})\omega\mathbf{k}, \tag{2.36}$$

$$\omega\tilde{\mathbf{B}} = -(\mathbf{B}_0\cdot\mathbf{k})\tilde{\mathbf{u}} + \delta(\mathbf{k}\cdot\tilde{\mathbf{u}})\mathbf{B}_0, \tag{2.37}$$

upon cancelling the common exponential factors. The variable ρ' has already been eliminated; our aim is now to eliminate components of $\tilde{\mathbf{u}}$ and $\tilde{\mathbf{B}}$, to obtain an equation linking ω and $\mathbf{k}$: the dispersion relation. We do this by defining

$$D = \mathbf{k}\cdot\tilde{\mathbf{u}} \qquad \text{and} \qquad Q = \hat{\mathbf{z}}\cdot(\mathbf{k}\times\tilde{\mathbf{u}}),$$

and manipulating equations (2.36) and (2.37) to obtain two equations, with each term as a multiple of D or Q.

For the moment, we will consider $D \neq 0$. In doing so, wave modes that propagate whilst conserving $\nabla\cdot\tilde{\mathbf{u}} = 0$ (i.e., Alfvén waves) are excluded in this analysis; these will be considered later in section 2.6 (see, for example, McLellan and Winterberg 1968). For now we shall consider so-called *magneto-gravity* waves, which, in general, do compress the fluid horizontally as they propagate, in the case $\delta = 0$ (SWMHD). If $\delta = 1$ (2-D compressible MHD) then these waves are known as magneto-acoustic waves.

We proceed by taking the dot product of equation (2.36) with $\mathbf{k}$, yielding

$$\omega^2 D - fi\omega Q = v_S^2 k^2 D - \frac{1}{\mu_0\rho_0}(\mathbf{B}_0\cdot\mathbf{k})(\mathbf{k}\cdot\tilde{\mathbf{B}})\omega + \frac{1}{\mu_0\rho_0}\delta k^2(\mathbf{B}_0\cdot\tilde{\mathbf{B}})\omega.$$

One can then eliminate $\tilde{\mathbf{B}}$ from this equation by taking the dot product of (2.37) with $\mathbf{k}$ and with $\mathbf{B}_0$ in turn. It is useful to establish the relationship

$$\tilde{\mathbf{u}} = \frac{1}{k^2}(D\mathbf{k} + Q(\hat{\mathbf{z}}\times\mathbf{k}))$$

for $\tilde{\mathbf{u}}$ in terms of the perpendicular vectors $\mathbf{k}$ and $\hat{\mathbf{z}}\times\mathbf{k}$ in this process. (This can be verified by taking the dot product with $\mathbf{k}$, and so on.) After some algebraic manipulation one arrives at

$$\begin{aligned}\omega^2 D - fi\omega Q = v_S^2 k^2 D + (1-2\delta)k^2 B_0^2\cos^2\theta D \\ - \frac{1}{\mu_0\rho_0}\delta(\mathbf{B}_0\cdot\mathbf{k})(\hat{\mathbf{z}}\cdot(\mathbf{k}\times\mathbf{B}_0))Q + \delta^2 k^2 B_0^2 D,\end{aligned} \tag{2.38}$$

where $B_0^2 = |\mathbf{B}_0|^2/(\mu_0\rho_0)$ is the square of the Alfvén speed and θ is the angle between the ambient magnetic field $\mathbf{B}_0$ and the direction of wave propagation $\mathbf{k}$. One can then take the z-component of the cross product of $\mathbf{k}$ with equations (2.36) and (2.37) in turn and combine to give

$$\omega^2 Q + fi\omega D = k^2 B_0^2 \cos^2\theta Q - \frac{1}{\mu_0\rho_0}\delta(\mathbf{B}_0\cdot\mathbf{k})(\hat{\mathbf{z}}\cdot(\mathbf{k}\times\mathbf{B}_0))D. \tag{2.39}$$

Writing equations (2.38) and (2.39) in matrix form, and noting that for non–trivial solutions the matrix of coefficients is singular, one can derive the dispersion relation

$$\begin{aligned}\omega^4 &- [k^2(v_S^2 + 2(1-\delta)B_0^2\cos^2\theta + \delta^2 B_0^2) + f^2]\omega^2 \\ &+ k^4 B_0^2\cos^2\theta[v_S^2 + (1-2\delta)B_0^2\cos^2\theta + \delta^2 B_0^2 - \frac{1}{\mu_0\rho_0}\delta^2(\hat{\mathbf{z}}\cdot(\mathbf{k}\times\mathbf{B}_0)/k)^2] = 0.\end{aligned} \tag{2.40}$$

By noting the equality $\frac{1}{\mu_0\rho_0}\left((\mathbf{k}\cdot\mathbf{B}_0)^2 + (\hat{\mathbf{z}}\cdot(\mathbf{k}\times\mathbf{B}_0))^2\right) = k^2B_0^2$, the last term in the relation can be simplified. Then the dispersion relation becomes

$$\begin{aligned}\omega^4 &- \left[k^2(v_S^2 + 2(1-\delta)v_A^2\cos^2\theta + \delta^2 v_A^2) + f^2\right]\omega^2 \\ &+ k^4 v_A^2\cos^2\theta\left[v_S^2 + (1-\delta)^2 v_A^2\cos^2\theta\right] = 0,\end{aligned} \tag{2.41}$$

where $v_A = B_0 = |\mathbf{B}_0|$ is the Alfvén speed. This is a quadratic in ω^2, and has real roots, since its determinant is equal to

$$k^4[2\delta v_A^2\cos^2\theta - 1]^2 + [\delta^2k^2v_A^2 + f^2]^2 + 2k^2(\delta^2k^2v_A^2 + f^2)[1 + 2(1-\delta)v_A^2\cos^2\theta], \tag{2.42}$$

which is positive. Further analysis confirming that frequency of linear waves in these systems is always real is considered in chapter 3. When $\delta = 0$, we replace v_S^2 with gH according to the equivalencies mentioned previously, and the dispersion relation (2.41) describes small–amplitude shallow water 'magneto-gravity' waves in rotating systems, which have been studied previously (Schecter et al., 2001, see). When $\delta = 1$, the relation describes small–amplitude 'magneto-acoustic' waves in 2-dimensional compressible rotating MHD flows, which have been studied previously by, for example, Priest (1982) and Narayanan (2012).

We will now analyse this dispersion relation to establish the properties of the waves in each system, and compare the two.

2.4.2 Analysis of the dispersion relation (2.41), with $f = 0$

In the absence of rotation, $f = 0$, this dispersion relation reduces to a quadratic in the square of the phase speed c^2, which satisfies

$$c = \frac{\omega}{k},$$

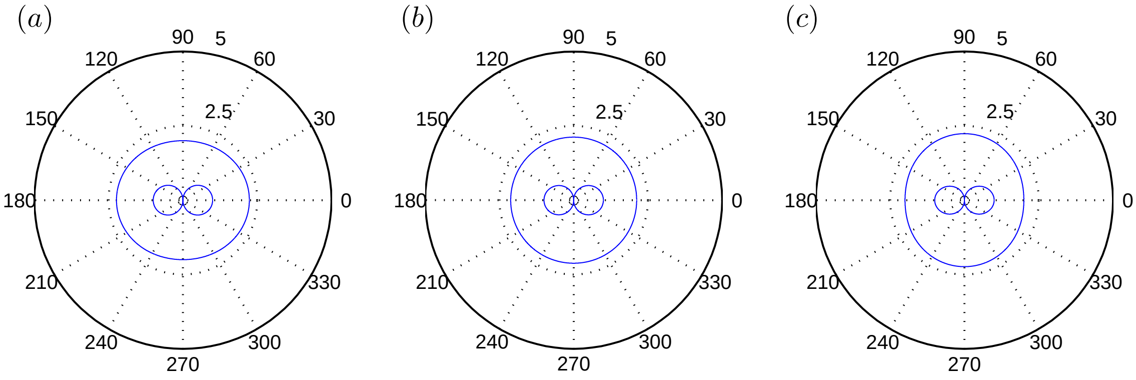

Figure 2.2 – Phase speeds of small–amplitude waves, with the ambient magnetic field as the x-axis, for the shallow water case, $\delta = 0$ (a), the magnetohydrodynamic case, $\delta = 1$ (c) Priest (1982); Goedbloed and Poedts (2004), and a case between the two physical systems, $\delta = 0.5$ (b).

where $k = |\mathbf{k}|$ is the magnitude of the wavevector. The speed c describes the speed of individual waves in the medium, and will be dependent on θ whenever a magnetic field is present, where θ is the angle between the direction of propagation of the wave and the background magnetic field. Solving (2.41) gives

$$c_{\pm}^2 = \frac{1}{2}\left(v_S^2 + 2(1-\delta)v_A^2\cos^2\theta + \delta^2 v_A^2 \pm \sqrt{(v_S^4 + 2\delta(\delta - 2\cos^2\theta)v_A^2 v_S^2 + \delta^4 v_A^4}\right). \quad (2.43)$$

One term in the discriminant has been omitted since it contains the factor $\delta(1-\delta)$, which would be zero in either physically relevant regime (one would have to keep this term in order to produce the centre plot in figure 2.2, in which $\delta = 0.5$, which represents a non-physical system between the two models).

If we align $\mathbf{B}_0$ with the x-axis, we can illustrate the solutions $c(\theta)$ on a polar diagram, as shown in figure 2.2. The length of a line from the origin to the curve, for some fixed value of θ, represents the phase speed of waves at that angle to the x-axis, i.e., to the basic state magnetic field. Although the dispersion relation (2.41) is a quartic equation, the roots come as two pairs, with values of differing signs in each pair; only the positive one has been plotted here, as the negative one corresponds to the mode with the same phase speed travelling in the opposite direction. The number of magneto-gravity (or magneto-acoustic) wave modes is then two, with each mode containing two 'sub-modes' of the same type travelling antiparallel to each other.

The shallow water case

When $\delta = 0$ (i.e., the shallow water case), the solutions (2.43) reduce to

$$c_+^2 = gH + v_A^2 \cos^2\theta \qquad \text{and} \qquad c_-^2 = v_A^2 \cos^2\theta, \tag{2.44}$$

where v_S^2 has been replaced with gH according to the equivalencies. One can see that the c_-^2 mode is always slower than the c_+^2 mode. It exists only in the presence of a magnetic field: it is a compressional Alfvén wave, travelling fastest along field lines. These Alfvén waves can travel in any direction except perpendicular to the magnetic field, through fluid interactions between areas with neighbouring field lines. This can be seen in figure 2.2(a), by noting that the length of a vertical line from the origin to the inner curve is zero. One can also verify that this inner curve describes circles passing through the origin, so that energy transfer via this wave mode is parallel to $\mathbf{B}_0$; we will discuss this in more depth in the section on group velocities later in this chapter.

The faster c_+^2 mode contains a hydrodynamic term, the gravity wave speed gH, as well as a magnetic component. This is a magneto-gravity hybrid mode, with both magnetic tension and gravity supplying the restoring force. Since the gravitational component is isotropic, and is in addition to the force supplied due to the field lines' reluctance to bend, this mode is faster in all directions than the compressional Alfvén mode.

The 2-D compressible case

When $\delta = 1$ (i.e., the 2-D compressible case), the solutions (2.43) become

$$c_\pm^2 = \frac{1}{2}\left(v_S^2 + v_A^2 \pm \sqrt{v_S^4 - 2v_A^2 v_S^2 \cos(2\theta) + v_A^4}\right). \tag{2.45}$$

The extreme values of this function of θ occur when $\theta = 0$ and when $\theta = \pi/2$. If we first consider the positive root c_+, we find that this wave mode propagates at a phase speed satisfying $c_+^2 = v_S^2$ when $\theta = 0$ (parallel to field lines), rising to $c_+^2 = v_S^2 + v_A^2$, as θ is increased to $\pi/2$ (perpendicular to field lines). The direction of propagation for these magneto-acoustic hybrid waves is fastest is perpendicular to the field. This is in contrast to the $\delta = 0$ (shallow water) case, where the preferred direction of travel was parallel to $\mathbf{B}_0$. This appears to confirm our suspicions that the two systems represented by $\delta = 0$ and $\delta = 1$ are not analogous.

Considering now the negative root of (2.45), we find that the square of the phase speed of this mode, c_-^2, lies between 0, when the wavevector is perpendicular to the ambient magnetic field, and v_A^2, when the wavevector is parallel to the field. This mode, again, has the properties of a compressional Alfvén mode in that it travels at the Alfvén speed along field lines and not at all perpendicular to them.

Yet more evidence that the analogy that exists between the two systems is broken with the introduction of a magnetic field is that the two phase speeds can coincide when $\delta = 1$, but not when $\delta = 0$. For example, if the Alfvén speed is equal to the sound speed (i.e. if $v_A = v_S$), then the phase speed of both the Alfvén and the magneto-acoustic modes is equal (to v_A) when $\theta = 0$; i.e., the determinant of (2.43) can be zero only in the compressible MHD case. One can also show that the curves representing the Alfvén mode are not circles when $\delta = 1$. This is almost imperceptible in the right hand plot of figure 2.2 Priest (1982); Goedbloed and Poedts (2004), but is evident from the analytical solution given in (2.45). This is another departure from the shallow water model.

2.4.3 Analysis of the dispersion relation (2.41), with nonzero f

Re-introducing rotation into the system means that the frequency ω is no longer a multiple of k, as is the case when $f = 0$. Dispersive effects come into play, meaning that waves with different wavenumbers propagate at different speeds. To visualise this, one can consider wavevectors perpendicular to the ambient magnetic field, i.e. $\theta = \pi/2$. Then the dispersion relation (2.41) gives $c_-^2 = 0$ (i.e. the Alfvén-like waves that cannot propagate perpendicular to field lines) and

$$c_+^2 = v_S^2 + \delta v_A^2 + \left(\frac{f}{k}\right)^2. \tag{2.46}$$

One can clearly see that the phase speed of these waves depends on the wavenumber $k = |\mathbf{k}|$. The restoring force in this case is a combination of pressure (or gravity, if $\delta = 0$) manifest in the first term, magnetic tension (from the second), and rotation (from the third); this would be an inertia-magneto-gravity hybrid mode.

More generally, for θ not necessarily equal to $\pi/2$, one can rearrange the dispersion relation (2.41) to obtain

$$\tilde{\omega}^4 - \left[\tilde{k}^2\left(v^2 + 2(1-\delta)\cos^2\theta + \delta^2\right) + 1\right]\tilde{\omega}^2 + \tilde{k}^4\cos^2\theta\left[v^2 + (1-\delta)^2\cos^2\theta\right] = 0, \tag{2.47}$$

where $\tilde{k} = kv_A/f$, $\tilde{\omega} = \omega/f$, and $v = v_S/v_A$. Solving this allows us to plot non-dimensional frequency against non-dimensional wavenumber to visualise their relationship. This has been done

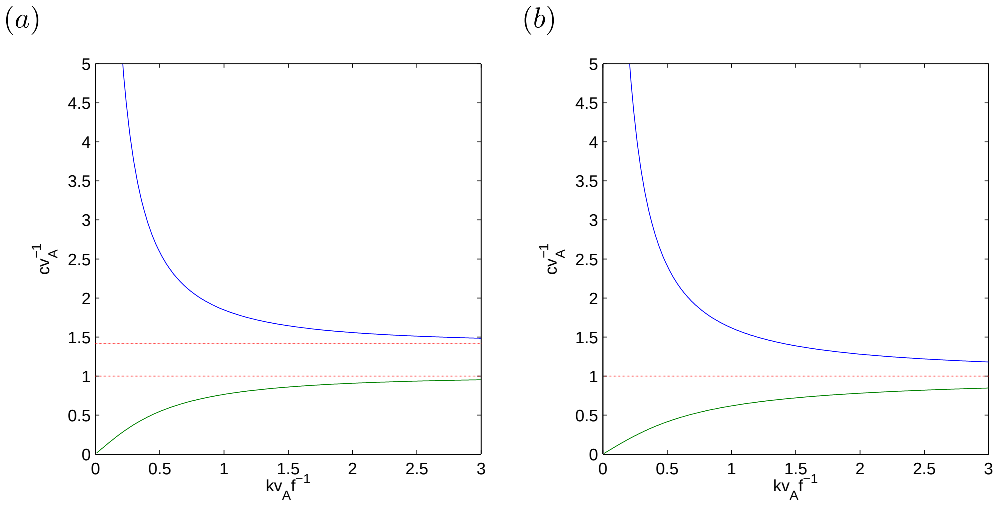

Figure 2.3 – Phase speeds of small–amplitude waves against wavenumber, for the shallow water case, $\delta = 0$ (a) and the 2-D compressible MHD case, $\delta = 1$ (b). The red lines depict the limit $f = 0$. These phase speeds represent waves moving parallel to the ambient magnetic field. In these figures, we have chosen $v_A = v_S$ for illustrative purposes.

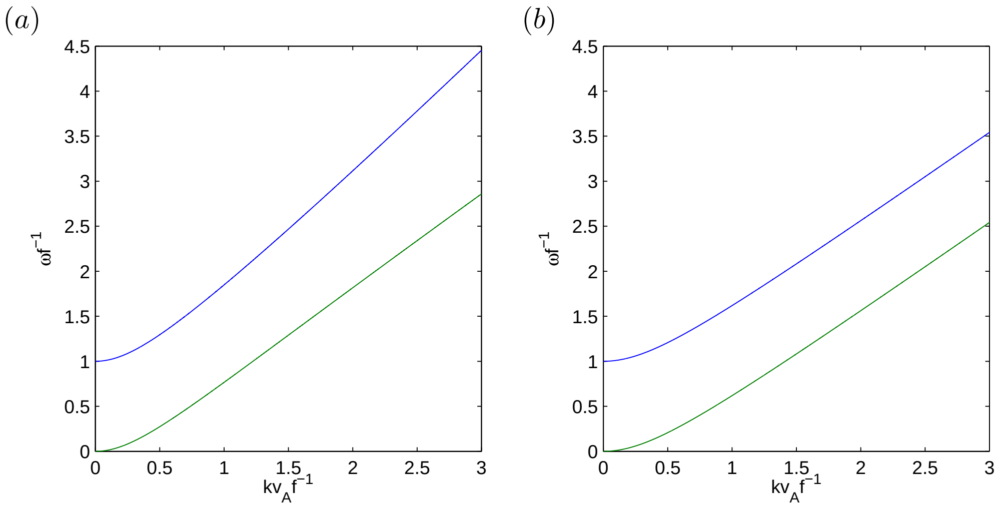

Figure 2.4 – Frequency of small–amplitude waves against wavenumber, for the shallow water case (a) and the magnetohydrodynamic case (b). Again, frequencies represent waves moving parallel to the ambient magnetic field.

in the shallow water case ($\delta = 0$) by Schecter et al. (2001). Keeping magnetic field strength and rotation rates constant is also another way of considering this relationship, which is plotted in figure 2.4. The frequency of the fast modes, represented in figure 2.4 with a blue curve, increases as θ is increased for the shallow water case for large kv_A/f. In the magnetohydrodynamic case, the frequency of the modes *decreases* with increasing θ, for large kv_A/f. The green curves, which represent the frequency of the slower modes, decreases to zero as θ is increased to $\pi/2$; this is also seen in figure 2.2 in the case $f = 0$.

Similarly, one can rearrange (2.41) to express $\tilde{c} = c/v_A$ in terms of $\tilde{k}$; this is plotted in figure 2.3. When the rotation rate is low, towards the right hand side of the graphs, the phase speeds are approximately those found in the non-rotating case, shown as red lines on the phase speed graphs in figure 2.3. The effect of rotation on propagation speed can be inferred by tracing the curves back to the left, towards the vertical axis. Alternatively, one could think of this as fixing f and varying the wavenumber k, so that the phase speeds of waves with longer wavelengths are towards the vertical axis on the left, and the shorter wavelengths towards the right. As predicted, when θ is increased to $\pi/2$, the phase speeds of the slower modes in both cases decrease to zero for all wavenumbers.

2.5 Group Velocity

Physically, perhaps a more important property of wave modes is the group velocity, denoted $\mathbf{c}_g$, which is the velocity of *packets* of waves. In this sense, it reveals the direction and relative speed of the transfer of energy around the system. So far we have considered phase velocities of wave modes present in the model, and how they are affected by magnetic field and other factors such as rotation, which tell us how fast the individual waves travel and in which direction. Our aim for this section is to investigate the effects of magnetic fields on group velocities in a similar manner, taking into account both field strength and orientation.

The group velocity is generally given by the formula

$$\mathbf{c}_g = \frac{\partial \omega}{\partial \mathbf{k}}. \tag{2.48}$$

However, to generate the polar diagrams described above, it is not enough to calculate the partial derivatives in (2.48) and plot them as a pair of parametric equations, because the angle with the

x axis would still be θ, the angle between $\mathbf{k}$ and $\mathbf{B}_0$. This would mean that any point on this curve would represent the speed of a wavepacket *comprised of waves travelling in that direction*. We require a new angle, ϕ, that denotes the angle at which the wave *packets* propagate (measured anticlockwise from the magnetic field), as opposed to the angle θ, which measures the direction of propagation of the waves themselves.

The general approach used in this work follows these three steps:

- Step 1: First find the partial derivatives of frequency, as in equation (2.48).
- Step 2: Project these derivatives onto vectors that are parallel and perpendicular to the wavevector $\mathbf{k}$.
- Step 3: Plot the resulting vectors as a polar plot, using the newly defined angle ϕ.

For compressible MHD, this has been done by Goedbloed and Poedts (2004). Here we thoroughly explain the method, using the dispersion relation (2.41), to verify previous results, and to say something new about the shallow water system. We shall take $f = 0$ for simplicity, so that the dispersion relation (2.41) takes the form

$$\omega^4 - R\omega^2 + S = 0, \tag{2.49}$$

where

$$R = (1 + \delta^2 v_A^2)k^2 + 2(1 - \delta)v_A^2 k_x^2 \tag{2.50}$$

and

$$S = v_A^2 \left(k^2 + (1 - \delta)^2 v_A^2 k_x^2\right) k_x^2, \tag{2.51}$$

noting that $\mathbf{k} = (k_x, k_y) = (k\cos\theta, k\sin\theta)$, where $k = |\mathbf{k}| = \sqrt{k_x^2 + k_y^2}$. Then (2.49) gives

$$\omega^2 = \frac{1}{2}\left(R \pm \sqrt{R^2 - 4S}\right). \tag{2.52}$$

Differentiating the general dispersion relation (2.49) implicitly with respect to k_x^2 and k_y^2 respectively, we find

$$\frac{\partial \omega^2}{\partial k_x^2} = \frac{\dfrac{\partial R}{\partial k_x^2}\omega^2 - \dfrac{\partial S}{\partial k_x^2}}{2\omega^2 - R} \qquad \text{and} \qquad \frac{\partial \omega^2}{\partial k_y^2} = \frac{\dfrac{\partial R}{\partial k_y^2}\omega^2 - \dfrac{\partial S}{\partial k_y^2}}{2\omega^2 - R}. \tag{2.53}$$

Since

$$\begin{aligned}\frac{\partial \omega^2}{\partial k_x^2} &= 2\omega \frac{\partial \omega}{\partial k_x}\frac{\partial k_x}{\partial k_x^2} \\ &= \frac{c}{\cos\theta}\frac{\partial \omega}{\partial k_x},\end{aligned} \tag{2.54}$$

and similarly for $\partial\omega^2/\partial k_y^2$, we have

$$\mathbf{c}_g = \frac{1}{c}\left(\cos\theta\frac{\partial \omega^2}{\partial k_x^2},\, \sin\theta\frac{\partial \omega^2}{\partial k_y^2}\right)^T, \tag{2.55}$$

where the partial derivatives of ω^2 are evaluated in (2.53). This completes step 1 in the process. Now, one could plot this vector parametrically with θ as the parameter. However, this would not illustrate the velocities of packets of waves in a given direction, but rather the velocities of the waves that comprise those packets. Hence we must define a new angle, ϕ, for the direction of propagation of these groups of waves, as outlined in steps 2 and 3.

To do this, we project (2.55) onto unit vectors in the direction of the wavevector $\hat{\mathbf{k}}$, and a vector perpendicular to this, which we shall call $\hat{\mathbf{k}}_\perp$. These are defined by

$$\hat{\mathbf{k}} = (\cos\theta, \sin\theta)^T \quad \text{and} \quad \hat{\mathbf{k}}_\perp = (\sin\theta, -\cos\theta)^T.$$

Projection onto $\hat{\mathbf{k}}$ yields

$$\mathbf{c}_g \cdot \hat{\mathbf{k}} = \frac{1}{c}\left(\cos^2\theta\frac{\partial \omega^2}{\partial k_x^2} + \sin^2\theta\frac{\partial \omega^2}{\partial k_y^2}\right). \tag{2.56}$$

We will now show that this projection, the right hand side of equation (2.56), is equal to the phase speed c. Replacing the partial derivatives according to equations (2.53), one finds

$$\begin{aligned}\mathbf{c}_g \cdot \hat{\mathbf{k}} &= \frac{1}{c}\left(\frac{\left(\cos^2\theta\frac{\partial R}{\partial k_x^2} + \sin^2\theta\frac{\partial R}{\partial k_y^2}\right)\omega^2 - \left(\cos^2\theta\frac{\partial S}{\partial k_x^2} + \sin^2\theta\frac{\partial S}{\partial k_y^2}\right)}{2\omega^2 - R}\right) \\ &= \frac{1}{ck^2}\left(\frac{\left(k_x^2\frac{\partial R}{\partial k_x^2} + k_y^2\frac{\partial R}{\partial k_y^2}\right)\omega^2 - \left(k_x^2\frac{\partial S}{\partial k_x^2} + k_y^2\frac{\partial S}{\partial k_y^2}\right)}{2\omega^2 - R}\right),\end{aligned} \tag{2.57}$$

the latter equality arising through a factorisation of k^{-2}.

Substituting according to equations (2.50) and (2.51), equation (2.57) becomes

$$\mathbf{c}_g \cdot \hat{\mathbf{k}} = \frac{1}{ck^2}\left(\frac{R\omega^2 - 2S}{2\omega^2 - R}\right). \tag{2.58}$$

Replacing ω^2 according to (2.52), this becomes

$$\begin{aligned}\mathbf{c}_g \cdot \hat{\mathbf{k}} &= \frac{1}{2ck^2}\left(\frac{R^2 - 4S \pm R\sqrt{R^2-4S}}{\pm\sqrt{R^2-4S}}\right)\\ &= \frac{1}{2ck^2}\left(\pm\sqrt{R^2-4S}+R\right),\end{aligned} \tag{2.59}$$

which equals the phase speed c using (2.52) and $\omega/k = c$. Concluding, the projection of group velocity in the direction of direction of the wavevector is equal to the phase speed, if the coefficients in the generalised dispersion relation (2.49) satisfy certain conditions. These conditions are that the coefficient of ω^2 is linear in k_x^2 and k_y^2 independently, and the coefficient of ω^0 is quadratic in these terms.

We have successfully projected our parametric expression for group velocity onto the unit wavevector (and obtained c). In order to complete step 2 of the process, it remains to find the projection onto $\hat{\mathbf{k}}_\perp$. This yields

$$\mathbf{c}_g \cdot \hat{\mathbf{k}}_\perp = \frac{\sin 2\theta}{2c}\left(\frac{\partial\omega^2}{\partial k_x^2} - \frac{\partial\omega^2}{\partial k_y^2}\right). \tag{2.60}$$

This describes the deviation of the group velocity curve from the phase velocity curve. Geometrically, one can think of the final group velocity vector as the sum of the perpendicular vectors $(\hat{\mathbf{k}} \cdot \mathbf{c}_g)\hat{\mathbf{k}}$ and $(\hat{\mathbf{k}}_\perp \cdot \mathbf{c}_g)\hat{\mathbf{k}}_\perp$. The first vector is a straight line from the origin to the phase speed curve, and represents the distance travelled by a wave that has passed through the origin in the direction of that line in a given time. The second vector, which has length given in (2.60), is parallel to the wave crest of that same wave. Their sum is the vector we wish to plot, as shown in figure 2.5. With this in mind, we can write this mathematically and move on to step 3.

The group velocity vector can be written as

$$\mathbf{c}_g = c\hat{\mathbf{k}} + \frac{\sin 2\theta}{2c}\left(\frac{\partial\omega^2}{\partial k_x^2} - \frac{\partial\omega^2}{\partial k_y^2}\right)\hat{\mathbf{k}}_\perp. \tag{2.61}$$

This is at an angle of

$$\phi = \theta - \tan^{-1}\left(\frac{\sin 2\theta}{2c^2}\left(\frac{\partial\omega^2}{\partial k_x^2} - \frac{\partial\omega^2}{\partial k_y^2}\right)\right) \tag{2.62}$$

to the ambient magnetic field. The second term on the right hand side of (2.62) above is the deviation angle from the direction of wave propagation, arising from the $\hat{\mathbf{k}}_\perp$ projection. One could use equations (2.53) to write an explicit definition of ϕ. Finally, the polar curves for group velocity are plotted with magnitude $|\mathbf{c}_g|$ against the angle ϕ.

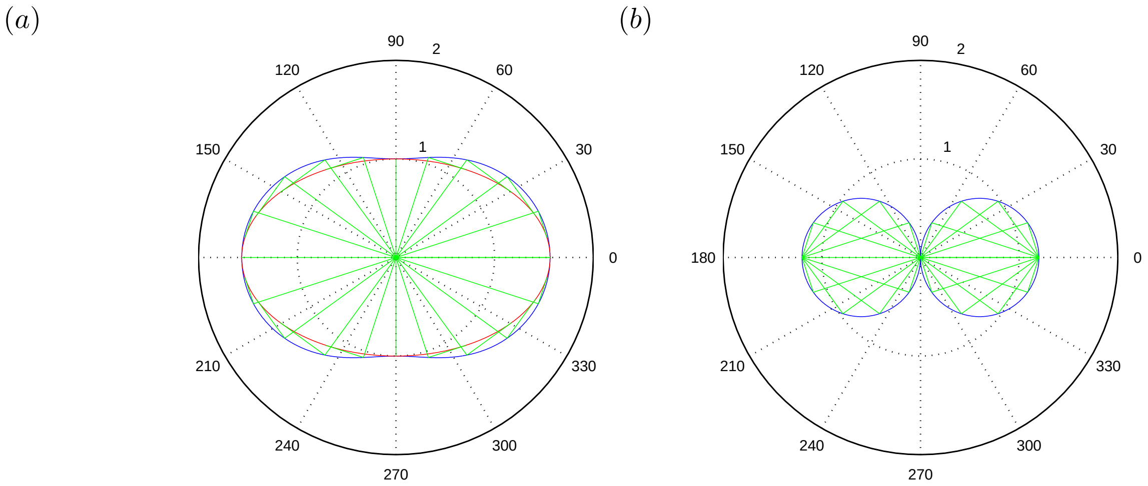

Figure 2.5 – Polar plots of phase velocity (in blue) and group velocity (in red), for the shallow water model ($\delta = 0$). The plots illustrate the two projections (in green) required to produce the group velocity curve; one from the origin to the phase speed curve, and the other perpendicular to this. Plot (a) shows the fast magneto-gravity mode ($+$ signs taken); plot (b) the slow mode ($-$ signs taken), with the group velocity curves in this case coinciding on two points due to the circular nature of the phase speed curves. The Alfvén speed has been chosen to satisfy $v_A = 1.2v_G$.

We should reiterate the fact that in figures 2.5-2.7, the angles against which the curves are plotted are different for the phase and group velocities. Choosing an angle from the x-axis, one can use the polar plots to read off the phase speed of the waves (speed of individual troughs) in that direction, and also the speed of a wavepacket that also travels in this direction. These wavepackets consist of waves that may well be travelling in directions other than the wavepacket (in fact, most are; we'll see examples of when both directions coincide later). This helps to explain the multi-valued group velocity curve in the compressible MHD case ($\delta = 1$). When the direction of propagation is close to the direction of the basic state magnetic field, that is when θ is close enough to 0 or π, the group speed can take two values for a fixed θ. This implies that a wavepacket travelling in that direction is comprised of waves travelling in one of two directions: there are two 'types' of wavepacket able to travel in that direction. One of these types will travel quicker than the other, depending on the wavevector of the waves that form it.

The differences between the shallow water and compressible MHD models are again highlighted in figure 2.6. For $\delta = 0$, for the shallow water case in plot (a), the slower Alfvén-like waves have circular phase speeds and group velocity 'curves' that are points on the x-axis, as predicted. These

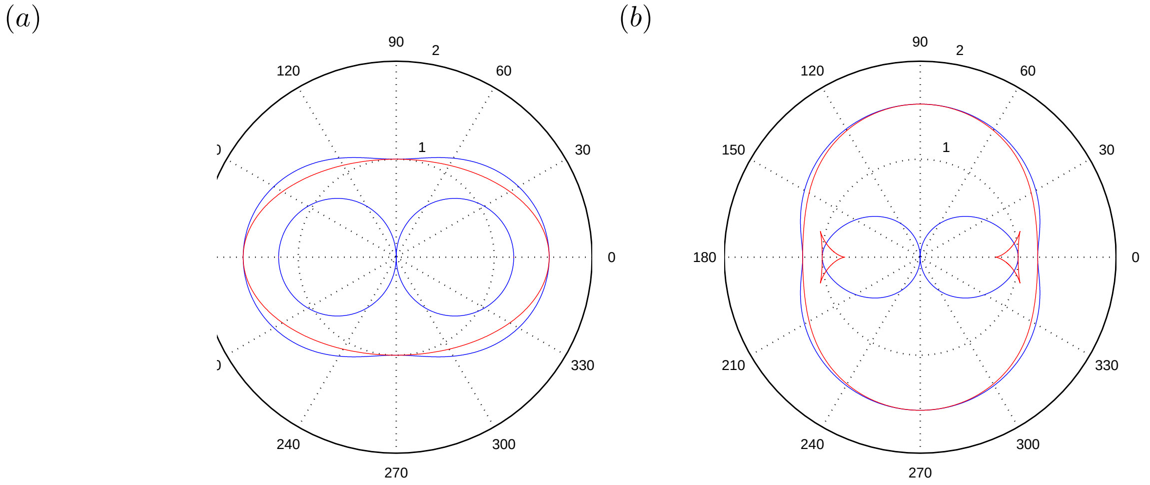

Figure 2.6 – Illustration of phase (blue) and group (red) velocity curves in polar form. Plot (a) shows wave modes in the shallow water model ($\delta = 0$); plot (b) the 2-D compressible model ($\delta = 1$) Goedbloed and Poedts (2004); Priest (1982). This further illustrates the breaking of the analogy between the two systems; the properties of both wave modes are different in each case. The group velocities of the slow modes develop a cusp as one deviates from the shallow water case (see figure 2.7 below), and the 'preferred' directions of propagation for the fast modes are perpendicular across the two systems.

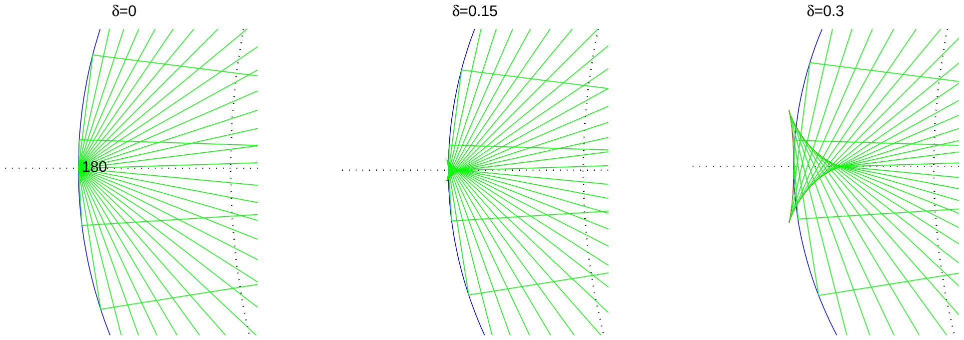

Figure 2.7 – Polar diagrams of phase and group velocities, as in figure 2.5, for the slow magneto-gravity mode. These plots are zoomed in on one of the foci of group velocity in the shallow water case (left hand plot in figure 2.6) to illustrate the formation of the cusp that is evident in the 2-D compressible MHD case. Green lines represent the group velocity projections, tracing out the group velocity curve. Again, $v_A = 1.2$ here.

points are barely visible on the polar plot, but indicate that the direction of travel of wavepackets (and hence energy transfer) is parallel to the imposed magnetic field. For the compressible MHD case ($\delta = 1$), on the other hand, this slower mode does not have phase speeds that are circles, as can be seen in figure 2.6(b). This difference is further compounded by the fact that the group velocity curves are no longer circles; indeed, they exhibit a cusp-like structure and multiple values of wavepacket speed for a given angle ϕ. The development of these cusps as δ is increased from $\delta = 0$ to $\delta = 0.3$ is illustrated in figure 2.7.

It is also worth noting that whenever the phase velocity curve crosses a radial line at right-angles, the group and phase velocities are equal in the direction of that radial line. This can be argued geometrically using the construction of the projections, but can just as well be shown algebraically. The $\hat{\mathbf{k}}_\perp$ component of (2.61) vanishes precisely when the second term in the right hand side of equation (2.62) does: i.e., when θ is a multiple of $\pi/2$. That is, when considering wave propagation parallel and perpendicular to the ambient magnetic field, the phase and group speeds coincide, and waves travel in the same direction and at the same speed as the packets they form.

2.6 Incompressible and irrotational waves

So far we have considered wave modes with nonzero $D = \mathbf{k} \cdot \tilde{\mathbf{u}}$ in equations (2.36) and (2.37). We shall now consider the case $D = 0$ which is physically equivalent to searching for linear waves that do not compress the fluid horizontally as they propagate. Then, using equations (2.38) and (2.39), we have

$$Q\left(if\omega + \frac{1}{2}\delta k^2 v_A^2 \sin(2\theta)\right) = 0 \qquad \text{and} \qquad Q\left(\omega^2 - k^2 v_A^2 \cos^2\theta\right) = 0. \tag{2.63}$$

Now, for nonzero Q, the first of these equations indicates that the frequency ω is imaginary, and so the waves have a growth rate associated with them, and we have instability. However, the second equation indicates that ω is real; these cases cannot both be true, in general. However, we can find specific parameter regimes in which both equations hold. One way the equations are compatible is when $Q = 0$, in addition to $D = 0$, which describes the trivial (motionless) scenario. Another way these equations can both be satisfied is when $f = \delta = 0$. Then ω is real, and we have the dispersion relation

$$\omega^2 = k^2 v_A^2 \cos^2\theta$$

for ω and Alfvén speed. This is the case only if $f = 0$ (for a nonrotating system) and $\delta = 0$, which corresponds to the shallow water regime. The rotating case, or the 2-D MHD case, cannot support waves of this type.

Similarly, one could look for solutions in which $Q = 0$ (flows with zero vorticity). Then equations (2.38) and (2.39) reduce to

$$D\left(if\omega + \frac{1}{2}\delta k^2 v_A^2 \sin(2\theta)\right) = 0 \qquad \text{and}$$
$$D\left(\omega^2 - v_S^2 k^2 - (1-2\delta)k^2 v_A^2 \cos^2\theta - \delta^2 k^2 v_A^2\right) = 0. \tag{2.64}$$

Again, we argue that for non-trivial solutions, the only way these equations are compatible is when $f = \delta = 0$ and

$$\omega^2 = gHk^2 + k^2 v_A^2 \cos^2\theta, \tag{2.65}$$

where v_S^2 has been replaced with gH as per the equivalencies outlined earlier (when $\delta = 0$ we are in the shallow water regime). This indicates that the non-rotating shallow water system supports magneto-gravity wave modes that propagate with zero vorticity.

2.6.1 Disturbance energy conservation

We have already established that seeking wave-like solutions is sensible, as we found that the determinant of the linking dispersion relation was positive in equation (2.42), so that there are no instabilities. We will now outline a more elegant approach which is more thorough and physically applicable, and will be of use in later chapters.

Earlier in the chapter (section 2.3) we derived a fully nonlinear conservation law (2.27) for the governing equations (2.7), (2.12) and (2.15). One can apply a similar analysis to the linearised equations (2.31a), (2.31b) and (2.31c), and obtain an energy conservation law for the *disturbance* energy of the system. This resulting conservation law for disturbance energies will then be used to show that the frequency ω is always real, and so the model only supports waves, on this base state of rest with a uniform field.

The kinetic energy is given by $\frac{1}{2}\rho h|\mathbf{u}|^2$, after integrating over the layer depth. If the perturbations are small, the leading term in this expression is $\frac{1}{2}\rho H|\mathbf{u}|^2$. We can find similar expressions for the gravitational potential and the magnetic energies, which are

$$\tilde{E}_K = \frac{1}{2}\rho H|\mathbf{u}'|^2, \tag{2.66a}$$

$$\tilde{E}_P = \frac{1}{2}\rho g\eta^2, \tag{2.66b}$$

$$\tilde{E}_M = \frac{1}{2\mu_0}H|\mathbf{B}'|^2, \tag{2.66c}$$

where the tilde represents a disturbance energy. $\tilde{E}_P$ is the potential energy, which has not changed in form since the last time we saw it in equation (2.27). It is worth noting that when deriving potential energy by integrating over the layer depth, one obtains a slightly different expression to that in (2.66b); it contains an extra $\frac{1}{2}\rho g H^2$. However, when taking the time derivative for the conservation law, this (constant) term will disappear. The gravitational potential energy of a blob of fluid is also dependent on the frame of reference. Any constant could be added to the right hand side of equation (2.66b), giving the potential energy from *some* reference height.

Adding up the energies given in (2.66) and taking the time derivative, one gets

$$\begin{aligned}\frac{\partial}{\partial t}\left(\tilde{E}_K + \tilde{E}_P + \tilde{E}_M\right) &= \rho H\mathbf{u}'\cdot\frac{\partial \mathbf{u}'}{\partial t} + \rho g\eta\frac{\partial \eta}{\partial t} + \frac{1}{\mu_0}H\mathbf{B}'\cdot\frac{\partial \mathbf{B}'}{\partial t} \\ &= -\rho g H\nabla\cdot(\eta\mathbf{u}') + \frac{1}{\mu_0}H\mathbf{B}_0\cdot\nabla(\mathbf{u}'\cdot\mathbf{B}'), \end{aligned} \tag{2.67}$$

the latter equality arising from the linear equations (2.31a), (2.31b) and (2.31c). These equations then satisfy the disturbance energy conservation law

$$\frac{\partial}{\partial t}\left(\frac{1}{2}\rho H|\mathbf{u}'|^2 + \frac{1}{2}\rho g\eta^2 + \frac{1}{2}\rho H|\mathbf{B}'|^2\right) + \nabla\cdot\left(\rho g H\eta\mathbf{u}' - \frac{1}{\mu_0}H(\mathbf{u}'\cdot\mathbf{B}')\mathbf{B}_0\right) = 0. \tag{2.68}$$

In section 2.3 we searched for wave-like solutions of the form (2.35), with the real part understood. We apply the same procedure to equation (2.68) above, after rearranging using the product rule, to arrive at

$$\omega\left(H(|\tilde{\mathbf{u}}|^2 + \frac{1}{\mu_0\rho}|\tilde{\mathbf{B}}|^2) + g|\tilde{\eta}|^2\right) = gH(\mathbf{k}\cdot\tilde{\mathbf{u}}^*)\tilde{\eta} - H(\mathbf{B}_0\cdot\mathbf{k})(\tilde{\mathbf{B}}\cdot\tilde{\mathbf{u}}^*) + c.c., \tag{2.69}$$

where $c.c.$ denotes the complex conjugate. Since the right hand side is real, and the terms in the brackets on the left hand side are also real, we conclude that ω must also be real. We then have no growth or decay, and motion is entirely wave-like.

2.7 Two-dimensional linear waves

After seeking wave-like solutions of the form

$$u = \hat{u}e^{i(kx+ly-\omega t)}, \tag{2.70}$$

the linear shallow water equations (2.31a-2.31c) can be written in matrix form as

$$\begin{pmatrix} \omega & -if & -gk & \frac{1}{\mu_0\rho}B_0k & 0 \\ if & \omega & -gl & 0 & \frac{1}{\mu_0\rho}B_0k \\ -Hk & -Hl & \omega & 0 & 0 \\ B_0k & 0 & 0 & \omega & 0 \\ 0 & B_0k & 0 & 0 & \omega \end{pmatrix} \begin{pmatrix} \hat{u} \\ \hat{v} \\ \hat{\eta} \\ \hat{B}_x \\ \hat{B}_y \end{pmatrix} = 0. \qquad (2.71)$$

Here, the ambient magnetic field has been aligned with the x-axis, so that $\mathbf{B}_0 = (B_0, 0)$. Making the determinant of the matrix equal to zero for non-trivial solutions, we obtain the dispersion relation

$$\omega^4 - \big((2v_A^2 + gH)k^2 + gHl^2 + f^2\big)\omega^2 + v_A^2k^2\big((v_A^2 + gH)k^2 + gHl^2\big) = 0, \qquad (2.72)$$

where $v_A = B_0/(\mu_0\rho)^{1/2}$ is the Alfvén speed, since the spurious zero-frequency mode does not satisfy the magnetic field condition (see appendix A). In the hydrodynamic case, this yields the dispersion relation for a 2-D inertia-gravity mode:

$$\omega^2 = v_G^2(k^2 + l^2) + f^2, \qquad (2.73)$$

where $v_G = \sqrt{gH}$ is the gravity wave speed. This is the well-known dispersion relation of Poincaré waves Pedlosky (1987).

If we omit rotation, we obtain the solutions

$$\omega_+^2 = (v_A^2 + v_G^2)k^2 + v_G^2l^2 \qquad \text{and} \qquad (2.74)$$

$$\omega_-^2 = v_A^2k^2. \qquad (2.75)$$

There appears to be a magnetically modified gravity wave mode and an Alfvén mode present in the system. In order to analyse these waves in more detail, we can consider the right eigenvector of the matrix given in equation (2.71), which is

$$\begin{pmatrix} \hat{u} \\ \hat{v} \\ \hat{\eta} \\ \hat{B}_x \\ \hat{B}_y \end{pmatrix} = \begin{pmatrix} v_G^2kl\omega \\ \omega(\omega^2 - (v_A^2 + v_G^2)k^2) \\ Hl(\omega^2 - v_A^2k^2) \\ -v_Av_G^2k^2l \\ -v_Ak(\omega^2 - (v_A^2 + v_G^2)k^2) \end{pmatrix}. \qquad (2.76)$$

For the positive root, $\omega_+^2 = c^2k^2 + l^2$, this reduces to

$$(k\omega_+, l\omega_+, H(k^2 + l^2), -v_A k^2, -v_A kl)^T. \tag{2.77}$$

For the negative root, $\omega_-^2 = \mathrm{Ma}^2k^2$, this reduces to

$$(l, -k, 0, -l, k)^T. \tag{2.78}$$

This wave propagates without perturbing the surface, and so magnetic tension takes the role of the restoring force. Two dimensional dynamics will be revisited in Chapter 6.

2.8 Summary and discussion

The chapter began with a derivation of the single-layer SWMHD equations first derived by Gilman (2000), which were then compared to those of two-dimensional compressible MHD. We verified that, in the absence of magnetic field, there is an analogy between the two systems in the linear regime, allowing one to infer the dynamics of one system from the other (see, for example, Vallis 2006). We found that the addition of magnetic field breaks this analogy, meaning we cannot use the huge variety of results from the well-studied compressible MHD system when considering the relatively new SWMHD case. However, this does open the door to new shallow water dynamics; we considered the differences in the linear waves of each system, starting with expressions for the phase speeds of the modes.

We found that the fast magnetogravity mode of the shallow water system propagates the fastest parallel to the ambient magnetic field, which differs from the 2-D compressible case in which the fast mode is quickest perpendicular to the field. Another difference between the two cases was manifest in the group velocity of the slow modes: in 2-D compressible MHD, wavepackets can travel at a slight angle to the ambient field (see Goedbloed and Poedts 2004). This means that energy can be transported by waves at an angle to the basic state magnetic field, as long as that angle is not too large. In the shallow water system, however, this angle is reduced to zero; wavepackets (and hence energy) can travel only along field lines.

An energy conservation law was also derived, in which we obtained a shallow water Poynting vector, which has not yet, to my knowledge, been identified. It differs from the usual (3-D) Poynting vector in a factor $1/2$ in front of the product of magnetic energy and velocity. However, this shallow water vector is not necessarily an energy flux, because the vectors involved are not the full three-dimensional velocity and magnetic field vectors. On the other hand, it does tell us something about how ‘horizontal’ magnetic energy is transported through the layer. There are two mechanisms for transport of this horizontal magnetic energy; it can be carried around by fluid motions, or along field lines whenever there is flow in that direction. In compressible MHD, these have an equal contribution to the flux, but in the shallow water case the latter mechanism dominates the magnetic energy flux.

We also found that only waves exist in linear SWMHD, for a motionless basic state with a uniform magnetic field. This was found by considering the disturbance energy conservation law (2.68), which was used to verify that the wave frequency is always real. This result will be expanded upon in the next chapter.

We will now discuss the implications of these findings by considering how our model applies to the tachocline; beginning with a short discussion of the parameter values one may choose, such as the value of H. The phase speed, c, of waves in a continuously stratified atmosphere approximately satisfies $c = N \times \text{height}/\pi \approx 354\text{m}\,\text{s}^{-1}$, using the values in table 1.1. The phase speed of gravity waves in our model, a single layer with constant density and height H, satisfies $c^2 = gH$. If we compare our model's phase speed with the physical value, we obtain the equivalent depth $H = 2.32\text{km}$, given $g = 54\text{m}\,\text{s}^{-2}$.

The speed of Alfvén waves, which are modes driven purely by magnetic tension, can be estimated using the values in table 1: we then have $|\mathbf{B}_0| = 0.2$, for a magnetic field strength of 2000G (see Hughes et al. 2007). Using the definition of Alfvén speed ($v_A = |\mathbf{B}_0|/(\mu_0\rho)^{1/2}$), we obtain an Alfvén speed of $13\text{m}\,\text{s}^{-1}$. This speed of magnetically driven waves would be less if the direction of propagation were at an angle to the ambient field; such waves cannot travel perpendicular to field lines at all.

Since the Alfvén speed and gravity wave speed are comparable in magnitude, both gravity and magnetic tension contribute similarly to the restoring force of magnetogravity modes, at least along field lines. Waves propagating perpendicular to the ambient magnetic field behave as in the hydrodynamic case, with gravity wave phase speeds and wavepackets consisting of waves travelling in the same direction as the packet, as the same speed. The magnetic augmentation kicks in when the wavevector is at angles other than $\pi/2$ to the field, and are at their highest when parallel.

We can also discuss the wavelength and frequency of the waves described by the model. Since the layer is shallow, we should stipulate that a typical wavelength is more than, say, ten times the layer depth, which we are taking to be $0.04R_\odot$. This wavelength of $0.4R_\odot \approx 2.78 \times 10^8$m gives a wavenumber of $k = 2.26 \times 10^{-8}\text{m}^{-1}$ (curvature would have more of an effect for waves much larger than this). Since the Alfvén speed is much lower than the gravity wave speed, magneto-gravity modes would propagate at around $350\text{m}\,\text{s}^{-1}$, using (2.44). Since the dispersion relation is of the form $\omega = ck$ in the absence of rotation, we have the frequency $\omega = 5 \times 10^{-7}\text{s}^{-1}$, which gives a period of 2.3 days.

Wave in the tachocline would be influenced by rotation, but not constrained by it. Given that fluid in the tachocline makes one rotation around the axis every 27 days, we have $f \approx 2/(27 \times 24 \times 60^2) = 8.57 \times 10^{-7}\text{s}^{-1}$. Comparing this to $\sqrt{gH}k \approx 4.25 \times 10^{-7}\text{s}^{-1}$, we find that the values are similar in magnitude, revealing that the Coriolis force has a comparable role to gravity and the Lorentz force in the propagation of waves. Of course, the extent of that role depends on the wavelength of the wave in question: rotation has less of an effect on small-scale waves. Also, since the Coriolis force in our equations is written as a multiple of $\mathbf{z} \times \mathbf{u}$, waves near the equator do not feel rotation and are driven by other forces.

The single layer model described in this chapter has a free surface which oscillates. This could represent the boundary between the overshoot and radiative regions of the tachocline, with the stably stratified fluid in the radiative sub-layer represented by the layer of the model. The radiative region of the Sun resides just underneath this layer, and would provide a stable base which is resistant to bulges of fluid from above, much like the rigid floor in our model. Waves would be excited by the turbulent motions of the overshoot sub-layer, which are in turn driven by convective plumes from the convective outer third (by radius) of the Sun (Hughes et al. 2007). However, the free surface of the model need not represent a physical boundary in the tachocline. The density jump over the free surface is how stratification is incorporated into the model, and so this surface could be interpreted as an abstract manifestation of a physical attribute we wish to replicate. Applying this model to the tachocline, which has no well-defined interfaces, is then justified.

To summarise, we have developed a model for the tachocline which supports huge-wavelength waves (up to 20% of the diameter of the Sun) which oscillate once every couple of days. These waves are a magnetic augmentation of Poincaré waves; i.e., they are driven by gravity, rotation and magnetic tension. They would exist in the radiative sub-layer of the tachocline, and may have some influence on the dynamics therein, such as energy transport. They may even affect the dynamics of the mechanism through which the Sun's large-scale magnetic field is maintained (see Jones et al. 2010). However, the model was restrictive in that only one magnetic configuration could be analysed; the aim of the next chapter is to alleviate this restriction.

Chapter 3

The n-layer model

3.1 Introduction

The aim of this chapter is to add more layers to the single layer model. We shall consider a system in which n immiscible shallow layers are stacked atop one another, each with their own (constant) density, which may differ from layer to layer. Historically, this has been studied to investigate the effects of more complex stratification, and hence to model more realistic vertical profiles of density (see, for example, Gill, 1982; Ovsyannikov, 1979). Although it is true that a multi-layer SWMHD model would allow us to investigate more intricate stratification profiles, it is not the main reason we choose to study n-layer models in our case. With more than one fluid layer we are able to model the effects of different magnetic field geometries, by allowing our basic state magnetic field to vary between layers.

It is quite fair to say that (at the time of writing) nobody really knows what the magnetic field geometry is in the tachocline. As discussed in Chapter 1, it is widely accepted that the field there is mostly toroidal, and so locally we shall continue to take horizontal basic state fields in every layer, although we will allow these to vary in intensity and direction. However, exactly what this horizontal structure is, and how it varies with height, is unknown. In light of this uncertainty, we develop a model in which a magnetic field can be tailored to one's taste.

We shall also consider the effects of adding a rigid lid at $z = 0$, in addition to considerations of the dynamics with a freely movable surface. The reasons one may choose to use a model with a rigid lid that keeps the fluid below $z = 0$ are physical ones. The tachocline, for example, does not contain a ‘free surface’; if we are to apply our model to a sub-layer contained by stratification (within the radiative layer of the tachocline, for example), then the fluid bounding the layer from above may be as resistant to a bulge from the layer as the fluid below. In this case, it may be prudent to model the layer with a fixed lid representing the restraining fluid above (see, for example, Gill, 1982)). Of course, the free surface (or any fluid-fluid interfaces) in the model need not necessarily correspond to physical surfaces in the tachocline, as discussed in Chapter 2.

In this chapter we shall more thoroughly define the n-layer model, and derive the governing equations of motion. We shall also derive an energy conservation law for the system, and use it to show that, in the linear regime, *only* waves are supported – there are no lurking instabilities for us to worry about. We will then confidently seek wave-like solutions of the governing equations and formulate a ‘generating’ equation, from which can be derived dispersion relations and equations describing the structure of the wave modes present. This generating equation will be used in Chapter 4, in which we will outline some examples, and highlight some interesting features.

Further discussions related to these results are outlined in the appendices. The focus of Appendix B is the derivation of an iterative formula useful in deriving the dispersion relation of the n-layer model. In Appendix D we discuss the so-called 1.5-layer models, in which one or more of the layers is deeper than the others (but still shallow in the shallow water sense). Fully nonlinear solutions of the SWMHD equations are derived in Appendix C.

3.2 The n-layer model and governing equations

The n-layer model consists of n immiscible inviscid shallow layers, one atop the other. Again, we take locally Cartesian coordinates, with gravity pointing in the negative z-direction, perpendicular to a horizontal floor. The system is horizontally infinite, with each layer having a constant density, which could vary from layer to layer. Permeating each layer is a unidirectional horizontal magnetic field, which can also be different in different layers, both in strength and orientation (measured in its angle to the x-axis). Each layer is also taken to be shallow, in the sense that the ratio of vertical to horizontal length scales is much less than unity; this means that each layer satisfies the shallow water equations, but with the appropriate conditions at the interfaces. These conditions are:

- The normal component of fluid velocity must be continuous over a fluid-fluid interface. That is, for the j^{th} interface, $\mathbf{u}_j \cdot \mathbf{n}_j = \mathbf{u}_{j+1} \cdot \mathbf{n}_j$ at $z = z_j$, where $\mathbf{n}_j$ is the normal to the interface,

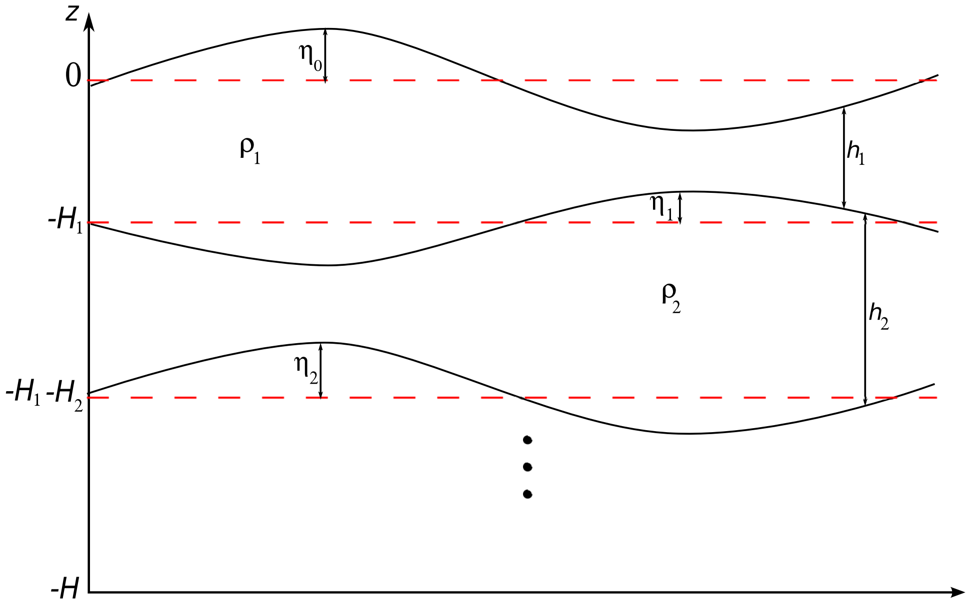

Figure 3.1 – Schematic of the n-layer free surface model.

and z_j is the z-coordinate of the interface.

- No magnetic flux through an interface. That is, $\mathbf{B}_j \cdot \mathbf{n}_j = 0$ at $z = z_j$. This is equivalent to imposing that all surfaces are magnetic field lines. (If field strength differs between layers j and $j+1$, this interface will also be a current sheet.)

Here, subscript j on a quantity or vector denotes the value(s) of that quantity in layer j, as shown in figure 3.1, with η_j bounding layer j from below. We also have the interface height z_j given by

$$z_j - \sum_{i=1}^{j-1} H_i + \eta_j. \tag{3.1}$$

It is worth noting that henceforth, $\mathbf{u}_3$ represents the two-dimensional velocity in layer 3, and not the three-dimensional velocity as in chapter 2. We now have $\mathbf{u}_3 = (u_3, v_3)$ and $\mathbf{B}_3 = (B_{x_3}, B_{y_3})$.

In reality, due to the presence of magnetic diffusion, current sheets (the interfaces) may be unstable to tearing modes. However, the multilayer constructions here are viewed as simple models of continuous field distributions where tearing modes are not necessarily present, which is why we ignore them. The interfaces may also be unstable to the Kelvin-Helmholtz instability when a nonzero basic state flow is considered (see Mak 2013 for more details).

As in the previous chapter, we shall build the governing equations by assuming magnetohydrostatic balance in the vertical component of the momentum equation, considering conservation of mass in a derivation of the equation for evolution of the interfaces and finally the magnetic induction equation, for each layer. First, however, we can speculate on the nature of the linear wave modes we might expect, and discuss the possible effects of adding a rigid lid to the surface.

When we look for linear waves in the n-layer system, we shall be considering waves of a fixed wavelength; the interfaces (and free surface, if there is one) will be oscillating with the same frequency and same wavelength. This is equivalent to stipulating that the height of any interface is a scalar multiple of the height of any other, as in Gill (1982). It turns out that the order of the differential equation governing fluid motion (the one obtained by combining the momentum, height and induction equations for all the layers) is of order n with this simplification, but without it is of order n^2.

Making this simplification that all interfaces move in phase (or antiphase) also allows us to make geometrical arguments about the number of modes we can expect. Each interface will act as a degree of freedom, suggesting the existence of n wave modes for the n-layer free surface model. One of these modes, for example, would be visualised by imagining all interfaces (including the surface) oscillating in phase, so that in one infinitesimal column with fixed x and y, every interface would be moving in one direction, up or down.

The rigid lid approximation

The n-layer model, for $n > 1$, can simulate the effects of stratification *without* a free surface; the fluid interfaces and their corresponding density jumps could endow the model with the vertical density variations we require. Placing a rigid lid at $z = 0$ inhibits surface motion, instead asserting a pressure $P = P(x, y, t)$ onto the fluid immediately below it, in response to that fluid's motions. The function P is not a known function; rather, it is whatever it has to be to ensure that $\eta = 0$. Rather than have constant pressure on a free surface, we impose $p_1 = P$ at $z = 0$. We shall derive the governing equations of a model with both η_0 included (nonzero if considering a free surface model) *and* the rigid lid pressure P included. At any stage in the subsequent derivations, one can put $P = 0$ and $\eta_0 \neq 0$ to get to the free surface regime, and similarly keeping $P \neq 0$ and maintaining $\eta_0 = 0$ will yield equations that govern fluid in the rigid lid system.

On geometrical arguments only, we expect the addition of a rigid lid to reduce the number of wave modes in the n-layer system to $n - 1$. This can be interpreted as the loss of a degree of freedom in fixing the surface motions. This lost mode will turn out to be related to the hydrodynamic barotropic, or surface, mode, which cannot propagate with zero total horizontal mass flux – the strict requirement that the rigid lid model demands.

3.2.1 Derivation of the governing equations

The momentum equation

As before, we start by considering pressure. We argued that the fluid in each shallow layer is in magnetohydrostatic balance, given by

$$\frac{\partial p_j}{\partial z} = -\rho_j g, \tag{3.2}$$

for total pressure p_j, in layer j. For example, the pressure in the top layer is given by integrating (3.2) over the depth of this layer:

$$p_1 = -\rho_1 g z + constant. \tag{3.3}$$

Now, if we have a rigid lid at $z = 0$ asserting a pressure P, then this constant of integration on the right hand side of the equation above is simply P. If we have a free surface, then $p_1 = 0$ at $z = \eta_0$ and the constant is $\rho_1 g \eta_0$ (which equals $\rho_1 g z_0$). Including both of these scenarios, we have

$$p_1 = \rho_1 g(z_0 - z) + P, \tag{3.4}$$

with the understanding that at any point we can put $\eta_0 = 0$ for the rigid lid case, and $P = 0$ for the free surface case. For layer 2, equation (3.2) holds with $j = 2$, since the layer is shallow. Integrating this, and applying continuity of pressure over the interface at $z = z_1$, we can make use of equation (3.4) to obtain

$$p_2 = \rho_2 g(z_1 - z) + \rho_1 g h_1 + P, \tag{3.5}$$

where $h_1 = z_0 - z_1$ is the total height of layer 1. This can be continued downwards, giving, in general

$$p_j = \rho_j g(z_{j-1} - z) + g \sum_{i=1}^{j-1} \rho_i h_i + P, \tag{3.6}$$

for layer j. The height h_j can be expressed as $h_j = H_j + \eta_{j-1} - \eta_j$. This can be interpreted physically as the gravitational potential energy of all the fluid above a point at height z (with a possible contribution from a lid), which cumulatively creates this pressure. We aim to use (3.6) to replace the pressure term, $\frac{1}{\rho_j}\nabla p_j$, in the equation for conservation of momentum. With this in mind, we can take the horizontal gradient of equation (3.6) to give

$$\frac{1}{\rho_j}\nabla p_j = g\nabla\eta_{j-1} + \frac{1}{\rho_j}g\sum_{i=1}^{j-1}\rho_i\nabla(\eta_{i-1}-\eta_i) + \frac{1}{\rho_j}\nabla P. \tag{3.7}$$

Writing the sum in a different way, by collecting together the η_i to form their own terms, this can be written as

$$\frac{1}{\rho_j}\nabla p_j = \frac{1}{\rho_j}g\sum_{i=1}^{j}\rho_i\nabla\left(\left(1-\frac{\rho_{i-1}}{\rho_i}\right)\eta_{i-1}\right). \tag{3.8}$$

Now, the term in the nested brackets in equation (3.8) is an important one. When multiplied by g, which this is, it is often called a 'reduced gravity', as in Gill (1982). It can be thought of as an effective gravity at the j^{th} interface; the effect of gravity on this interface which takes into account the density jump there. For example, gravity will have much more on an influence on the motion of an interface if the fluid below is much more dense than the fluid above. This was first demonstrated experimentally by Benjamin Franklin in 1792 with a container filled with oil and water. He noted that, when disturbed, the surface of the oil would remain relatively still (since there is a large density difference between the oil and the air above it) whereas the oil-water interface moved drastically (the density jump between oil and water is relatively low). This density jump is measured by the reduced gravity g^r_{i-1}, which we shall define here as

$$g^r_{i-1} = \left(1-\frac{\rho_{i-1}}{\rho_i}\right)g. \tag{3.9}$$

For a free surface, we take $\rho_0 = 0$ so that the 'fluid' above the surface has zero density, and the equation above gives the effective gravity g, as expected. On the other hand, if two adjacent layers have the same density, the effective gravity will be zero, as expected. We can substitute equation (3.9) into (3.8), and substitute this again into the horizontal component of the momentum equation for layer j, to arrive at

$$\frac{\partial\mathbf{u}_j}{\partial t} + \mathbf{u}_j\cdot\nabla\mathbf{u}_j = -\frac{1}{\rho_j}\sum_{i=1}^{j}g^r_{i-1}\rho_i\nabla\eta_{i-1} - \frac{1}{\rho_j}\nabla P + \frac{1}{\mu_0\rho}\mathbf{B}_j\cdot\nabla\mathbf{B}_j. \tag{3.10}$$

The height equation

The equations that govern the evolution of the interfaces are found simply by integrating the solenoidal constraints on velocity. For layer j we have

$$\frac{\partial w_j}{\partial z} = -\nabla\cdot\mathbf{u}_j. \tag{3.11}$$

This can be integrated over the layer depth, noting that w_j should equal the material derivative of an interface at that interface. This gives

$$[w_j]_{z_j}^{z_{j-1}} = -h_j \nabla \cdot \mathbf{u}_j, \tag{3.12}$$

which can be written as

$$\frac{D}{Dt}\left(\eta_{j-1} - \eta_j\right) + h_j \nabla \cdot \mathbf{u}_j = 0, \tag{3.13}$$

after applying the boundary conditions at each interface bounding the layer. Rearranging gives the desired equation

$$\frac{\partial h_j}{\partial t} + \nabla \cdot \big(h \mathbf{u}_j\big) = 0. \tag{3.14}$$

A depth-averaging procedure can be used to derive (3.14) in a similar manner as for (2.13).

The induction equation

The magnetic field evolves under the shallow water induction equation (2.15) in each layer, namely

$$\frac{\partial \mathbf{B}_j}{\partial t} = \mathbf{B}_j \cdot \nabla \mathbf{u}_j - \mathbf{u}_j \cdot \nabla \mathbf{B}_j. \tag{3.15}$$

We have not yet used the boundary conditions we have imposed on magnetic field, i.e., that the interfaces are magnetic field lines. If the fluid was unperturbed, the interfaces would be horizontal. This would align with our basic state magnetic field, and the conditions would be satisfied. Invoking the solenoidal constraint on magnetic field and integrating gives

$$[B_{zj}]_{z_j}^{z_{j-1}} = -\left(\nabla \cdot \mathbf{B}_j\right) h_j, \tag{3.16}$$

Now, imposing no magnetic flux over interface j, which has normal

$$\left(\frac{\partial \eta_j}{\partial x}, \frac{\partial \eta_j}{\partial y}, -1\right), \tag{3.17}$$

gives

$$B_{zj} = \mathbf{B}_j \cdot \nabla \eta_{j-1} \text{ at } z = z_{j-1} \qquad \text{and} \qquad B_{zj} = \mathbf{B}_j \cdot \nabla \eta_j \text{ at } z = z_j. \tag{3.18}$$

Equation (3.16) then becomes

$$\mathbf{B}_j \cdot \nabla \big(\eta_{j-1} - \eta_j\big) = -\left(\nabla \cdot \mathbf{B}_j\right) h_j, \tag{3.19}$$

which can be re-expressed as

$$\nabla \cdot \big(h_j \mathbf{B}_j\big) = 0. \tag{3.20}$$

This is the condition on magnetic field analogous to equation (2.18) in the single layer case. In a similar manner, one can again verify that if (3.20) holds initially, then it holds for all times by algebraically verifying the identity

$$\frac{\partial}{\partial t}\left(h_j \mathbf{B}_j\right) = \nabla \times \big(\mathbf{B}_j \times (h \mathbf{u}_j)\big), \tag{3.21}$$

and taking the divergence.

To summarise, the governing equations of the j^{th} layer in the n-layer model are given by

$$\frac{\partial \mathbf{u}_j}{\partial t} + \mathbf{u}_j \cdot \nabla \mathbf{u}_j = -\frac{1}{\rho_j}\sum_{i=1}^{j} g_{i-1}^{r} \rho_i \nabla \eta_{i-1} - \frac{1}{\rho_j}\nabla P + \frac{1}{\mu_0 \rho}\mathbf{B}_j \cdot \nabla \mathbf{B}_j, \tag{3.10}$$

$$\frac{\partial h_j}{\partial t} + \nabla \cdot \big(h_j \mathbf{u}_j\big) = 0, \tag{3.14}$$

$$\frac{\partial \mathbf{B}_j}{\partial t} = \mathbf{B}_j \cdot \nabla \mathbf{u}_j - \mathbf{u}_j \cdot \nabla \mathbf{B}_j, \tag{3.15}$$

with

$$\nabla \cdot \big(h_j \mathbf{B}_j\big) = 0. \tag{3.20}$$

It is useful to note that equations (3.14) ($j = 1 \ldots n$) can be written in terms of the displacement quantities η_i. For the bottom layer we have $h_n = H_n + \eta_{n-1}$, since the floor is flat. Equation (3.14) can then easily be written in terms of η_{n-1} and $\mathbf{u}_n$. The left hand side of the height equation for the $(n-1)^{\text{th}}$ layer can then be expressed as a single derivative of η_{n-2} by eliminating the η_{n-1}, and so on. In general, an equation for the evolution of the $(j-1)^{\text{th}}$ interface can be found by adding up the equations (3.14) of all the layers below it, leading to

$$\frac{\partial \eta_{j-1}}{\partial t} + \sum_{i=j}^{n} \nabla \cdot \left(h_j \mathbf{u}_j\right) = 0. \tag{3.22}$$

This can be used in place of equation (3.14).

3.3 Energy conservation

In a similar (albeit brisker) manner as employed in the previous chapter for the single layer case, we shall derive an energy conservation law for the n-layer system, and use it to show that the frequency of linear wave-like solutions is always real in a stably stratified system.

We know that kinetic energy is given as the integral of $\rho|\mathbf{u}|^2/2$ over the layer. Similarly, gravitational potential energy is calculated as the integral of $\rho g z$ and magnetic energy the integral of $\rho|\mathbf{B}|^2/2$. For layer j, we consider

$$E_{Kj} = \frac{1}{2}\rho_j|\mathbf{u}_j|^2 h_j, \tag{3.23a}$$

$$\mathcal{E}_{Pj} = \frac{1}{2}\rho_j g\left(\eta_{j-1}^2 - \eta_j^2\right) + \text{constant}, \tag{3.23b}$$

$$E_{Mj} = \frac{1}{2\mu_0}|\mathbf{B}_j|^2 h_j, \tag{3.23c}$$

where $h_j = H_j + \eta_{j-1} - \eta_j$ is the height of layer j. We should note that in the expressions above, E_{Kj} is indeed the kinetic energy, and E_{Mj} the magnetic energy, but $\mathcal{E}_{Pj}$ is not the potential energy we have been describing. We shall refer to it as *pseudo potential energy* (see, for example, Warneford and Dellar, 2013; Ripa, 1993); this will be discussed later, but for now let us work with the expressions above to derive some kind of pseudo-energy conservation law.

Taking the time derivative of equations (3.23) and adding gives

$$\frac{\partial \mathcal{E}_j}{\partial t} = \rho_j h_j\left(\mathbf{u}_j\cdot\frac{\partial \mathbf{u}_j}{\partial t} + \frac{1}{\mu_0\rho_j}\mathbf{B}_j\cdot\frac{\partial \mathbf{B}_j}{\partial t}\right) + \frac{1}{2}\rho_j\left(|\mathbf{u}_j|^2 + \frac{1}{\mu_0\rho_j}|\mathbf{B}_j|^2\right)\frac{\partial h_j}{\partial t} + \frac{1}{2}\rho_j g\frac{\partial}{\partial t}\left(\eta_{j-1}^2 - \eta_j^2\right), \tag{3.24}$$

where $\mathcal{E}_j = E_{Kj} + \mathcal{E}_{Pj} + E_{Mj}$ is the total pseudo-energy in layer j. Making use of equations (3.10), (3.14), (3.15) and (3.22), this becomes

$$\frac{\partial \mathcal{E}_j}{\partial t} = -\frac{1}{2}\rho_j\nabla\cdot\left(h_j|\mathbf{u}_j|^2\mathbf{u}_j\right) + \frac{1}{\mu_0}h_j B_j\cdot\nabla\left(\mathbf{u}_j\cdot\mathbf{B}_j\right) - \frac{1}{2\mu_0}\nabla\cdot\left(h_j|\mathbf{B}_j|^2\mathbf{u}_j\right) - h_j\mathbf{u}_j\cdot\nabla P - h_j\sum_{i=1}^{j} g_{i-1}^r\rho_i\mathbf{u}_j\cdot\nabla\eta_{i-1} + \rho_j g\left(\eta_{j-1}\frac{\partial\eta_{j-1}}{\partial t} - \eta_j\frac{\partial\eta_j}{\partial t}\right). \tag{3.25}$$

We aim to make the right hand side a divergence, so that it forms a conservation law. The first and third terms on the right hand side are already a divergence, as is the second term after taking the constraint (3.20) into consideration. It is not surprising that the magnetic and kinetic energy terms have already formed divergences, without having to sum over all the layers. This is because both these energies are confined to the layer they ‘began’ in, due to our choice of boundary conditions. For example, kinetic energy is carried by the flow velocity, and this cannot cross an interface; the interface would simply move with any probing blob of fluid. In a similar manner, though it is not as straightforward as magnetic energy flux is not simply carried by the flow, magnetic energy cannot cross an interface either. This can be inferred from the shallow water Poynting flux, keeping in mind that the magnetic field is parallel to the interface. Only gravitational potential energy can be transferred across layers by the movement of the interfaces.

We shall now continue to manipulate the other terms (in the lower line of equation (3.25)) into divergences, by adding over all n-layers. The fourth term involving the rigid lid pressure P becomes a divergence since, if a lid was present, there would be no net horizontal mass flux below it, and so the sum $h_j\mathbf{u}_j$ would be divergence-free. The only other terms to reconcile will contribute towards the integral of the product of pressure and velocity in the energy flux. In order to manipulate these into a divergence, some careful algebra is required. Firstly, note that by reversing the order of summation, we have

$$-\sum_{j=1}^{n} h_j\mathbf{u}_j\cdot\left(\sum_{i=1}^{j} g^r_{i-1}\rho_i\nabla\eta_{i-1}\right) = -\sum_{j=1}^{n} g^r_{j-1}\rho_j\left(\sum_{i=j}^{n} h_i\mathbf{u}_i\right)\cdot\nabla\eta_{j-1}. \tag{3.26}$$

We also have

$$g\sum_{j=1}^{n}\rho_j\left(\eta_{j-1}\frac{\partial\eta_{j-1}}{\partial t}-\eta_j\frac{\partial\eta_j}{\partial t}\right) = g\sum_{j=1}^{n}\rho_j\eta_{j-1}\frac{\partial\eta_{j-1}}{\partial t} - g\sum_{j=2}^{n}\rho_{j-1}\eta_j\frac{\partial\eta_j}{\partial t}, \tag{3.27}$$

by relabelling the dummy index in the last sum and making use of the fact that $\eta_n = 0$. We can then invoke the definition of reduced gravity (3.9) to obtain

$$\begin{aligned} g\sum_{j=1}^{n}\rho_j\left(\eta_{j-1}\frac{\partial\eta_{j-1}}{\partial t}-\eta_j\frac{\partial\eta_j}{\partial t}\right) &= \sum_{j=2}^{n} g^r_{j-1}\rho_j\eta_{j-1}\frac{\partial\eta_{j-1}}{\partial t} + g\rho_1\eta_0\frac{\partial\eta_0}{\partial t} \\ &= -\sum_{j=1}^{n} g^r_{j-1}\rho_j\eta_{j-1}\left(\sum_{i=j}^{n}\nabla\cdot(h_i\mathbf{u}_i)\right), \end{aligned} \tag{3.28}$$

by virtue of equation (3.22). This, combined with the right hand side of equation (3.26), creates a divergence.

Finally, we can therefore write down the conservation law

$$\frac{\partial\mathcal{E}}{\partial t} + \nabla\cdot\mathcal{F} = 0, \tag{3.29}$$

where $\mathcal{E} = \mathcal{E}_1 + \mathcal{E}_2 + \cdots + \mathcal{E}_n$ is the total pseudo-energy of the n-layer system, and $\mathcal{F}$ is the pseudo-energy flux, given by

$$\mathcal{F} = \sum_{j=1}^{n}\left(\big(E_{Kj} + h_jP\big)\mathbf{u}_j + g^r_{j-1}\rho_j\eta_j\sum_{i=1}^{n} h_i\mathbf{u}_i + \mathbf{S}_j\right), \tag{3.30}$$

where $\mathbf{S}_j$ is the shallow water Poynting vector, given by

$$\mathbf{S}_j = \frac{1}{\mu_0}h_j\left(\frac{1}{2}|\mathbf{B}_j|^2\mathbf{u}_j - (\mathbf{u}_j\cdot\mathbf{B}_j)\mathbf{B}_j\right). \tag{3.31}$$

The term involving P in the flux is nonzero only in the presence of a rigid lid. It is worth noting that equation (3.29) is not the only conservation law of the system. It is a law of conservation of pseudo-energy, which contains only squared (small) quantities. The potential energy one would get by integrating $g\rho_j z$ over the layer is

$$E_{Pj} = \frac{1}{2}g\rho_j\left(\eta_{j-1}^2 - \eta_j^2\right) + g\rho_j\left(\eta_j\sum_{i=1}^{j} H_i - \eta_{j-1}\sum_{i=1}^{j-1} H_i\right) + \text{constant}. \tag{3.32}$$

We only need to add the equation

$$\left(\sum_{i=1}^{j-1} H_i\right)\frac{\partial}{\partial t}\left(\eta_{j-1} - \eta_j\right) + \left(\sum_{i=1}^{j-1} H_i\right)\nabla\cdot\left(h_j\mathbf{u}_j\right) = 0, \tag{3.33}$$

found using equation (3.14), to the pseudo-energy conservation law (3.29) to obtain the (non-pseudo) conservation of energy equation:

$$\begin{aligned}\frac{\partial}{\partial t}\left(\frac{1}{2}\rho_j h_j|\mathbf{u}_j|^2 + \frac{1}{2}g\rho_j\left(z_{j-1}^2 - z_j^2\right) + \frac{1}{2\mu_0}h_j|\mathbf{B}|^2\right)& \\ +\nabla\cdot\left(\left(\frac{1}{2}\rho_j h_j|\mathbf{u}_j|^2 + h_j P\right)\mathbf{u}_j + \rho_j g_{j-1}^r z_{j-1}\sum_{i=j}^{n} h_i\mathbf{u}_i + \mathbf{S}_j\right) &= 0,\end{aligned} \tag{3.34}$$

with the sum from $j = 1$ to $j = n$ understood. In the time derivative, the kinetic, potential and magnetic energies are recognisable. The first term in the flux indicates that kinetic energy is transported directly by the velocity, as expected. The term involving P is the integrated pressure-velocity product brought about by the lid, if present. The penultimate term is the product of the gravitational potential energy of the $(j-1)^{\text{th}}$ interface and the horizontal mass flux of the fluid below it. The final term is the shallow water Poynting flux given in (3.31). The conservation law (3.34) reduces to the free-surface hydrodynamic limit given by Stewart and Dellar (2010) in the absence of rotation.

The problem with the energy conservation law in the form (3.34) is that the potential energy as defined in (3.32) contains a term that is linear in (small) disturbance quantities. This means that kinetic energy, for example, is asymptotically smaller than potential energy in this system, which is itself not sign-definite. We require a measure of potential energy that describes the energy available for conversion to kinetic energy. This is conveniently encapsulated in our previous conservation law (3.29) for pseudo-energy.

3.3.1 Disturbance energy conservation

The aim of this section is to show that the frequency of small-amplitude wave-like perturbations is always real in a stably stratified layer, and so rule out any possibilities of instability for our choice of basic state.

As in the single layer case, one can make small perturbations about a motionless basic state with a uniform horizontal magnetic field. Substitution of $\mathbf{u}_j = \mathbf{u}'_j$ and $\mathbf{B}_j = \mathbf{B}_{0j} + \mathbf{B}'_j$, where a dash represents a small (perturbed) quantity, into (3.34) (in a similar manner as in chapter 2) yields a corresponding conservation law for these small perturbations. However, to outline another method which is slightly simpler in the n-layer model, we shall derive the disturbance energy law by first linearising the governing equations about the basic state considered above.

Equations (3.10), (3.22) and (3.15) linearise to

$$\frac{\partial \mathbf{u}'_j}{\partial t} = -\frac{1}{\rho_j}\sum_{i=1}^{j} g^r_{i-1}\rho_i \nabla \eta_{i-1} - \frac{1}{\rho_j}\nabla P + \frac{1}{\mu_0 \rho_j}\mathbf{B}_{0j}\cdot\nabla\mathbf{B}'_j, \tag{3.35a}$$

$$\frac{\partial \eta_{j-1}}{\partial t} + \sum_{i=j}^{n} H_i \nabla\cdot\mathbf{u}'_i = 0, \tag{3.35b}$$

$$\frac{\partial \mathbf{B}'_j}{\partial t} = \mathbf{B}_{0j}\cdot\nabla\mathbf{u}'_j, \tag{3.35c}$$

after neglecting all terms that are quadratic in dashed (small) quantities. This is equivalent to restricting our attention to small-amplitude waves, so that any product of quantities that are individually of the same order of magnitude as the small amplitude are much smaller than terms involving just one instance of a small quantity.

Using the linear equations (3.35), we obtain

$$\begin{aligned}\rho_j H_j \left(\mathbf{u}'_j\cdot\frac{\partial \mathbf{u}'_j}{\partial t} + \frac{1}{\mu_0\rho_j}\mathbf{B}'_j\cdot\frac{\partial \mathbf{B}'_j}{\partial t}\right) &+ \rho_j g^r_{j-1}\eta_{j-1}\frac{\partial \eta_{j-1}}{\partial t}\\ &= -H_j\sum_{i=1}^{j} g^r_{i-1}\rho_i \mathbf{u}'_j\cdot\nabla\eta_{i-1} - \rho_j g^r_{j-1}\eta_{j-1}\sum_{i=j}^{n} H_i\nabla\cdot\mathbf{u}'_i\\ &\qquad - H_j\mathbf{u}'_j\cdot\nabla P + \frac{1}{\mu_0}H_j\mathbf{B}_{0j}\cdot\nabla(\mathbf{u}'_j\cdot\mathbf{B}'_j).\end{aligned} \tag{3.36}$$

After again employing the idea of reversing the order of summation, adding over all the layers, and observing that $\nabla\cdot\mathbf{u}'_j = 0$ in the presence of a rigid lid, we find

$$\frac{\partial E'}{\partial t} + \nabla\cdot F' = 0, \tag{3.37}$$

where

$$E' = \frac{1}{2}\sum_{j=1}^{n} \rho_j \left(H_j \left(|\mathbf{u}'_j|^2 + \frac{1}{\mu_0 \rho_j} |\mathbf{B}'_j|^2 \right) + g^r_{j-1} \eta^2_{j-1} \right) \tag{3.38}$$

is the disturbance energy, and

$$F' = \sum_{j=1}^{n} \left(\rho_j g^r_{j-1} \eta_{j-1} \sum_{i=j}^{n} H_i \mathbf{u}'_i + \frac{1}{\mu_0} H_j \mathbf{B}_{0j} (\mathbf{u}'_j \cdot \mathbf{B}'_j) + H_j P \mathbf{u}'_j \right) \tag{3.39}$$

is the associated flux.

We will now consider wave-like motion by substituting the ansatz (2.35) into this conservation law in a similar manner as in the derivation of (2.69). Substitution of $\mathbf{u}' = \tilde{\mathbf{u}} e^{i(\mathbf{k}\cdot\mathbf{x} - \omega t)}$, and similar expressions for $\mathbf{B}'$ and η, into equation (3.37) gives

$$\begin{aligned} &\omega \left(\rho_j H_j \left(|\tilde{\mathbf{u}}_j|^2 + \frac{1}{\mu_0 \rho_j} |\tilde{\mathbf{B}}_j|^2 \right) + g^r_{j-1} |\tilde{\eta}_j|^2 \right) \\ &\qquad = H_j \sum_{i=1}^{j} g^r_{j-1} \rho_i (\mathbf{k} \cdot \tilde{\mathbf{u}}^*_j) \tilde{\eta}_{i-1} + H_j (\mathbf{k} \cdot \tilde{\mathbf{u}}^*_j) P - \frac{1}{\mu_0} H_j (\mathbf{B}_{0j} \cdot \mathbf{k})(\tilde{\mathbf{B}}_j \cdot \tilde{\mathbf{u}}_j) + c.c. \end{aligned} \tag{3.40}$$

The right hand side of (3.40) is real and, provided all the reduced gravities are positive, the coefficient of ω is positive. Hence we conclude that ω is real. If one or more of the reduced gravities is negative, corresponding to the system *not* being stably stratified, then the coefficient of ω may be zero, and we could not draw any conclusions about ω. Arguments involving the boundedness of the disturbance energy give the broader result that ω is always real, given positive reduced gravities.

3.4 Linear waves

Now we have established that the stratified model only supports waves, we can look for wave-like solutions unimpeded. We begin by seeking solutions of the form (2.35) of the linearised equations (3.35). This gives

$$\omega \tilde{\mathbf{u}}_j = \frac{1}{\rho_j} \sum_{i=1}^{j} g^r_{i-1} \rho_i \mathbf{k} \tilde{\eta}_{i-1} + \frac{1}{\rho_j} \mathbf{k} \tilde{P} - \frac{1}{\mu_0 \rho_j} \left(\mathbf{B}_{0j} \cdot \mathbf{k} \right) \tilde{\mathbf{B}}_j, \tag{3.41a}$$

$$\omega (\tilde{\eta}_{j-1} - \tilde{\eta}_j) = H_j \mathbf{k} \cdot \tilde{\mathbf{u}}_j, \tag{3.41b}$$

$$\omega \tilde{\mathbf{B}}'_j = - \left(\mathbf{B}_{0j} \cdot \mathbf{k} \right) \tilde{\mathbf{u}}_j, \tag{3.41c}$$

after cancelling a factor $-i$ in each case. Note that the second equation has arisen from linearisation of the alternative height equation (3.14). [Note also that the instances of i in the summation convention in the equation above are dummy variables and are distinct from the imaginary constant i.]

We now eliminate $\tilde{\mathbf{u}}_j$ and $\tilde{\mathbf{B}}_j$ in favour of the $\tilde{\eta}_j$ and $\tilde{P}$. We do this in two stages: first, we take the product of equation (3.41a) with ω (equivalent to taking a time derivative in real space), and eliminating $\tilde{\mathbf{B}}_j$ according to (3.41c), giving

$$\left(\omega^2 - \frac{1}{\mu_0 \rho_j}(\mathbf{B}_{0j} \cdot \mathbf{k})^2\right) \tilde{\mathbf{u}}_j = \frac{\omega}{\rho_j} \sum_{i=1}^{j} g_{i-1}^r \rho_i \mathbf{k} \tilde{\eta}_{i-1} + \frac{\omega}{\rho_j} \mathbf{k} \tilde{P}. \tag{3.42}$$

We then take the dot product of this equation with $H_j \mathbf{k}$ and eliminate $\mathbf{u}_j'$ according to equation (3.41b), to get

$$\omega \left(\omega^2 - \frac{1}{\mu_0 \rho_j}(\mathbf{B}_{0j} \cdot \mathbf{k})^2\right) (\tilde{\eta}_{j-1} - \tilde{\eta}_j) + \omega \frac{H_j}{\rho_j} \sum_{i=1}^{j} g_{i-1}^r \rho_i k^2 \tilde{\eta}_{i-1} + \omega \frac{H_j}{\rho_j} k^2 \tilde{P} = 0, \tag{3.43}$$

where $k = |\mathbf{k}|$ is the amplitude of the wavevector. Now, $\omega = 0$ is a solution of this equation, implying that the governing equations (3.35) support a zero frequency mode. However, this is not compatible with the linear magnetic field condition

$$\nabla \cdot \left((\eta_{j-1} - \eta_j)\mathbf{B}_{0j} + H_j \mathbf{B}_j'\right) = 0, \tag{3.44}$$

found by linearising equation (3.20). One way to show this is to find the solutions of equations (3.35) and substitute them into (3.44); a full explanation of this is given in appendix A. This is the first time the linearised magnetic field condition (3.44) has been considered in this derivation. It is satisfied by solutions of (3.43) when $\omega \neq 0$. In fact, one could use this linearised condition (3.44) in place of the induction equation (3.41c) in this derivation – see Appendix A for further details.

We conclude that $\omega \neq 0$, and we can write equation (3.43) as

$$\left(c^2 - v_{Aj}^2\right) (\tilde{\eta}_{j-1} - \tilde{\eta}_j) - \frac{H_j}{\rho_j} \sum_{i=1}^{j} g_{i-1}^r \rho_i \tilde{\eta}_{i-1} + \frac{H_j}{\rho_j} \tilde{P} = 0, \tag{3.45}$$

where the phase speed c is given by

$$c = \frac{\omega}{k}. \tag{3.46}$$

We have also introduced a second speed v_{Aj}, which is the Alfvén speed in layer j. It is defined as

$$v_{Aj} = \frac{1}{\sqrt{\mu_0 \rho_j}} |\mathbf{B}_{0j}| \cos \theta_j, \tag{3.47}$$

where θ is the angle between the ambient magnetic field $\mathbf{B}_{0j}$ and the direction of propagation of the wave $\mathbf{k}$.

Equation (3.45) is really a system of n equations ($j = 1 \dots n$) of n unknowns $\tilde{\eta}_0, \tilde{\eta}_1, \cdots \tilde{\eta}_{n-1}$ and P (noting that either $\tilde{\eta}_0 = 0$ or $P = 0$, making one of the $n+1$ variables known). An important point to make is that the direction of propagation, θ, is tied up in the Alfvén speed (3.47); this is the only way the magnetic field parameters appear in the equations. The influence of magnetic field is felt *only* through this product, and so the relative sizes of the v_{A_j} are the important factors here. In the next chapter we will experiment with different values of these v_{A_j}, which can be altered in different ways. For example, if one wanted to consider the special case with $v_{A_1} = v_{A_2}$, one could achieve this by setting $|\mathbf{B}_{01}|\rho_1^{-1/2} = |\mathbf{B}_{02}|\rho_2^{-1/2}$ and keeping the fields parallel so that $\theta_1 = \theta_2$; then equation (3.47) would return the same values for these upper two layers. Alternatively, one could set $|\mathbf{B}_{01}|\rho_1^{-1/2} = 2|\mathbf{B}_{02}|\rho_2^{-1/2}$ and have $\theta_1 = \pi/3$ and $\theta_2 = 0$; then the products given by (3.47) would be the same, even with this new magnetic configuration.

It should be noted that this is only the case when one is considering wave motion in a particular (fixed) direction. This will be the case for most of this work, but not all; in the group velocities section, for example, wave motion in all directions is considered. In that case, the specifics of the magnetic geometry are important, as we shall see.

Another important point to note is that if indeed we wanted to consider the case of equal field strengths in two layers (say, layers 1 and 2 without loss of generality) then the relationship between the Alfvén speeds involves some incarnation of reduced gravity (3.9) due to the appearance of the density ratio, as we should expect.

Discussion of wave modes in the n-layer model

Equation (3.45) will be the starting point for much of the work in the next chapter, in which we will consider the special cases $n = 2$ and $n = 3$. It allows us to derive the dispersion relation of the n-layer system, by eliminating the $\tilde{\eta}_j$ (and possibly $\tilde{P}$), from which we can find valuable information about the wave modes supported in the model. Indeed, one can infer knowledge of the n-layer system, just by inspecting equation (3.45). In the free surface case, for example, with $\tilde{P} = 0$, the variables we would have to eliminate to find the dispersion relation (the η_j) each have coefficients containing c^2. When these equations are combined in the elimination process, a polynomial in c^2 of order n would be produced, indicating the existence of n modes, each consisting of two waves travelling in opposite directions, as predicted at the beginning of the chapter.

Of these n wave modes, we shall label the one with the highest phase speed a ‘fast’ mode, and the remaining $n - 1$ 'slow' modes. In general, there may not be a huge distinction between the phase speeds of the fast mode and the fastest slow mode; however, in the case $g_j^r \ll g$, which is ubiquitous in both geophysical and astrophysical phenomena including the solar tachocline, the fast mode propagates much quicker than the others, at least in the hydrodynamic limit, as we shall see. We shall also discover that this definition of a 'fast' mode is well-defined in that a fast mode retains its 'fastness', this faster phase speed than all the other modes, even as magnetic field strength is increased. In the hydrodynamic limit, this fast mode is often referred to as the barotropic, or surface mode (see, for example, Gill, 1982), as it travels by perturbing the surface more than the interfaces. The faster speed then arises due to the higher effective (or reduced) gravity at the surface that at the fluid-fluid interfaces, a trait arising from the higher density jump there.

3.4.1 Nondimensionalisation

Making equations nondimensional is favourable because dealing with *relative* variables, such as velocities, is often more convenient than working with the absolute quantities. For example, the knowledge that the gravity wave speed is twice the Alfvén wave speed sheds as much light on the dynamics of the system as knowledge of their actual values. The nondimensional process also makes the governing equations simpler, with nondimensional parameters determining things like stratification settings, or field strength relative to a fixed value, easy to spot in the equations. The effect on the wave dynamics of changing these parameters is usually more evident.

Equation (3.45) can be nondimensionalised by dividing through by the factor gH, the square of the gravity wave speed. This in turn gives us

$$\zeta_j^2(\tilde{\eta}_{j-1} - \tilde{\eta}_j) - \frac{\beta_j}{\rho_j}\left(\sum_{i=1}^{j} \alpha_{i-1,i}\rho_i\tilde{\eta}_{i-1} + \bar{P}\right) = 0, \tag{3.48}$$

where $\bar{P} = \tilde{P}/g$ and the parameters ζ_j^2 are given by

$$\zeta_j^2 = c^2 - {v_A}_j^2, \tag{3.49}$$

after scaling the phase speed c and the Alfvén speeds v_{Aj} with $\sqrt{gH}$. The nondimensional parameters $\alpha_{i,j}$ and β_j are stratification parameters, defined by

$$\alpha_{i,j} = 1 - \frac{\rho_i}{\rho_j}, \tag{3.50}$$

and

$$\beta_j = \frac{H_j}{H}. \tag{3.51}$$

The parameter $\alpha_{i,j}$ measures the density jump between layers i and j, and is the nondimensional reduced gravity g_j^r/g when $i = j-1$. The β_j are fractional undisturbed layer depths and represent $j-1$ controlled variables, since $\beta_1 + \beta_2 + \cdots + \beta_n = 1$.

All magnetic terms are now ensconced in the ζ_j, which reduce to the hydrodynamic phase speed c when magnetic field is removed. Taking this one step further, if we stipulate that the v_{Aj} are equal over all the layers, then the ζ_j are also equal, and take values given in terms of the stratification parameters $\alpha_{i,j}$ and β_j only. In this case, the graph of phase speed against magnetic field strength is a hyperbola; for large field strengths the wave modes all travel at this constant Alfvén speed.

In general, however, the ζ_j will not be equal, and the phase speed will depend on some combination of stratification parameters and Alfvén speeds. However, we can still say something about the phase speeds when the Alfvén speeds are large. The terms in the large brackets in equation (3.48) are unaffected by field strength, and so if v_{Aj} is very large in layer j, then the phase speed c will also have to be approximately as large, in order for the first term to balance the smaller terms. That is, of course, unless there is some kind of suppression of interface motion, which we shall look into in more detail in the next chapter.

In a similar nondimensionalisation process as in the derivation of equation (3.48), we now turn our attention to the governing equations, (3.10). We scale velocity and L/T with $\sqrt{gH}$, where L and T are typical horizontal length and time scales respectively. Magnetic field $\mathbf{B}_j$ is scaled with $\sqrt{\mu_0 \rho_j g H}$. Since the product $\rho_1 g H$ has the units of pressure, we scale P with this quantity. The governing equations given by (3.10) are then, in dimensionless form,

$$\frac{\partial \mathbf{u}_j}{\partial t} + \mathbf{u}_j \cdot \nabla \mathbf{u}_j = -\frac{1}{\rho_j} \sum_{i=1}^{j} \alpha_{i-1,i} \rho_i \nabla \eta_{i-1} - (1-\alpha_{1,j}) \nabla \bar{P} + \mathbf{B}_j \cdot \nabla \mathbf{B}_j, \tag{3.52a}$$

$$\frac{\partial h_j}{\partial t} + \nabla \cdot \big(h_j \mathbf{u}_j\big) = 0, \tag{3.52b}$$

$$\frac{\partial \mathbf{B}_j}{\partial t} = \mathbf{B}_j \cdot \nabla \mathbf{u}_j - \mathbf{u}_j \cdot \nabla \mathbf{B}_j, \tag{3.52c}$$

with

$$\nabla \cdot \big(h_j \mathbf{B}_j\big) = 0, \qquad \text{and} \qquad h_j = 1 + \eta_{j-1} - \eta_j. \tag{3.52d}$$

3.5 Summary and discussion

The main aims of this chapter were to extend the single layer SWMHD model to an n-layer system, to show that this system supports linear wave-like motion only, and to derive an equation that we can use to generate dispersion relations and other useful physical properties of the wave modes present. Along the way, we showed that there are no zero-frequency modes (see appendix A for further details), as well as showing that there are no instabilities in the stably stratified linear case. Searching for wave-like solutions of the equations is then well-founded, and will be expanded upon in the next chapter.

The main reason one would choose to use a SWMHD multi-layer model over that of a single layer is to investigate the effects of differing magnetic field geometries. Owing to the great uncertainty of the magnetic structure in the tachocline, the need for a model that allows for large variations in field strength and direction is warranted. The only restriction in this model is that magnetic fields have to be locally horizontal, which is one of the few points most applied mathematicians agree on! The reason for this unanimity is that the high velocity shear within the tachocline, which has been shown to be present inarguably using helioseismology (Schou et al., 1997; Christensen-Dalsgaard et al., 1996, and others), stretches out any vertical variations of magnetic field along the direction of shear, which is horizontal.

The simplifying assumptions we made in this chapter were the same as those in chapter 2; the fluid is inviscid, perfectly conducting, of constant density and with zero curvature. Each layer in this model is also shallow, so that our attention is restricted to wavelengths much greater than the typical height of a layer. In addition, we imposed that the layers were immiscible. By linearising the governing equations, we then restricted our attention further to small-amplitude waves. The disturbance energy conservation law (3.34) showed that in a stably stratified system, only waves are supported. Then, small disturbances of the model will not grow exponentially and violate our linear assumptions, so we need not worry about any lurking instabilities. However, if any of the g_j^r are negative then we can draw no such conclusions, since it would then be conceivable that the coefficient of ω^2 in equation (3.40) is zero, and so frequency could take an imaginary value. This is sensible physically, as one would expect some kind of unstable behaviour if heavier fluid lies above lighter fluid, for a great enough density jump, via a baroclinic instability.

After establishing the stability of the model, we then went ahead and looked for waves in the linear system. After some algebra, we ended the chapter with the derivation of equation (3.45) which will be used in the next chapter, which contains $n = 2$ and $n = 3$ examples.

Two useful results following from the work in this chapter are outlined in Appendices B and C. The former is an outline of a method of finding the n-layer dispersion relation inductively, which is computationally faster than the standard method for $n > 2$. The latter is an investigation into some fully nonlinear solutions of the governing equations (3.52).

An alternative method of calculating the n-layer dispersion relation was also mentioned, with further explanation in appendix B.

Chapter 4

The 2 and 3-layer models

4.1 Introduction

Chapter 3 dealt with the general n-layer system. Here, in order to consider the wave motions in more detail, we will look at the specific cases of the 2- and 3-layer models.

The 2-layer model is of particular interest, as it is the simplest multi-layer system, and is often used to model hydrodynamic phenomena. For example, the Earth's atmosphere is stably stratified (for the most part) and supports dynamics with an aspect ratio favourable for a shallow water analysis (see, for example, Gill, 1982). The tropopause (the boundary between the troposphere and the stratosphere) could be represented by an interface between two fluid layers in the model. In models of the oceans, the thermocline is often represented by the interface; in such models, the lower layer is often much deeper than the upper layer too, leading to a 1.5-layer approach (see appendix D for more details).

Of course, the 2-layer model can also be used to simulate the dynamics of a continuously stratified layer, with the interface being a property of the model only. This model interface not only allows us to control stratification more precisely, but in our case also to investigate further vertical variations of magnetic field.

The 3-layer model allows us to take this one step further, giving more possibilities for the basic state magnetic field, and hence possibilities of new dynamics. As in the 2-layer section, the focus will be on the transition from the hydrodynamic to the magnetic regimes, and the effect on the speeds and flow structure of the wave modes supported by the system.

The chapter will begin by outlining the 2-layer free-surface model, including the governing equations and the derivation of the 2-layer dispersion relation. The linear wave modes supported by the system in the absence of magnetic field will be discussed, with their phase speed and wave structure examined. Different magnetic fields will then be introduced in three separate examples, in order to fully investigate the magnetic influence on the modes. A similar analysis on the 2-layer rigid lid model will follow. The group velocities and the relative orientation of the two horizontal magnetic fields will also be considered, for both the free surface and rigid lid cases.

The second half of the chapter will focus on the 3-layer system, and is similar in structure. After the model outline, specific examples will be chosen to highlight new dynamics of the system; there are too many different magnetic field configurations in the 3-layer set-up to coherently study them all, since there are many orderings of the magnitudes of the Alfvén speeds, and many ways of constructing these from relative field strengths and orientations.

4.2 The 2-layer model

We shall begin our analysis of many layered systems by first considering the simplest extension to the single layer model: the 2-layer case. The set-up is as shown in figure 3.1 with $n = 2$, so that $\eta_2 = 0$. This has been studied extensively in the hydrodynamic regime (see, for example, Gill, 1982; Ovsyannikov, 1979), and so we will be comparing our results to these established ones throughout, and investigating the effects of adding magnetic field. The approach will then be to outline the magnetic field geometries that produce interesting results, and discuss those in turn.

The equations that govern the 2-layer system follow from (3.52) with $n = 2$. The equations for conservation of momentum can be written as

$$\frac{\partial \mathbf{u}_1}{\partial t} + \mathbf{u}_1 \cdot \nabla \mathbf{u}_1 = -\nabla(\eta_0 + P) + \mathbf{B}_1 \cdot \nabla \mathbf{B}_1, \tag{4.1a}$$

$$\frac{\partial \mathbf{u}_2}{\partial t} + \mathbf{u}_2 \cdot \nabla \mathbf{u}_2 = -(1 - \alpha_{1,2})\nabla(\eta_0 + P) - \alpha_{1,2}\nabla\eta_1 + \mathbf{B}_2 \cdot \nabla \mathbf{B}_2, \tag{4.1b}$$

and the equations for the evolution of magnetic field and surface/interface heights as

$$\frac{\partial h_j}{\partial t} + \nabla \cdot (h_j \mathbf{u}_j) = 0, \tag{4.2a}$$

$$\frac{\partial \mathbf{B}_j}{\partial t} = \mathbf{B}_j \cdot \nabla \mathbf{u}_j - \mathbf{u}_j \cdot \nabla \mathbf{B}_j, \tag{4.2b}$$

for layer j, where $j = 1, 2$. These are accompanied by the divergence-free condition on magnetic field, which is

$$\nabla \cdot (h_j \mathbf{B}_j) = 0,$$

and the non-dimensional layer height is $h_j = \beta_j + \eta_{j-1} - \eta_j$. Note that the nondimensional parameter $\alpha_{1,2}$ is a measure of the density jump over the fluid-fluid interface, and β_j is the fractional layer depth of layer j.

Our focus is on linear waves, which are described by equations that are found by linearising the governing equations about a basic state. As previously discussed, the basic state is motionless, with a horizontal ambient magnetic field in each layer. We consider small-amplitude (infinitesimal) perturbations to this state, stipulating that these perturbations are so small that any terms that contain products of these small quantities are negligible. The linearised momentum equations are

$$\frac{\partial \mathbf{u}_1'}{\partial t} = -\nabla(\eta_0 + P) + \mathbf{B}_{01} \cdot \nabla \mathbf{B}_1', \tag{4.3a}$$

$$\frac{\partial \mathbf{u}_2'}{\partial t} = -(1 - \alpha_{1,2})\nabla(\eta_0 + P) - \alpha_{1,2}\nabla\eta_1 + \mathbf{B}_{02} \cdot \nabla \mathbf{B}_2'. \tag{4.3b}$$

The corresponding linearised height and induction equations become

$$\frac{\partial h_j}{\partial t} + \beta_j \nabla \cdot \mathbf{u}_j' = 0, \tag{4.4a}$$

$$\frac{\partial \mathbf{B}_j'}{\partial t} = \mathbf{B}_{0j} \cdot \nabla \mathbf{u}_j', \tag{4.4b}$$

with associated solenoidal condition

$$\mathbf{B}_{0j} \cdot \nabla h_j + \beta_j \nabla \cdot \mathbf{B}_j' = 0.$$

Then, seeking sinusoidal solutions that vary as $e^{i(\mathbf{k}\cdot\mathbf{x} - \omega t)}$ (i.e., of the form (2.35)), we can use the equivalences $\partial_t \to -i\omega$ and $\nabla \to i\mathbf{k}$ to write equations (4.3) as

$$\omega\tilde{\mathbf{u}}_1 - \mathbf{k}(\tilde{\eta}_0 + \tilde{P}) + (\mathbf{B}_{01} \cdot \mathbf{k})\,\tilde{\mathbf{B}}_1 = 0, \tag{4.5a}$$

$$\omega\tilde{\mathbf{u}}_2 - (1 - \alpha_{1,2})\mathbf{k}(\tilde{\eta}_0 + \tilde{P}) - \alpha_{1,2}\mathbf{k}\tilde{\eta}_1 + (\mathbf{B}_{02} \cdot \mathbf{k})\,\tilde{\mathbf{B}}_2 = 0. \tag{4.5b}$$

Similarly, equations (4.4) become

$$\omega(\tilde{\eta}_0 - \tilde{\eta}_1) - \beta_j \mathbf{k} \cdot \tilde{\mathbf{u}}_j = 0, \tag{4.6a}$$

$$\omega\tilde{\mathbf{B}}_j + \big(\mathbf{B}_{0j} \cdot \mathbf{k}\big)\,\tilde{\mathbf{u}}_j = 0, \tag{4.6b}$$

together with

$$\big(\mathbf{B}_{0j} \cdot \mathbf{k}\big)\,(\tilde{\eta}_0 - \tilde{\eta}_1) + \beta_j \mathbf{k} \cdot \tilde{\mathbf{B}}_j = 0.$$

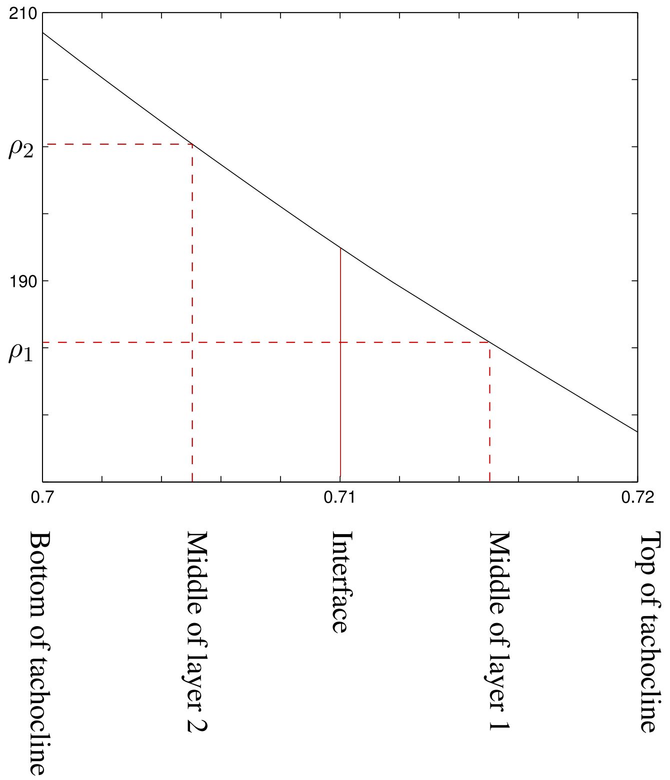

Figure 4.1 – Plot of the density profile of the tachocline, using data from model S from Christensen-Dalsgaard et al. (1996). The black curve is the density, against distance from the centre of the Sun (x-axis, in units of solar radius $R_\odot$) as inferred by helioseismology. The method used to calculate the densities of the layers in the 2-layer model is shown in red. This profile refers to the stably stratified radiative sub-layer of the tachocline.

These equations can be used to derive some more properties of the wave modes, such as structure and relative mass flux for each layer.

The multi-layer SWMHD model derived in Chapter 3 can be applied to many shallow astrophysical objects, as discussed in Chapter 1, but the primary aim in this thesis is to use it to model the solar tachocline. We have already established the model height of $H = 6.54\,\mathrm{m}$ and the gravitational acceleration $g = 54\,\mathrm{m\,s^{-1}}$ in Chapter 2, section 2.8. The values of the stratification parameters are not mutually exclusive, since the fractional layer thickness will affect the average density in each layer, and so the value of $\alpha_{1,2}$. For example, we could take median values of the density profile as inferred by helioseismology. If $\beta_1 = \beta_2 = 0.5$, so that the undisturbed layer depths were equal, the flat base at $0.7R_\odot$ and the surface at $0.72R_\odot$, then the interface would be at $0.71R_\odot$ and we would take density readings at $0.715R_\odot$ for ρ_1 and at $0.705R_\odot$ for ρ_2. This is shown in figure 4.1, which displays the density profile as inferred using helioseismology by Charbonneau et al. (1999) *et al.* This gives the values $\rho_1 = 185\,\mathrm{kg\,m^3}$ and $\rho_2 = 201\,\mathrm{kg\,m^3}$, so the value of $\alpha_{1,2}$ is then $\alpha_{1,2} \approx 0.08$.

This small value of $\alpha_{1,2}$ is typical of many physical systems such as the Earth's ocean and atmosphere. Indeed, we are able to exploit the fact that $\alpha_{1,2} \ll 1$ to make analytic progress, allowing us to probe further the physics of the supported modes.

We should also keep in mind that all speeds (including phase speeds and Alfvén speeds) have been scaled with the gravity wave speed, $\sqrt{gH}$.

4.3 The 2-layer free-surface model

In allowing free surface motion, we stipulate that $P = 0$ in equation (3.48). This then gives us the pair of equations

$$\zeta_1^2(\tilde{\eta}_0 - \tilde{\eta}_1) - \beta_1\tilde{\eta}_0 = 0, \tag{4.7a}$$

$$\zeta_2^2\tilde{\eta}_1 - (1-\alpha_{1,2})\beta_2\tilde{\eta}_0 - \alpha_{1,2}\beta_2\tilde{\eta}_1 = 0, \tag{4.7b}$$

in the two variables η_0 and η_1. There are also four independent parameters: $\alpha_{1,2}$, β_1 (say), and the two Alfvén speeds v_{A1} and v_{A2}, since $\beta_2 = 1 - \beta_1$. These equations can be written in matrix form as

$$\begin{pmatrix} \zeta_1^2 - \beta_1 & -\zeta_1 \\ -(1-\alpha_{1,2})\beta_2 & \zeta_2^2 - \alpha_{1,2}\beta_2 \end{pmatrix} \begin{pmatrix} \tilde{\eta}_0 \\ \tilde{\eta}_1 \end{pmatrix} = 0, \tag{4.8}$$

from which we can derive the dispersion relation for the 2-layer model by noting that the determinant of the matrix of coefficients is zero for non-trivial solutions. This gives

$$\zeta_1^2\zeta_2^2 - \beta_1\zeta_2^2 - \beta_2\zeta_1^2 + \alpha_{1,2}\beta_1\beta_2 = 0, \tag{4.9}$$

where $\zeta_j^2 = c^2 - v_{Aj}^2$. This can be written as

$$c^4 - \left(v_{A1}^2 + v_{A2}^2 + 1\right)c^2 + v_{A1}^2 v_{A2}^2 + \beta_1 v_{A2}^2 + \beta_2 v_{A1}^2 + \alpha_{1,2}\beta_1\beta_2 = 0, \tag{4.10}$$

when the brackets are expanded. Note that the phase speed c has been scaled with $\sqrt{gH}$ here. Note also that this relation is quadratic in c^2, indicating the existence of two values of c^2, one for each wave mode, as predicted in the discussion in section 3.4. Each $\pm$ pair of values of c correspond to waves propagating in opposite directions, but of the same type; in this work only different values of c^2 indicate different modes.

Note that the dispersion relation (4.9) could also have been derived using equations (4.5) and (4.6) by eliminating all but one of the variables. However, this would only be repeating the analysis undertaken in Chapter 3, in which the general case was considred.

Hydrodynamic reduction

In the hydrodynamic regime, ζ_j^2 reduces to c^2, and hence the dispersion relation (4.10) reduces to the well known relation

$$c^4 - c^2 + \alpha_{1,2}\beta_1\beta_2 = 0 \tag{4.11}$$

(see, for example, Gill, 1982). This can then be solved to give

$$c_+^2 \approx 1 - \alpha_{1,2}\beta_1\beta_2, \qquad \text{and} \qquad c_-^2 \approx \alpha_{1,2}\beta_1\beta_2, \tag{4.12}$$

making use of the property $\alpha_{1,2} \ll 1$. The value $c_+^2 \approx 1$ corresponds to a physical phase speed (after undoing the scaling) of a little less than gH, the surface gravity wave speed. The value of c_-^2 translates to $g^r H_1 H_2$, which involves the reduced gravity at the interface.

In the previous chapter, we made a distinction between the fastest mode and the others. Similarly, here, the mode with the greatest phase speed will be denoted the ‘fast’ mode, and the other the ‘slow’ mode. It is immediately obvious that the value of c_-^2 is much lower than 1, the approximate value of c_+^2. In this sense, the distinction between the fast and the slow modes is stark. This is due to the difference in effective gravity at the surface and interface. As the fast mode perturbs the surface more than the interface, it travels faster because the density jump over the free surface is relatively large – this mode is often referred to as the barotropic mode in hydrodynamic literature. The slow mode is not as fast because it is mainly internal, with the interface moving more than the surface, and the interface does not feel the full effect of gravity due to the similar density of the fluid above. This is called the baroclinic mode in studies without magnetic field. Here, we will continue to call them the ‘fast’ and ‘slow’ modes, since the introduction of magnetic field can affect the waves’ structures, and blur this structural definition.

Our definition of the ‘fast’ mode, however, remains true even as magnetic field strength is introduced, and holds for all field strengths. Indeed, when v_{A1} and v_{A2} are large, the phase speed

c must also be large to balance the ${v_A}_1^2{v_A}_2^2$ term. The dominant balance of terms is then

$$c^4 - \left({v_A}_1^2 + {v_A}_2^2\right) c^2 + {v_A}_1^2{v_A}_2^2 = 0, \tag{4.13}$$

from which we find values of c equal to the ${v_A}_j^2$, so that each wave mode propagates at a speed close to an Alfvén speed. Even in this regime, the fast mode propagates with the greatest phase speed (approximately either the greatest of the v_{Aj} or $\sqrt{{v_A}_j^2 + 1}$ if the Alfvén speeds are equal). Magnetic tension then provides the biggest component of the restoring force, balancing inertia in the momentum equation. The relative importance of each term in the momentum equation can be seen in more detail in table 4.1.

Single layer reduction

Note that when the two layers are identical, the system is reduced to the single layer case. This is verified by substituting $\rho_1 = \rho_2$, so that both layers have the same density, and $v_{A1} = v_{A2}$, into the dispersion relation (4.10). Note that this does not necessarily mean that the magnetic fields have the same magnitude and direction, only that the product given in (3.47) is the same in each layer. Then the dispersion relation gives

$$c_+^2 = 1 + {v_A}_1^2, \qquad \text{and} \qquad c_-^2 = {v_A}_1^2. \tag{4.14}$$

The fast mode is the magneto-gravity dispersion relation found in the single layer case. The slow mode is the incompressible Alfvén mode found at the end of Chapter 2.

Structural and flow properties

Equations (4.7) provide a formula for the ratio $\tilde{\eta}_1/\tilde{\eta}_0$, on eliminating the phase speed c. This ratio sheds light on the structure of the wave modes, and facilitates physical interpretation of them. The ratio $\mu = \tilde{\eta}_0/\tilde{\eta}_1$ satisfies

$$(1 - \alpha_{1,2})\beta_2\mu^2 - \left(1 - 2\alpha_{1,2}\beta_2 + {v_A}_1^2 - {v_A}_2^2\right)\mu + \left({v_A}_1^2 - {v_A}_2^2 - \alpha_{1,2}\beta_2\right) = 0. \tag{4.15}$$

To determine the horizontal flow structure, one can calculate the ratio of the velocities in each layer, in the x-direction, say. This is accomplished by eliminating the $\tilde{\mathbf{B}}_j$ from equations (4.5) using (4.6b) to give

$$\left(\omega^2 - k^2 v_{A1}^2\right) \tilde{\mathbf{u}}_1 = \mathbf{k}\tilde{\eta}_0\omega, \tag{4.16a}$$

$$\left(\omega^2 - k^2 v_{A2}^2\right) \tilde{\mathbf{u}}_2 = (1-\alpha_{1,2})\mathbf{k}\tilde{\eta}_0\omega + \alpha_{1,2}\mathbf{k}\tilde{\eta}_1\omega, \tag{4.16b}$$

where the Alfvén speeds v_{Aj} are given in (3.47). After dividing the x-components of the resulting two equations and algebraically manipulating, one arrives at

$$\frac{u_1}{u_2} = \frac{\zeta_2^2}{\zeta_1^2}\left(\frac{\mu}{(1-\alpha_{1,2})\mu + \alpha_{1,2}}\right), \tag{4.17}$$

where $\tilde{\mathbf{u}}_j = (u_j, v_j)$. Note that a corresponding formula for flow in the y-direction can be derived in the same way; it is identical to (4.17) above, but with v_j replacing u_j.

We can also derive another formula for the ratio of the divergences of velocity in each layer, which would be useful in our investigation of the flow structure of the modes. To do this, we look for solutions of equation (4.4a) of the form (2.35) for $j = 1$ and $j = 2$. Taking the ratio, we arrive at

$$\frac{\mathbf{k}\cdot\tilde{\mathbf{u}}_1}{\mathbf{k}\cdot\tilde{\mathbf{u}}_2} = \frac{\beta_2}{\beta_1}(\mu - 1), \tag{4.18}$$

which, together with the solutions of (4.15), can be used to infer more details of the horizontal velocity structure for each mode.

Finally, before considering some special cases and specific model set-ups, we can also derive expressions for the ratios of the terms in the momentum equations for each layer, enabling us to calculate the relative importance of each term, and the main driving/restoring forces of the waves. In layer 1 for example, the ratio of the inertial term to the surface displacement term can be expressed as the ratio of the x-components of the first two terms of equation (4.5a) as $gk\tilde{\eta}_0/\omega u_1$. One can then use equation (4.16a) to rewrite the numerator, and arrive at

$$\frac{(\omega^2 - k^2 v_{A1}^2)u_1}{\omega^2 u_1} = \frac{\zeta_1^2}{c^2}, \tag{4.19}$$

for non-trivial results, upon dividing by k^2. This process is a little trickier for layer 2 owing to the extra interface term, but progress can be made by eliminating u_2 instead of $\tilde{\eta}_0$. The result is that the ratio of the first term on the right of (4.1b) to the first term on the right is

$$\frac{(1-\alpha_{1,2})\mu\zeta_2^2}{c^2((1-\alpha_{1,2})\mu + \alpha_{1,2})}. \tag{4.20}$$

This has been repeated for all possible ratios, and the resulting expressions displayed in tables 4.1 and 4.2. Note that some information in the tables is redundant, since some entries can be

	$\frac{\partial \mathbf{u}_1'}{\partial t}$	$\nabla \eta_0$	$\mathbf{B}_{01} \cdot \nabla \mathbf{B}_1'$
$\frac{\partial \mathbf{u}_1'}{\partial t}$	-	$\frac{\zeta_1^2}{c^2}$	$\frac{{v_A}_2^2}{c^2}$
$\nabla \eta_0$		-	$\frac{{v_A}_1^2}{\zeta_1^2}$
$\mathbf{B}_{01} \cdot \nabla \mathbf{B}_1'$			-

Table 4.1 – Expressions for the ratios of terms in the momentum equations for layer 1. The x-components of the terms across the top of the table are the numerators of the fractions.

	$\frac{\partial \mathbf{u}_2'}{\partial t}$	$(1-\alpha_{1,2})\nabla \eta_0$	$\alpha_{1,2}\nabla \eta_1$	$\mathbf{B}_{02} \cdot \nabla \mathbf{B}_2'$
$\frac{\partial \mathbf{u}_2'}{\partial t}$	-	$\frac{(1-\alpha_{1,2})\mu}{\upsilon}\frac{\zeta_2^2}{c^2}$	$\frac{\alpha_{1,2}}{\upsilon}\frac{\zeta_2^2}{c^2}$	$\frac{{v_A}_2^2}{c^2}$
$(1-\alpha_{1,2})\nabla \eta_0$		-	$\frac{\alpha_{1,2}}{(1-\alpha_{1,2})\mu}$	$\frac{\upsilon}{(1-\alpha_{1,2})\mu}\frac{{v_A}_2^2}{\zeta_2^2}$
$\alpha_{1,2}\nabla \eta_1$			-	$\frac{\upsilon}{\alpha_{1,2}}\frac{{v_A}_2^2}{\zeta_2^2}$
$\mathbf{B}_{02} \cdot \nabla \mathbf{B}_2'$				-

Table 4.2 – Expressions for the ratios of terms in the momentum equation for layer 2, where $\upsilon = (1-\alpha_{1,2})\mu + \alpha_{1,2}$.

calculated by multiplying or dividing existing ratios. However, all possibilities have been included for completion and ease of use, if one notes that the blank spaces can be quickly filled in by taking the reciprocal of the appropriate entry.

We are now in a position to investigate the types of waves that can exist in the 2-layer free surface model. We will start by considering the simplest scenarios, such as equal Alfvén speeds in each layer, and work towards more elaborate magnetic geometries which highlight interesting mode properties. Our main focus will be on the effects of introducing a magnetic field to the hydrodynamic system mentioned earlier. In order to make such a comparison, however, one must first fully describe the hydrodynamic regime against which we shall compare.

4.3.1 The hydrodynamic regime

Just after deriving the dispersion relation for linear waves (4.10) we considered the hydrodynamic case (with no magnetic fields) to make sure that the relation reduced to that of Gill (1982). We should go one step further than this, and fully describe the wave modes in the absence of magnetic field, in order that we can make comparisons later.

Previously, we found that the hydrodynamic modes satisfy (4.11), and that the fast mode propagates at a phase speed close to the surface gravity speed, and the slow mode is $\mathcal{O}(\alpha_{1,2})$ smaller than this, for small $\alpha_{1,2}$. We can investigate the structure of these modes using (4.15).

Fast (barotropic) mode

For the fast mode, with phase speed $c_+^2 \approx 1$ given by (4.12), we have $\mu_+ \approx 1/\beta_2$ when $\alpha \ll 1$. This indicates that the amplitude of the fluid-fluid interface is approximately β_2 times the surface displacement for any point in the (x, y) plane. For example, if one considers equal layer depths so that $\beta_1 = \beta_2 = 0.5$, then the surface amplitude is approximately twice that of the interface; this is illustrated on the left hand side of figure 4.2. Since the density jump at the surface is much greater than at the interface, the effective gravity is stronger here, and hence also the restoring force. The influence of the interface motion on the phase speed of this mode is then small compared to that of the surface, which explains the fact that the phase speed value is close to that of the surface gravity wave.

Use of equation (4.17) gives the ratio $u_1/u_2 \approx 1 + \alpha_{1,2}\beta_1$, which indicates that horizontal velocities in each layer are approximately equal. Furthermore, the ratio of divergence of velocities, given by equation (4.18) gives $\mathbf{k} \cdot \mathbf{u}_1' \approx \mathbf{k} \cdot \mathbf{u}_2'$, so that the horizontal fluid flow in each layer is approximately the same. This indicates a net horizontal movement of fluid as the wave propagates, so that the flux through a vertical cross-section would oscillate with the same frequency as the wave. This is true whenever the surface is moving, but in this case the surface is moving more than the interface, so that the mass flux of each layer conspires to create a larger net mass flux.

If we consider a layer of fresh water (on Earth) of density $1000\,\mathrm{kg\,m}^3$ lying over a layer of salty water with density $1027\,\mathrm{kg\,m}^3$, we have $\alpha_{1,2} \approx 0.0263$, which is certainly small enough to make our simplifications valid. If, for example, the layers were each 0.5 m deep, the phase speed of the fast mode would be around $3.1\,\mathrm{m\,s}^{-1}$. These are essentially surface gravity waves, similar to the ones visible on a beach.

Slow (baroclinic) mode

The slow mode, with phase speed $c_-^2 \approx \alpha_{1,2}\beta_1\beta_2$, highlights the stark difference between the 'fast' and 'slow' modes in the hydrodynamic regime when $\alpha_{1,2}$ is small. For this mode, $\mu \approx -\alpha_{1,2}\beta_2$, which indicates surface displacements much lower than those at the interface. For this reason, this mode is often called an *internal* mode, and the fast mode a *surface* mode. However, as magnetic field is increased, this internal/surface property is blurred somewhat, and so we shall stick to our 'fast' and 'slow' definitions. Since the ratio μ is negative in this instance, it follows that the surface and interface are in antiphase, not in phase as in the fast mode. This means that as the interface rises, the surface drops directly above.

To further investigate the physics of the slow mode, one can verify that $u_1/u_2 \approx \beta_2/\beta_1$; the ratio of the divergences also gives $\mathbf{k} \cdot \tilde{\mathbf{u}}_1/\mathbf{k} \cdot \tilde{\mathbf{u}}_2 \approx \beta_2/\beta_1$. This can be written in dimensional form as $\beta_1\nabla \cdot \mathbf{u}_1 + \beta_2\nabla \cdot \mathbf{u}_2 \approx 0$, indicative of a low horizontal mass flux. This means that the flux in each layer has opposite sign, and sums destructively (rather than constructively as in the fast mode). Since the net mass flux is small, the surface motions are also small, in the sense that surface motion is much less than interface motion.

For our $1\,\mathrm{m}$ deep example as in the fast mode analysis above, the phase speed of internal waves would be around $0.064\,\mathrm{m\,s^{-1}}$, and would propagate almost entirely internally, with the surface amplitude a mere 0.013 of the interface displacement. This was observed by Benjamin Franklin in 1762 and attributed to the dead water phenomenon in which ships would find themselves stuck in water, unable to move, inadvertently giving energy to these internal waves instead of aiding propulsion.

The aim of the first half of this chapter is to investigate how these two modes are affected by the introduction of magnetic fields. We will consider three examples, each with a different basic state magnetic field configuration, and analyse any imposed changes on the phase speeds and flow structure of the modes. For the 2-layer system, there are three categories for this basic state field: one in which the Alfvén speeds in each layer are equal, and two in which one is larger than the other. We shall therefore consider a specific example from each of these regimes, and discuss general cases.

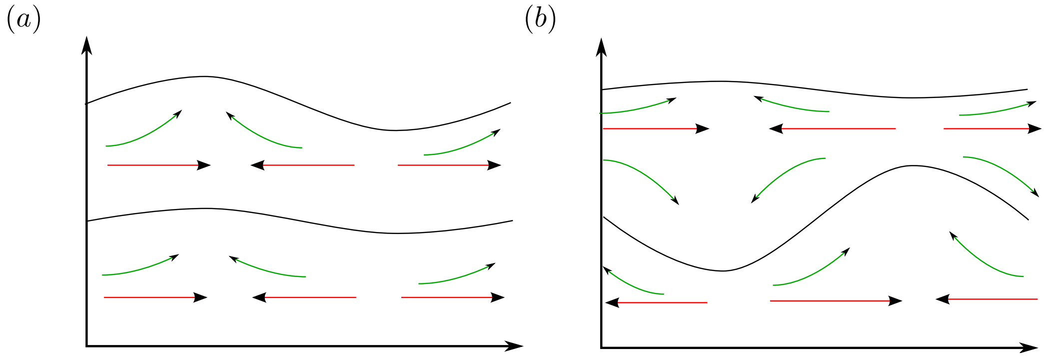

Figure 4.2 – Schematics illustrating the motion of fluid and relative surface and interface displacements for the case $v_{A_1} = v_{A_2}$. Red arrows denote horizontal fluid motion and the green arrows denote the actual motion of the fluid in each layer. Figure (a) is the surface mode, and (b) the internal mode. These diagrams are accurate for all magnetic field strengths (including the hydrodynamic regime) provided the Alfvén speeds are equal in each layer; only the wave speeds are affected by changes in field strength. Note that the arrows are for illustration purposes only, and the length of an arrow does not represent the flow speed.

4.3.2 Example 1: Equal Alfvén speeds

A good starting point when considering the effects of adding magnetic field to this configuration is to consider the simplest case: when the Alfvén speeds v_{A1} and v_{A2} are equal, so that $\zeta_1 = \zeta_2$. This *does not* mean that the magnetic field strength is the same in each layer; this will be discussed later. It does, however, greatly simplify the equations for μ and u_1/u_2, since these ratios are independent of field strength if the Alfvén speeds are the same. In this case, the structure of the wave modes is the same as in the hydrodynamic case described above. From the dispersion relation (4.9) the phase speeds are given by

$$c_-^2 \approx \alpha_{1,2}\beta_1\beta_2 + v_{A1}^2, \qquad \text{and} \qquad c_+^2 \approx 1 + v_{A1}^2, \tag{4.21}$$

for $\alpha_{1,2} \ll 1$. The curves of phase speed against v_{A_1} are then hyperbolae, as shown in figure 4.3. Equation (4.15) gives the values

$$\mu_- \approx -\alpha_{1,2}\beta_2, \qquad \text{and} \qquad \mu_+ \approx \frac{1}{\beta_2}. \tag{4.22}$$

One can see that the surface perturbations are independent of field strength and match those in the hydrodynamic case. Since the $\mu_\pm$ are constants for all field strengths, so are the ratios u_1/u_2, by equation (4.17). This means that the only change in the behaviour of these waves brought about by the introduction of a magnetic field is in the phase speeds, so long as the magnetic field is configured in such a way as to maintain $v_{A1} = v_{A2}$. Since the wave structure remains unchanged, we shall spend the remainder of this example talking about the changes induced in the phase speeds of the waves.

The fast mode

For the fast mode, in the absence of a magnetic field the phase speed is a small (order α) correction of the gravity wave speed $\sqrt{gH}$. However, as the magnetic field strength is increased from zero, the phase speed also increases, approaching v_{A_1} when the the field strength is much greater than unity. Tables 4.1 and 4.2 indicate that the main restoring force of waves is magnetic tension only when v_{A1} exceeds the gravity wave speed $\sqrt{gH}$, and as one can see from table 1, that is unlikely to be the case for the tachocline.

Nevertheless, we can investigate the high field strength regime further using tables 4.1 and 4.2. As $c_+^2 \to 1 + v_{A1}^2$ (which is the case when $v_{A1} \gg 1$), the dominant balance in the momentum equation for layer 1 switches from being between inertial and surface displacement terms (as in the hydrodynamic case) to being between the inertial and magnetic field terms. The magnetic tension becomes the restoring force for large field strengths: a property of Alfvén waves. In layer 2 also, the driving of fluid motion is caused mainly by the surface perturbations, with the interface displacement having an effect of order α in the hydrodynamic case. Again, the magnetic tension assumes more and more of this role as field strength is increased. This fast mode is shown in figure 4.2(a).

The slow mode

When v_{A_1} is very small, the speed of the internal mode is order α of the gravity wave speed, for $\alpha \ll 1$. Even small increases in field strength, however, cause the speed of this slow wave mode to increase until, for large values of v_{A_1}, the phase speed does not deviate much from the Alfvén speed itself. This mode also propagates with low total horizontal mass flux (the ratio u_1/u_2 has not changed from the hydrodynamic case): another property of incompressible Alfvén waves. In fact, the field strength does not have to increase much before this Alfvén-like behaviour kicks in. For the fast mode, v_{A1} had to be much bigger than the gravity wave speed (1 in our non-dimensional nomenclature) in order for the phase speed to be sufficiently close to the Alfvén speed, but for

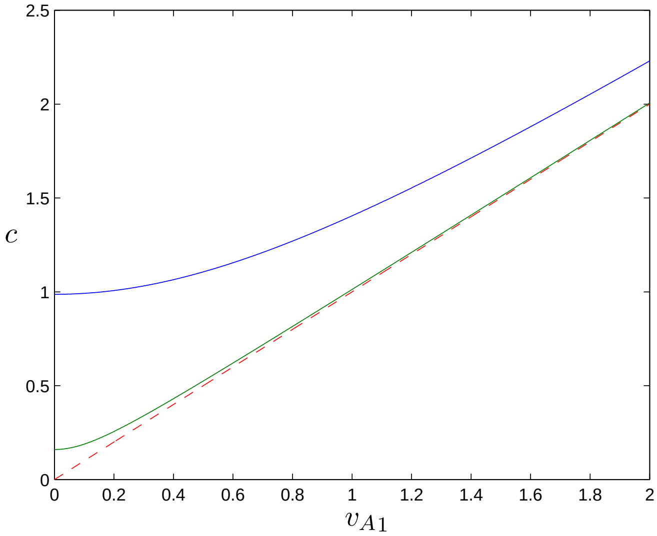

Figure 4.3 – Plots of phase speed against the Alfvén speed v_{A1} for the special case $v_{A1} = v_{A2}$. The curve representing the fast mode (blue) and the slow mode (red) are hyperbolae, both approaching the common Alfvén speed (red). In this figure, the stratification parameters are chosen to be $\alpha_{1,2} = 0.1$, with $\beta_1 = \beta_2 = 0.5$.

the slow mode, it is required only that $v_{A1}^2 \gg \alpha_{1,2}$. In this sense, the slow mode 'picks up' an Alfvén-like velocity for lower values of v_{A1}. This can also be seen in figure 4.3, as the approach of the green curve (slow mode) to the red dotted line (Alfvén speed) is much quicker than that of the blue curve (fast mode).

Further investigation of the high magnetic field strength regime, in which $c \rightarrow v_{A_1}$, can be undertaken using tables 4.1 and 4.2, in which we find that the role of restoring force is handed over to the Lorentz term much more readily than for the fast mode. Also, since the structure of the modes remains unchanged as the field strength is varied, we know that this slow mode has many of the physical properties of its hydrodynamic counterpart: it propagates with low net horizontal mass flux, for example. A schematic of the structure of this mode is shown in figure 4.2(b).

4.3.3 Example 2: Equal magnetic field strengths

In reality, it is likely that the magnetic field has constant strength and orientation throughout the depth of the layer. It would then be of more appeal physically to model the system with a uniform ambient magnetic field running through both layers. We have already mentioned that owing to our scaling of magnetic field at the start of Chapter 2, if one wanted to model a physical phenomenon in which two layers have the same magnetic field strength, the choice of $v_{A1} = v_{A2}$ is not what we require. The appropriate relation is

$$v_{A2}^2 = (1 - \alpha_{1,2}) v_{A1}^2, \tag{4.23}$$

making use of equation (3.47). One can also note that everything in this example not only applies to a constant unidirectional magnetic field permeating both layers, but also any combinations of the $|\mathbf{B}_{0j}|$ and θ_j in equation (3.47), such that (4.23) is satisfied. This is the only example in which the interfaces need not be current sheets, since one choice of magnetic configuration consists of parallel fields of equal strength.

In this example, the ratios $\mu_\pm$ and u_1/u_2 *are* affected by magnetic field strength, and so the structure of the wave modes will change as v_{A1} is varied. In keeping with the format of the previous example, we shall find expressions for the phase speeds and other properties, and then discuss each mode in turn.

We already know that in the limit of large field strength, each mode travels at an Alfvén speed: see equation (4.13). In this case, we have $c_+ \to v_{A1}$ for the fast mode and $c_- \to v_{A2}$ for the slow mode, since $v_{A1} > v_{A2}$. The interesting dynamics in this example happen for lower magnetic field strengths.

Substitution of (4.23) into the dispersion relation (4.10) gives

$$c^4 - \left((2 - \alpha_{1,2}) v_{A1}^2 + 1\right) c^2 + (1 - \alpha_{1,2}) v_{A1}^2 + (1 - \alpha_{1,2}\beta_1) v_{A1}^2 + \alpha_{1,2}\beta_1\beta_2 = 0. \tag{4.24}$$

Since our approach is to investigate the deviations from the well-known hydrodynamic case, we shall begin our magnetic analysis with smaller field strengths. When v_{A1} is $\mathcal{O}(1)$ (i.e., if the Alfvén speed in layer 1 is at most the gravity wave speed gH), then the phase speeds, for small $\alpha_{1,2}$, are given by

$$\begin{aligned} c_+^2 &\approx 1 + (1 - \alpha_{1,2}\beta_2) v_{A1}^2, \qquad \text{and} \\ c_-^2 &\approx \alpha_{1,2}\beta_1\beta_2 + (1 - \alpha_{1,2}\beta_1) v_{A1}^2. \end{aligned} \tag{4.25}$$

The correction terms on the right hand sides show the deviations from the hydrodynamic values (initial terms, see equation (4.12)) when a magnetic field has been introduced. Inspection of (4.25) indicates that for Alfvén speeds up to the gravity wave speed, the phase speeds of the supported

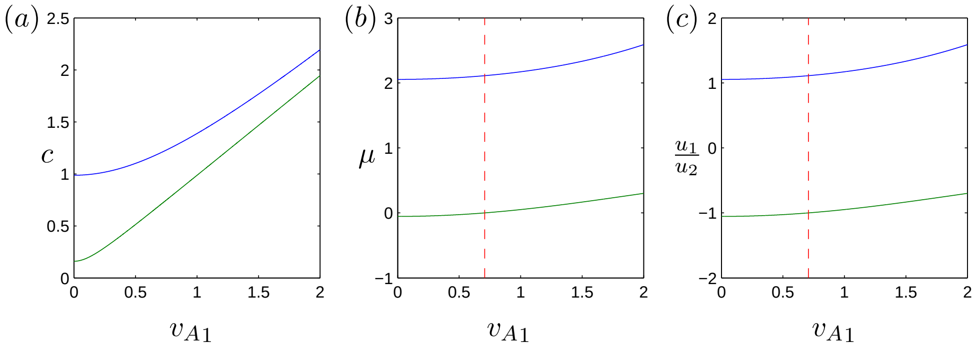

Figure 4.4 – Plots of phase speed (a), μ (b), and u_1/u_2 (c) against the Alfvén speed v_{A1} for the special case $v_{A2}^2 = (1-\alpha_{1,2})v_{A1}^2$, which could be used to model equal magnetic field strength in both layers as in example 2. The red dotted lines indicate the value $v_{A1} = \sqrt{\beta_2}$, at which the slow mode becomes purely internal. The stratification parameters are $\beta_1 = \beta_2 = 0.5$ and $\alpha_{1,2} = 0.1$.

modes are similar to that in the previous example, displayed in figure 4.3. This is not surprising, since the factor $1 - \alpha_{1,2}$ is not very different from 1 (as in the previous example) when $\alpha_{1,2}$ is small.

From (4.15), the ratio of surface to interface displacements μ satisfies

$$(1-\alpha_{1,2})\beta_2\mu^2 - \left(1 - \alpha_{1,2}(\beta_2 - v_{A1}^2)\right)\mu + \alpha_{1,2}(v_{A1}^2 - \beta_2) = 0. \tag{4.26}$$

The ratio μ vanishes for one of the modes if $v_{A1}^2 = \beta_2$. Then the surface would cease moving, and the mode in question would propagate entirely within the fluid – we shall discuss this in more detail later.

The fast mode

As well as increasing the phase speed of the fast mode (figure 4.4(a)), increasing magnetic field strength (or v_{A1}) also increases μ, so that the surface wave amplitude grows compared to that of the interface. This can be seen in figure 4.4(b), where the blue curve (representing the fast mode) rises monotonically. In fact, this rise continues as v_{A1} increases, so that in the large field strength limit $\mu \to \infty$. This can also be deduced from (4.26) by considering the dominant balance of terms, assuming μ is large (the other case, with μ not large, will be considered when discussing the slow mode). This indicates that magnetic field suppresses fluid interface motion in this regime. The left hand schematics in figure 4.5 illustrate this behaviour, by portraying snapshots of the mode structure at different magnetic field strengths.

We expect, then, that the horizontal fluid motion in the lower layer will approach zero as the field strength increases, and indeed this is the case; the expression for the fraction $\mathbf{k}\cdot\tilde{\mathbf{u}}_1/\mathbf{k}\cdot\tilde{\mathbf{u}}_2$, equation (4.18) contains μ in the product, and so also increases with v_{A1}. A similar analysis on the ratio u_1/u_2 indicates that $u_2 \to 0$, as expected. In the limit, the fluid in the lower layer becomes stagnant and wave motion is confined entirely to the upper layer.

The slow mode

In the absence of magnetic field, the surface perturbation amplitude of the slow mode is much less than the interface displacement, as can be seen in the small negative axis intercept of the green curve in figure 4.4(b). As magnetic field is introduced, this ratio of surface to interface displacements increases, eventually passing through zero and becoming positive.

Just before our discussion of the fast mode in this example, we found that the ratio μ is zero when the Alfvén speed in the top layer satisfied $v_{A1}^2 = \beta_2$. This implies that $\tilde{\eta}_0 = 0$ for $\tilde{\eta}_1 \neq 0$, which describes a wave that travels without perturbing the surface at all. Thus, for this specific value of v_{A_1}, the internal mode becomes *purely* internal, and the phase velocity is $c = \sqrt{\beta_2}$ from (4.10). At this internal transition, the phase velocity is exactly the Alfvén speed v_{A_1}, characteristic of an Alfvén wave.

To further examine the Alfvén traits of the purely internal mode, we can consider the ratios of the terms in the momentum equations using tables 4.1 and 4.2. For the top layer, we have the acceleration and Lorentz terms balancing exactly, indicating the driving mechanism for the propagation of these waves is magnetic tension alone: another trait of Alfvén waves. For the bottom layer, again, the dominant balance is between the magnetic tension and the acceleration terms, with the interface having an effect of order α and the surface having, predictably, no effect at all.

The net mass flux of this mode is zero, as can be seen by putting $\mu = 0$ into equation (4.18). This is another property of incompressible Alfvén modes, which propagate in this way. Indeed, inspection of figure 4.4(c) reveals that $u_1 = -u_2$ for this internal structure (in the graphs, $\beta_1 = \beta_2$).

It is worth taking a moment to speculate about the 2-layer rigid lid model, which we shall discuss in the next section. One could add a flat lid to the surface of this purely internal mode, and not affect the wave dynamics at all. In this sense, it should be the case that the (only) mode of the rigid

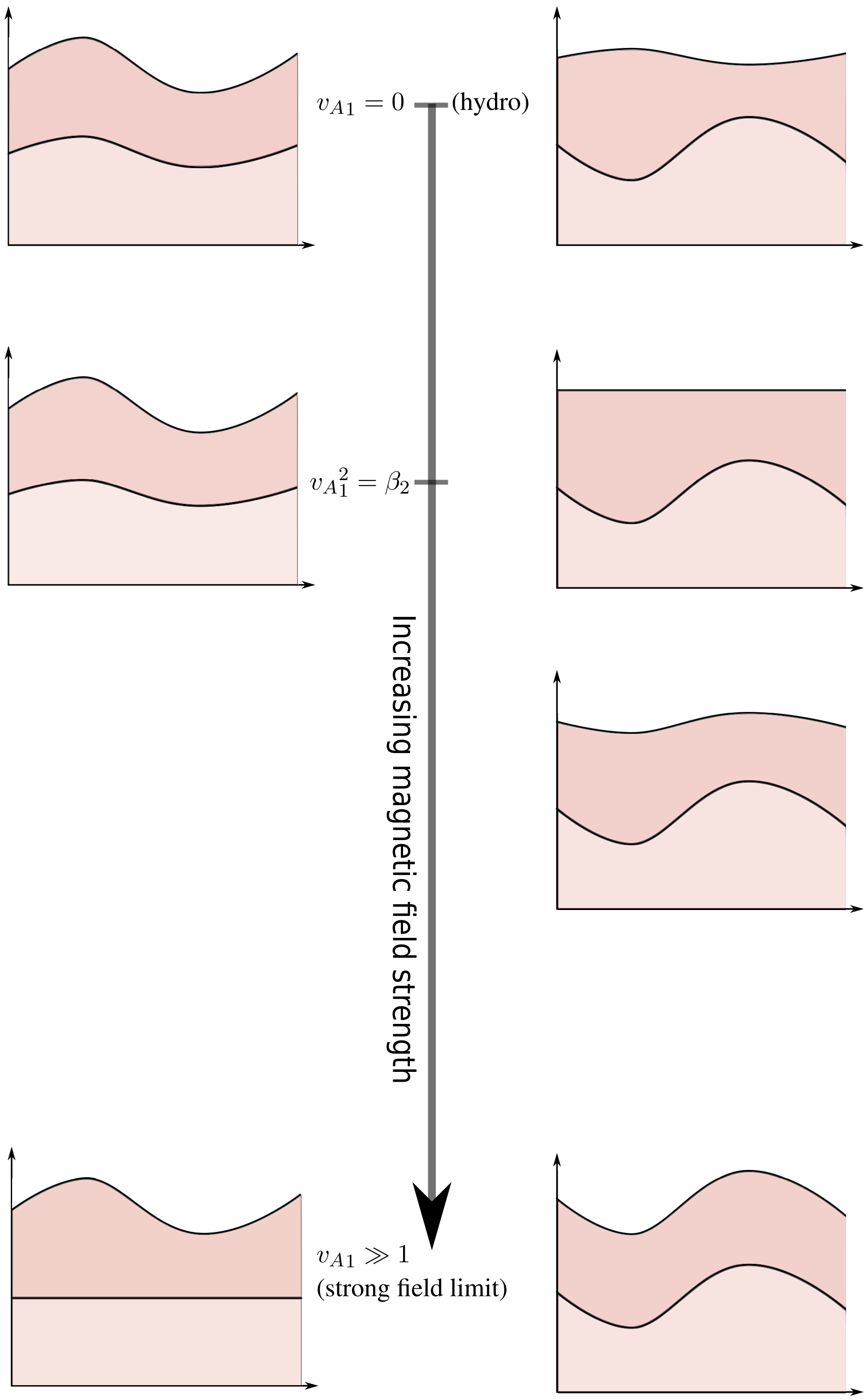

Figure 4.5 – Schematics showing the effects of magnetic field on wave structure for $v_{A2}^2 = (1 - \alpha_{1,2})v_{A1}^2$, as in example 2. The fast mode is on the left, and the slow on the right.

lid system coincides *exactly* with this one, when ${v_A}_1^2 = \beta_2$. We shall verify this later.

Increasing the magnetic field strengths (or, more accurately, the Alfvén speeds) further, we can investigate the transition of the slow mode from this purely internal behaviour by considering the regime $v_{A1} \to \infty$. As can be seen in figure 4.4, for ${v_A}_1^2 > \beta_2$ (red dotted line), μ becomes positive, and so the surface and interface are in phase in this regime: the disturbances are proportional. Equation (4.26) gives $\mu \to 1$ as $v_{A1} \to \infty$, meaning the η_j take similar values in the high field strength regime. This is illustrated in the schematics on the right hand side column of figure 4.5, which depicts the structural transition from the hydrodynamic regime, through the purely internal phase, and to the high magnetic field strength limit.

An important point to make before moving onto example 3, is that the ratios μ and u_1/u_2 are related. Note the similarities between figures 4.4(b) and 4.4(c); it transpires that these ratios are proportional. It is not at all obvious from equations (4.15) and (4.17) that this is the case, but by comparing equations (4.7) and (4.16)one obtains the relationship

$$\frac{\beta_1 u_1}{\beta_2 u_2} = \mu - 1. \tag{4.27}$$

Physically, the left hand side of this equation is interpreted as the ratio of the horizontal mass fluxes, and we would expect this to relate directly to the ratio of interface displacements. For the purely internal mode, for example, the surface does not move and the ratio of the mass fluxes is -1 (the meaning of the last term in the equation above). If the surface *is* moving, out of phase with the interface, say, then the mass flux in the upper layer has to compensate for the interface displacement caused by the mass flux in the lower layer, and then a little more to ensure the surface is moving.

Now we have verified the relationship (4.27), we need only plot μ, and infer the properties of the ratio u_1/u_2 from this.

4.3.4 Example 3: Magnetic field in one layer only

One may wish to model a shallow system in which a magnetic field permeates only one part of the layer in question. An example could be that of Jupiter's atmosphere: the conductivity of the hydrogen increases suddenly with depth as the pressure becomes high enough to induce metallic properties of the gas, as discussed in Chapter 1. In this example, we will simplify this scenario by considering the 2-layer model with one hydrodynamic layer.

Field in top layer

In the previous example, we discussed a specific example of the case $v_{A1} > v_{A2}$. Here, we shall extend this analysis, and consider the extreme case $v_{A2} = 0$, in which the bottom layer is hydrodynamic.

Putting $v_{A2}^2 = \gamma v_{A1}^2$, where $0 \leq \gamma < 1$, describes the regime in which the Alfvén speed is faster in the top layer. Substitution into equation (4.15) gives the value of v_{A1} at which the mode goes purely internal, namely

$$v_{A1}^2 = \frac{\alpha_{1,2}\beta_2}{1-\gamma}. \tag{4.28}$$

One can immediately see that v_{A1} has real solutions only when $\gamma < 1$, so that the purely internal behaviour can only exist when the Alfvén speed in the upper layer is greater than that in the lower layer. It is straightforward to verify that the corresponding phase speed for this value of v_{A1}^2 is also v_{A1}, indicative of an Alfvén-like mode as in example 2. It is also worth noting that the closer γ is to 1, the stronger the magnetic field has to be to induce this internal quality.

One can also investigate the high magnetic field strength regime, to study the change in the wave properties as the field strength is increased. The interface ratio μ tends to 1 for the slow mode and ∞ for the fast mode, regardless of γ. This means that the wave structure of the modes in the high field strength limit is identical to that illustrated in figure 4.5, even if $v_{A2} = 0$. The phase speed of the waves, however, requires some extra thought. We know that if both Alfvén speeds are large, then the phase speeds of the modes will equal them (one each) in the limit; but if $v_{A2} = 0$, only one value of c^2 (for the fast mode) can match the high Alfvén speed. The other value (c_-^2) must be $\mathcal{O}(1)$; indeed, considering the balance of terms in the dispersion relation (4.10), we have

$$c^4 - v_{A1}^2 c^2 + \beta_2 v_{A1}^2 \approx 0, \tag{4.29}$$

leading to

$$c^2 \approx v_{A1}^2 \qquad \text{and} \qquad c^2 \approx \beta_2. \tag{4.30}$$

Interpreting these values physically, in the high field strength limit, the fast mode propagates entirely in the upper layer with a single-layer magneto-gravity phase speed, the hydrodynamic lower layer remaining motionless. For the slow mode, the upper layer acts as an extension to the surface, with both surface and interface motions equivalent, as in example 2. The general case $v_{A1} > v_{A2}$, then, is very similar to that considered in the previous example, pictured in figure 4.5.

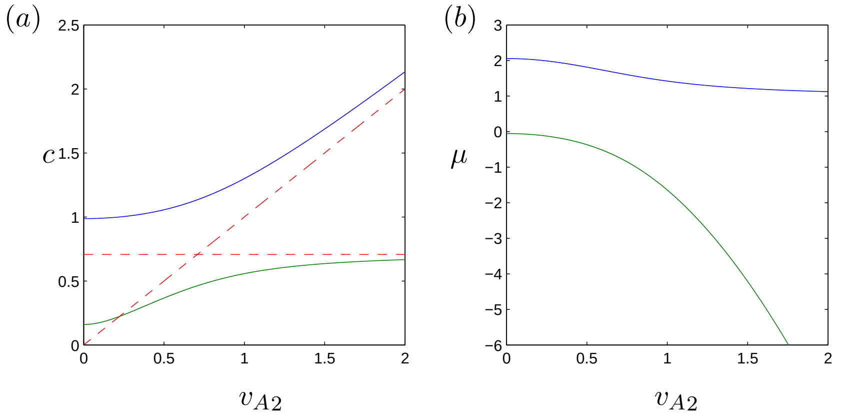

Figure 4.6 – Graphs of (a) phase speed and (b) μ for the special case $v_{A1} = 0$, as in example 3. Blue and green curves correspond to fast and slow modes, respectively. The horizontal red dotted line represents the phase speed $c = \sqrt{\beta_1}$, the hydrodynamic value that the slow mode tends towards in the high magnetic field strength limit. The diagonal red dotted line traces $c = v_{A2}$.

Field in bottom layer

It remains to consider the case $v_{A1} < v_{A2}$. We have concluded that if $\gamma \geq 1$ there is no purely internal behaviour, and so we know the surface will be in motion for all magnetic field strengths in this case. In fact, there are not many distinct properties of the modes in this regime – but there are some subtle points to note, as well as an interesting feature which applies to the case with magnetic field in either layer. First, we shall examine the similarities and differences between this model (with the field in the bottom layer only) and the previous one (in which field was in the top layer). The dispersion relation (4.10), with $v_{A1} = 0$ gives

$$c^4 - \left(v_{A2}^2 + 1\right) c^2 + \beta_1 v_{A2}^2 + \alpha_{1,2}\beta_1\beta_2 = 0, \tag{4.31}$$

from which we can plot the phase speeds of the two modes, as in figure 4.6. One can see that the phase speeds tend towards $\sqrt{\beta_1}$ (slow mode) and v_{A2} (fast) as $v_{A2} \to \infty$. We anticipate that the reason for this hydrodynamic gravity wave speed in the presence of a high strength magnetic field may be due to the magnetised layer being confined somehow for one of the modes; indeed, the ratio $\mu \to -\infty$ confirms that the interface stops moving in the high field strength limit. Then the slow mode propagates entirely in the upper layer, with the lower plasma stagnant. The ratio μ for the fast mode tends to 1, giving an upper layer that exhibits only vertical fluid motion, the lower layer providing the wave motion close to the Alfvén speed.

Concluding, the main difference between the cases $v_{A1} = 0$, $v_{A2} \neq 0$ and $v_{A1} \neq 0$, $v_{A2} = 0$ is

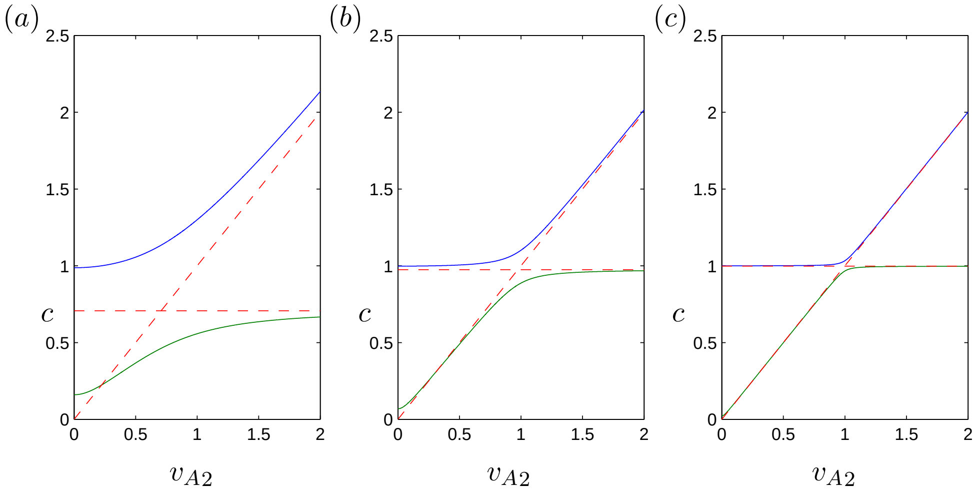

Figure 4.7 – Plots of phase speed against Alfvén speed v_{A2} for the case $v_{A1} = 0$. Plot (a) displays the curves for $\beta_1 = 0.5$, plot (b) $\beta_1 = 0.95$, and plot (c) $\beta_1 = 0.995$. One can see that as $\beta_1 \to 1$, the curves become more and more similar to the red dotted lines (which trace $c = \sqrt{\beta_1}$ and $c = v_{A2}$), and the avoidance point becomes more pronounced.

that in the high field strength regime, the structure of the wave modes is swapped when magnetic field is transferred to the other layer. That is, when the bottom layer is hydrodynamic, the wave structures are as in figure 4.5 (fast mode on bottom left, slow bottom right); when the *top* layer is hydrodynamic, the bottom left figure shows the structure of the *slow* mode, and vice-versa.

Hydrodynamic behaviour in large field strength regimes, and the 'avoidance point'

The discovery of another feature of the two layer system when the magnetic field is in one layer only is inspired by equation (4.31). The last term on the left hand side can be made smaller in two ways: by making $\alpha_{1,2}$ small, or by making β_2 small (so that the lower (magnetised) layer is very thin compared to the total layer depth). Choosing the latter of these two options gives $c_-^2 \approx 1$ and $c_+^2 \approx v_{A2}^2$, shown as red dotted lines in figure 4.6.

This highlights an interesting 'avoidance point' close to the point $(\sqrt{\beta_1}, \sqrt{\beta_1})$ in (c, v_{A2}) space, around which the two phase speed curves appear to 'swap' behaviour. As v_{A2} is increased from zero, the fast mode has (an approximately constant) phase velocity of $\sqrt{\beta_1}$, and the slow mode has a phase velocity of v_{A2}. That is, however, until the field strength gets sufficiently close to the avoidance point, at which the phase speed curves would otherwise intersect; the curves avoid each other by swapping behaviour, so that as v_{A2} is increased beyond $\sqrt{\beta_1}$, the fast mode propagates close to the Alfvén speed, and the slow mode at the (now slower) hydrodynamic speed of $\sqrt{\beta_1}$. There is, in some sense, a behavioural shift between the two modes of the system, wherein the slow mode transfers its Alfvén properties to the fast, and the fast its hydrodynamic properties to the slow. Avoidance points first appeared in the study of two-state systems in the discipline of quantum mechanics.

At first glance, the idea that a system in which the bottom layer (which is magnetised) can produce a wave mode with a phase speed close to the Alfvén speed is counter-intuitive. It seems to imply that an extremely thin magnetised lower layer can support a wave mode with magnetic tension as the main restoring force, even for low field strengths. This is explained by recognising that the surface and interface perturbations are themselves infinitesimal in amplitude due to the linearisation process, and so there are no physical violations, such as an interface moving through the floor. However small one makes β_2, there will always be 'enough' fluid to house a magnetic field, to provide magnetic tension for a contribution to a restoring force.

To illustrate this, for $\beta_1 = 0.999$, as in figure 4.7(c), the fast mode is very much a surface mode in the low field strength regime, with the interface perturbations over 200 times the interface amplitude. The slow mode is very internal, with the interface disturbances -2000 times those at the surface, so that the magnetised lower layer has much more say in the motion of the wave. As field strength is increased past $\sqrt{\beta_1}$, the ratio μ for the fast mode approaches 1, so that fluid in the upper layer has low horizontal motion and the magnetised lower layer is the main driver of wave motion. For the slow mode, the ratio μ drops off to $-\infty$ and the interface stops moving, leaving a hydrodynamic upper layer that is largely unaffected by the stationary plasma below.

Of course, one can apply similar analysis to the case with $v_{A2} = 0$, and the magnetic field is instead confined to the upper layer, with much the same results.

4.3.5 Group velocities

So far in this chapter, we have taken into account only the relative sizes of the products v_{Aj}, and their effect on phase speed and mode structure. Here we will consider the additional effects of varying the angle between the magnetic fields as well as the field strength, and consider the effects on both phase and group velocities. In addition, the speed of propagation in all horizontal directions will be examined, enabling one to determine the speed and direction of energy transfer.

As in section 2.5, we shall produce polar plots of phase speed by making use of the dispersion relation (4.10), and plot these alongside the corresponding group velocity polar plots, as in the single layer case. The dispersion relation is of the form (2.49), and so we will be able to apply the analysis used in section 2.5.

However, there is a slight complication: there are now *two* angles to consider, since the magnetic field in each layer makes an angle with the x-axis. This introduces another control variable, Θ, which we shall define as the difference in the angles between the magnetic fields. Then, if we keep the field in the upper layer aligned with the x-axis, without loss of generality, the θ given in our definition of Alfvén speed (3.47) remains unchanged for layer 1. Thus, an angle measured anticlockwise from the x-axis in the polar plots will again be equal to θ, for any chosen direction. However, the angle between this direction and the field in the *lower* layer will be $\theta - \Theta$; the relation between the angles is shown in figure 4.8.

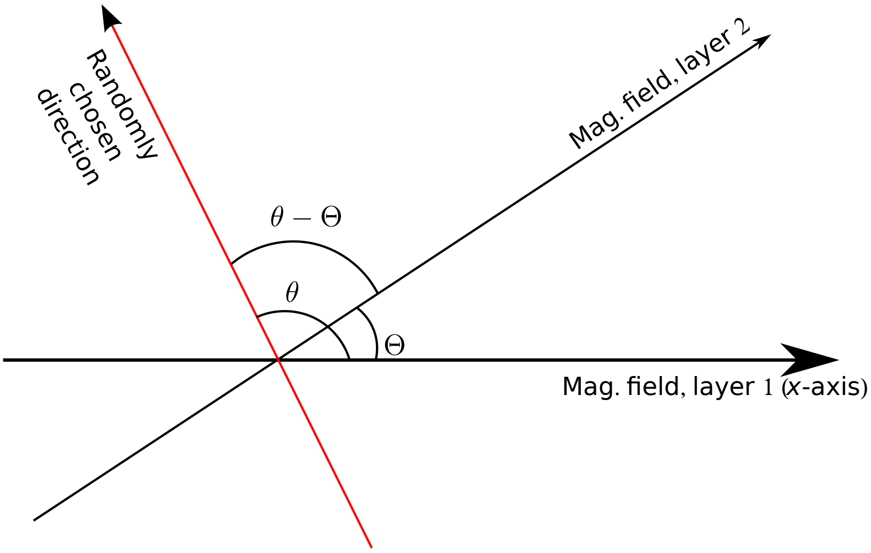

Figure 4.8 – An illustration of the different angles involved in the polar plots of phase speed, given a direction of propagation (red arrow)

Given any direction, as in the figure above, the Alfvén speeds in this direction are given by (3.47), with $\theta_1 = \theta$ and $\theta_2 = \theta - \Theta$, the angles between the chosen direction of propagation and the magnetic fields. This gives

$$v_{A1} = \frac{1}{\mu_0 \rho_1}|\mathbf{B}_{01}|\cos\theta = \frac{c_{A_1}}{k}k_x, \tag{4.32a}$$

$$v_{A2} = \frac{1}{\mu_0 \rho_2}|\mathbf{B}_{02}|\cos(\theta - \Theta) = \frac{c_{A_2}}{k}(k_x\cos\Theta + k_y\sin\Theta), \tag{4.32b}$$

where $\mathbf{k} = (k_x, k_y)$ is the wavevector, with $k = \sqrt{k_x^2 + k_y^2}$, and $c_{A_j} = |\mathbf{B}_{0j}|/(\mu_0\rho_j)^{1/2}$ are the maximum Alfvén speeds. By substituting these expressions into the dispersion relation (4.10), we obtain an equation of the form

$$\omega^4 - R\omega^2 + S = 0, \tag{4.33}$$

with

$$\begin{aligned} R =& k^2 + c_{A_1}^2 k_x^2 + c_{A_2}^2 (k_x \cos\Theta + k_y \sin\Theta)^2, && (4.34\text{a}) \\ S =& c_{A_1}^2 c_{A_2}^2 k_x^2 (k_x \cos\Theta + k_y \sin\Theta)^2 + \beta_2 c_{A_1}^2 k_x^2, \\ &+ \beta_1 c_{A_2}^2 (k_x \cos\Theta + k_y \sin\Theta)^2 + \alpha_{1,2}\beta_1\beta_2 k^4. && (4.34\text{b}) \end{aligned}$$

Our aim, as in section 2.5, is to find the partial derivatives of group velocity, project them onto perpendicular unit vectors, and plot this projection on a polar diagram. Making use of the chain rule as given in (2.54), one can project the partial derivatives of group velocity onto the vectors $\hat{\mathbf{k}} = (\cos\theta,\, \sin\theta)$ and $\hat{\mathbf{k}}_\perp = (-\sin\theta,\, \cos\theta)$, as in section 2.5. These projections are given by

$$\begin{aligned} \hat{\mathbf{k}} \cdot \frac{\partial\omega}{\partial\mathbf{k}} =& \frac{1}{c}\cos^2\theta \frac{\partial\omega^2}{\partial k_x^2} + \frac{1}{c}\sin^2\theta \frac{\partial\omega^2}{\partial k_y^2}, && (4.35\text{a}) \\ \hat{\mathbf{k}}_\perp \cdot \frac{\partial\omega}{\partial\mathbf{k}} =& \frac{1}{2c}\sin(2\theta)\left(\frac{\partial\omega^2}{\partial k_x^2} - \frac{\partial\omega^2}{\partial k_y^2}\right). && (4.35\text{b}) \end{aligned}$$

In the 2-layer case, by differentiating implicitly and using the expressions for R and S in equations (4.34) above, these become

$$\begin{aligned} \hat{\mathbf{k}} \cdot \frac{\partial\omega}{\partial\mathbf{k}} =& \frac{\mathcal{K}^+(R)\omega^2 - \mathcal{K}^+(S)}{(2\omega^2 - R)ck^2}, && (4.36\text{a}) \\ \hat{\mathbf{k}}_\perp \cdot \frac{\partial\omega}{\partial\mathbf{k}} =& \frac{\mathcal{K}^-(R)\omega^2 - \mathcal{K}^-(S)}{(2\omega^2 - R)ck^2}, && (4.36\text{b}) \end{aligned}$$

where the operators $\mathcal{K}^\pm$ are given by

$$\begin{aligned} \mathcal{K}^+ \equiv& k_x^2 \frac{\partial}{\partial k_x^2} + k_y^2 \frac{\partial}{\partial k_y^2}, && (4.37\text{a}) \\ \mathcal{K}^- \equiv& k_x k_y \left(\frac{\partial}{\partial k_x^2} - \frac{\partial}{\partial k_y^2}\right). && (4.37\text{b}) \end{aligned}$$

The rest of the algebraic manipulation is very similar to that in section 2.5, and so we shall not repeat it here. The $\hat{\mathbf{k}}$ projection is equal to the phase speed in that direction, as before.

The polar plots of the phase (blue) and group (red) velocities are shown in figures 4.9 and 4.10. There are now 5 controllable parameters:

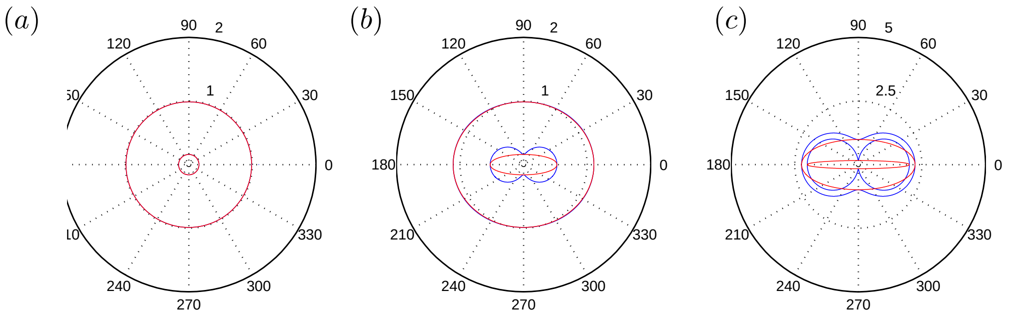

Figure 4.9 – Polar plots of phase velocity (blue) and group velocity (red). The magnetic fields in each layer are parallel, aligned with the x-axis, and for simplicity $c_{A_1} = c_{A_2}$. These plots illustrate the transition from the hydrodynamic case in plot (a) ($c_{A_j} = 0$), through $c_{A_j} = 0.5$ in plot (b), to $c_{A_j} = 2$ in plot (c). In the absence of magnetic field, the phase speeds and group velocities coincide as the system exhibits a directional isotropy; this is lost once magnetic field is introduced.

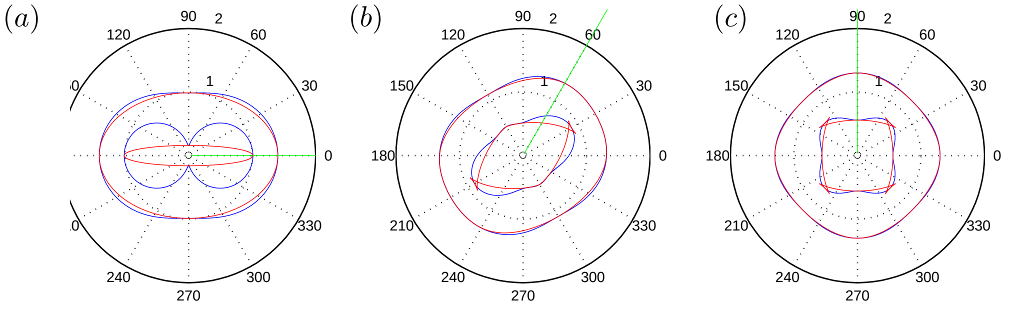

Figure 4.10 – Polar diagrams illustrating the effect of changing Θ, the angle between the magnetic fields in the two layers. The magnetic field in the upper layer is aligned with the x-axis, with the field in layer 2 aligned with the green line. In these plots, $\Theta = 0$ in (a), $\Theta = \pi/3$ in (b), and $\Theta = \pi/2$ in (c). We have chosen to display the case with $c_{A_j} = 1$, for $j = 1, 2$.

- $\alpha_{1,2}$, measuring the density jump over the interface,
- β_1, or how the fluid is subdivided into its layers ($\beta_2 = 1 - \beta_1$),
- c_{A_j}, for $j = 1, 2$: the strength of the magnetic fields,
- Θ, the angle between the fields.

In order to make meaningful plots, we have to decide which of these to vary, whilst keeping everything else constant. We shall continue to focus our attention on the effects of increasing magnetic field strength, and hence keep the stratification parameters $\alpha_{1,2}$ and β_j constant. For now, we will also suppose that $c_{A_1} = c_{A_2}$, so that the maximum Alfvén speeds are the same in each layer.

In these polar plots, a straight line drawn from the origin will meet two blue curves: the first will represent the slow mode, and the distance from the origin to this curve will be the speed of the slow mode in that direction; the second will represent the fast mode. The line will also intersect two red curves, which represent the group velocities. Because the phase and group velocities are plotted against a different angle, the distance from the origin to a red curve will be the speed of a wavepacket moving in that direction, which may well be composed of waves that propagate in other directions. This was discussed in more detail in section 2.5.

The polar plots in figure 4.9 show the effect of increasing field strength, keeping the magnetic fields aligned (and equal in magnitude). In the hydrodynamic case, shown in figure 4.9(a), we have a directional isotropy; waves propagate at the same speed in all directions. This is to be expected, since there is no magnetic tension in a certain direction to complement the restoring force of the modes. Gravity is the sole driver of motion, and this does not favour a particular direction.

For non-zero magnetic fields, waves travel faster along field lines than across them. This is because the Lorentz force is parallel to these lines, and so contributes to wave speed in this direction only. Modes travelling perpendicular to the field will not feel its presence at all. As the magnetic field strength is increased, this anisotropy gains in magnitude, and the phase speed curves become more circular in nature. As discussed in section 4.9, circular phase speed paths represent Alfvén waves; hence these magneto-acoustic modes become more and more Alfvén-like as magnetic field strength is increased. The group velocities, similarly, tend towards the two points of the Alfvén modes, the red curves becoming flatter for higher c_{A_j}. This process occurs for both fast and slow modes, but the slow mode always exhibits these properties more starkly than the fast mode.

Figure 4.10 shows polar plots for differing Θ, for fixed maximum Alfvén speeds $c_{A_j} = 1$. Figure 4.10(a) illustrates the case with parallel magnetic fields, $\Theta = 0$; this would lie somewhere between figures 4.9(b) and 4.9(c). One can see that as Θ is increased, cusps develop in the group velocity curve of the slow mode. The elongated curve distorts, but also rotates by $\Theta/2$ about the origin, at least for small Θ. This is due to the combination of the Lorentz forces from the two layers acting preferentially at an angle between the two fields. As θ is increased towards $\pi/2$, as in figure 4.10(c), the combined magnetic tension from both layers is the same in all directions. However, this does not mean that we regain the isotropy of the hydrodynamic case, because the surface motions have more of an effect on the upper layer, which carries just one of these fields, in one direction. Nevertheless, we do gain some symmetry when $\Theta = \pi/2$: the polar plots have rotational symmetry of order 4. This occurs because we have set $c_{A_1} = c_{A_2}$ and $\beta_1 = \beta_2$.

The full dependence of $\hat{\mathbf{k}}_\perp \cdot \frac{\partial \omega}{\partial \mathbf{k}}$ on the various parameters is given by the formula

$$\begin{aligned}\hat{\mathbf{k}}_\perp \cdot \frac{\partial \omega}{\partial \mathbf{k}} =& \frac{\sin(2\theta)}{2c(2c^2 - Rk^{-2})} \Bigg(c^2 \Big(c_{A_1}^2 + c_{A_2}^2 \cos(2\Theta) + \frac{1}{2} c_{A_2}^2 \sin(2\Theta) \big(\tan\theta - \cot\theta \big) \Big) \\ & - c_{A_2}^2 (2c_{A_1}^2 + \beta_1) \cos^2\theta \cos^2\Theta - c_{A_2}^2 (c_{A_1}^2 - \beta_1) \sin^2\theta \sin^2\Theta \\ & + 0.5 c_{A_2}^2 (c_{A_1}^2 + \beta_1) \cos^2\Theta \big(\cot\theta \sin(2\Theta) + 2\sin^2\Theta \big) \\ & - c_{A_2}^2 \sin(2\Theta) \big(\frac{3}{4} c_{A_1}^2 \sin(2\theta) + \frac{1}{2} \beta_1 \sin^2\theta \tan\theta \big) \\ & - \beta_1 c_{A_2}^2 \sin^2\theta \cos^2\Theta - \beta_2 c_{A_1}^2 \Bigg). \end{aligned} \tag{4.38}$$

This rather complicated-looking equation was then programmed into MATLAB, and used to make the polar plots 4.9 - 4.11. It allows one to input values for the parameters with no restrictions.

Figure 4.11 is an example of the complicated phase and group velocity curves one can obtain in the 2-layer system. The angle between the two magnetic fields is $\pi/4$ radians, and one (in the x-direction) is half the strength of the other, leading to the elongation along the green line. One can also see that the cusps are more pronounced than in figure 4.10, brought on partly by the change in relative layer depths. This example also highlights the propensity for group velocities to exceed the phase velocities; for the slow mode, for example, wavepackets propagating at $\pi/6$ radians from the x-axis travel at a (scaled) value of around 1.5 (the third circular dotted line from the origin), which is faster than individual waves in any direction.

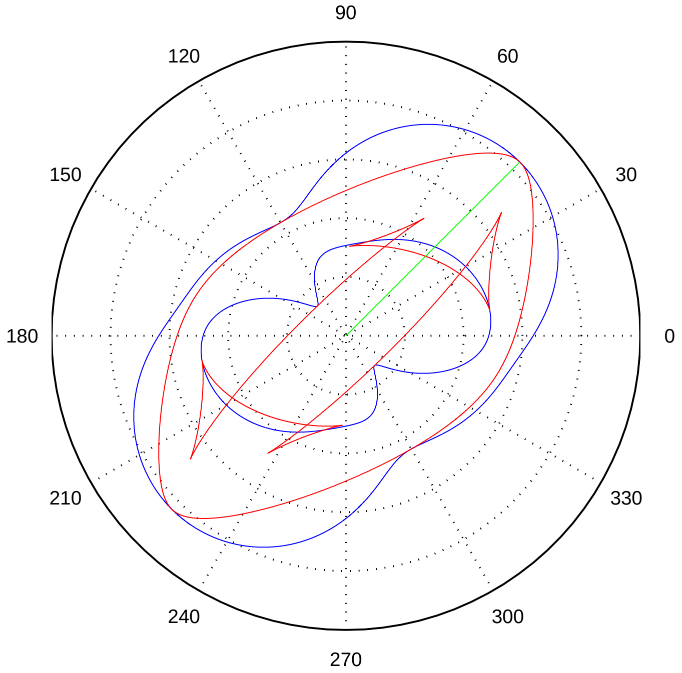

Figure 4.11 – An example of the phase and group velocities of the 2-layer free surface model for the values $\alpha_{1,2} = 0.1$, $\beta_1 = 0.7$, $c_{A_1} = 1$, $c_{A_2} = 2$, and $\Theta = \pi/4$. These values were chosen at random, to illustrate the complexity of the system.

4.4 The 2-layer rigid lid model

We anticipate that the addition of a rigid lid will suppress one of the modes, since it reduces the degrees of freedom in the system. Indeed, one can check that the coefficients of the η_1 and P in (3.48) do not both contain a c^2, and as there are two equations, the determinant of the matrix of coefficients must be linear in c^2. Geometrically, too, there is only one way the interface can exhibit sinusoidal motion when the surface is restrained.

Putting $\eta_0 = 0$ and allowing $P \neq 0$ in equation (3.48), we have

$$\begin{pmatrix} \frac{\beta_1}{\rho_1} & \zeta_1^2 \\ -\frac{\beta_2}{\rho_2} & \zeta_2^2 - \alpha_{1,2}\beta_2 \end{pmatrix} \begin{pmatrix} \bar{P} \\ \tilde{\eta}_1 \end{pmatrix} = 0, \tag{4.39}$$

from which, for non-trivial solutions, we obtain the dispersion relation

$$\beta_1\zeta_2^2 + (1-\alpha_{1,2})\beta_2\zeta_1^2 - \alpha_{1,2}\beta_1\beta_2 = 0. \tag{4.40}$$

This can be expanded to give

$$(1-\alpha_{1,2}\beta_2)c^2 = \beta_1 {v_A}_2^2 + (1-\alpha_{1,2})\beta_2 {v_A}_1^2 + \alpha_{1,2}\beta_1\beta_2. \tag{4.41}$$

As anticipated, since there is only one value of c^2, only one mode is supported in this system. The hydrodynamic phase speed is an $\mathcal{O}(\alpha_{1,2}^2)$ correction of $\alpha_{1,2}\beta_1\beta_2$, that of the slow mode in the free surface case. The fast mode has been suppressed by the addition of the lid because it requires movement of a surface; if the surface is held in place, the only motion possible is at the interface, at which the density jump is much lower than at the surface, and so the remaining wave mode is slow.

The structure of the remaining mode is trivial, since the surface and floor are flat. For any choice of parameters, the wave will propagate at the interface only. We also know in advance that there will be no net horizontal mass flux, because the surface does not move and the fluid is incompressible, and so the relationship $\beta_1 u_1 + \beta_2 u_2 = 0$ will hold in all cases. We will instead focus on other properties of this system, drawing parallels to the free surface case wherever possible.

4.4.1 Magnetic dominance

For small $\alpha_{1,2}$, we can approximate the dispersion relation (4.41) by

$$c^2 \approx \beta_1(1+\alpha_{1,2}\beta_2){v_A}_2^2 + \beta_2(1-\alpha_{1,2}\beta_1){v_A}_1^2 + \alpha_{1,2}\beta_1\beta_2. \tag{4.42}$$

The final term is the only non-magnetic term in this equation, which is $\mathcal{O}(\alpha_{1,2})$ in magnitude. Equation (4.42) is a hyperbola in (c, v_{Aj}) space, with a small y-intercept (indeed, the phase speed curves would be hyperbolae even if $\alpha_{1,2}$ were not small).

Intuitively, magnetically dominated modes would occur in the high field strength limit. Then the last term becomes negligible, and the weighted average of Alfvén speeds can be found: for example, for the general case, this speed is

$$c^2 \to \frac{\beta_1}{1-\alpha_{1,2}\beta_2}{v_A}_2^2 + \frac{(1-\alpha_{1,2})\beta_2}{1-\alpha_{1,2}\beta_2}{v_A}_1^2, \tag{4.43}$$

which, in the $\alpha_{1,2} \ll 1$ regime, reduces to $\beta_1(1+\alpha_{1,2}\beta_2){v_A}_2^2 + \beta_2(1-\alpha_{1,2}\beta_1){v_A}_1^2$. This differs from the free surface model, in which each mode would travel at an Alfvén speed.

To investigate further the similarities and differences with the free surface model, we should investigate the simplest case: the relationship $v_{A1} = v_{A2}$, which was the first example explored in the free surface model. Then

$$c^2 = v_{A1}^2 + \frac{\alpha_{1,2}\beta_1\beta_2}{1 - \alpha_{1,2}\beta_2}. \tag{4.44}$$

This can be compared with (4.21), the phase speed of the slow mode found in example 1 in section (4.3.2). The expressions match, as least up to order $\alpha_{1,2}$. As field strength is increased so that $v_{A1}^2 > \alpha_{1,2}$, this match becomes closer still.

As for magnetic dominance, there are two ways in which the final term in (4.44) can be minimised: when $\alpha_{1,2}$ is small, or when the product $\beta_1\beta_2$ is small. The former of these options is equivalent to making the density jump over the layers small, so that the model becomes more and more like a single layer of confined fluid of constant density. Then the restoring force is predominantly magnetic tension, and the mode propagates like an Alfvén wave. Alternatively, if either of the β_j are small, then this last term is also small, and magnetic tension dominates. Indeed, one can verify that as $\beta_j \to 0$, $c^2 \to v_{Aj}^2$.

This curiosity that the thinner a layer is, the more its magnetic field contributes to the wave motion, has been visited in the free surface case. The infinitesimal motions of the interface are affected much more directly by a thinner layer's magnetic field, because the vertical component of this field changes (linearly) over a much smaller spatial scale than in the other layer.

4.4.2 The link to the free surface case

We have shown in section 4.3.3 that, with a free surface, there exists a purely internal mode, one that propagates entirely within the fluid and does not perturb the surface. We speculated that it would coincide with a mode in the rigid lid model, under certain conditions. We can check this by eliminating the phase speed from equations (4.39), obtaining the relation

$$\left(\frac{1}{\rho_1}\beta_1 + \frac{1}{\rho_2}\beta_2\right)\bar{P} = (v_{A1}^2 - v_{A2}^2 - \alpha_{1,2}\beta_2)\tilde{\eta}_1. \tag{4.45}$$

One can see that when $v_{A1}^2 = v_{A2}^2 + \alpha_{1,2}\beta_2$, the pressure exerted by the lid is zero. This clause was exactly that derived in the free surface case for $\tilde{\eta}_0 = 0$. Thus, the two systems (free surface and rigid lid) coincide exactly when the relationship (4.28) is satisfied.

We can also consider the group velocity polar diagrams, and compare them to those found in the free surface case. The process is simpler with the rigid lid model, since there is only one mode.

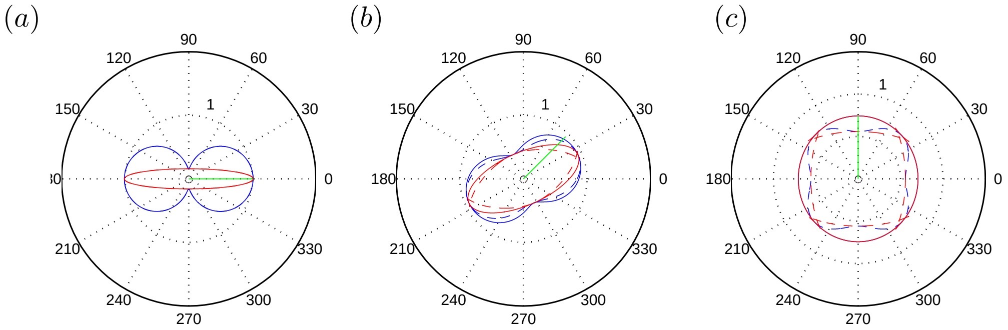

Figure 4.12 – Polar plots of the phase and group velocities of the 2-layer rigid lid model (solid lines), compared with those of the slow mode in the free surface case (dotted lines). It is hard to distinguish between the blue curves (phase velocity) and the red (group) for the case $\Theta = 0$ in plot (a), as the curves almost lie atop one another. However, the effect of adding a rigid lid is much clearer as the angle between the magnetic fields is increased; $\Theta = \pi/4$ in plot (b) and $\Theta = \pi/2$ in plot (c). In plot (c), the solid blue curve lies almost underneath the solid red curve, indicating that the addition of a rigid lid makes the phase and group speeds very similar in magnitude..

The $\hat{\mathbf{k}}_\perp$ projection in this case is

$$\hat{\mathbf{k}}_\perp \cdot \frac{\partial\omega}{\partial\mathbf{k}} = \frac{\sin(2\theta)}{2c(1-\alpha_{1,2}\beta_2)}\Bigg(\beta_1 c_{A_2}^2\Big(\cos(2\Theta) + \frac{1}{2}\sin(2\Theta)(\tan\theta - \cot\theta)\Big) + (1-\alpha_{1,2})\beta_2 c_{A_1}^2\Bigg). \quad (4.46)$$

This expression has been used to plot the phase and group velocities, alongside those of the slow mode of the free-surface model, for comparison (figure 4.12). When the magnetic fields in each layer are aligned so that $\Theta = 0$, these curves almost overlap each other, and it is very difficult to distinguish between the systems. In this case, adding a lid has little effect on the wave mode. However, as Θ is increased, so that the magnetic fields are not aligned, the rigid lid curves do not develop the cusps of the free surface case, and the two sets of curves diverge from each other. In the extreme case with perpendicular fields ($\Theta = \pi/2$) the curves are markedly different.

As in the free surface case, the system is controlled by five parameters ($\alpha_{1,2}$, β_1, the B_{0j} and Θ); varying these only has the effect of rotating the phase and group velocity curves and/or squashing them towards their line of symmetry – cusps are never developed. This implies that the addition of a rigid lid to the 2-layer system forbids the existence of different wavepackets that travel in the same direction, but are composed of waves with different wavevectors. In the rigid lid case, each

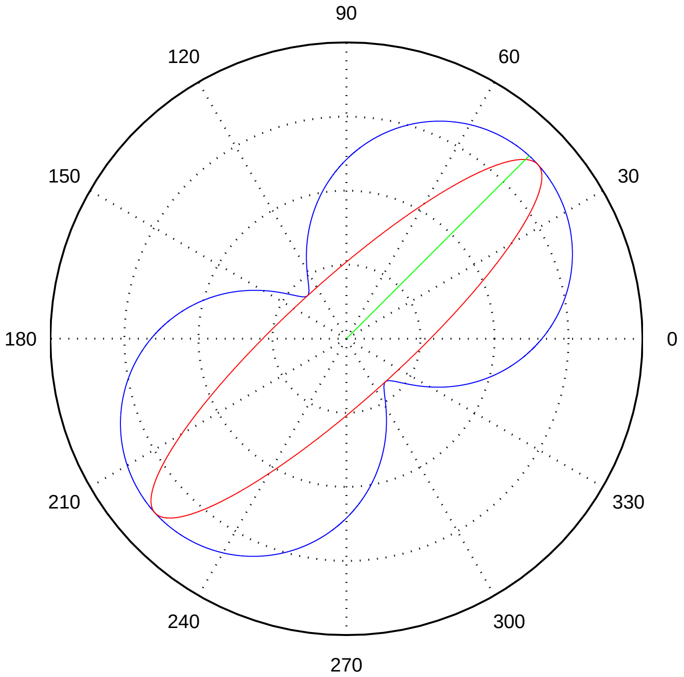

Figure 4.13 – Polar plots of the phase and group velocities of the 2-layer rigid lid model for $\alpha_{1,2} = 0.1$, $\beta_1 = 0.7$, $|\mathbf{B}_{01}| = 1$, $|\mathbf{B}_{02}| = 2$, and $\Theta = \pi/4$. These values are chosen to match those in the free surface case, for comparison with figure 4.11.

wavepacket is comprised of its own unique waves, or, put another way, energy in a given direction is transported by waves with only one wavevector.

Figure 4.13 shows the phase and group velocities for the same parameter values as figure 4.11 in the free surface section. The substantial cusps of the previous image are gone, and the curves look very different.

Finally, a note about figure 4.12(c) is warranted. At first glance it appears that the rigid lid curves are circles, but they are not. We could expect the rigid lid curves to be 'more circular' than those for the free surface case, because the stronger effective gravity at the surface is no longer present; the only gravitational component of the restoring force is through motion of the interface. When the magnetic fields are perpendicular and equal in strength, the motion of the interface introduces a small departure (for small $\alpha_{1,2}$) from isotropy.

4.5 Rotation in the 2-layer model

One can also consider the effects of rotation on the 2-layer free surface model. It is expected that the addition of rotation will introduce additional modes, with rotation as the driving force (i.e. inertial waves), as well as modifying the magneto-gravity modes already present. We shall investigate exactly what changes arise by deriving a dispersion relation for the rotating system. The approach is similar to that in the single layer case, and so some details will be omitted here. With the rotation axis parallel to the $\hat{\mathbf{z}}$-axis (perpendicular to the plane), and the factor f (twice the rotation rate Ω, scaled with the gravity wave speed $\sqrt{gH}$) measuring the rate of rotation, the change in the governing equations is the addition of a Coriolis term $f\hat{\mathbf{z}}\times\mathbf{u}_j$ on the left hand side of the momentum equations, which become

$$\frac{\partial \mathbf{u}_1'}{\partial t} + f\hat{\mathbf{z}}\times\mathbf{u}_1' = -\nabla\eta_0 + \frac{1}{\mu_0\rho_1}\mathbf{B}_{01}\cdot\nabla\mathbf{B}_1', \tag{4.47a}$$

$$\frac{\partial \mathbf{u}_2'}{\partial t} + f\hat{\mathbf{z}}\times\mathbf{u}_2' = -(1-\alpha_{1,2})\nabla\eta_0 - \alpha_{1,2}\nabla\tilde{\eta}_1 + \frac{1}{\mu_0\rho_2}\mathbf{B}_{02}\cdot\nabla\mathbf{B}_2', \tag{4.47b}$$

after linearising. The corresponding height and induction equations (4.4) remain unchanged. We then seek wave-like solutions of the form (2.35) and combine the three resulting equations for each layer to obtain

$$(\omega^2 - k^2 v_{A1}^2)\tilde{\mathbf{u}}_1 + if\omega\hat{\mathbf{z}}\times\tilde{\mathbf{u}}_1 = \beta_1(\mathbf{k}\cdot\tilde{\mathbf{u}}_1)\mathbf{k} + \beta_2(\mathbf{k}\cdot\tilde{\mathbf{u}}_2)\mathbf{k}, \tag{4.48a}$$

$$(\omega^2 - k^2 v_{A2}^2)\tilde{\mathbf{u}}_2 + if\omega\hat{\mathbf{z}}\times\tilde{\mathbf{u}}_2 = (1-\alpha_{1,2})\beta_1(\mathbf{k}\cdot\tilde{\mathbf{u}}_1)\mathbf{k} + \beta_2(\mathbf{k}\cdot\tilde{\mathbf{u}}_2)\mathbf{k}. \tag{4.48b}$$

Taking the dot product of equations (4.48) with $\mathbf{k}$ gives

$$\omega^2 D_1 - if\omega Q_1 = \beta_1 k^2 D_1 + \beta_2 k^2 D_2, \tag{4.49a}$$

$$\omega^2 D_2 - if\omega Q_2 = (1-\alpha_{1,2})\beta_1 k^2 D_1 + \beta_2 k^2 D_2, \tag{4.49b}$$

where $D_j = \mathbf{k}\cdot\mathbf{u}_j$ and $Q_j = \hat{\mathbf{z}}\cdot(\mathbf{k}\times\mathbf{u}_j)$. Taking the $\hat{\mathbf{z}}$-component of the cross product of (4.48a,b) with $\mathbf{k}$ gives

$$\omega^2 Q_1 + if\omega D_1 = 0, \tag{4.50a}$$

$$\omega^2 Q_2 + if\omega D_2 = 0. \tag{4.50b}$$

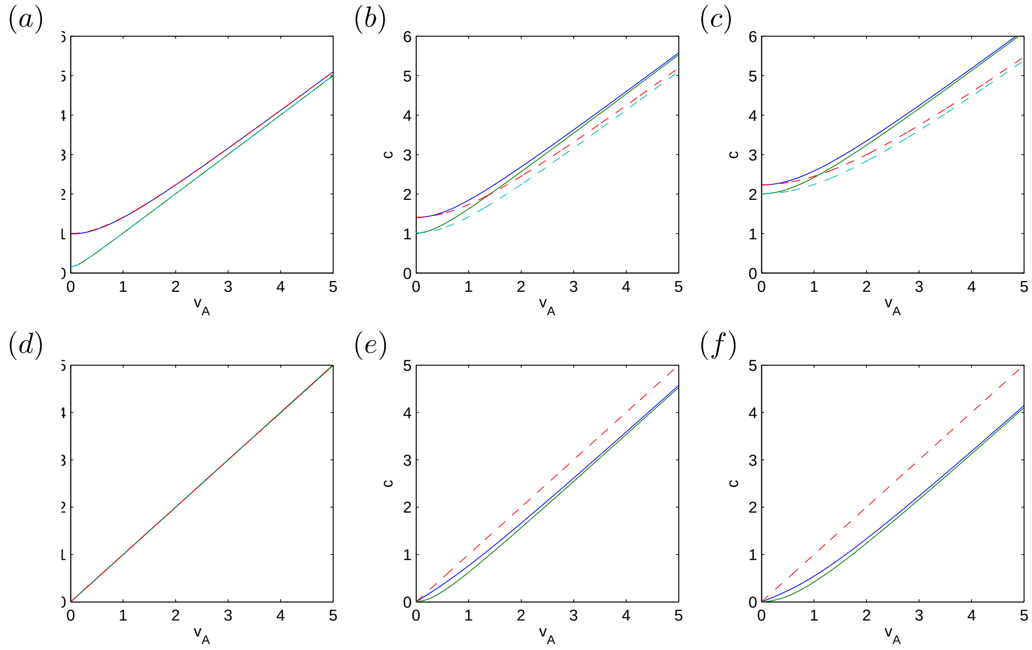

Figure 4.14 – Phase speed curves illustrating the four inertial magneto-gravity modes in the 2-layer free surface model. The magnetic field strength and direction is the same in both layers. The rotation measure $\bar{f}$ increases from (a, d) $\bar{f} = 0$, to (b, e) $\bar{f} = 1$, to (c, f) $\bar{f} = 2$. The top three plots show the deviation of the wave modes from their hydrodynamic $c^2 = gH + \bar{f}^2$ and $c^2 = \alpha\beta_1\beta_2 gH + \bar{f}^2$ expressions (dotted curves). The lower three plots illustrate the 'Alfvén' modes, and how these deviate from $c = v_A$ (dotted line) as rotation is increased.

Equations (4.49)-(4.50) can be written in matrix form as

$$\begin{pmatrix} \zeta_1^2 - \beta_1 & -\beta_2 & -i\bar{f}c & 0 \\ -(1-\alpha_{1,2})\beta_1 & \zeta_2^2 - \beta_2 & 0 & -i\bar{f}c \\ i\bar{f}c & 0 & \zeta_1^2 & 0 \\ 0 & i\bar{f}c & 0 & \zeta_2^2 \end{pmatrix} \begin{pmatrix} D_1 \\ D_2 \\ Q_1 \\ Q_2 \end{pmatrix} = 0, \qquad (4.51)$$

where $\bar{f} = f/k^2$ and $\zeta_j^2 = c^2 - v_{Aj}^2$, with the definition of v_{Aj} given in (3.47). Setting the determinant of the matrix above to be zero, we arrive at the dispersion relation

$$\zeta_1^4\zeta_2^4 - \left(\beta_1\zeta_1^2\zeta_2^4 + \beta_2\zeta_1^4\zeta_2^2 + \bar{f}^2c^2\zeta_1^4 + \bar{f}^2c^2\zeta_2^4\right) \\ + \bar{f}^4c^4 + \beta_1\bar{f}^2c^2\zeta_1^2 + \beta_2\bar{f}^2c^2\zeta_2^2 + \alpha_{1,2}\beta_1\beta_2\zeta_1^2\zeta_2^2 = 0. \qquad (4.52)$$

This is, in general, quartic in c^2 and so has four pairs of roots, twice the number without rotation if a magnetic field is present. Note that in the absence of rotation, the terms containing $\bar{f}$ in equation

(4.52) are zero and one is able to factorise $\zeta_1^2\zeta_2^2$ out of the left hand side. This yields two Alfvén roots and two magnetogravity roots satisfying the two–layer dispersion relation derived previously.

In the presence of rotation but the absence of magnetic field, the ζ_j^2 become c^2, leading to a factor of c^4 in the left hand side. This then yields two zero frequency modes, representing geostrophic balance in the two layer system, and two inertia–gravity wave modes, which satisfy the quadratic equation (in c^2)

$$c^4 - (1 + 2\bar{f}^2)c^2 + \bar{f}^4 + \bar{f}^2 + \alpha_{1,2}\beta_1\beta_2 = 0. \tag{4.53}$$

For $\alpha_{1,2} \ll 1$, the non-zero roots are thus given by

$$\begin{aligned} c_+^2 &\approx 1 + \bar{f}^2, \\ c_-^2 &\approx \alpha_{1,2}\beta_1\beta_2 + \bar{f}^2. \end{aligned}$$

This is the dispersion relation of hydrodynamic inertia-gravity waves, as expected. Figure 4.14 illustrates the effect of rotation on the phase speed of the magneto-gravity modes of the free surface model.

4.6 The 3-layer model

As previously discussed, considering models with more layers not only enables greater control over stratification settings, but also over magnetic field configurations. The greater varieties of vertical structure of magnetic field supported by the 3-layer model allow wave dynamics that are not present in simpler systems.

We shall again consider the nondimensional density jumps, $\alpha_{1,2}$ and $\alpha_{2,3}$ to be small for the following analyses. For the tachocline, we can estimate these values in a similar manner to the derivation in the 2-layer model, using the density profile in figure 4.1. Taking the bottom of the tachocline to be at $0.7R_\odot$ and the top to be at $0.72R_\odot$, as in the 2-layer case, the densities of the equally thick layers can be accurately estimated by finding densities at distances $0.70\dot{3}R_\odot$, $0.71R_\odot$, and $0.71\dot{6}R_\odot$ from the centre of the Sun. This gives densities $\rho_1 = 183.2\text{kg}\,\text{m}^{-3}$, $\rho_2 = 192.5\text{kg}\,\text{m}^{-3}$, and $\rho_3 = 202.9\text{kg}\,\text{m}^{-3}$, leading to $\alpha_{1,2} = 0.0483$ and $\alpha_{2,3} = 0.0513$. These are sufficiently less than 1 for small α approximations to be valid.

The starting point of our analysis is the governing equations (3.52) with $n = 3$ and $\eta_3 = 0$. The momentum equations for layers 1, 2 and 3 are

$$\frac{\partial \mathbf{u}_1'}{\partial t} = -\nabla(\eta_0 + P) + \frac{1}{\mu_0\rho_1}\mathbf{B}_{01}\cdot\nabla\mathbf{B}_1', \tag{4.54a}$$

$$\frac{\partial \mathbf{u}_2'}{\partial t} = -(1-\alpha_{1,2})\nabla(\eta_0 + P) - \alpha_{1,2}\nabla\eta_1 + \frac{1}{\mu_0\rho_2}\mathbf{B}_{02}\cdot\nabla\mathbf{B}_2', \tag{4.54b}$$

$$\frac{\partial \mathbf{u}_2'}{\partial t} = -(1-\alpha_{1,3})\nabla(\eta_0 + P) - (1-\alpha_{2,3})\alpha_{1,2}\nabla\eta_1 - \alpha_{2,3}\nabla\eta_2 + \frac{1}{\mu_0\rho_3}\mathbf{B}_{03}\cdot\nabla\mathbf{B}_3', \tag{4.54c}$$

after linearising about the motionless basic state with $\mathbf{B}_j = \mathbf{B}_{0j} + \mathbf{B}_j'$. The height and induction equations are

$$\frac{\partial h_j}{\partial t} + \beta_j\nabla\cdot\mathbf{u}_j' = 0, \tag{4.55}$$

with $h_j = \beta_j + \eta_{j-1} - \eta_j$ and $\eta_3 = 0$, and

$$\frac{\partial \mathbf{B}_j'}{\partial t} = \mathbf{B}_{0j}\cdot\nabla\mathbf{u}_j'. \tag{4.56}$$

These are complemented by the solenoidal condition on magnetic field

$$\beta_j\nabla\cdot\mathbf{B}_j' + \mathbf{B}_{0j}\cdot\nabla(\eta_{j-1} - \eta_j) = 0. \tag{4.57}$$

Now, the standard procedure used to derive a dispersion relation is to combine the linear equations and seek wave-like solutions. This was done in the derivation of (3.48) which, for $n = 3$, yields

$$(\zeta_1^2 - \beta_1)\tilde{\eta}_0 - \zeta_1^2\tilde{\eta}_1 - \frac{\beta_1}{\rho_1}\bar{P} = 0, \tag{4.58}$$

$$-(1-\alpha_{1,2})\beta_2\tilde{\eta}_0 + (\zeta_2^2 - \alpha_{1,2}\beta_2)\tilde{\eta}_1 - \zeta_2^2\tilde{\eta}_2 - \frac{\beta_2}{\rho_2}\bar{P} = 0, \tag{4.59}$$

$$-(1-\alpha_{1,3})\beta_3\tilde{\eta}_0 - (1-\alpha_{2,3})\alpha_{1,2}\beta_3\tilde{\eta}_1 + (\zeta_3^2 - \alpha_{2,3}\beta_3)\tilde{\eta}_2 - \frac{\beta_3}{\rho_3}\bar{P} = 0. \tag{4.60}$$

These equations can now be used to derive the dispersion relation for the free-surface and rigid lid cases. As in the 2-layer system, we will begin by analysing the free-surface case. However, this time we need to be more selective with the cases we investigate, owing to the increased number of controllable parameters, which are

- stratification parameters: $\alpha_{1,2}$, $\alpha_{2,3}$, β_1 and β_2
- magnetic parameters: v_{Aj} for $j = 1, 2, 3$. These are in turn comprised of magnetic field strength and orientation.

The approach for the 3-layer model will thus be slightly different to that of the 2-layer system: we will identify interesting properties of the supported wave modes, and then discuss the parameter regime that they inhabit, making links to earlier results where possible.

4.7 The 3-layer free-surface model

For the case $\bar{P} = 0$, equations (4.58) admit non-trivial solutions that satisfy the dispersion relation

$$\zeta_1^2\zeta_2^2\zeta_3^2 - \sum_{i\neq j\neq k}\beta_i\zeta_j^2\zeta_k^2 + \sum_{i\neq j\neq k}\alpha_{i,j}\beta_i\beta_j\zeta_k^2 - \alpha_{1,2}\alpha_{2,3}\beta_1\beta_2\beta_3 = 0. \tag{4.61}$$

This can be expanded to give

$$\begin{aligned} c^6 - (1 + \sum_i v_{A_i}^2)c^4 + (\sum_{i\neq j}(v_{A_i}^2 v_{A_j}^2 + \alpha_{i,j}\beta_i\beta_j) + \sum_i (1-\beta_i)v_{A_i}^2)c^2 \\ - (v_{A_1}^2 v_{A_2}^2 v_{A_3}^2 + \sum_{i\neq j\neq k}(\alpha_{i,j}\beta_i\beta_j v_{A_k}^2 + \beta_i v_{A_j}^2 v_{A_k}^2) + \alpha_{1,2}\alpha_{2,3}\beta_1\beta_2\beta_3) = 0. \end{aligned} \tag{4.62}$$

As predicted in section 3.4, this is a cubic in c^2, so the system supports three modes. The hydrodynamic limit can be inferred most easily using (4.61), by replacing ζ_j with c. One can also check that in the high field strength limit, phase speeds tend to the Alfvén speeds: for example, if the magnetic field in layers 1 and 3 only were large, then two of the modes would travel with approximate speeds v_{A1} and v_{A2}.

We can also show that the 3-layer dispersion relation reduces to the 2-layer relation under the appropriate conditions. Putting $v_{A1} = 0$ and $\beta_1 = 0$, so that $\beta_2 = 1 - \beta_3$, describes a 3-layer system in which the top layer is hydrodynamic with zero thickness. Then the dispersion relation (4.62) reduces to

$$c^2 \left(c^4 - (1 + v_{A2}^2 + v_{A3}^2)c^2 + v_{A2}^2 v_{A3}^2 + \alpha_{2,3}\beta_2\beta_3 + \beta_2 v_{A3}^2 + \beta_3 v_{A2}^2 + \alpha_{2,3}\beta_2\beta_3\right) = 0, \quad (4.63)$$

which gives the 2-layer relation (4.10).

Using equations (4.58), we can also derive expressions for the relative surface displacements. These are given by

$$\mu_1 = \frac{\zeta_1^2}{\zeta_1^2 - \beta_1} \quad (4.64)$$

and

$$\mu_2 = \frac{\zeta_2^2}{\zeta_2^2 - \alpha_{1,2}\beta_2 - (1 - \alpha_{1,2})\beta_2\mu_1}, \quad (4.65)$$

where μ_j is the ratio of the interfaces bounding layer j, so that $\mu_1 = \tilde{\eta}_0/\tilde{\eta}_1$ and $\mu_2 = \tilde{\eta}_1/\tilde{\eta}_2$. Note that use can be made of equation (4.64) to give

$$\mu_2 = \frac{\zeta_2^2(\zeta_1^2 - \beta_1)}{\zeta_1^2\zeta_2^2 - \beta_2\zeta_1^2 - \beta_1\zeta_2^2 + \alpha_{1,2}\beta_1\beta_2}. \quad (4.66)$$

It is no coincidence that the denominator is the 2-layer dispersion relation. Indeed, if the lower interface were not moving, then μ_2 would be undefined, and the 2-layer dispersion relation would be satisfied. The upper layers would exhibit the same dynamics as in the 2-layer model, with the lower interface acting as a rigid floor to the fluid above.

Equations (4.64)-(4.65) can be used to determine the physical appearance of the three modes for prescribed magnetic field and stratification; these will be displayed in future schematics. Also of interest are the horizontal fluid motions in each layer, the behaviour of which can be captured in the ratios of the fluid velocity in one layer to that in another, and so we shall now derive these ratios. After seeking solutions to the momentum equations (4.54) and eliminating the magnetic field using the linearised induction equation (4.56), we have

$$\zeta_1^2\tilde{\mathbf{u}}_1 = c\hat{\mathbf{k}}\tilde{\eta}_0, \tag{4.67a}$$

$$\zeta_2^2\tilde{\mathbf{u}}_2 = (1-\alpha_{1,2})c\hat{\mathbf{k}}\tilde{\eta}_0 + \alpha_{1,2}c\hat{\mathbf{k}}\tilde{\eta}_1, \tag{4.67b}$$

$$\zeta_3^2\tilde{\mathbf{u}}_3 = (1-\alpha_{1,3})c\hat{\mathbf{k}}\tilde{\eta}_0 + (1-\alpha_{2,3})\alpha_{1,2}c\hat{\mathbf{k}}\tilde{\eta}_1 + \alpha_{2,3}c\hat{\mathbf{k}}\tilde{\eta}_2, \tag{4.67c}$$

where $\hat{\mathbf{k}} = \mathbf{k}/|\mathbf{k}|$ is the unit wavevector. From (4.67), we can find the ratios of the x- components of the velocities, namely

$$\frac{u_1}{u_2} = \frac{\zeta_2^2}{\zeta_1^2}\left(\frac{\mu_1}{(1-\alpha_{1,2})\mu_1 + \alpha_{1,2}}\right) \tag{4.68a}$$

and

$$\frac{u_2}{u_3} = \frac{\zeta_3^2}{\zeta_2^2}\left(\frac{(1-\alpha_{1,2})\mu_1\mu_2 + \alpha_{1,2}\mu_2}{(1-\alpha_{1,3})\mu_1\mu_2 + (1-\alpha_{2,3})\alpha_{1,2}\mu_2 + \alpha_{2,3}}\right), \tag{4.68b}$$

where $\tilde{\mathbf{u}}_j = (u_j, v_j)$. Seeking wave-like solutions of the height equations (4.55), one can verify that the ratios for horizontal divergence of fluid between the layers are

$$\frac{\mathbf{k}\cdot\tilde{\mathbf{u}}_1}{\mathbf{k}\cdot\tilde{\mathbf{u}}_2} = \frac{\beta_2}{\beta_1}\left(\frac{\mu_1-1}{\mu_2-1}\right)\mu_2 \tag{4.69}$$

and

$$\frac{\mathbf{k}\cdot\tilde{\mathbf{u}}_2}{\mathbf{k}\cdot\tilde{\mathbf{u}}_3} = \frac{\beta_3}{\beta_2}(\mu_2-1). \tag{4.70}$$

Finally, before considering specific cases, we can determine the role that each term in the momentum equations plays in the behaviour of the waves. As in section 4.3, by considering the ratios of the terms in the governing equations, their relative importance can be studied. The derivation of equations (4.54), after seeking wave-like solutions and manipulating the ratios of the terms, leads to the expressions given in table 4.3 for layer 1, table 4.4 for layer 2, and table 4.5 for layer 3. In the tables, the terms across the top are the numerators and the terms down the left hand column are the denominators in the ratios under scrutiny. These tables will then be referred to in the specific examples.

4.7.1 Example 1: Equal Alfvén speeds and the hydrodynamic reduction

The simplest case to consider is when $v_{A1} = v_{A2} = v_{A3}$. The hydrodynamic regime is a special case of this, with the $v_{Aj} = 0$. The dispersion relation (4.61) reduces to a cubic in ζ_1^2, given by

$$\zeta_1^6 - \zeta_1^4 + (\alpha_{1,2}\beta_1\beta_2 + \alpha_{1,3}\beta_1\beta_3 + \alpha_{2,3}\beta_2\beta_3)\zeta_1^2 - \alpha_{1,2}\alpha_{2,3}\beta_1\beta_2\beta_3 = 0. \tag{4.71}$$

	$\frac{\partial \mathbf{u}_1'}{\partial t}$	$\nabla \eta_0$	$\mathbf{B}_{01} \cdot \nabla \mathbf{B}_1'$
$\frac{\partial \mathbf{u}_1'}{\partial t}$	-	$1 - \frac{v_{A1}^2}{c^2}$	$\frac{v_{A1}^2}{c^2}$
$\nabla \eta_0$		-	$\frac{v_{A1}^2}{\zeta_1^2}$
$\mathbf{B}_{01} \cdot \nabla \mathbf{B}_1'$			-

Table 4.3 – Expressions for the relative importance of each term in the momentum equations, for layer 1, expressed as ratios with the term across the top of the table as the numerator.

	$\frac{\partial \mathbf{u}_2'}{\partial t}$	$(1-\alpha_{1,2})\nabla \eta_0$	$\alpha_{1,2}\nabla \eta_1$	$\mathbf{B}_{02} \cdot \nabla \mathbf{B}_2'$
$\frac{\partial \mathbf{u}_2'}{\partial t}$	-	$\frac{(1-\alpha_{1,2})\mu_1\zeta_2^2}{c^2\nu_2}$	$\frac{\alpha_{1,2}\zeta_2^2}{c^2\nu_2}$	$\frac{v_{A2}^2}{c^2}$
$(1-\alpha_{1,2})\nabla \eta_0$		-	$\frac{\alpha_{1,2}}{(1-\alpha_{1,2})\mu_1}$	$\frac{v_{A2}^2\nu_2}{(1-\alpha_{1,2})\mu_1\zeta_2^2}$
$\alpha_{1,2}\nabla \eta_1$			-	$\frac{\nu_2 v_{A2}^2}{\alpha_{1,2}\zeta_2^2}$
$\mathbf{B}_{02} \cdot \nabla \mathbf{B}_2'$				-

Table 4.4 – Expressions for the ratios of the terms in the momentum equations for layer 2, where $\nu_2 = (1-\alpha_{1,2})\mu_1 + \alpha_{1,2}$.

This can then be solved to give three values of ζ_1^2 (one for each mode) in terms of the stratification parameters. For example, when the system is linearly stratified, so that

$$\alpha_{1,2} = \alpha_{2,3} = \alpha \qquad \text{and} \qquad \beta_1 = \beta_2 = \beta_3 = \frac{1}{3}, \tag{4.72}$$

the solutions are, to order α,

$$\zeta_1^2 \approx 1 - \frac{4}{9}\alpha, \qquad \zeta_1^2 \approx \frac{\alpha}{3}, \qquad \zeta_1^2 \approx \frac{\alpha}{9}. \tag{4.73}$$

These are the phase speeds of the waves in a 3-layer system in which the layers are of equal (undisturbed) depth, and in which the density jumps over the interfaces are identical (in addition to each layer having a magnetic field configuration such that the Alfvén speed does not change between layers). However, other stratification parameters would still give constant values for the ζ_j; linear stratification was chosen for mathematical simplicity.

Equations (4.73) describe hyperbolae in the (v_{A1}, c) plane, and so phase speeds approach the common Alfvén speed in the high field strength regime. As before, one of these modes is greater than the others for all stratification parameter values. This represents the 'fast' mode and the

	$\frac{\partial \mathbf{u}_3'}{\partial t}$	$(1-\alpha_{1,3})\nabla\eta_0$	$(1-\alpha_{2,3})\alpha_{1,2}\nabla\eta_1$	$\alpha_{2,3}\nabla\eta_2$	$\mathbf{B}_{03}\cdot\nabla\mathbf{B}_3'$
$\frac{\partial \mathbf{u}_3'}{\partial t}$	-	$\frac{(1-\alpha_{1,3})\mu_1\mu_2\zeta_3^2}{\nu_3 c^2}$	$\frac{(1-\alpha_{2,3})\alpha_{1,2}\mu_2\zeta_3^2}{\nu_3 c^2}$	$\frac{\alpha_{2,3}\zeta_3^2}{\nu_3 c^2}$	$\frac{v_{A_3}^2}{c^2}$
$(1-\alpha_{1,3})\nabla\eta_0$		-	$\frac{\alpha_{1,2}}{(1-\alpha_{1,2})\mu_1}$	$\frac{\alpha_{2,3}}{(1-\alpha_{1,3})\mu_1\mu_2}$	$\frac{\nu_3 v_{A_3}^2}{(1-\alpha_{1,3})\mu_1\mu_2\zeta_3^2}$
$(1-\alpha_{2,3})\alpha_{1,2}\nabla\eta_1$			-	$\frac{\alpha_{2,3}}{(1-\alpha_{2,3})\alpha_{1,2}\mu_2}$	$\frac{\nu_3 v_{A_3}^2}{(1-\alpha_{2,3})\alpha_{1,2}\mu_2\zeta_3^2}$
$\alpha_{2,3}\nabla\eta_2$				-	$\frac{\nu_3 v_{A_3}^2}{\alpha_{2,3}\zeta_3^2}$
$\mathbf{B}_{03}\cdot\nabla\mathbf{B}_3'$					-

Table 4.5 – Expressions for the ratios of the terms in the momentum equation for layer 3. Here, $\nu_3 = (1-\alpha_{1,3})\mu_1\mu_2 + (1-\alpha_{2,3})\alpha_{1,2}\mu_2 + \alpha_{2,3}$.

others ‘slow’ modes, sticking to our definition from chapter 3. Although it is true that for strong magnetic fields this fast mode does not travel much faster than the slow modes, its speed is greater nonetheless, and our definition holds.

Mode structure

Since in many physical systems, including the tachocline, the reduced (effective) gravity is much smaller than gravity itself, we shall take $\alpha \ll 1$ in this analysis. The fast mode is a magneto-gravity hybrid, with an expression for phase speed containing a hydrodynamic part equal to the gravity wave speed, and so we would expect its structure to be primarily barotropic, with the surface displacements greater than those at the interfaces, at least in the hydrodynamic regime. The slow modes we expect to have largely interfacial motion, with smaller disturbances at the surface, since their non-magnetic terms in the expressions for phase speed are of order α. In the absence of field, these should be baroclinic (internal) modes, which differ in how the interfaces are perturbed.

We can check this hypothesis by considering the ratios of surface and interface displacements, (4.64)-(4.65). Since the (equal) ζ_j are constants, given by (4.73), so too are the ratios of surface and interfaces. In the case of linear stratification, as outlined above in equation (4.72), these ratios can be written as fractions in which the numerator and denominator has been calculated to $\mathcal{O}(\alpha)$:

$$\mu_1 = \frac{9-4\alpha}{6-4\alpha}, \qquad \mu_2 = \frac{2(9-10\alpha)}{9-13\alpha}, \tag{4.74}$$

for the fast mode and

$$\mu_1 = -\frac{\alpha}{1-\alpha}, \qquad \mu_2 = 1, \tag{4.75}$$

$$\mu_1 = -\frac{\alpha}{3-\alpha}, \qquad \mu_2 = -\frac{3-\alpha}{3+\alpha}, \tag{4.76}$$

for the slow modes (so that (4.74) are describe the fast mode, (4.75) the first slow mode and (4.76) the second slow mode). These expressions can be further simplified using the binomial expansion with $\alpha \ll 1$ to give

$$\mu_1 = \frac{2}{3} + \frac{1}{3}\alpha, \qquad \mu_2 = 2 + \frac{2}{3}\alpha, \tag{4.77}$$

and

$$\mu_1 = -\alpha, \qquad \mu_2 = 1, \tag{4.78}$$

$$\mu_1 = -\frac{1}{3}\alpha, \qquad \mu_2 = -1 + \frac{2}{3}\alpha. \tag{4.79}$$

The surface mode has interface displacements that increase with each higher interface, exhibiting the barotropic-like nature of the hydrodynamic case. The first slow mode is analogous to the 2-layer hydrodynamic (or equal Alfvén speeds) slow mode in that the surface displacement is $\mathcal{O}(\alpha)$ of the interface motion, and the ratio μ_2 is 1, indicating that the two interfaces move in phase with the same amplitude. This is akin to the middle layer behaving as if it were an extended single interface, containing horizontally stagnant fluid which transfers the motion of one of its bounding interfaces to the other.

The second slow mode, however, has no such counterpart in the 2-layer model. It is unique to the 3-layer system, in as much as it is not supported by any simpler models. This can be seen by considering the ratio μ_2, which is approximately -1 for this mode. This indicates that the interfaces move in antiphase, so that as one interface rises the other falls, for fixed horizontal coordinates; such motion clearly requires at least two fluid-fluid interfaces. The ratio μ_1 shows that this is also an internal mode, with a surface amplitude equal to $\alpha/3$ times that of the first interface.

Fluid velocities

As the ζ_j are equal and the flow structure does not change with varying field strength, the fluid velocity too is constant, for each layer. For the fast mode, for which $\zeta_1^2 \approx 1 - 4\alpha/9$, one can verify that the ratios u_1/u_2, $\mathbf{k} \cdot \tilde{\mathbf{u}}_1/\mathbf{k} \cdot \tilde{\mathbf{u}}_2$, u_2/u_3, and $\mathbf{k} \cdot \tilde{\mathbf{u}}_2/\mathbf{k} \cdot \tilde{\mathbf{u}}_3$ are all approximately equal to 1. This indicates that horizontal fluid motion is roughly the same in each layer (note that this can be generalised to other magnetic field geometries by saying that the horizontal flux is the same in each layer). The vertical velocity, however, is not the same in each layer, since the interface disturbances are different. This is outlined in figure 4.15.

For the first slow mode, for which $\zeta_1^2 \approx \alpha/3$, equation (4.68) gives $u_2/u_3 = 0$, with u_1/u_2 undefined. This is consistent with the idea that fluid in the middle layer has only vertical velocity; similar expressions for the ratios of horizontal fluid divergences confirm this. Going one step further, we can multiply equations (4.68a) and (4.68b) together to verify that $u_1/u_3 \approx -1$, so that the fluid in the top layer moves in (almost) the opposite manner to that in the bottom: the order α correction to this ratio explains the slight movement of the surface.

For the second slow mode, for which $\zeta_1^2 \approx \alpha/9$, we have $u_1/u_2 \approx -1/2$ (and similarly for the ratio of divergences), so that fluid in the middle layer moves twice as fast, and in the opposite direction to, the fluid in the top layer. In the same vein, we find the same relationship with the

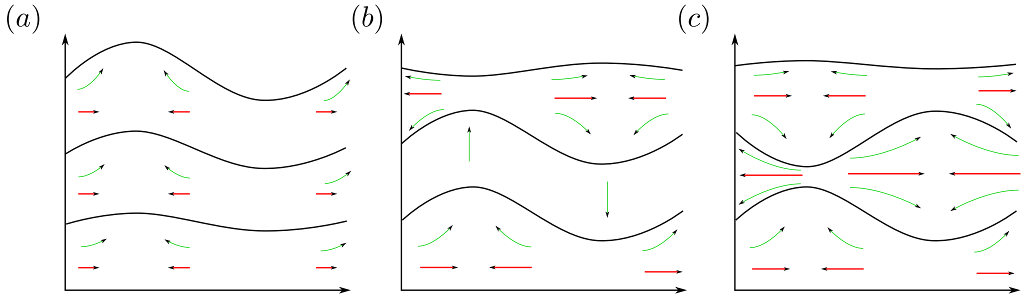

Figure 4.15 – Schematics of interface motion for the linearly stratified case, when $v_{A1} = v_{A2} = v_{A3}$. Schematic (a) is the fast mode, with higher interface displacements having greater amplitudes. Schematic (b) is the first slow mode, which is analogous to the slow mode in the 2-layer system. Finally, (c) is the (as yet unique) second slow mode, which in this case is 'even more internal' than the former, in that the surface perturbations are a smaller fraction of that of the interfaces.

fluid in the lower layer. This new mode propagates with the fluid-fluid interfaces in antiphase, as shown in figure 4.15c.

4.7.2 Example 2: Equal magnetic field strengths

There are many regimes to explore in the 3-layer model, and so we have to be selective in the regimes we study. Another interesting case is when the magnetic fields are aligned, and equal in magnitude. We have already found that when the Alfvén speeds are equal in each layer, the magnetic field has no influence on the wave structure: only on the phase speed. However, as much as we have learned from this, this result is for a very specific magnetic structure, which is unlikely to exist in nature.

In general, both phase speed *and* wave structure will be affected by magnetic field strength. This dependence can be complicated; we shall examine the specific case of a constant, uniform ambient magnetic field permeating all three layers, and frequently discuss the implications in the linearly stratified case. We will first highlight some mathematical curiosities in the equations for structure, and then use them to discuss the properties of each wave mode in turn.

As discussed in the derivation of equation (4.23), the appropriate relation between Alfvén speeds when the magnetic fields are constant and uniform is

$$v_{Aj}^2 = (1 - \alpha_{i,j}) v_{Ai}^2. \tag{4.80}$$

This could then simulate a uniform, unidirectional magnetic field permeating all layers (although it actually applies to more than this, since the field orientation is built into the definition of v_{Aj} in equation (3.47)). Hence, for linear stratification ($\alpha_{1,2} = \alpha_{2,3} = \alpha$ and $\beta_1 = \beta_2 = \beta_3 = 1/3$), we have

$$\zeta_j^2 = c^2 - (1-\alpha)^{j-1} {v_{A1}}^2, \tag{4.81}$$

since $\alpha_{1,3} = 1 - (1-\alpha_{1,2})(1-\alpha_{2,3})$. In a similar manner to the previous example, we can calculate the ratios of the interfaces and velocities in order to study the structure of the modes. These are plotted in figure 4.16.

One can see that for the slow modes, μ_1 and μ_2 cross the x-axis. For example, $\mu_1 = 0$ when $\zeta_1^2 = 0$, using equation (4.64). At this point, the dispersion relation (4.61) gives

$$\zeta_2^2\zeta_3^2 - \alpha_{1,2}\beta_2\zeta_3^2 - \alpha_{1,3}\beta_3\zeta_2^2 + \alpha_{1,2}\alpha_{2,3}\beta_2\beta_3 = 0. \tag{4.82}$$

This is satisfied by a mode that propagates without perturbing the surface, and so should coincide exactly with the 3-layer rigid lid model when the Alfvén speeds satisfy

$${v_{A1}}^2 = \frac{1}{3}\left(1 \pm \sqrt{\frac{1-\alpha}{2-\alpha}}\right), \tag{4.83}$$

together with equation (4.80) when the system is linearly stratified. Equation (4.83) was derived from the dispersion relation, and gives the values of the zeros of the curves in figure 4.16(b). Note that in the graphs, α takes the slightly exaggerated value of 0.1, for illustrative purposes. There is also the possibility that $\mu_2 = 0$ when $\zeta_2^2 = 0$. The dispersion relation then yields

$$(\zeta_1^2 - \alpha_{1,2}\beta_1)(\zeta_3^2 - \alpha_{2,3}\beta_3) = 0, \tag{4.84}$$

from which we find $\zeta_3^2 = \alpha\beta$, since $\zeta_1^2 = \alpha\beta$ is incompatible with $\zeta_2^2 = 0$. We thus find that that when $\mu_2 = 0$, v_{A1} must satisfy

$${v_{A1}}^2 = \frac{\beta_3}{1-\alpha_{1,2}}. \tag{4.85}$$

At this particular value of v_{A1}, the middle interface is stationary, and we have a kind of partition into two systems: the top layer would act as in the single layer case, and the lower two as in the 2-layer rigid lid model.

We will now discuss these structural properties in more detail, applying them to the three modes supported by the system.

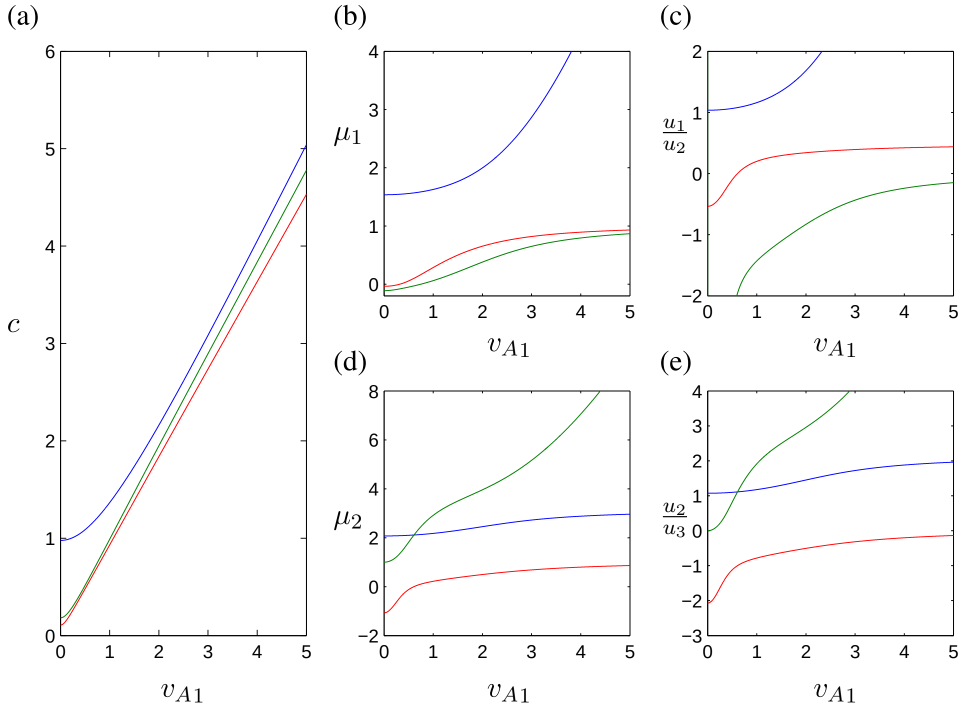

Figure 4.16 – Graphs of wave properties in the 3-layer free surface model when the magnetic fields are equal in strength and orientation (or, more generally, when equation (4.80) is satisfied). Blue curves represent the fast mode, green the first slow mode, and red the second (new) slow mode. Plots show the linearly stratified case with $\alpha = 0.1$.

The fast mode

As can be seen in figure 4.16(a) (blue curve), the phase speed of the fast mode increases with increasing magnetic field strength. The curve that traces the departure from the hydrodynamic value of $c^2 = 1 - 4\alpha_{1,2}/9$ to the high strength limit of $c^2 = v_{A1}^2$ (since each mode tends to an Alfvén speed, and v_{A1} is the highest) is hyperbolic in the plane. During this transition, magnetic tension plays more of a role in the restoring force, eventually taking over as the main driver of fluid motion in the upper layer, as can be checked using table 4.3.

From the blue curves in figures 4.16(b)-(e) we may infer that the interface and velocity ratios do not have any singularities or zeros for finite values of v_{A1}. This indicates that the surface and interfaces remain in motion for this mode, excluding the high strength limit. Indeed, μ_2 remains $\mathcal{O}(1)$ for all field strengths. On the other hand, $\mu_1 \to \infty$ as $v_{A1} \to \infty$, indicating that the first interface (and hence the second, since μ_2 is finite) is suppressed by increasing magnetic field strength. The mode becomes even more of a 'surface' mode, the higher the strength of the magnetic field.

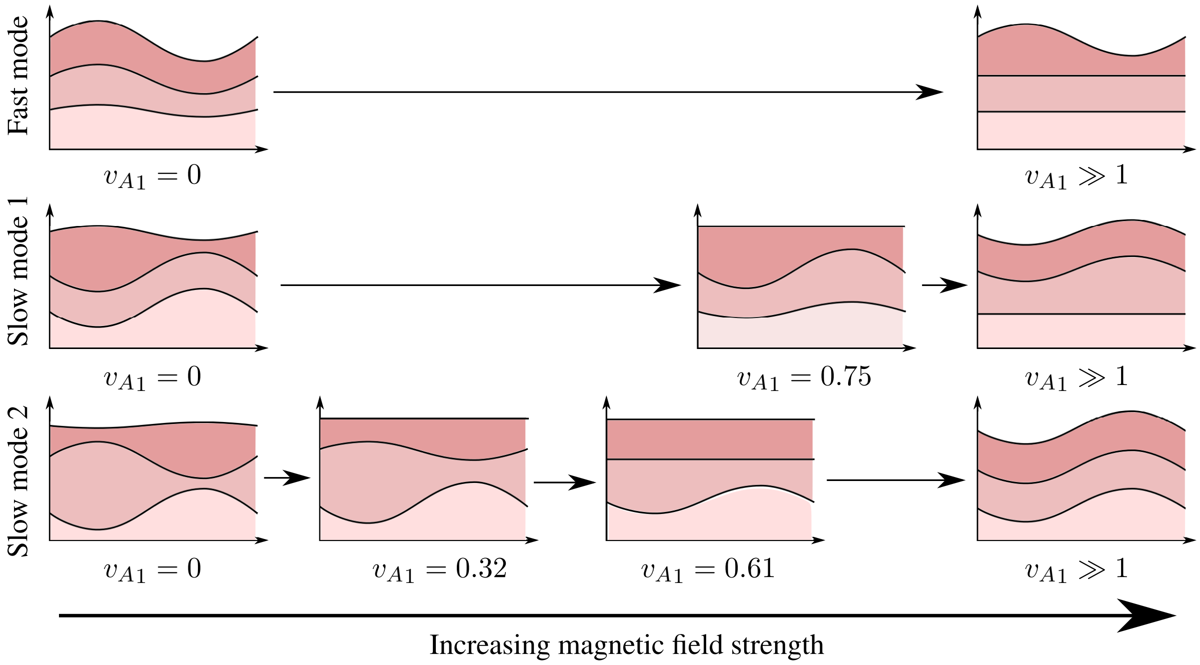

Figure 4.17 – Illustrations of the effect of increasing magnetic field strength on the three wave modes for the case of equal magnetic field strengths, as in example 2. The top row is the behaviour of the first slow mode, including the purely internal phase. The second row is the second slow mode, and the third is the fast mode. These can be viewed alongside figure 4.16. The values of v_{A1} have been calculated based on a linearly stratified profile, with $\alpha = 0.1$.

This behaviour is reflected in figures 4.16(c),(e), which display the ratios of horizontal fluid velocities. The ratio u_2/u_3 remains finite, whereas $u_1/u_2 \to \infty$ as $v_{A1} \to \infty$, so that the fluid in the lower two layers becomes stagnant. This is illustrated in figure 4.17.

In the high field strength regime, in which the interfaces are stationary, we can more precisely define the $\mathcal{O}(1)$ correction to the Alfvénic phase speed. When μ_1 is undefined, we have $\zeta_1^2 = \beta_1$. This is the single-layer dispersion relation for magneto-gravity hybrid modes; the first interface acts as a rigid flat floor to the fluid above.

The first slow mode

In the hydrodynamic regime, the first slow mode is as pictured in figure 4.15(b). Inspection of the green curves in figure 4.16(b) reveals that the ratio μ_1 passes through zero. Using equation (4.64), this occurs when $\zeta_1 = 0$. This yields the 3-layer rigid lid dispersion relation as previously discussed, since the surface is stationary when $\mu_1 = 0$. This model should coincide exactly with the rigid lid model when the pressure exerted by the lid is zero, for the value of Alfvén speed satisfying equation (4.83), taking the plus sign. In the linearly stratified case, taking the slightly exaggerated value of $\alpha = 0.1$, this is $v_{A1} \approx 0.75$, which is displayed in figure 4.17.

Analysis of tables 4.3-4.5 reveals the balance of terms at this purely internal stage. For the upper layer, we find that motion is driven solely by magnetic field, as expected. This ties in with $\zeta_1 = 0$, since then $c = v_{A1}$ and the mode is Alfvénic in nature, with magnetic tension as the restoring force. The fluid in the middle layer is driven mainly by magnetic tension, with the first interface having an effect of order $\alpha_{1,2}$. The motion in the lowest layer is also dominated by the Lorentz force.

In the absence of field, the ratio u_1/u_2 undefined, since in this case the fluid velocity in the middle layer is purely vertical. Introducing magnetic field changes this, so that the fluid-fluid interfaces are no longer in phase with matching amplitudes. The ratio u_1/u_2 does, however, always stay negative, so that the fluid in the upper two layers moves in opposite directions. Similarly, the ratio u_2/u_3 is zero when $v_{A1} = 0$, since u_2 is zero for this mode without field, and increases as v_{A1} is increased, remaining positive thereafter; i.e., the fluid in the lower two layers always moves in the same direction.

For Alfvén speeds greater than those at the purely internal stage (when equation (4.83) is satisfied), the surface then moves in phase with the first interface, whereas for lower values of v_{A1} it was in antiphase. In the high magnetic field strength regime, the ratio $\mu_1 \to 1$, so that the surface and first interface perturbations become the same in amplitude. We also have $\mu_2 \to \infty$, indicative of a stationary lower interface. Thus high field strengths suppress motion in the lowest layer for this mode, with wave motion confined to the upper layers. The horizontal velocity of fluid in the top layer also decreases, with the ratio $u_1/u_2 \to 0$ as $v_{A1} \to \infty$.

The second slow mode

This mode, which is unique to the 3-layer system, undergoes the most change as magnetic field is varied. Represented by the red curves in figure 4.16, we find that both μ_1 and μ_2 pass through zero at different values of v_{A1}. We have found that $\mu_1 = 0$ if $\zeta_1 = 0$, which led to equation (4.83). Taking the plus sign gives the value of the Alfvén speed for the purely internal stage of the first slow mode, whereas taking the negative sign will give the value at which this second slow mode goes internal. This is illustrated in figure 4.16(b), in which the green curve passes through zero at a higher value of v_{A1} than the red curve. In the linearly stratified case with $\alpha = 0.1$, the Alfvén speed at which the behaviour is purely internal is $v_{A1} \approx 0.32$. At this stage we see that the mode is similar to the purely internal stage of the other slow mode, except that here the fluid-fluid interfaces are in antiphase. This is shown in figure 4.17.

Increasing field strength further, we find that μ_2 becomes zero when equation (4.85) is satisfied. This occurs when $\zeta_2 = 0$, giving an Alfvén wave with speed v_{A2}; this is to be expected, because if the first interface is stationary, then the sole driver of motion in the second layer is magnetic tension. Indeed, inspection of table 4.4 confirms this. We also have a finite value of μ_1 at this point, so that the surface is also stationary. The upper layer is then motionless, with all wave dynamics occurring in the lower two layers. As previously discussed, we then recover the 2-layer rigid lid dispersion relation for the case when the pressure exerted by the lid is zero.

At this second internal stage, $u_2/u_3 = -1$, so that the horizontal flux through any vertical surface is zero. This stage also marks the change from the interfaces being in antiphase, to being in phase. The surface, too, oscillates in the same phase, and as field strength is increased further, all three amplitudes become comparable in size. In the limit $v_{A1} \to \infty$, both μ_1 and μ_2 tend to 1, so that the fluid velocities in the upper two layers is purely vertical.

4.7.3 Example 3: Field in middle layer only

In our search for wave–like dynamics different to those of the two–layer system, we consider the special case of one magnetised layer of fluid sandwiched between two non-magnetised layers. When $v_{A1} = v_{A3} = 0$, the dispersion relation (4.62) reduces to

$$\begin{aligned} c^6 - (1 + v_{A2}^2)c^4 + \left(\alpha_{1,2}\beta_1\beta_2 + \alpha_{1,3}\beta_1\beta_3 + \alpha_{2,3}\beta_2\beta_3 + (1-\beta_2)v_{A2}^2\right) c^2 \\ - \left(\alpha_{1,3}\beta_1\beta_3 v_{A2}^2 + \alpha_{1,2}\alpha_{2,3}\beta_1\beta_2\beta_3\right) = 0. \quad (4.86) \end{aligned}$$

This reduces further to

$$c^6 - (1 + v_{A2}^2)c^4 + \left(\frac{2}{3}v_{A2}^2 + \frac{\alpha}{9}(4-\alpha)\right) c^2 - \frac{\alpha}{9}\left((2-\alpha)v_{A2}^2 + \frac{\alpha}{3}\right) = 0, \qquad (4.87)$$

when the system is linearly stratified, with $\alpha_{1,2} = \alpha_{2,3} = \alpha$ and $\beta_1 = \beta_2 = \beta_3 = 1/3$. This has an exact solution

$$c^2 = \frac{\alpha}{3}, \qquad (4.88)$$

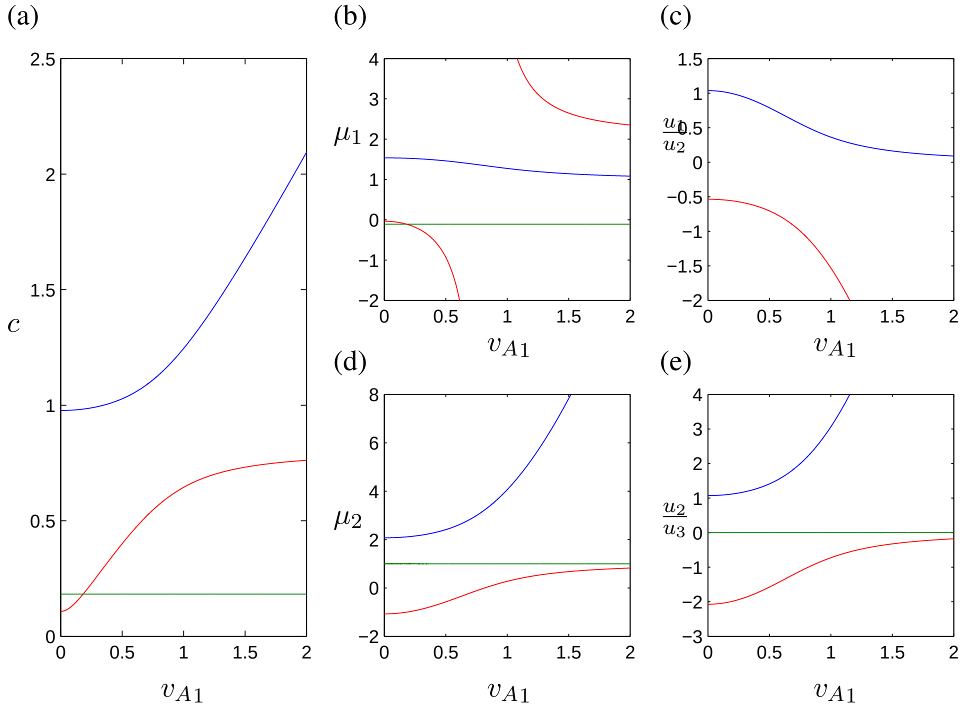

Figure 4.18 – As in figure 4.16, for the 3-layer free surface model with $v_{A1} = v_{A3} = 0$. Plots show the linearly stratified case with $\alpha = 0.1$.

for all values of v_{A2}, as illustrated in figure 4.18, denoting a wave mode that travels at a constant speed, regardless of the strength of the magnetic field in the middle layer. Since one root is known, equation (4.87) can be factorised to obtain

$$\left(c^2-\frac{\alpha}{3}\right)\left(c^4-\left(1+v_{A2}^2-\frac{\alpha}{3}\right)c^2+\frac{2}{3}v_{A2}^2-\frac{\alpha}{3}\left(v_{A2}^2-\frac{1}{3}\right)\right)=0. \tag{4.89}$$

One can thus determine the phase speeds of these three wave modes to order α, as

$$\begin{aligned} c^2 &= \frac{\alpha}{3}, \\ c^2 &\approx \frac{1}{2}\left(1+v_{A2}^2-\frac{\alpha}{3}\pm\left(1-\frac{2}{3}v_{A2}^2+v_{A_2}^4\right)^{1/2}\left(1+\frac{\alpha}{3}\left(\frac{3v_{A2}^2-5}{3-2v_{A2}^2+3v_{A_2}^4}\right)\right)\right). \end{aligned} \tag{4.90}$$

In the hydrodynamic limit $v_{A2}^2 = 0$, the latter two roots reduce to those found in section 4.7.1: $c^2 = 1 - 4\alpha/9$ and $c^2 = \alpha/9$.

We can also calculate the phase speeds in the limit of high field strength, for general stratification settings. Using the dispersion relation (4.86), we find that the phase speed of the fast mode tends to v_{A2}, as we would expect. When c is $\mathcal{O}(1)$, the dominant balance of terms is

$$c^4-(1-\beta_2)c^2+\alpha_{1,3}\beta_1\beta_3=0. \tag{4.91}$$

This can be solved to give approximations of phase speeds in the presence of a strong field. If we stipulate further that $\beta_1 = \beta_3$ and $\alpha_{1,2} = \alpha_{2,3} = \alpha$, so that the system stratification is in some sense symmetrical, we have

$$c_{\pm}^2 = \beta_1(1 \pm (1 - \alpha)). \tag{4.92}$$

Thus, the phase speeds of the two slow modes in the high field strength regime approximately satisfy $c^2 = \alpha\beta_1$ (which we knew) and $c^2 = 2\beta_1$. This represents a wave moving at the gravity wave speed, when $2H_1$ is the height of the layer.

Before considering each mode in turn, we should point out that for each of these modes, the fluid motion in the upper layer is driven by surface movements only, as can be verified in table 4.3. Similarly, in the bottom layer, fluid velocity is driven mainly by the surface, since this layer is hydrodynamic also; magnetic field can only affect motion in the middle layer, in this example.

The fast mode

For the fast mode, the transition from the hydrodynamic to the magnetic regimes is smooth in the sense that there are no zeros or singularities in any of the property ratios, as in the previous example. Inspection of figure 4.18 reveals that the phase speed of this mode increases with magnetic field strength, and approaches the Alfvén speed v_{A2} in the limit $v_{A2} \to \infty$. The ratio μ_1 does not vary much, taking a value around 1.5 for low Alfvén speeds and tending towards 1 at high Alfvén speeds, indicating that the surface and first interface motions remain in phase and of comparable magnitude for all field strengths. The ratio μ_2, however, increases sharply, indicating that the second interface motion is suppressed by field.

As $\mu_1 \to 1$, the fluid velocity in the upper layer becomes purely vertical, so that in the high field strength limit the top layer is bounded by interfaces that are moving in phase with the same amplitude. Since the lower interface is stationary in this regime, the fluid in the lowest layer also has no horizontal velocity (in fact, it has no velocity at all). From equation (4.65), $\mu_2 = 0$ gives the phase speed $c = v_{A2}$, and equations (4.68) verify that $u_1 = u_3 = 0$. This Alfvénic nature is to be expected, since in the high field strength regime we expect the fast mode to have a restoring force dominated by magnetic tension. The mode structures at high field strengths is illustrated in figure 4.19.

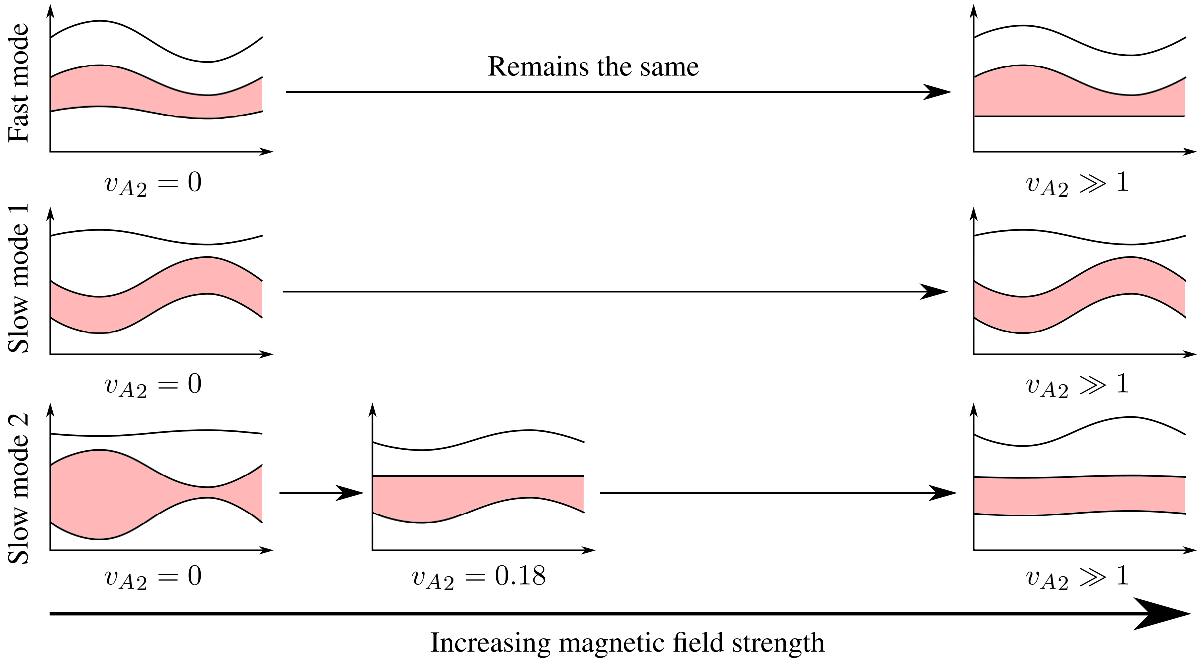

Figure 4.19 – Schematics of the mode structures in the 3-layer free surface model with $v_{A1} = v_{A3} = 0$.

The first slow mode

Intriguingly, this mode is completely unaffected by magnetic field in the linearly stratified case. The phase speed remains at $\sqrt{\alpha\beta_1}$ (for $\alpha_{1,2} = \alpha_{2,3} = \alpha$ and $\beta_1 = \beta_3$), and the mode structure remains in its hydrodynamic state for all field strengths. Recall that in the hydrodynamic case, $\mu_1 = 1$, so that both interfaces move in phase with the same amplitude, and the fluid in the middle layer has vertical motion only; this is maintained for all values of v_{A2}. The Lorentz force can only affect the horizontal fluid velocity in a layer if this speed is nonzero. Checking the balance of terms in the momentum equation for the second layer (see table 4.4), we find that the interface terms balance exactly, with no other input. Further, the magnetic field in this layer can only affect fluid *in that layer*, and since there is no horizontal movement, it has no influence on the entire system, for this mode.

The second slow mode

Since there *is* horizontal fluid motion in the middle layer in the hydrodynamic case for this mode, changes in magnetic field do change wave structure. As v_{A2} is increased from zero, the phase speed rises until at some field strength it reaches the value $\alpha\beta_1$ (with $\alpha_{1,2} = \alpha_{2,3} = \alpha$ and

$\beta_1 = \beta_3$, as before). At this point, the phase speed of this mode coincides with the first slow mode. Using the dispersion relation (4.86), this occurs when $c = v_{A2}$, so that magnetic tension is the restoring force for layer 2. Both slow modes travel at the same speed when $v_{A2}^2 = \alpha\beta_1$, but the driving forces (not to mention the wave structures) are different for each mode. This is the first time we have seen the phase speed of two modes match, but this coincidence can only happen with two slow modes; our partition of the modes into one 'fast' mode and the other 'slow' modes is intact.

Considering values of v_{A2} slightly greater than $\alpha\beta_1$, we find that the first interface motion ceases. This occurs when μ_1 is undefined, or when $\zeta_1 = \beta_1$ using equation (4.64). Since $v_{A1} = v_{A3} = 0$ in this example, we can replace both ζ_1^2 and ζ_3^2 with β_1 in the dispersion relation (4.86), as $c^2 = \beta_1$. This gives

$$v_{A2}^2 = \frac{\beta_1(1-\beta_1) - \alpha_{2,3}\beta_3(1-\beta_3)}{(1-\alpha_{2,3})\beta_3} \tag{4.93}$$

as the equation that v_{A2} satisfies when the first interface stops moving. Further stipulating that $\beta_1 = \beta_3$, this becomes

$$v_{A2}^2 = 1 - \beta_1. \tag{4.94}$$

For v_{A2} greater than this value of the Alfvén speed, this interface moves in phase with both the surface and second interface.

We found that the phase speed and structure of the first slow mode was independent of magnetic field because the motion in the middle layer (which houses the field) had no horizontal component. We also know that in the high field strength limit, the second slow mode has a phase speed that tends towards the hydrodynamic value $\sqrt{2\beta_1}$. Thus we expect, in this regime, that the fluid-fluid interfaces have the same amplitude, so that the fluid motion in the middle layer is purely vertical and therefore immune to further increases in magnetic tension. Indeed, one can see that the ratio μ_1 tends towards 1 in figure 4.18, and the phase speed tends towards $\sqrt{2/3}$. In this limit, the force balance in the momentum equations is the same as for the first internal mode.

4.7.4 Non-linear stratification

So far, we have made analytic progress by deriving expressions and figures for which $\alpha_{1,2} = \alpha_{2,3} = \alpha$ and $\beta_1 = \beta_2 = \beta_3$, which we have dubbed 'linear stratification', since this represents a system in which each sublayer is the same thickness, with equal density jumps over the interfaces.

This simplification has enabled us to continue with an otherwise complicated analysis, and generate results that are representative of the dynamics of the modes supported by a model with general stratification settings.

However, it is worth taking a small departure from this simplification to investigate a curiosity in the behaviour of the three modes and their properties. In this short section we will consider the case with $\alpha_{1,2} = \alpha_{2,3} = \alpha$, as before, but this time vary the β_j from $1/3$. This may be of interest in physical applications, perhaps to model the dynamics of a thin layer sandwiched between two thicker layers that take up most of the depth, or vice versa. We shall again discuss the case with $v_{A1} = v_{A3} = 0$, so that we can compare our results with those in example 3 above.

In the linearly stratified case in example 3 we found a wave mode, the behaviour of which does not depend on the magnetic field in the middle layer. The natural question arises as to whether such waves exist when the stratification is not linear. It is clear that the terms involving v_{A2} in the dispersion relation (4.86) must cancel if we are to obtain a root independent of field strength. Equating the sum of these terms to zero gives

$$c^4 - (1 - \beta_2)c^2 + \alpha(2 - \alpha)\beta_1\beta_3 = 0, \tag{4.95}$$

from which one can calculate c for given layer depths. For example, in the 'symmetrically stratified' case with $\beta_1 = \beta_3$, the values of c^2 that would remove all field strength from the dispersion relation are given by

$$c_\pm^2 = \beta_1(1 \pm (1 - \alpha)), \tag{4.96}$$

which, of course, is the same equation that is satisfied in the high field strength regime. One should bear in mind that these are not necessarily solutions of the dispersion relation; they are simply those values of c that would cancel off the terms involving v_{A2}^2. One of these values is $c_-^2 = \alpha\beta_1$, which is also a root of (4.86). The other value is $c_+^2 = \beta(2 - \alpha)$. This value of c_+ does not, however, satisfy (4.86) and so we discard it. A root must satisfy the dispersion relation in its entirety, which is equivalent to satisfying (4.95) *and* the hydrodynamic dispersion relation

$$c^6 - c^4 + \alpha(\beta_1\beta_2 + (2 - \alpha)\beta_1\beta_3 + \beta_2\beta_3)c^2 - \alpha^2\beta_1\beta_2\beta_3 = 0, \tag{4.97}$$

derived from (4.62). Equations (4.95) and (4.97) can be solved simultaneously by factorising and substituting, to obtain

$$c^2 = \frac{2\alpha\beta_1\beta_3}{\beta_1 + \beta_3}. \tag{4.98}$$

This is a solution of equations (4.95) and (4.97), perhaps with constraints on the value of the β_i. Substituting this expression for c^2 into (4.95) we find

$$\alpha^2\beta_1\beta_3(\beta_1-\beta_3)^2=0, \tag{4.99}$$

which implies that $\beta_1=\beta_3$.

This is a generalisation of the field-independent mode found earlier. If the system is symmetrically stratified with $\beta_1=\beta_3$, then the mode with phase speed satisfying $c^2=\alpha\beta_1$ travels as if there were no magnetic field present at all, regardless of its strength. However, any slight change introduced to this stratification profile upsets the picture somewhat. We may investigate this by introducing an offset parameter δ such that

$$\beta_3=\beta_1+\delta. \tag{4.100}$$

For example, consider the case $\delta=1/5$, with $\beta_1=1/3$ as before, so that $\beta_2=2/15$ and $\beta_3=8/15$. Multi–layered hydrodynamic models of the ocean often have a deeper lower layer, so this set-up would lend itself to that kind of application. Plots of phase speed and the corresponding ratios for all three wave modes in this case are shown in figure 4.20. It appears that the internal modes 'swap' behaviour for a certain value of v_A; we will examine this transition point to determine the nature of this swap.

This 'avoidance point' occurs on the line $c=\sqrt{\alpha\beta_1}$. Not only do the slow modes swap behaviour at the avoidance point, a singularity has been introduced in the red μ_2 curve for the second slow mode. This is inevitable, because with $\delta=0$ (figure 4.18), the values of μ_2 for the internal modes are of opposite sign, implying that for one mode the interfaces are in phase, and for the other, in antiphase. In order for these modes to swap behaviour, one of the interfaces would have to stop moving in order to change phase and reproduce the properties previously owned by the other mode. When $\zeta_1^2=c^2=\alpha\beta_1$, for the first slow mode, the ratio μ_2 is given by $\mu_2=\zeta_2^2/\zeta_2^2$, from equation (4.65). If $\zeta_2^2\neq 0$, then we can cancel off the ζ_2^2 to find $\mu_2=1$. However, any straight line representing horizontal phase speed will have to cross the line $c=v_{A2}$ at some point, which is when μ_2 has a chance to become undefined.

This opportunity for μ_2 to become infinite does not occur in the $\delta=0$ case, because the phase speed does not change, so that $\zeta_1^2=\alpha\beta_1$ for all Alfvén speeds; we can then cancel off the ζ_2^2 to give $\mu_2=1$ (everywhere except at an infinitesimal point). However, if the phase speed deviates from this, which is the case when $\delta\neq 0$, then μ_1 is no longer constant and the expression for μ_2

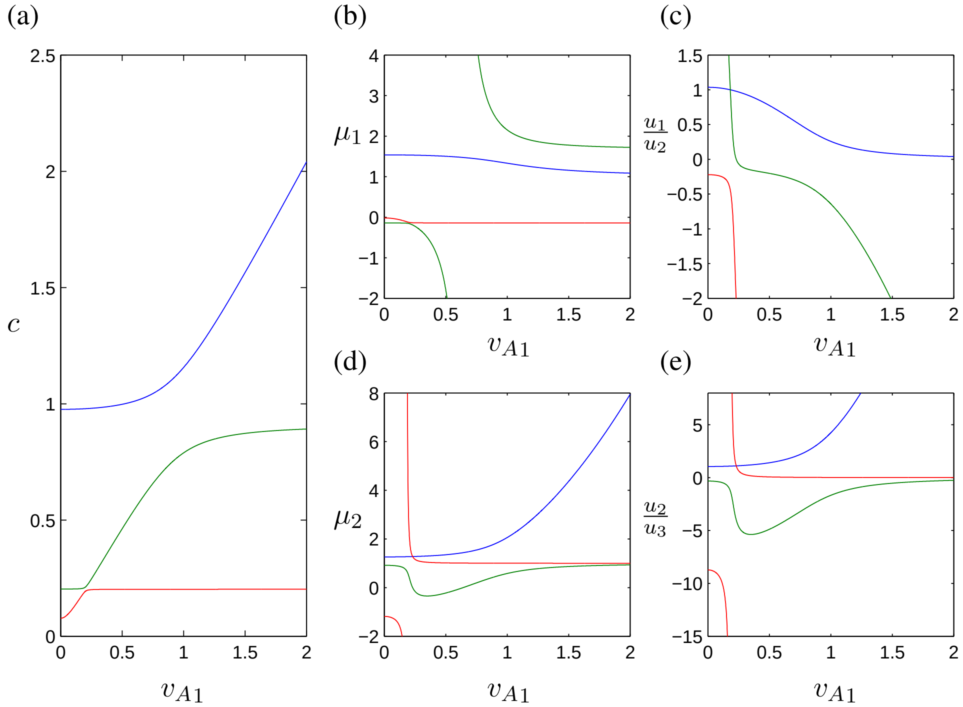

Figure 4.20 – Graphs of wave properties in the 3-layer free surface model when $v_{A1} = v_{A3} = 0$. For this figure $\alpha_{1,2} = \alpha_{2,3} = 0.1$ and $\beta_1 = 1/3$, $\beta_2 = 2/15$, and $\beta_3 = 8/15$.

cannot be simplified in this way, and growth of the ratio towards an asymptote is possible. The structure of the modes is, of course, inextricably linked to the phase speeds.

To shed more light on this avoidance point phenomenon, we can analyse the points at which the phase speed curves of the slow modes intersect the line $c = v_{A2}$. Substituting $\zeta_2^2 = 0$ into (4.86), we find that c (and hence v_{A2}) satisfies

$$c^4 - \alpha(\beta_1 + \beta_3)c^2 - \alpha\beta_1\beta_3 = 0, \tag{4.101}$$

for nonzero β_2, from which $c^2 = \alpha\beta_1$ and $c^2 - \alpha\beta_3$. From this it is clear that the curves only intersect when $\beta_1 = \beta_3$; any nonzero value of δ will give phase speed curves that do not coincide, leading to swapping behaviour.

4.7.5 Group velocities

Using the dispersion relation (4.62), the group velocities can be found in the same manner as outlined in the single and 2-layer models. This process is slightly trickier with the 3-layer system,

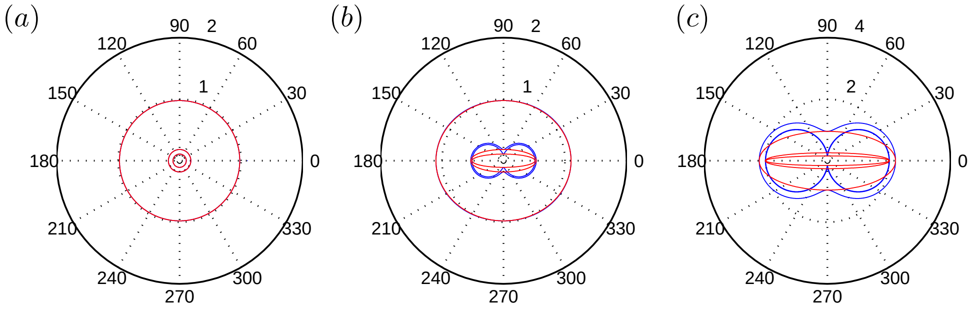

Figure 4.21 – Polar plots of phase and group velocities for the modes in the 3-layer system. Blue curves represent phase speeds, and red group speeds. Plot (a) depicts the hydrodynamic case, plot (b) the case $v_A = 0.5$, and (c) the case $v_A = 2$. Ambient magnetic field has been aligned with the x-axis.

but follows the same basic steps. One can even calculate exact expressions using the cubic formula, but the resulting expressions are horrendously long and so shall not be shown here.

If we take magnetic field orientations into account, as we did in section 4.3.5, there are ten independent parameters at our disposal: four stratification parameters and six magnetic parameters. Again, we shall be selective in the cases we study, and concentrate on the case $v_{A1} = v_{A2} = v_{A3}$ in this section. We shall also consider only linear stratification, so that $\alpha_{1,2} = \alpha_{2,3} = \alpha$ and $\beta_j = 1/3$ for $j = 1, 2, 3$. For the figures, we shall again adopt the value $\alpha = 0.1$ for the density jumps. Again, this is a slight departure from the likely physical values of $\alpha_{1,2} = 0.052$ and $\alpha_{2,3} = 0.054$ for the tachocline (see introduction of this chapter) but this is intended so that the properties are easier to identify.

Figure 4.21 contains polar plots of phase speed (blue) and group velocity (red). Figure 4.21(a) shows the curves in the hydrodynamic case, which are circles. This is to be expected, since the only restoring force is gravity, which acts equally in all directions. As magnetic field is introduced, in figure 4.21(b), the effect of the Lorentz force on fluid motion is introduced and the direction of the field lines (x-axis) is favoured in the sense that waves travel faster in this direction. This was the case in the 2-layer model, but in this example we have two internal modes. Each of these modes behave in a similar fashion as the field strength is increased (figure 4.21(c)), but one approaches the high strength limit before the other.

It is worth mentioning the influence of the value of α in these plots, since we have discussed physical values and why we exaggerate these when plotting the figures. For $\alpha \ll 1$, the hydrodynamic phase speeds of the slow modes are tiny compared to that of the fast mode, and so the phase and group curves would consist of one circle of radius $\mathcal{O}(1)$ and two virtually indistinguishable small circles. Introducing magnetic field elongates these smaller circles in the direction of the imposed field, as previously seen, but not in the perpendicular direction. As a result, the curves look like circles that pass through the origin, very much like those for Alfvén waves. There is much clearer distinction between these when α is increased, because the phase speed can then be seen to not be circular, and the group velocities more than just points on the x-axis. The same effect is present in the rigid lid model, and can be seen in figure 4.23. Furthermore, the gap between the fast and slow modes is decreased, so that the curves in the figures are not too far apart, and are more aesthetically pleasing.

4.8 The 3-layer rigid lid model

As in the 2-layer model, we will now consider the effect of adding a rigid lid to the system. This will prevent surface motion, keeping the fluid below $z = 0$ with a flat lid, which will respond to the fluid motions immediately below it by asserting a pressure field. Using equation (3.45), the dispersion relation for this model is

$$\sum_{i\neq j\neq l}(1-\alpha_{1,i})\beta_i\zeta_j^2\zeta_l^2 - \sum_{i\neq j\neq l}\alpha_{i,j}\beta_i\beta_j\zeta_l^2 + \alpha_{1,2}\alpha_{2,3}\beta_2\beta_3\zeta_1^2 + \alpha_{1,2}\alpha_{2,3}\beta_1\beta_2\beta_3 = 0, \quad (4.102)$$

making use of (3.48). We can study the dynamics of the system using the eigenvector of the matrix of coefficients from equation (3.48). This is equivalent to deriving expressions that describe the wave structure found earlier, but highlights another way of considering the problem. This eigenvector is

$$\begin{pmatrix} \bar{P} \\ \tilde{\eta}_1 \\ \tilde{\eta}_2 \end{pmatrix} = \begin{pmatrix} -\rho_1\zeta_1^2\zeta_2^2 \\ \beta_1\zeta_2^2 \\ \beta_1\zeta_2^2 + (1-\alpha_{1,2})\beta_2\zeta_1^2 - \alpha_{1,2}\beta_1\beta_2 \end{pmatrix}. \quad (4.103)$$

From this we can immediately see that when $\zeta_1 = 0$, the lid exerts no pressure onto the fluid immediately below, and when $\zeta_2 = 0$, both $\bar{P}$ and η_1 are zero. The behaviour of these Alfvén-like modes is directly analogous to the purely internal modes in the free surface case.

4.8.1 Parallels with the 2-layer models

At first glance of the eigenvector (4.103), $\tilde{\eta}_2 = 0$ when the 2-layer rigid lid dispersion relation (4.40) is satisfied. However, this is not allowed by (4.102), and so all modes perturb this interface. However, it is possible for a mode to propagate without perturbing the *highest* interface, $\tilde{\eta}_1$. This occurs when $\zeta_2 = 0$, coinciding with the free surface case. This mode then has the dynamics of the corresponding mode in the 2-layer rigid lid model.

If $\beta_j \rightarrow 0$, $c^2 \rightarrow {v_A}_j^2$ for one of the modes. As in the 2-layer rigid lid case, the thinner a layer, the greater the influence of this layer's magnetic field on this mode. If this is the top layer ($j = 1$), this upper layer acts as an elastic boundary to the fluid below, and the system behaves as in the two layer free surface model. To compare the modes in the two systems, we can calculate the phase speeds in each case. In the 3-layer rigid lid model, we have $c^2 = {v_A}_1^2$ and $c^2 = (1 - \alpha_{1,2})\beta_2 {v_A}_3^2 + (1 - \alpha_{1,3})\beta_3 {v_A}_2^2 + (1 - \alpha_{1,2})\alpha_{2,3}\beta_2\beta_3$. The corresponding modes in the 2-layer system are $c^2 = {v_A}_1^2$ and $c^2 = {v_A}_2^2 + \alpha_{1,2}\beta_2$. One can see that in both cases, v_{A1} has no effect on the other mode. Again, this does not violate any kinematic constraints such as fluid moving through a boundary, because the perturbations are infinitesimal.

Of course, there are some differences between the modes of the rigid lid model and the internal modes of the free surface system. One of these is that in the high field strength regime, the two supported modes do not tend to one of the individual Alfvén speeds; they each approach a complicated combination of them all.

4.8.2 Field dependence

The addition of a rigid lid also removes any possibility of field-independent modes. For the case with magnetic field in the middle layer, we have only an approximate field independent root; the phase speed curves swap behaviour at an avoidance point in a similar manner to the free surface case when $\beta_1 \neq \beta_3$. Figure 4.22 shows the linearly stratified case, which can be compared directly with figure 4.18. In the free surface case the phase speed of the two slow modes coincides, but with a rigid lid this does not happen.

This is not to say that it cannot happen with other stratification settings. The curves avoid each other close to the point where they would otherwise intersect the line $c = v_{A2}$. The dispersion

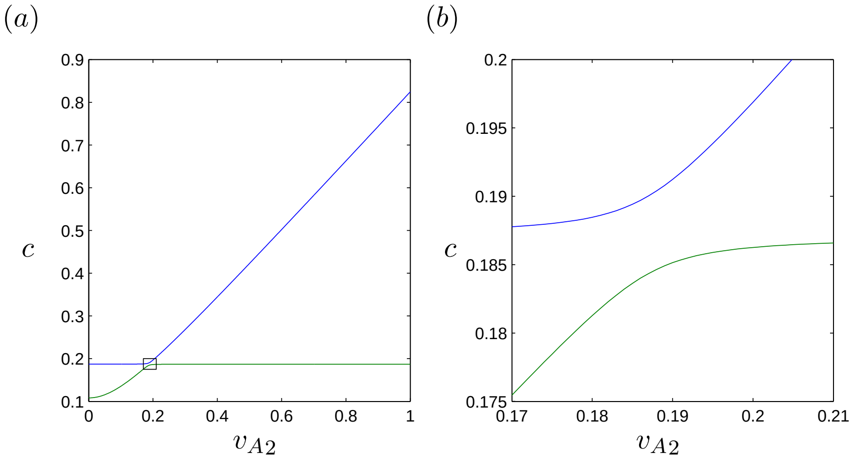

Figure 4.22 – Phase speed versus v_{A2} for the 3-layer rigid lid system, when the magnetic field is confined to the middle layer, in the linearly stratified case with $\alpha = 0.1$. Plot (b) is a zoomed in plot of the avoidance point, as outlined in plot (a) with a black box.

relation then yields

$$((1 - \alpha_{1,2})\zeta_1^2 - \alpha_{1,2}\beta_1)(\zeta_3^2 - \alpha_{2,3}\beta_3) = 0, \tag{4.104}$$

giving values of phase speed satisfying $c^2 = \alpha_{1,2}\beta_1/(1 - \alpha_{1,2})$ and $c^2 = \alpha_{2,3}\beta_3$, since we are considering the case $v_{A1} = v_{A3} = 0$. These coincide when

$$\frac{\beta_1}{\beta_3} = \frac{(1 - \alpha_{1,2})\alpha_{2,3}}{\alpha_{1,2}}. \tag{4.105}$$

If equation (4.105) were satisfied, then not only do both slow modes propagate at the same speed, but the field strength at which the upper interface becomes stationary for each mode coincides. Considering the momentum equation for the upper layer, there are two possible forces that balance acceleration: the first is magnetic tension, and the second is the pressure from the lid. The former is zero when field is confined to the middle layer, and so the fluid in the top layer is motionless when the pressure exerted by the lid is zero. The interface is then motionless also, and fluid motion in the middle layer is driven solely by the Lorentz force, giving rise to an Alfvén-like wave.

The relationship between β_1 and β_3 given in (4.105) becomes $\beta_1 = (1 - \alpha)\beta_3$ when $\alpha_{1,2} = \alpha_{2,3} = \alpha$. This differs from the relationship found in the free surface case (in which $\beta_1 = \beta_3$) in the small α correction. This means that when a rigid lid is present, the stratification settings of the system that permit the coincidence of the phase speeds of the slow modes is not the 'symmetrical stratification' we found in the free surface model.

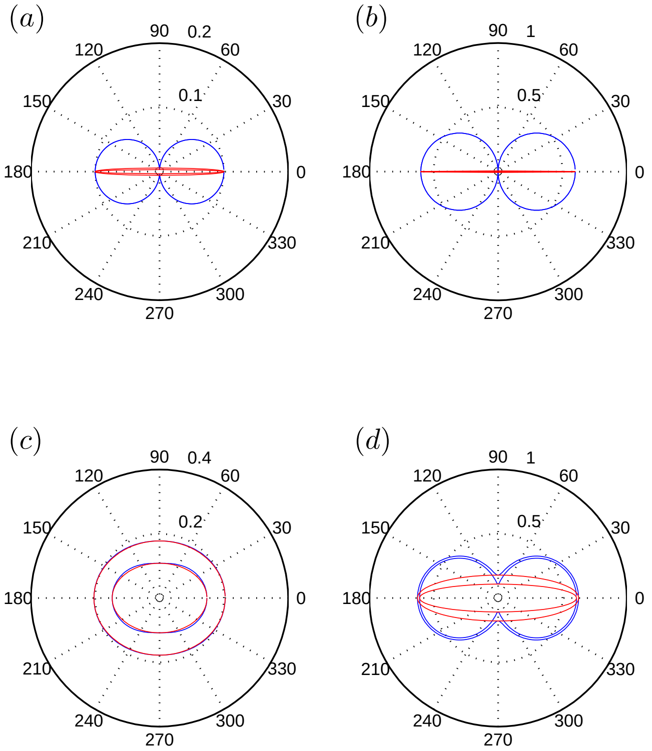

Figure 4.23 – Polar plots of phase and group velocities for the modes in the 3-layer rigid lid system. As before, blue and red curves represent phase and group velocities respectively. For plots (a) and (c), field strength is relatively small, at $v_A = 0.1$. For plots (b) and (d), $v_A = 0.6$. In plots (a) and (b), $\alpha = 10^{-4}$, and in plots (c) and (d) we have $\alpha = 0.1$.

4.8.3 Group Velocities

Using the dispersion relation (4.102), we can calculate phase and group velocities for the rigid lid model in a similar manner as in the free surface case. We shall consider linear stratification, keeping the magnetic fields in the same direction in each layer, with $v_{A1} = v_{A2} = v_{A3}$, as before. We shall continue to investigate the effects of increasing magnetic field strength, but also consider the role played by α.

Figure 4.23 shows polar plots of phase (blue) and group (red) velocities for the two supported modes. Increasing the Alfvén speed increases the phase and group velocities in the direction of the magnetic field, with phase velocity curves tending to circles and the group velocity curves flattening out. In the limit $v_{A2} \to \infty$, the red curves tend to points on the x-axis as the waves become more Alfvénic in nature. We have seen this in the free surface and 2-layer models.

Increasing α, on the other hand, makes the modes less Alfvén-like in nature. In figures 4.23(a) and (b), with $\alpha = 10^{-4}$, the curves are almost circles, reflecting the Alfvénic property described above, whereas in figures 4.23(c) and (d), the restoring force perpendicular to the magnetic field becomes more apparent. This is because as the density jump between the layers is increased, their contribution to the restoring force (which is the same in every direction) increases, so that there is less disparity between this force in different directions for fixed v_{Aj}.

4.9 Summary and discussion

The addition of layers to the single layer model has allowed us to investigate the effects of different variations of basic state magnetic field. In the tachocline, the strength and vertical structure of the magnetic field is not known; however, it is accepted that the field lines are horizontal. The ambient field in n-layer model can emulate any such physical phenomenon, and in this chapter, specific examples were discussed, and the supported wave dynamics studied.

The 2-layer model

After outlining the well-known 2-layer hydrodynamic wave modes (see, for example, Gill, 1982), the effects of introducing a magnetic field were investigated. We found that when the field is configured such that the Alfvén speeds are equal in both layers, the phase velocity is the only property that is affected. In the tachocline, where the Alfvén speed is around $13\mathrm{m\,s}^{-1}$, the phase speed of the magneto-gravity modes in this case would be $23\mathrm{m\,s}^{-1}$ for the fast mode, with the magnetically dominant slow mode propagating only fractionally faster than the Alfvén speed. These speeds are measured along field lines; perpendicular to this both modes travel slower. This is most striking for the slow mode, which has only reduced gravity as the restoring force in this direction. The fast mode also travels more slowly perpendicular to field lines, which is not true in non-shallow MHD systems. The structure of both these modes, however, remains constant, so that the fast mode remains a 'surface mode', with surface perturbations much greater than those at the interface, and vice versa for the slow mode, which retains its 'internal' quality.

In general, we found that magnetic field *does* affect wave structure. The slow mode, for example, underwent a purely internal phase when the magnetic field strength was equal over both layers. At this specific field strength, for which we found $v_A = \sqrt{\beta_2}$, the surface stopped moving entirely. With $\beta_2 = 1/2$, this gives a dimensional Alfvén speed of approximately $13\text{m}\,\text{s}^{-1}$, which is thought to be the case for the tachocline, as argued in Chapter 1.

We also found that when the field was in the upper layer, one mode has Alfvénic properties, and one has hydrodynamic properties, and this is more pronounced when the layers are unevenly split. As magnetic field strength is increased, the modes swap behaviour when $v_{A2} = \sqrt{\beta_1}$. Again, this approximately corresponds to the Alfvén speed in the tachocline, and so the tachocline would reside around the 'avoidance point', in this case. However, it is very unlikely that there is a hydrodynamic sublayer of the tachocline, since fluid motion originating from overshooting plumes would produce magnetic fields through magnetic induction. However, models in which the lower layer is magnetised and the upper layer hydrodynamic, as in the example in section 4.3.4, could be applied to the Jovian atmosphere, for example, where electrical conductivity decreases with height.

When investigating group velocities, we found that the introduction of a magnetic field significantly increased the speed of both waves and wavepackets along field lines for the slow mode. The fast mode also propagated faster along field lines, which differs from the MHD case, in which the fast magneto-acoustic mode travels fastest perpendicular to field lines. In the tachocline, the scaled (nondimensional) magnetic field strength would be approximately $|B_0| = 0.7$, which is represented best by figures 4.9(b) (in which $|B_0| = 0.5$) and 4.10 (in which $|B_0| = 1$). This implies that for the fast mode, the phase and group velocities do not differ very much at all, and energy is transported with wavepackets comprised of waves that move (almost) in that direction.

When the magnetic field in each layer is not aligned, cusps can develop in the group velocity curve of the slow mode. This creates a multi-valued group velocity for a given direction of propagation, so that wavepackets travelling in that direction can be comprised of one of three 'types' of waves. This would occur whatever the strength of field, as long as the fields were not aligned, and so could be the case for the tachocline. It is likely that in reality, the field lines do not all point in the same direction, and so the system could be modelled with nonzero Θ. In this case, in a small vicinity around the mean direction of the two magnetic field directions, there would be more than one way for energy to be transported by wavepackets in the tachocline.

The 3-layer model

In the 3-layer model we again found that magnetic field only affects the structure of the modes if the Alfvén speeds in each layer differ. In the case where the magnetic fields were aligned and of the same strength, there are more scenarios in which modes can become purely internal, so that the surface does not move. The second slow mode, which has no analogue in any simpler systems, has two field strengths at which the surface ceases to move. The second of these values occurs at a dimensional Alfvén speed of approximately $12\mathrm{m\,s}^{-1}$, which is very close to our predicted Alfvén speed in the tachocline. It is also the value at which the upper interface stops moving, and so this slow mode propagates in the lower two layers only.

The first slow mode, analogous to the slow mode of the 2-layer system, propagates without perturbing the surface at an Alfvén speed of approximately $14\mathrm{m\,s}^{-1}$, which is again close to the physical predicted value. In the tachocline, where wave motion is likely to be a combination of all three wave modes, surface motion may be almost entirely due to the fast mode, in this case.

We also found that if the magnetic field is in the middle layer and the upper and lower layers were of the same depth, the first slow mode is entirely unaffected by magnetic field strength. As previously argued, this is unlikely to be applicable to the tachocline, but may be of some use in the studies of planetary atmospheres.

The tachocline, and many other physical systems, are continuously stratified with smooth continuous vertical profiles of magnetic field. This is represented more accurately with a model with even more layers, with the infinite-layer model being best of all. The system would then have a continuous spectrum of modes, and any addition of these could be manifest in the tachocline.

So far we have discussed linear waves; that is, small-amplitude long-wavelength waves. In the next chapter we shall consider weakly nonlinear effects, in which we allow greater surface perturbations and study the effects of the nonlinear terms on the waves.

Chapter 5

Weakly nonlinear and dispersive waves

5.1 Introduction

Until now, linear analysis has allowed us to examine the types of modes supported by a system, which involves seeking solutions with just one unchanging Fourier component, with the understanding that the sum of any number of such solutions is also a solution. In this case waves have infinitesimal amplitudes, but in reality, of course, this is not the case; the ultimate goal is to understand the wave dynamics of physical systems, which involve finite disturbances. One step towards this is with a weakly nonlinear analysis, in which disturbances are small but not infinitesimal. In weakly nonlinear analysis, a solution can still be expressed as a superposition of plane waves, but the amplitude of these waves can change over time. It is a bridge between linear analysis (in which the amplitudes do not change) and fully nonlinear analysis, as in chapter 6 (in which we cannot form another solution by adding existing ones). In this chapter, we consider two distinct problems: dispersion and solitons, and wave interactions and resonance.

Nonlinear effects in shallow water theory play an important role in the propagation of tsunamis, hydraulic bores, and wave-breaking, amongst many other phenomena (see, for example, Gill, 1982; Acheson, 1990; Vallis, 2006). One such effect is nonlinear steepening, which can occur when the wave has finite amplitude. The wave crests move faster than the troughs because they have a greater height (and wave speed increases with height), which makes the leading face of the wave steeper. This steepening effect can be countered by dispersion, which arises in non-shallow systems from a non-hydrostatic term (it can also be countered by rotation, but this will be covered in Chapter 6). The balance of nonlinear steepening and dispersion can give rise to wave-like solutions that propagate without change of shape; such solitons and cnoidal waves are well-documented in hydrodynamics (see, for example, Acheson (1990)).

It is one aim of this chapter to investigate the effect of magnetic field on these surface profiles. This will be achieved by nondimensionalising the governing equations of MHD for a single layer (2.1), and later for the 2-layer system, introducing a small parameter measuring the perturbation amplitude relative to the layer depth, and a long timescale, in which long-time dynamics take place. These equations are not the shallow water equations, since they contain a non-hydrostatic term, but in the subsequent analysis the small value of the ratio of typical vertical to horizontal length scales will be exploited. An asymptotic analysis will then be carried out and a Korteweg de Vries (KdV) equation derived. The magnetic influence on the coefficients of the terms in this equation will be scrutinised, since these coefficients determine the types of solution available; for example, light/dark solitons and cnoidal waves. A similar analysis will then be applied to the 2-layer rigid lid model; we shall find that the magnetic field configuration plays a much more interesting role in this case.

For example, modes with wavenumbers $k = 2$ and $k = 3$ can interact through the small nonlinear terms to produce a $k = 5$ and a $k = 1$ mode, since the nonlinear terms are quadratic and $\cos(3x)\cos(2x) = \frac{1}{2}(\cos(5x) + \cos(x))$. These secondary excited modes arise through small terms (the nonlinear terms each have a coefficient containing the small parameter ϵ), and so changes take time to arise: this long-time will be the product of ϵ and the 'fast' timescale. This means that if one excited the $k = 2$ and $k = 3$ modes only, eventually a $k = 1$ and $k = 5$ mode would appear. Given more time, these secondary modes may feed back onto the original ones, and so on.

When this energy exchange occurs between three waves only, the resulting phenomenon is called three-wave resonance. The periodic long-time modulations in amplitude of waves exhibiting resonance is also well-known; here we shall investigate the effects of adding a magnetic field on the resonance conditions, the period of the modulations, and the Jacobi elliptic parameter, which is a measure of how sinusoidal (or hyperbolic trigonometric) the wave form is.

Finally, we shall consider the single layer rotating shallow water model, and look for three-wave resonance in the model. In the presence of rotation, resonant triads are not trivially found, and since the system is dispersive, waves with different wavenumbers propagate at different speeds. Not only does the addition of rotation make the surface evolution more aesthetically pleasing, it will also serve as a basis for comparison in Chapter 6, which deals with the fully nonlinear solution of the 1.5D rotating shallow water system.

5.2 The KdV equation for single layer SWMHD

The single layer set-up is two-dimensional, in x (horizontal) and z (vertical), with gravity in the negative z-direction as before. We drop the subscript 0 on the free surface height η_0, instead just writing η, since there is only one moving surface. As before, we consider a motionless basic state with a magnetic field of strength B_0 in the horizontal (x-direction). Then, for two-dimensional flow, equations (2.1) and (2.2) are

$$\frac{\partial \mathbf{u}}{\partial t} + u\frac{\partial \mathbf{u}}{\partial x} + w\frac{\partial \mathbf{u}}{\partial z} = -\frac{1}{\rho}\nabla\tilde{p} + \frac{1}{\mu_0\rho}\left((B_0 + B_x)\frac{\partial \mathbf{B}}{\partial x} + B_z\frac{\partial \mathbf{B}}{\partial z}\right), \tag{5.1a}$$

$$\frac{\partial \mathbf{B}}{\partial t} + u\frac{\partial \mathbf{B}}{\partial x} + w\frac{\partial \mathbf{B}}{\partial z} = (B_0 + B_x)\frac{\partial \mathbf{u}}{\partial x} + B_z\frac{\partial \mathbf{u}}{\partial z}, \tag{5.1b}$$

together with solenoidal conditions on velocity and magnetic field

$$\frac{\partial u}{\partial x} + \frac{\partial w}{\partial z} = 0, \tag{5.2a}$$

$$\frac{\partial B_x}{\partial x} + \frac{\partial B_z}{\partial z} = 0. \tag{5.2b}$$

Here, the two-dimensional velocity and magnetic field are given by $\mathbf{u} = (u, w)$, $\mathbf{B} = (B_x, B_z)$, and $\tilde{p}$ is the pressure perturbation:

$$\tilde{p} = p + B_0^2/2 - p_{atm} + \rho g z, \tag{5.3}$$

which is the sum of mechanical pressure, magnetic pressure and gravity terms.

We will now nondimensionalise these equations to identify the relative importance of the terms. We scale time t as the ratio of a typical length scale L to a typical speed $\sqrt{gH}$, the gravity wave speed. A typical horizontal velocity u is scaled as this gravity wave speed multiplied by the factor $\epsilon = \hat{\eta}/H$, where $\hat{\eta}$ is a typical surface perturbation height. By taking this non-dimensional parameter ϵ to be small, so that $\epsilon \ll 1$, we are ensuring that the perturbed speed is a fraction of order ϵ of the gravity wave speed. Physically, taking this parameter to be small corresponds to restricting the surface perturbations, so that they are much less than the layer depth.

The x-component of the perturbed magnetic field B_x (which, when scaled with $\sqrt{\mu_0\rho}$ as in previous chapters, has units of speed) is scaled with $\epsilon\sqrt{\mu_0\rho g H}$. Vertical velocity w and magnetic

$\tilde{p} \sim \rho g \hat{\eta}$	$u \sim \sqrt{\frac{g}{H}}\hat{\eta}$
$t \sim \frac{L}{\sqrt{gH}}$	$w \sim \frac{\sqrt{gH}}{L}\hat{\eta}$
$B_x \sim \sqrt{\frac{\mu_0 \rho g}{H}}\hat{\eta}$	$B_z \sim \frac{\sqrt{\mu_0 \rho g H}}{L}\hat{\eta}$

Table 5.1 – The scalings used in the nondimensionalisation of the governing equations.

field B_z are scaled according to the solenoidal constraints on velocity and field (5.2). Pressure $\tilde{p}$ is scaled with $\rho g H \times \epsilon = \rho g \hat{\eta}$, the $\rho g H$ factor arising from the nondimensionalisation of the equation for hydrostatic balance in the vertical. These scalings are summarised in table 5.1.

We also introduce a long time variable τ, which is related to time t by $\tau = \epsilon t$, thus allowing the investigation of the long-time dynamics of the system. All time derivatives are then replaced according to $\partial_t \to \partial_t + \epsilon \partial_\tau$.

Writing out equations (5.1) in component form and using these scalings gives

$$\frac{\partial u}{\partial t} + \frac{\partial \tilde{p}}{\partial x} - Ma\frac{\partial B_x}{\partial x} = \epsilon\left(-\frac{\partial u}{\partial \tau} - u\frac{\partial u}{\partial x} - w\frac{\partial u}{\partial z} + B_x\frac{\partial B_x}{\partial x} + B_z\frac{\partial B_x}{\partial z}\right), \tag{5.4a}$$

$$\frac{\partial \tilde{p}}{\partial z} = \delta\left(-\frac{\partial w}{\partial t} + Ma\frac{\partial B_z}{\partial x} + \epsilon\left(-\frac{\partial w}{\partial \tau} - u\frac{\partial w}{\partial x} - w\frac{\partial w}{\partial z} + B_x\frac{\partial B_z}{\partial x} + B_z\frac{\partial B_z}{\partial z}\right)\right), \tag{5.4b}$$

and the induction equation

$$\frac{\partial \mathbf{B}}{\partial t} - \mathrm{Ma}\frac{\partial \mathbf{u}}{\partial x} = \epsilon\left(-\frac{\partial \mathbf{B}}{\partial \tau} + B_x\frac{\partial \mathbf{u}}{\partial x} + B_z\frac{\partial \mathbf{u}}{\partial z} - u\frac{\partial \mathbf{B}}{\partial x} - w\frac{\partial \mathbf{B}}{\partial z}\right). \tag{5.4c}$$

The non-dimensional parameters ϵ, δ and Ma are defined as

$$\epsilon = \frac{\hat{\eta}}{H}, \tag{5.5a}$$

$$\delta = \frac{H^2}{L^2}, \tag{5.5b}$$

$$\mathrm{Ma} = \frac{B_0}{\sqrt{gH}}. \tag{5.5c}$$

The parameter δ is a measure of the aspect ratio of the layer of fluid, which is small in shallow water flow. In the previous chapters, we set $\delta = 0$ in the vertical momentum equation (5.4b); this is the shallow water approximation, with $\partial\tilde{p}/\partial z = 0$ (hydrostatic balance). In this chapter, however, we will take $0 < \delta \ll 1$.

Although the layer is shallow ($\delta \ll 1$ implies that $H \ll L$), we are not using the *shallow water* equations to model the dynamics. The supported wave modes will thus have wavelengths that are much longer than the undisturbed layer depth. The inclusion of the non-hydrostatic terms will affect the modes over the long time scale τ.

In addition to $\delta \ll 1$, we impose $\epsilon \ll 1$, so that the amplitudes of these long-wavelength modes are much smaller than the undisturbed layer depth H. This advances the linear work from Chapter 2, in which the surface displacements were infinitesimal. We thus have $L \gg H \gg \hat{\eta}$: typical horizontal length scales are much greater than the vertical ones, which are in turn much greater than the surface perturbations.

We also take $\epsilon = \delta$ in the following analysis, which is equivalent to establishing a link between the amplitude and the wavelength of the modes; it is the imposition that, for a fixed layer depth, a typical surface disturbance amplitude $\hat{\eta}$ scales with H^3/L^2. With this in place, one can replace δ with ϵ in the above scaled equations. Alternatively, one could apply the further scalings

$$\begin{pmatrix} \partial_{x^*} \\ u^* \\ \mathrm{Ma}^* \\ B_x^* \end{pmatrix} = \left(\frac{\delta}{\epsilon}\right)^{1/2} \begin{pmatrix} \partial_x \\ u \\ \mathrm{Ma} \\ B_x \end{pmatrix}, \quad \text{and} \quad \begin{pmatrix} \partial_{t^*} \\ w^* \\ p^* \\ B_z^* \end{pmatrix} = \left(\frac{\delta}{\epsilon}\right) \begin{pmatrix} \partial_t \\ w \\ p \\ B_z \end{pmatrix},$$

which has the effect of putting $\delta = \epsilon$, and the subsequent analysis can be carried forward unhindered. Alternative assumptions are possible, and a Green-Naghdi equation rather than a Korteweg de Vries equation can be derived using different scalings Dellar (2002a).

Equations (5.4) are supplemented by the solenoidal constraints on magnetic field and velocity, given by equations (5.2).

Boundary conditions

We must also impose boundary conditions on the flow. These will be the same as those derived in Chapter 2, but we will need to nondimensionalise them. In the multi-layer work in Chapters 3 and 4, we imposed that the total pressure (gas + magnetic) is constant on the surface. Then $p + \mathrm{Ma}^2/2 = p_{atm}$ on the surface, and equation (5.3) gives the (dimensional) condition $\tilde{p} = \rho g \eta$ on the surface (recall that we are writing $\eta_0 = \eta$ for aesthetic reasons). This is nondimensionalised according to table 5.1 to give $\tilde{p} = \eta$ at $z = \eta$. Applying a Taylor expansion about the undisturbed surface height $z = 0$, we have

$$\tilde{p}|_{z=0} + \epsilon\eta \left.\frac{\partial \tilde{p}}{\partial z}\right|_{z=0} + \cdots = \eta. \tag{5.6a}$$

We also impose that the floor is impermeable, as before. At the floor $z = -H$ (dimensional), this means ensuring vertical flow here is zero, i.e., $w = 0$. At the surface we have $w = D\eta/Dt$ to ensure continuity of the free surface, so that vertical flow matches the material derivative of the free surface height, at $z = \eta$. Nondimensionalising, this is

$$w = 0 \text{ at } z = -1 \qquad \text{and} \qquad w = \frac{\partial \eta}{\partial t} + \epsilon u \frac{\partial \eta}{\partial x} \text{ at } z = \epsilon\eta. \tag{5.6b}$$

Finally, we insist that the floor and surface are perfectly conducting, so there is no magnetic flux through them. This gives

$$B_z = 0 \text{ at } z = -1 \qquad \text{and} \qquad B_z = (\mathrm{Ma} + \epsilon B_x)\frac{\partial \eta}{\partial x} \text{ at } z = \epsilon\eta, \tag{5.6c}$$

which are equivalent to the imposition that the floor and surface are magnetic field lines.

The solenoidal conditions on field and velocity can be combined with the appropriate boundary conditions, in the following way: equations (5.2) are integrated over the layer depth, and the resulting expressions for B_z and w are replaced according to the boundary conditions (5.6b,c), yielding

$$\frac{\partial \eta}{\partial t} + \epsilon\frac{\partial \eta}{\partial \tau} + \epsilon u \frac{\partial \eta}{\partial x} = -\int_{-1}^{0} \frac{\partial u}{\partial x}\, dz - \int_{0}^{\epsilon\eta} \frac{\partial u}{\partial x}\, dz. \tag{5.7}$$

The timescale τ has been introduced with the ‘fast’ time t, as previously. Applying similar reasoning with equations (5.2b) and (5.6c) gives

$$(\mathrm{Ma} + \epsilon B_x)\frac{\partial \eta}{\partial x} = -\int_{-1}^{0} \frac{\partial B_x}{\partial x}\, dz - \int_{0}^{\epsilon\eta} \frac{\partial B_x}{\partial x}\, dz. \tag{5.8}$$

The integrals in equations (5.7) and (5.8) have been split into two parts: an integral over the undisturbed layer depth, and an $\mathcal{O}(\epsilon)$ integral corresponding to the disturbance. This latter term is the integral of an $\mathcal{O}(1)$ expression over a thin strip of order ϵ, and so is itself of order ϵ.

5.2.1 Asymptotic analysis

The aim is to investigate the wave-like dynamics of the system beyond the linear regime (and in this chapter, the nonlinear corrections are small since $\epsilon \ll 1$). We do this by considering each variable as a sum of an $\mathcal{O}(1)$ linear part plus small correction terms. Expressing each variable as a power series in ϵ (so that the first term is $\mathcal{O}(1)$, the second is an $\mathcal{O}(\epsilon)$ correction, the next $\mathcal{O}(\epsilon^2)$, and so on) gives, for u,

$$u = u^{(0)} + \epsilon u^{(1)} + \epsilon^2 u^{(2)} + \cdots . \tag{5.9}$$

The plan is to substitute (5.9), along with similar expressions for the other variables, into the governing equations (5.4) and boundary conditions (5.7)-(5.8). We shall then equate the coefficients of like powers of ϵ to find expressions for the $u^{(j)}$. The vertical component of the momentum equation will be used to find an expression for $\tilde{p}^{(0)}$, which will then be used to replace the pressure term in the horizontal momentum equation. This reduces the number of governing equations to four. Three of these contain time derivatives, and will be used to obtain expressions for the variables. The fourth can be shown to be satisfied by these solutions.

Leading order analysis

The governing equations (5.4) at leading order, after substitution according to (5.9), are given by

$$\frac{\partial u^{(0)}}{\partial t} + \frac{\partial \tilde{p}^{(0)}}{\partial x} - \mathrm{Ma}\frac{\partial B_x^{(0)}}{\partial x} = 0, \tag{5.10a}$$

$$\frac{\partial \tilde{p}^{(0)}}{\partial z} = 0, \tag{5.10b}$$

$$\frac{\partial B_x^{(0)}}{\partial t} - \mathrm{Ma}\frac{\partial u^{(0)}}{\partial x} = 0, \tag{5.10c}$$

$$\frac{\partial B_z^{(0)}}{\partial t} - \mathrm{Ma}\frac{\partial w^{(0)}}{\partial x} = 0, \tag{5.10d}$$

together with the combined solenoidal constraints and boundary conditions (5.7-5.8), which are, to leading order,

$$\frac{\partial \eta^{(0)}}{\partial t} = -\int_{-1}^{0} \frac{\partial u^{(0)}}{\partial x}\, dz, \tag{5.11a}$$

$$\mathrm{Ma}\frac{\partial \eta^{(0)}}{\partial x} = -\int_{-1}^{0} \frac{\partial B_x^{(0)}}{\partial x}\, dz. \tag{5.11b}$$

We also have the boundary condition on pressure (5.6a), which gives $\tilde{p}^{(0)} = \eta^{(0)}$ at $z = 0$. Together with equation (5.10b), this implies that $\tilde{p}^{(0)} = \eta^{(0)}$ for *all* values of z, and this expression for $\tilde{p}^{(0)}$ will be substituted into (5.10a). Since this term is independent of z, it is consistent to look for solutions of $u^{(0)}$ and $B_x^{(0)}$ that are also independent of z, as in the standard shallow water approximation. Indeed, at this order, the equations conform to those of shallow water since there are no non-hydrostatic terms involved (these will be present at the next order).

One can also note that the z component of the induction equation, (5.10d), is redundant as it is implied by (5.2b) and (5.10c). Similarly, equations (5.11) can also be simplified as the integrands are independent of z, leading to the reduced system of equations

$$\frac{\partial u^{(0)}}{\partial t} + \frac{\partial \eta^{(0)}}{\partial x} - \mathrm{Ma}\frac{\partial B_x^{(0)}}{\partial x} = 0, \tag{5.12a}$$

$$\frac{\partial B_x^{(0)}}{\partial t} - \mathrm{Ma}\frac{\partial u^{(0)}}{\partial x} = 0, \tag{5.12b}$$

$$\frac{\partial \eta^{(0)}}{\partial t} + \frac{\partial u^{(0)}}{\partial x} = 0, \tag{5.12c}$$

$$\mathrm{Ma}\frac{\partial \eta^{(0)}}{\partial x} + \frac{\partial B_x^{(0)}}{\partial x} = 0. \tag{5.12d}$$

Equations (5.12a-c) can be written in matrix form as

$$\frac{\partial \mathbf{a}^{(0)}}{\partial t} + M\frac{\partial \mathbf{a}^{(0)}}{\partial x} = 0, \tag{5.13}$$

where

$$\mathbf{a}^{(j)} = (u^{(j)}, \eta^{(j)}, B_x^{(j)})^T. \tag{5.14}$$

[Note: we will reconcile equation (5.12d), which is not part of this system, later.] The matrix M is given by

$$M = \begin{pmatrix} 0 & 1 & -\mathrm{Ma} \\ 1 & 0 & 0 \\ -\mathrm{Ma} & 0 & 0 \end{pmatrix}. \tag{5.15}$$

We then transfer to a frame of reference moving to the right with speed c and seek travelling solutions of (5.13) that are functions of θ, given by

$$\theta = x - ct. \tag{5.16}$$

This gives

$$u^{(0)} = u^{(0)}(\theta, \tau), \tag{5.17}$$

and similarly for the other variables. The eigenvalue c matches the phase speed of the linear waves in the medium, so that our frame of reference follows these waves, allowing us to capture the long-time dynamics of the free surface. One can now take advantage of the equivalences $\partial_t \rightarrow -c\partial_\theta$ and $\partial_x \rightarrow \partial_\theta$ to write

$$(M - cI)\frac{\partial \mathbf{a}^{(0)}}{\partial \theta} = 0, \tag{5.18}$$

where I is the identity matrix. For non-trivial solutions we deduce that $M - cI$ is singular, which leads to the dispersion relation

$$c(c^2 - \mathrm{Ma}^2 - 1) = 0. \tag{5.19}$$

From this we get three eigenvalues for phase speed: $c = 0$, and $c_\pm = \pm\sqrt{\mathrm{Ma}^2 + 1}$. The value $c = 0$ represents the spurious zero frequency mode, which is excluded courtesy of the fourth unused equation (5.12d). This is because if $c = 0$, equations (5.12a,d) are incompatible. However, the other non-zero eigenvalues are not only supported by the three equations in (5.13), but also the unused (5.12d); see later verification.

A right eigenvector that corresponds to the non-zero positive eigenvalue $c = \sqrt{\mathrm{Ma}^2 + 1}$ in equation (5.18) is given by

$$\frac{\partial \mathbf{a}^{(0)}}{\partial \theta} = (c, 1, -\mathrm{Ma})^T. \tag{5.20}$$

Now we set $\eta^{(0)} = A(\theta, \tau)$, where the function A describes the shape of the free surface to leading order, and aim to determine the function A. Using the eigenvector given by equation (5.20), we deduce that $u^{(0)} = cA$ and $B_x^{(0)} = -\mathrm{Ma}A$. Making use of equations (5.2), one can then find expressions for $w^{(0)}$ and $B_z^{(0)}$ by integration, applying the boundary conditions at $z = -H$. Summarising, we have

$$\begin{aligned}
\eta^{(0)} &= A, \\
u^{(0)} &= cA, \\
w^{(0)} &= -(z+1)c\frac{\partial A}{\partial \theta}, \\
B_x^{(0)} &= -\mathrm{Ma}A, \\
B_z^{(0)} &= (z+1)\mathrm{Ma}\frac{\partial A}{\partial \theta}.
\end{aligned} \tag{5.21}$$

Expressions (5.21) are the solutions of the linear problem, when all small terms are neglected (small terms include the nonlinear *and* non-hydrostatic terms, so at leading order we are in the linear shallow water regime). Indeed, one can verify that they satisfy equation (5.12d) by substitution. Expressions (5.21) are not known explicitly, because we do not know the form of the function A. To find this, we need to perform a similar analysis at $\mathcal{O}(\epsilon)$.

Order ϵ analysis

Equating the coefficients of ϵ in (5.4), recalling that we are taking $\delta = \epsilon$, gives

$$\frac{\partial u^{(1)}}{\partial t} + \frac{\partial \tilde{p}^{(1)}}{\partial x} - \mathrm{Ma}\frac{\partial B_x^{(1)}}{\partial x} = -\frac{\partial u^{(0)}}{\partial \tau} - u^{(0)}\frac{\partial u^{(0)}}{\partial x} + B_x^{(0)}\frac{\partial B_x^{(0)}}{\partial x}, \tag{5.22a}$$

$$\frac{\partial \tilde{p}^{(1)}}{\partial z} = -\frac{\partial w^{(0)}}{\partial t} + \mathrm{Ma}\frac{\partial B_z^{(0)}}{\partial x}, \tag{5.22b}$$

$$\frac{\partial \mathbf{B}^{(1)}}{\partial t} - \mathrm{Ma}\frac{\partial \mathbf{u}^{(1)}}{\partial x} = -\frac{\partial \mathbf{B}^{(0)}}{\partial \tau} + B_x^{(0)}\frac{\partial \mathbf{u}^{(0)}}{\partial x} - u^{(0)}\frac{\partial \mathbf{B}^{(0)}}{\partial x}. \tag{5.22c}$$

Since it is known that the first order variables are independent of z, all appropriate z-derivatives have been omitted. Making use of the solutions of the leading order variables (5.21), equations (5.22) can be rewritten as

$$\frac{\partial u^{(1)}}{\partial t} + \frac{\partial \tilde{p}^{(1)}}{\partial x} - \mathrm{Ma}\frac{\partial B_x^{(1)}}{\partial x} = -\eta\frac{\partial A}{\partial \theta} - c\frac{\partial A}{\partial \tau}, \tag{5.23a}$$

$$\frac{\partial \tilde{p}^{(1)}}{\partial z} = -(z+1)\frac{\partial^2 A}{\partial \theta^2}, \tag{5.23b}$$

$$\frac{\partial B_x^{(1)}}{\partial t} - \mathrm{Ma}\frac{\partial u^{(1)}}{\partial x} = \mathrm{Ma}\frac{\partial A}{\partial \tau}, \tag{5.23c}$$

$$\frac{\partial B_z^{(1)}}{\partial t} - \mathrm{Ma}\frac{\partial w^{(1)}}{\partial x} = c\mathrm{Ma}(z+1)\frac{\partial^2 A}{\partial \theta^2}. \tag{5.23d}$$

Following the reasoning in the leading order case, we now make use of the pressure boundary condition, which is $\tilde{p}^{(1)} = \eta^{(1)}$ at $\mathcal{O}(\epsilon)$, from (5.6a). Together with equation (5.23b), we obtain

$$\tilde{p}^{(1)} = \eta^{(1)} - \left(\frac{1}{2}z^2 + z\right)\frac{\partial^2 A}{\partial \theta^2}. \tag{5.24}$$

The aim is to replace the instance of $\tilde{p}^{(1)}$ in (5.23a), by first differentiating (5.24) with respect to x. The resulting equation is then integrated over the layer depth, as before, removing all explicit instances of z. Then equation (5.23a) can be written as

$$\frac{\partial \bar{u}^{(1)}}{\partial t} + \frac{\partial \eta^{(1)}}{\partial x} - \mathrm{Ma}\frac{\partial \bar{B}_x^{(1)}}{\partial x} = -c\frac{\partial A}{\partial \tau} - \eta\frac{\partial A}{\partial \theta} - \frac{1}{3}\frac{\partial^3 A}{\partial \theta^3}, \tag{5.25}$$

where the overbar represents a depth-averaged quantity, so that

$$\bar{u}^{(1)} = \int_{-1}^{0} u^{(1)}\, dz. \tag{5.26}$$

Complementing (5.23) are the two order ϵ equations derived from (5.7-5.8), which are

$$\frac{\partial \eta^{(1)}}{\partial t} + \frac{\partial \eta^{(0)}}{\partial \tau} + u^{(0)}\frac{\partial \eta^{(0)}}{\partial x} = -\int_{-1}^{0} \frac{\partial u^{(1)}}{\partial x}\, dz - \eta^{(0)}\frac{\partial u^{(0)}}{\partial x}, \tag{5.27a}$$

$$\mathrm{Ma}\frac{\partial \eta^{(1)}}{\partial x} + B_x^{(0)}\frac{\partial \eta^{(0)}}{\partial x} = -\int_{-1}^{0} \frac{\partial B_x^{(1)}}{\partial x}\, dz - \eta^{(0)}\frac{\partial B_x^{(0)}}{\partial x}. \tag{5.27b}$$

Equation (5.27a) gives

$$\frac{\partial \eta^{(1)}}{\partial t}+\frac{\partial \bar{u}^{(1)}}{\partial x}=-\frac{\partial A}{\partial \tau}-2c\eta\frac{\partial A}{\partial \theta}. \tag{5.28}$$

Equations (5.25) and (5.28), along with the depth averaged (5.23c), can be written in matrix form as

$$\frac{\partial \bar{\mathbf{a}}^{(1)}}{\partial t}+M\frac{\partial \bar{\mathbf{a}}^{(1)}}{\partial x}=\mathbf{r}, \tag{5.29}$$

where the matrix M is given as in (5.15), and $\mathbf{r}$ is given by

$$\mathbf{r}=\begin{pmatrix} -c\frac{\partial A}{\partial \tau}-A\frac{\partial A}{\partial \theta}-\frac{1}{3}\frac{\partial^3 A}{\partial \theta^3} \\ -\frac{\partial A}{\partial \tau}-2cA\frac{\partial A}{\partial \theta} \\ \mathrm{Ma}\frac{\partial A}{\partial \tau} \end{pmatrix}. \tag{5.30}$$

The vector $\bar{\mathbf{a}}^{(1)}$ is given by (5.14), but with horizontal velocity and magnetic field depth-averaged over the layer.

We now seek solutions of (5.29) that are functions not only of $\theta = x - ct$, but also of $\xi = x + ct$. The moving coordinate ξ represents a frame of reference moving to the left with speed c. The leading order solution is the sum of an arbitrary function of θ (multiplied by an eigenvector) and an arbitrary function of ξ (multiplied by an eigenvector). We choose one of these, to consider unidirectional waves.

Considering the order ϵ variables now as functions of θ, ξ and τ, the equivalences $\partial_t \to -c\partial_\theta + c\partial_\xi$ and $\partial_x \to \partial_\theta + \partial_\xi$ can be implemented. Equation (5.29) can then be written as

$$(M-cI)\frac{\partial \bar{\mathbf{a}}^{(1)}}{\partial \theta}+(M+cI)\frac{\partial \bar{\mathbf{a}}^{(1)}}{\partial \xi}=\mathbf{r}. \tag{5.31}$$

Now, taking the transpose of equation (5.18) gives the left eigenvector $(\partial \mathbf{a}^{(0)}/\partial\theta)^T(M-cI)=0$, since the matrix $(M-cI)$ is its own transpose. Inspired by this, we left multiply (5.31) by the vector $(\partial \mathbf{a}^{(0)}/\partial\theta)^T$, obtaining

$$\left(\frac{\partial \mathbf{a}^{(0)}}{\partial \theta}\right)^T(M+cI)\frac{\partial \bar{\mathbf{a}}^{(1)}}{\partial \xi}=\left(\frac{\partial \mathbf{a}^{(0)}}{\partial \theta}\right)^T\mathbf{r}. \tag{5.32}$$

The right hand side of this equation is a function of θ and τ, but not ξ. This is significant because, upon integration to find the solutions of $\mathbf{a}^{(1)}$, there would be a multiple of ξ in the result. Thus, if we let $\xi \to \infty$, by letting either time or the spatial coordinate get very large, the solutions of $\mathbf{a}^{(1)}$ would be unbounded. We therefore deduce a boundedness condition for the system:

$$\left(\frac{\partial \mathbf{a}^{(0)}}{\partial \theta}\right)\cdot\mathbf{r}=0. \tag{5.33}$$

Using equations (5.20) and (5.33) we thus obtain the equation:

$$c\frac{\partial A}{\partial \tau}+\frac{3}{2}A\frac{\partial A}{\partial \theta}+\frac{1}{6}\frac{\partial^3 A}{\partial \theta^3}=0. \tag{5.34}$$

This is the well-known Korteweg-de Vries (KdV) equation, the solution of which describes the shape of the free surface; such solutions include sech^2 profiles and cnoidal waves. [Note that the coefficient of $\frac{\partial A}{\partial \tau}$, c, can be absorbed into a rescaling of τ.] Importantly, the introduction of magnetic field has not introduced any new dynamics in the system; only the time over which the dynamics take place is affected. No new surface profiles are brought about by the inclusion of field, and so we conclude that an electrically conducting layer of fluid would support the same long-time surface profile as the hydrodynamic one, albeit over a slightly altered timescale.

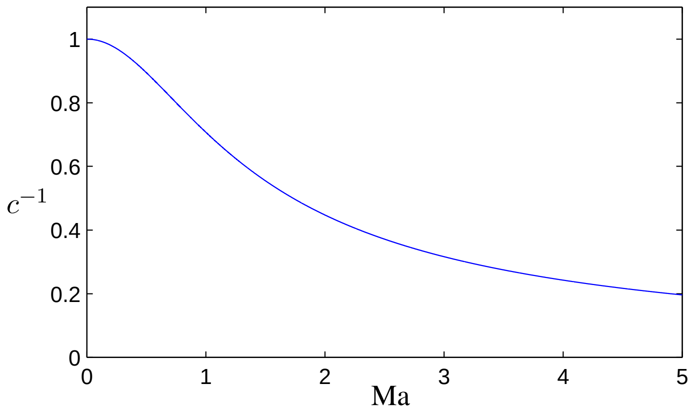

Figure 5.1 – A plot of the coefficient $c^{-1}=(\text{Ma}^2+1)^{-1/2}$ against magnetic field strength, Ma.

This altered timescale is $c^{-1}\tau$; the coefficient c^{-1} is plotted in figure 5.1, against magnetic field strength. One can verify that , when Ma $\ll 1$, then $c^{-1}=(1+\text{Ma}^2)^{-1/2}\approx 1-\text{Ma}^2/2$. Indeed, inspection of figure 5.1 reveals that the departure of the curve from the vertical axis (hydrodynamic regime) is approximately horizontal, so that for small field strengths the change in the long-timescale is small.

When the magnetic field strength is very high, $c\to \text{Ma}$, and so the coefficient c^{-1} tends to zero. This indicates that the stronger the magnetic field, the longer the timescale of solitons or cnoidal waves. We will not solve equation (5.34) for the function A, since the solutions of the KdV equation are well-known (see, for example, Korteweg and de Vries, 1895; Acheson, 1990).

As well as supporting single solitons, the KdV equation also allows two solitons to pass through each other without change of shape, with a slight shift in phase. Other non-steady solutions include Stokes waves, which are periodically varying wavetrains (see, for example, Whitham, 1974).

$$
\begin{array}{ll}
\tilde{p}_j \sim \rho_j g \hat{\eta}_1 & t \sim \frac{L}{\sqrt{GH}} \\
u_j \sim B_{x_j} \sim \sqrt{\frac{g}{H}}\hat{\eta}_1 & w_j \sim B_{z_j} \sim \frac{\sqrt{gH}}{L}\hat{\eta}_1
\end{array}
$$

Table 5.2 – Scalings for the 2-layer rigid lid model.

Concluding, small perturbations in a shallow layer of fluid, in which weak dispersion from a non-hydrostatic term balances nonlinear steepening, can exist in the form of solitons or cnoidal waves. The introduction of magnetic field to this model amounts to a rescaling of the time scale on which long-term dynamics take place. The aim of the next section is to find out if the magnetic field structure in the two-layer rigid lid model has more of an effect on the types of waves supported.

5.3 KdV for 2-layer SWMHD

One can extend the analysis of weakly nonlinear waves by considering the 2-layer rigid lid model. The method we shall follow will be similar to the derivation above of the single layer KdV equation, in which we found that changes in magnetic field do not introduce new dynamics or different types of solutions. Our aim is again to derive a long-time evolution equation using a solvability condition; we will be particularly interested to see whether a more complicated magnetic field structure will affect more than just the time scaling. In this section, the derivations will be slightly briefer than those in section 5.1 due to similarities in structure.

Of course, as well as the equations and boundary conditions imposed on the flow in the previous sections, we also require interface conditions, as outlined in Chapter 3. Ensuring continuity of pressure over the interface η_1, the governing equations are the same in each layer, and are given by equations (5.1). Nondimensionalising according to table 5.2, gives equations (5.4) for each layer.

Boundary conditions

The rigid lid exerts a pressure P on the fluid immediately below it, in response to the fluid movements in the upper layer. The total (dimensional) pressure in layer 1, π_1, must also be P at the lid. We must also ensure the continuity of (total dimensional) pressure over the interface. Making use of (5.3), this can be written as $\tilde{p}_2 = \tilde{p}_1 + (\rho_2 - \rho_1)gz$ at $z = -H_1 + \eta_1$, in dimensional form. Replacing z and taking the x derivative gives

$$\frac{\partial \tilde{p}_2}{\partial x} = \frac{\partial \tilde{p}_1}{\partial x} + \frac{\partial \eta_1}{\partial x}\left((\rho_2 - \rho_1)g + \frac{\partial \tilde{p}_1}{\partial z} - \frac{\partial \tilde{p}_2}{\partial z}\right) \qquad \text{at} \qquad z = -H_1 + \eta_1, \tag{5.35}$$

taking care to differentiate the x dependence hidden in the z dependence. Nondimensionalising this with $\tilde{p}_j \sim \rho_j g \hat{\eta}_1$ (as in table 5.2), we have

$$\tilde{p}_1 = P \text{ at } z = 0, \qquad \frac{\partial \tilde{p}_2}{\partial x} = (1-\alpha)\frac{\partial \tilde{p}_1}{\partial x} + \frac{\partial \eta_1}{\partial x}\left(\alpha + (1-\alpha)\epsilon\frac{\partial \tilde{p}_1}{\partial z} - \epsilon\frac{\partial \tilde{p}_2}{\partial z}\right) \text{ at } z = -\beta_1 + \epsilon\eta_1, \tag{5.36}$$

where $\alpha = 1 - \rho_1/\rho_2$ and $\epsilon = \hat{\eta}_1/H$.

In addition to continuity of pressure over the interface, we also have boundary conditions on velocity at the floor and rigid lid. Imposing that the floor and lid are impermeable, the condition on the vertical component of velocity is

$$w_1 = 0 \text{ at } z = 0, \qquad \text{and} \qquad w_2 = 0 \text{ at } z = -1. \tag{5.37}$$

As in Chapter 3, vertical velocity should equal the material derivative of the interface displacement, immediately above and below the interface; hence $w_j = \partial\eta_1/\partial t + \mathbf{u}\cdot\nabla\eta_1$ at $z = \eta_1$. Equating this with the expressions for w_j found by integrating (5.2a), applying the boundary conditions (5.37) and nondimensionalising according to table 5.2, these become

$$\frac{\partial \eta_1}{\partial t} + \epsilon\frac{\partial \eta_1}{\partial \tau} + \epsilon u_1\frac{\partial \eta_1}{\partial x} = \int_{-\beta_1}^{0} \frac{\partial u_1}{\partial x}\,dz - \int_{-\beta_1}^{-\beta_1+\epsilon\eta_1} \frac{\partial u_1}{\partial x}\,dz, \tag{5.38a}$$

$$\frac{\partial \eta_1}{\partial t} + \epsilon\frac{\partial \eta_1}{\partial \tau} + \epsilon u_2\frac{\partial \eta_1}{\partial x} = -\int_{-1}^{-\beta_1} \frac{\partial u_2}{\partial x}\,dz - \int_{-\beta_1}^{-\beta_1+\epsilon\eta_1} \frac{\partial u_2}{\partial x}\,dz, \tag{5.38b}$$

where $\beta_j = H_j/H$.

On the floor, the lid, and at the interface, the normal component of magnetic field vanishes, i.e.

$$B_{z_1} = 0 \quad \text{at} \quad z = 0, \qquad\qquad B_{z_2} = 0 \quad \text{at} \quad z = -1, \tag{5.39a}$$

$$B_{z_1} - B_{x_1}\frac{\partial \eta_1}{\partial x} = B_{z_2} - B_{x_2}\frac{\partial \eta_1}{\partial x} = 0 \quad \text{at} \quad z = -\beta_1 + \epsilon\eta_1. \tag{5.39b}$$

In a similar manner to the derivation of (5.38), the divergence–free constraint on magnetic field can be integrated and the boundary conditions in (5.39) implemented, to obtain

$$(\mathrm{Ma}_1 + \epsilon B_{x_1})\frac{\partial \eta_1}{\partial x} = \int_{-\beta_1}^{0} \frac{\partial B_{x_1}}{\partial x}\,dz - \int_{-\beta_1}^{-\beta_1+\epsilon\eta_1} \frac{\partial B_{x_1}}{\partial x}\,dz, \tag{5.40a}$$

$$(\mathrm{Ma}_2 + \epsilon B_{x_2})\frac{\partial \eta_1}{\partial x} = -\int_{-1}^{-\beta_1} \frac{\partial B_{x_2}}{\partial x}\,dz - \int_{-\beta_1}^{-\beta_1+\epsilon\eta_1} \frac{\partial B_{x_2}}{\partial x}\,dz. \tag{5.40b}$$

5.3.1 Leading order analysis

At leading order in ϵ, we have magnetohydrostatic balance in the vertical for both layers, as in the single layer case; i.e. $\partial\tilde{p}_j^{(0)}/\partial z = 0$ for $j = 1, 2$. Integrating and applying the boundary condition $\tilde{p}_1 = P$ at $z = 0$ gives $\tilde{p}_1^{(0)} = P^{(0)}(x, t)$ throughout layer 1. Applying the interface condition in (5.36) gives the horizontal components of the momentum equations to leading order,

$$\frac{\partial u_1^{(0)}}{\partial t} + \frac{\partial P^{(0)}}{\partial x} - \mathrm{Ma}_1\frac{\partial B_{x_1}^{(0)}}{\partial x} = 0, \tag{5.41a}$$

$$\frac{\partial u_2^{(0)}}{\partial t} + (1-\alpha)\frac{\partial P^{(0)}}{\partial x} + \alpha\frac{\partial \eta_1^{(0)}}{\partial x} - \mathrm{Ma}_2\frac{\partial B_{x_2}^{(0)}}{\partial x} = 0. \tag{5.41b}$$

The components of the induction equations for each layer are

$$\frac{\partial B_{x_j}^{(0)}}{\partial t} - \mathrm{Ma}_j\frac{\partial u_j^{(0)}}{\partial x} = 0, \tag{5.42a}$$

$$\frac{\partial {B_z}_j^{(0)}}{\partial t} - \mathrm{Ma}_j\frac{\partial w_j^{(0)}}{\partial x} = 0, \tag{5.42b}$$

for $j = 1, 2$. The integrated solenoidal conditions on velocity (5.38) and magnetic field (5.40) are, to leading order,

$$\frac{\partial \eta_1^{(0)}}{\partial t} - \beta_1\frac{\partial u_1^{(0)}}{\partial x} = 0, \qquad \frac{\partial \eta_1^{(0)}}{\partial t} + \beta_2\frac{\partial u_2^{(0)}}{\partial x} = 0, \tag{5.43a}$$

$$\mathrm{Ma}_1\frac{\partial \eta_1^{(0)}}{\partial x} - \beta_1\frac{\partial B_{x_1}^{(0)}}{\partial x} = 0, \qquad \mathrm{Ma}_2\frac{\partial \eta_1^{(0)}}{\partial x} + \beta_2\frac{\partial B_{x_2}^{(0)}}{\partial x} = 0, \tag{5.43b}$$

since the leading order terms are taken to be independent of z as before. The difference of equations (5.43a) can be physically interpreted as zero horizontal mass flux, as expected in the rigid lid case.

Equations (5.41)-(5.43) form a system of ten equations with ten unknowns ($u_1^{(0)}$, $u_2^{(0)}$, $w_1^{(0)}$, $w_2^{(0)}$, $P^{(0)}$, $\eta_1^{(0)}$, $B_{x_1}^{(0)}$, $B_{x_2}^{(0)}$, ${B_z}_1^{(0)}$, and ${B_z}_2^{(0)}$). In principle, one could write the equations in matrix form in order to solve, but we shall adopt the method used in the single layer case, for simplicity. We will solve a select few of the equations (the time-evolution ones) for a corresponding number of the unknowns, find the remaining unknowns using the solenoidal conditions of flow and field, and later verify that the remaining unused equations are satisfied. We shall solve equations (5.41), (5.42a), and (5.43a).

Seeking travelling solutions of these six equations of the form $f(\theta)$, where $\theta = x - ct$, these six equations can be written in matrix form as

$$M^{-}\frac{\partial \mathbf{a}^{(0)}}{\partial \theta} = 0, \tag{5.44}$$

where

$$M^{\pm} = \begin{pmatrix} \pm c & 0 & -\mathrm{Ma}_1 & 0 & 0 & 1 \\ 0 & \pm c & 0 & -\mathrm{Ma}_2 & \alpha & 1-\alpha \\ -\mathrm{Ma}_1 & 0 & \pm c & 0 & 0 & 0 \\ 0 & -\mathrm{Ma}_2 & 0 & \pm c & 0 & 0 \\ -\beta_1 & 0 & 0 & 0 & \pm c & 0 \\ 0 & \beta_2 & 0 & 0 & \pm c & 0 \end{pmatrix}, \tag{5.45}$$

and the vector $\mathbf{a}^{(0)}$ is defined by

$$\mathbf{a}^{(j)} = \left(u_1^{(j)},\, u_2^{(j)},\, B_{x_1}^{(j)},\, B_{x_2}^{(j)},\, \eta_1^{(j)},\, P^{(j)}\right)^T. \tag{5.46}$$

By ensuring that the matrix M^- is singular, one can verify the dispersion relation

$$\beta_1\zeta_2^2 + (1-\alpha)\beta_2\zeta_1^2 - \alpha\beta_1\beta_2 = 0, \tag{5.47}$$

where

$$\zeta_j^2 = c^2 - \mathrm{Ma}_j^2. \tag{5.48}$$

Equation (5.47) is equivalent to (4.40) found in section 4.4. Furthermore, a right eigenvector of M^- is

$$(-\beta_2 c,\, \beta_1 c,\, \beta_2\mathrm{Ma}_1,\, -\beta_1\mathrm{Ma}_2,\, \beta_1\beta_2,\, -\beta_2\zeta_1^2)^T, \tag{5.49}$$

which gives us expressions for the first order variables. If we prescribe an as yet unknown function to the interface displacement, say $\eta_1^{(0)} = \beta_1\beta_2 h(\theta,\tau)$, then we have

$$\begin{aligned} u_1^{(0)} &= -\beta_2 c h, \\ u_2^{(0)} &= \beta_1 c h, \\ B_{x_1}^{(0)} &= \beta_2\mathrm{Ma}_1 h, \\ B_{x_2}^{(0)} &= -\beta_1\mathrm{Ma}_2 h, \\ \eta_1^{(0)} &= \beta_1\beta_2 h, \\ P^{(0)} &= -\beta_2\zeta_1^2 h, \end{aligned}$$

and

$$\begin{aligned} w_1^{(0)} &= \beta_2 c \frac{\partial h}{\partial \theta} z, \\ w_2^{(0)} &= -\beta_1 c \frac{\partial h}{\partial \theta}(z+1), \\ B_{z_1}^{(0)} &= -\beta_2 \mathrm{Ma}_1 \frac{\partial h}{\partial \theta} z, \\ B_{z_2}^{(0)} &= \beta_1 \mathrm{Ma}_2 \frac{\partial h}{\partial \theta}(z+1). \end{aligned} \tag{5.50}$$

The expressions for vertical flow and field have been calculated using equations (5.2), and the boundary conditions (5.39). As before, the equations not used in this derivation, (5.42b) and (5.43b), are satisfied by the non-trivial solutions given in (5.50), as can be easily verified.

Before proceeding to the next order, one can note that $\mathbf{b}^T M^- = 0$, where

$$\mathbf{b}^T = \big((1-\alpha)\beta_1\beta_2 c,\ -\beta_1\beta_2 c,\ -(1-\alpha)\beta_1\beta_2\mathrm{Ma}_1,\ \beta_1\beta_2\mathrm{Ma}_2,\ -(1-\alpha)\beta_2\zeta_1^2,\ -\beta_1\zeta_2^2\big). \tag{5.51}$$

This has been derived using (5.45) and the dispersion relation (5.47).

5.3.2 Order ϵ analysis

The governing equations to order ϵ are given by equations (5.22) for each layer, together with

$$\frac{\partial \eta_1^{(1)}}{\partial t} - \beta_1 \frac{\partial \bar{u}_1^{(1)}}{\partial x} = -\frac{\partial \eta_1^{(0)}}{\partial \tau} - \eta_1^{(0)} \frac{\partial u_1^{(0)}}{\partial x} - u_1^{(0)} \frac{\partial \eta_1^{(0)}}{\partial x}, \tag{5.52a}$$

$$\frac{\partial \eta_1^{(1)}}{\partial t} + \beta_2 \frac{\partial \bar{u}_2^{(1)}}{\partial x} = -\frac{\partial \eta_1^{(0)}}{\partial \tau} - \eta_1^{(0)} \frac{\partial u_2^{(0)}}{\partial x} - u_2^{(0)} \frac{\partial \eta_1^{(0)}}{\partial x}, \tag{5.52b}$$

from equation (5.38). Again, the overbar denotes a depth average over the appropriate layer, so that, for example,

$$\bar{u}_1^{(1)} = \frac{1}{\beta_1} \int_{-\beta_1}^{0} u_1^{(1)}\, dz. \tag{5.53}$$

We also have

$$\mathrm{Ma}_1 \frac{\partial \eta_1^{(1)}}{\partial x} - \beta_1 \frac{\partial \bar{B}_{x_1}^{(1)}}{\partial x} = -B_{x_1}^{(0)} \frac{\partial \eta_1^{(0)}}{\partial x} - \eta_1^{(0)} \frac{\partial B_{x_1}^{(0)}}{\partial x}, \tag{5.54a}$$

$$\mathrm{Ma}_2 \frac{\partial \eta_1^{(1)}}{\partial x} + \beta_2 \frac{\partial \bar{B}_{x_2}^{(1)}}{\partial x} = -B_{x_2}^{(0)} \frac{\partial \eta_1^{(0)}}{\partial x} - \eta_1^{(0)} \frac{\partial B_{x_2}^{(0)}}{\partial x}, \tag{5.54b}$$

from equations (5.40). Making use of the expressions for the first order variables (5.50), the z-component of the momentum equation (5.22b) gives

$$\tilde{p}_1^{(1)} = \frac{1}{2}\beta_2 \zeta_1^2 \frac{\partial^2 h}{\partial \theta^2} z^2 + P^{(1)}, \tag{5.55}$$

for the modified pressure in the upper layer, since $\tilde{p}^{(1)} = P^{(1)}$ at $z = 0$. Applying the same procedure for the lower layer, and then differentiating with respect to x, we have

$$\frac{\partial \tilde{p}_1^{(1)}}{\partial x} = \frac{1}{2}\beta_2\zeta_1^2\frac{\partial^3 h}{\partial\theta^3}z^2 + \frac{\partial P^{(1)}}{\partial x}, \tag{5.56}$$

$$\frac{\partial \tilde{p}_2^{(1)}}{\partial x} = -\frac{1}{2}\beta_1\zeta_2^2\frac{\partial^3 h}{\partial\theta^3}(z+1)^2 + \frac{\partial f}{\partial x}, \tag{5.57}$$

where $f = f(x,t)$ is to be determined from the continuity of pressure condition over the interface. Making use of equation (5.36), noting that the $\tilde{p}_j^{(0)}$ are independent of z, gives

$$\frac{\partial \tilde{p}_2^{(1)}}{\partial x} = (1-\alpha)\frac{\partial \tilde{p}_1^{(1)}}{\partial x} + \alpha\frac{\partial \eta_1^{(1)}}{\partial x} \text{ at } z = -\beta_1. \tag{5.58}$$

Equation (5.58) allows us to determine the function f, and (5.57) becomes

$$\frac{\partial \tilde{p}_2^{(1)}}{\partial x} = \frac{1}{2}\beta_1\left((\beta_2^2 - (z+1)^2)\zeta_2^2 + (1-\alpha)\beta_1\beta_2\zeta_1^2\right)\frac{\partial^3 h}{\partial\theta^3} + (1-\alpha)\frac{\partial P^{(1)}}{\partial x} + \alpha\frac{\partial \eta^{(1)}}{\partial x}. \tag{5.59}$$

Replacing the $\tilde{p}_j^{(1)}$ in the horizontal momentum equations at order ϵ gives

$$\frac{\partial \bar{u}_1^{(1)}}{\partial t} + \frac{\partial P^{(1)}}{\partial x} - \mathrm{Ma}_1\frac{\partial \bar{B}_{x_1}^{(1)}}{\partial x} = -\frac{1}{6}\beta_1^2\beta_2\zeta_1^2\frac{\partial^3 h}{\partial\theta^3} - \frac{\partial u_1^{(0)}}{\partial\tau} - u_1^{(0)}\frac{\partial u_1^{(0)}}{\partial x} + B_{x_1}^{(0)}\frac{\partial B_{x_1}^{(0)}}{\partial x}, \tag{5.60a}$$

$$\begin{aligned}\frac{\partial \bar{u}_2^{(1)}}{\partial t} + (1-\alpha)\frac{\partial P^{(1)}}{\partial x} + \alpha\frac{\partial \eta^{(1)}}{\partial x} - \mathrm{Ma}_2\frac{\partial \bar{B}_{x_2}^{(1)}}{\partial x} = \\ -\frac{1}{6}\beta_1\beta_2(2\beta_2\zeta_2^2 + 3(1-\alpha)\beta_1\zeta_1^2)\frac{\partial^3 h}{\partial\theta^3} - \frac{\partial u_2^{(0)}}{\partial\tau} - u_2^{(0)}\frac{\partial u_2^{(0)}}{\partial x} + B_{x_2}^{(0)}\frac{\partial B_{x_2}^{(0)}}{\partial x}.\end{aligned} \tag{5.60b}$$

Each equation has been depth-averaged over the layer it governs according to (5.53). Making use of the expressions for the first order variables (5.50), one can write equations (5.60), (5.22c) and (5.52) in matrix form as

$$M^-\frac{\partial \bar{\mathbf{a}}_1^{(1)}}{\partial\theta} + M^+\frac{\partial \bar{\mathbf{a}}_1^{(1)}}{\partial\xi} = \mathbf{r}, \tag{5.61}$$

after seeking solutions that are functions of $\theta = x - ct$ and $\xi = x + ct$. The vector $\mathbf{r}$ is given by

$$\mathbf{r} = \begin{pmatrix} -\frac{1}{6}\beta_1^2\beta_2\zeta_1^2\frac{\partial^3 h}{\partial\theta^3} + \beta_2 c\frac{\partial h}{\partial\tau} - \beta_2^2\zeta_1^2 h\frac{\partial h}{\partial\theta} \\ -\frac{1}{6}\beta_1\beta_2\left(2\beta_2\zeta_2^2 + 3(1-\alpha)\beta_1\zeta_1^2\right)\frac{\partial^3 h}{\partial\theta^3} - \beta_1 c\frac{\partial h}{\partial\tau} - \beta_1^2\zeta_2^2 h\frac{\partial h}{\partial\theta} \\ -\beta_2\mathrm{Ma}_1\frac{\partial h}{\partial\tau} \\ \beta_1\mathrm{Ma}_2\frac{\partial h}{\partial\tau} \\ -\beta_1\beta_2\frac{\partial h}{\partial\tau} + 2\beta_1\beta_2^2 ch\frac{\partial h}{\partial\theta} \\ -\beta_1\beta_2\frac{\partial h}{\partial\tau} - 2\beta_1^2\beta_2 ch\frac{\partial h}{\partial\theta} \end{pmatrix}. \tag{5.62}$$

Left–multiplying by the vector $\mathbf{b}^T$ given in (5.51) yields the boundedness condition $\mathbf{b} \cdot \mathbf{r} = 0$, which gives

$$2c(1-\alpha\beta_2)\frac{\partial h}{\partial \tau}+3(\beta_1^2\zeta_2^2-(1-\alpha)\beta_2^2\zeta_1^2)h\frac{\partial h}{\partial \theta}+\frac{1}{3}\beta_1\beta_2\left(\beta_2\zeta_2^2+(1-\alpha)\beta_1\zeta_1^2\right)\frac{\partial^3 h}{\partial \theta^3}=0. \quad (5.63)$$

However, we wish to find a KdV equation that the surface profile satisfies, as in section 5.2. To do this, we put $\eta_1^{(0)} = A_1(\tau, \theta)$, so that $h = A_1/(\beta_1\beta_2)$. Then the KdV equation for the 2-layer rigid lid model is given by

$$2c\beta_1\beta_2(1-\alpha\beta_2)\frac{\partial h}{\partial \tau}+3(\beta_1^2\zeta_2^2-(1-\alpha)\beta_2^2\zeta_1^2)h\frac{\partial h}{\partial \theta}+\frac{1}{3}\beta_1^2\beta_2^2\left(\beta_2\zeta_2^2+(1-\alpha)\beta_1\zeta_1^2\right)\frac{\partial^3 h}{\partial \theta^3}=0. \quad (5.64)$$

When $\alpha = 1$, so that the upper layer has zero density, the dispersion relation (5.47) gives $\zeta_2^2 = \beta_2$, and equation (5.64) reduces to

$$c\frac{\partial h}{\partial \tau}+\frac{3}{2}h\frac{\partial h}{\partial \theta}+\frac{1}{6}\beta_2^3\frac{\partial^3 h}{\partial \theta^3}=0. \quad (5.65)$$

In the limit $\beta_2 \to 1$, so that the lower layer has a depth of H, this reduces further to the single layer KdV equation given by (5.34).

5.3.3 Analysis of the 2-layer rigid lid KdV equation

The magnetic field strengths can be chosen so that the coefficients of hh_θ and $h_{\theta\theta\theta}$ can take any combination of signs. If both these coefficients are positive, one has soliton solutions (Korteweg and de Vries 1895) for decaying boundary conditions at infinity and cnoidal wave solutions otherwise; if they are both negative, the waves will travel in the opposite direction. If they differ in sign, these solitons become ‘dark’, being localised regions of depression rather than elevation. Dark solitons have the same sech^2 profile as ‘bright’ solitons, but are upside-down (Drazin and Johnson, 1989). The ordering of the signs will determine the direction of propagation. Table 5.3 displays these possibilities.

We shall take the positive square root for the phase speed c in the coefficients of the three terms in equation (5.64) without loss of generality, since taking the opposite sign amounts to changing the sign of c, which describes a wave propagating to the left rather than the right. By similar reasoning, to explore all the possible combinations of signs of these coefficients it suffices to consider only the latter two coefficients in (5.64).

From the dispersion relation (5.47), one has

$$(1-\alpha\beta_2)\zeta_1^2 = \alpha\beta_1\beta_2 - \beta_1 V, \tag{5.66}$$

$$(1-\alpha\beta_2)\zeta_2^2 = \alpha\beta_1\beta_2 + (1-\alpha)\beta_2 V, \tag{5.67}$$

where $V = \mathrm{Ma}_1^2 - \mathrm{Ma}_2^2$ can take any real value. We can use these to determine when the coefficients of the terms in the KdV equation (5.64) pass through zero. The coefficient of $A_1\partial_\theta A_1$ is zero when

$$(1-\alpha)V = \alpha((1-\alpha)\beta_2^2 - \beta_1^2), \tag{5.68}$$

and the coefficient of $\partial_{\theta\theta\theta}A_1$ is zero when

$$(1-\alpha)(\beta_2-\beta_1)V = -\alpha\beta_1\beta_2(1-\alpha\beta_1). \tag{5.69}$$

Upon first inspection, one can note that if the fluid is equally divided into two sublayers, that is if $\beta_1 = \beta_2 = 1/2$, then no configuration of magnetic fields will make the coefficient of $h_{\theta\theta\theta}$ negative; in fact, in this case the coefficient takes the positive but very small ($\ll 1$) value $\alpha c/48$.

We have to be careful, however, since small values of these coefficients could violate the asymptotic expansions used in the derivation, if $\alpha c/48$ is $\mathcal{O}(\epsilon)$. One would need to choose a smaller value of ϵ to avoid this. Calculating the axis interceptions as above is useful in determining the existence of the sign changes with changing field strength, but not for calculating the exact magnetic field geometry required for these changes.

Soliton solutions

The KdV equation (5.64) is in the form

$$\mu\frac{\partial A_1}{\partial\tau} + \nu A_1\frac{\partial A_1}{\partial\theta} + \upsilon\frac{\partial^3 A_1}{\partial\theta^3} = 0, \tag{5.70}$$

and has a well-known soliton solution that is satisfied by ensuring that the surface and its spatial derivatives are zero at infinity (see, for example, Acheson 1990). This is found by seeking a travelling solution, i.e., a function of $\Xi = \theta - \chi\tau$, where χ is the speed of the travelling form. Then derivatives with respect to τ can be written in terms of Ξ. The analytic solution of the KdV is well understood (see Vallis, 2006, for example); here we shall give a brief explanation. After integrating once and putting the constant of integration equal to zero, according to the conditions

	$\upsilon > 0$	$\upsilon < 0$
$\nu > 0$	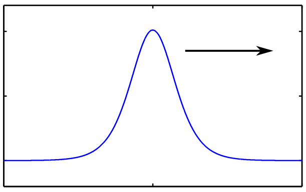	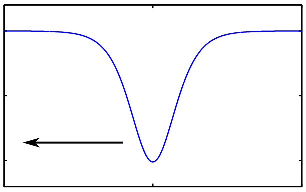
$\nu < 0$	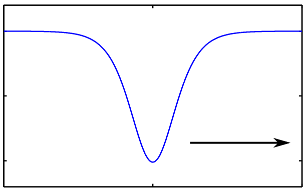	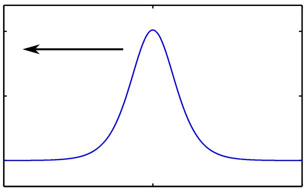

Table 5.3 – Types of solitons supported by the 2-layer rigid lid system.

at infinity, one multiplies the equation by h_Ξ and integrates again. Putting the integration constant to zero once more gives

$$\upsilon\left(\frac{dA_1}{d\Xi}\right)^2 = \mu\chi A_1^2 - \frac{1}{3}\nu A_1^3. \tag{5.71}$$

This can be solved by separating variables, giving

$$A_1 = \frac{\mu\chi}{\nu}\,\mathrm{sech}^2\left(\sqrt{\frac{\mu\chi}{4\upsilon}}\,\Xi\right). \tag{5.72}$$

Note that υ and χ have to have the same sign for real solutions, so that the sign of υ determines the direction of propagation. This only applies when the coefficient υ is positive; were it negative, then (5.71) does not support real solutions, unless χ is negative, so that the wave is moving to the left rather than to the right. then we can multiply through by -1 and proceed as above. This is equivalent to taking negative ν, which makes the right hand side of (5.72) negative. Thus, if the magnetic fields were structured so that $\upsilon < 0$, we would have a ‘dark’ soliton of depression moving to the left, as opposed to a ‘bright’ soliton of elevation moving to the right in the $\upsilon > 0$ regime.

The speed of the soliton is related to its amplitude by $\chi = \nu/\mu\times$amplitude. Its width also depends on the amplitude, since the coefficient of Ξ in the brackets in equation 5.72 can be rewritten in terms of the amplitude. Of course, the solitary wave can be viewed as being infinitely wide, since the surface is never flat.

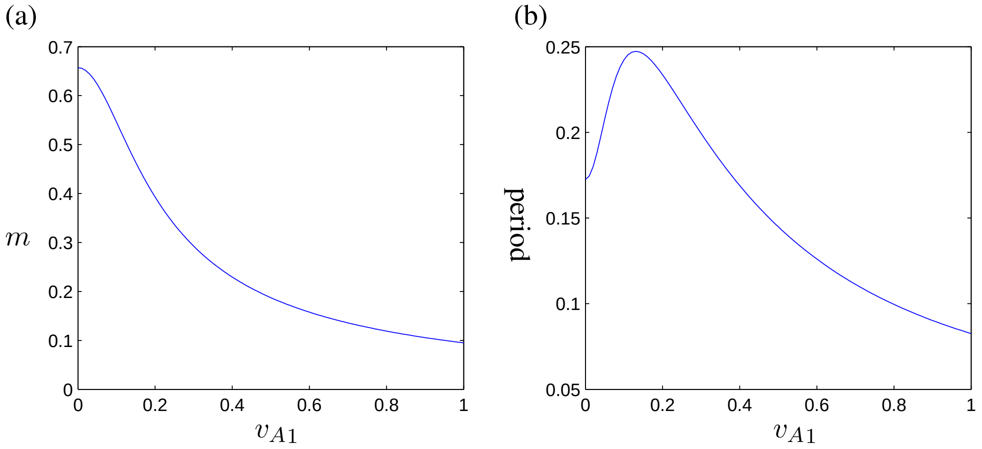

Figure 5.2 – Plots of the cnoidal parameter m (left) and period (right), for increasing magnetic field strength. In this figure, $\beta_1 = \beta_2 = 1/2$, and $\alpha = 0.1$. The magnetic field is configured so that $v_{A2} = 0.3 v_{A1}$.

If both ν and υ are negative, then a bright soliton moving to the left is supported, since changing the sign of χ gives equation (5.71), and so on. Various possibilities are displayed in table 5.3.

Cnoidal solutions

If we do not impose that the interface and its derivatives vanish at infinity, then cnoidal waves satisfy equation (5.64). Following the same method as for soliton solutions, (5.64) yields

$$\left(\frac{dA_1}{d\Xi}\right)^2 = -\frac{\nu}{3\upsilon}A_1^3 + \frac{\chi\mu}{\upsilon}A_1^2 + a_1 A_1 + a_2, \tag{5.73}$$

where a_1 and a_2 are constants of integration. Equations of this form are satisfied by the Jacobi elliptic function sn; a full derivation of such solutions is contained in section 5.4 (see Whitham, 1974, for further reading).

Some solutions have been plotted in figure 5.3, with differing magnetic field strengths. For the plots, the constants of integration take the values $a_1 = 10^2$ and $a_2 = 10^4$. Plots of the cnoidal parameter m (defined in equation (5.103)) and period (see equation (5.108)) are displayed in figure 5.2.

For low magnetic field strengths, the cnoidal form of the fluid-fluid interface has a relatively large m value, so that it has sharp troughs and wider peaks. As the field strength is increased, the period of these waves increases until a maximum is reached, and then starts decreasing. At the same time, the value of m decreases, so that the waves become more sinusoidal in nature.

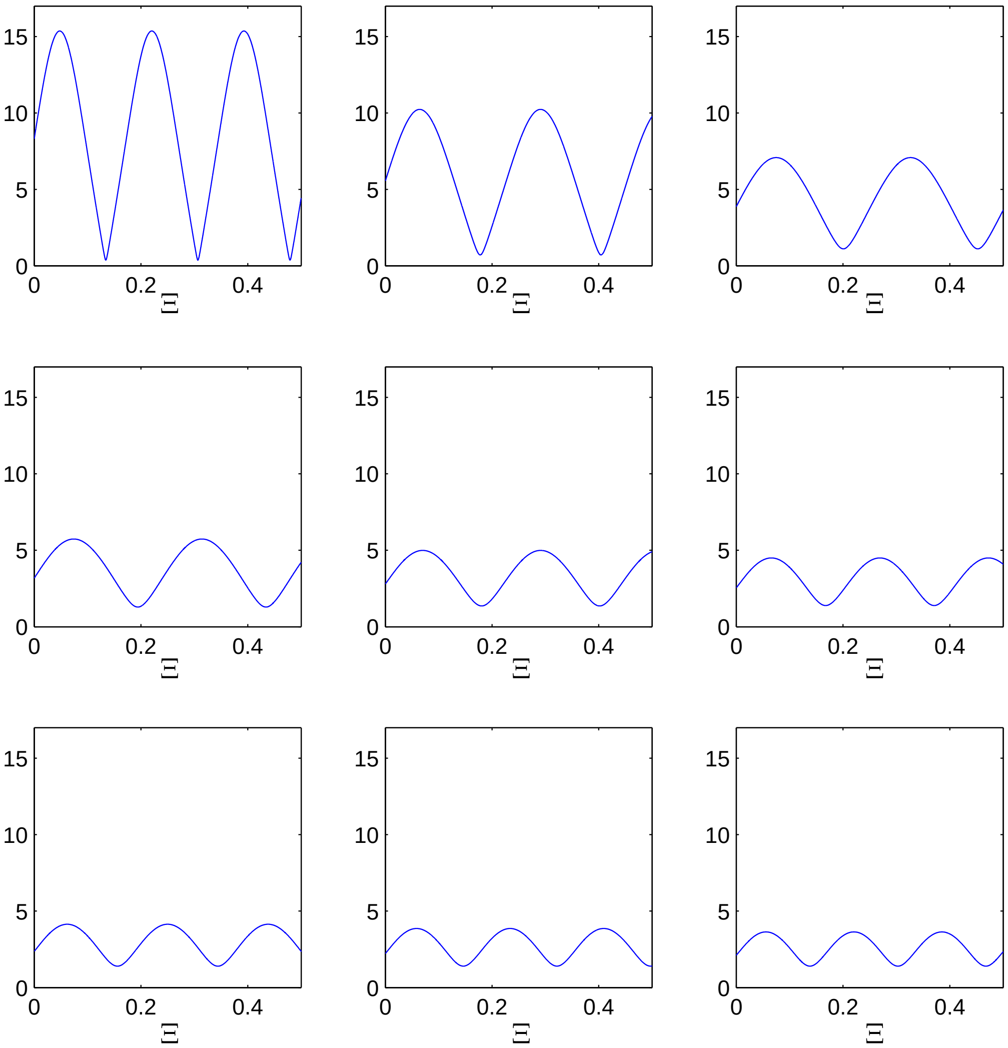

Figure 5.3 – Interface plots of the cnoidal waves, with the same set-up as in figure 5.2. Magnetic field strength is increased from left to right. The period of the waves initially rises, then falls as field strength increases further. The cnoidal parameter m decreases, leading to waves that are more sinusoidal. As in figure 5.2, $\beta_1 = \beta_2 = 1/2$, and $\alpha = 0.1$, with $v_{A2} = 0.3 v_{A1}$.

5.4 Three-wave resonance

We will now return to the single layer (but still weakly non-hydrostatic) model, continuing to look for weakly nonlinear solutions to equations (5.4). However, we will now take the leading order solution to be a *set* of waves and analyse how these waves interact nonlinearly. This is particularly interesting when a 'resonant triad' is taken (see, for example, Craik, 1985; Grimshaw, 2005), where the waves in the set interact resonantly.

The phonomenon of three-wave resonance is important in physical scenarios because it provides a very efficient way of transferring energy between different length scales. For example, in the tachocline there may be lots of small-scale wave motion, triggered by overshooting convective plumes from the solar convection zone, for example, that are very difficult to detect by observation. However, a resonance mechanism can provide a way for these small-scale modes to feed others with different frequencies and wavenumbers that might be easier to detect from a distance.

The linear dispersion relations we have been working with so far (in the absence of rotation) have all been of the form

$$\omega = ck, \tag{5.74}$$

where c is a constant. This particularly simple form allows us to determine phase speeds (that do not depend on k) of modes, and to find derivatives of frequency with relative ease. Equation (5.74) also supports wave triads, in which three wave modes exchange energy resonantly. The idea is that individual wave solutions can be added to form another solution, as in the linear case, but the amplitudes of the individual modes can vary over long timescales. We shall see that these modulations can be similar in magnitude to the amplitudes of the waves themselves.

We will first define, and then show the existence of the triad. A resonant triad is three sinusoidal waves, with frequencies ω_j and wavenumbers k_j, for $j = 1, 2, 3$, such that $\omega_1 + \omega_2 + \omega_3 = 0$ and $k_1 + k_2 + k_3 = 0$. Three such waves exist in our system, since (5.74) admits waves satisfying $\omega_1 = ck_1$, $\omega_2 = ck_2$, and $\omega_3 = -c(k_1 + k_2)$. This triad consists of two waves propagating in one direction, and the third, which has a wavenumber equal to the sum of the others when k_1 and k_2 are positive, travelling in the opposite direction.

Nonlinear terms can introduce variations in the amplitudes of the plane waves in a Fourier decomposition. This means that any two of the modes in the triad will excite the third, as explained in section 5.1. Of course, in a real physical scenario, given an initial excitation of the modes in the triad, yet more modes would be excited that were not before, but these do not enter into the $\mathcal{O}(\epsilon)$ analysis, and do not feed into the amplitude equations.

5.4.1 Derivation of the equations for resonant triad interactions

Having proved the existence of a triad, we can seek solutions of the leading order variables as before, but this time we shall search for wave–like solutions, prescribing the form of the travelling solution A in equations (5.21). We shall look for solutions

$$\eta^{(0)} = {\sum_{n=1}^{3}}' F_n(\tau) e^{i\theta_n}, \tag{5.75}$$

where

$$\theta_n = k_n x - \omega_n t, \tag{5.76}$$

and the dash on the summation symbol denotes the addition of the complex conjugates of the terms in the series, as well as the terms themselves. We also have ω_n and k_n linked via the dispersion relation. The solution form given in (5.75) describes the sum of the three resonant waves of the triad, with complex amplitudes F_j that are allowed to vary over the long time scale τ. The complex conjugate is added to ensure the solutions of the leading order variables are real.

The definition of θ_n given in (5.76) is slightly different to that in equation (5.16) in section 5.2.1. However, θ_n is still a function of $x - ct$, since $\theta_n = k_n(x - ct)$, and so we can follow the analysis in the previous section. However, we could not use our previous definition of θ, (5.16), because there would be no way to distinguish the θ_n. Note also that $\theta_1 + \theta_2 + \theta_3 = 0$ for the waves in the triad.

The relationship between the first order variables is given by equation (5.13), giving the expressions for the other leading order variables:

$$\begin{aligned} u^{(0)} &= c{\sum_{n=1}^{3}}' F_n e^{i\theta_n}, \quad & w^{(0)} &= -i(z+1)c{\sum_{n=1}^{3}}' k_n F_n e^{i\theta_n}, \\ B_x^{(0)} &= -\mathrm{Ma}{\sum_{n=1}^{3}}' F_n e^{i\theta_n}, \quad & B_z^{(0)} &= i\mathrm{Ma}(z+1){\sum_{n=1}^{3}}' k_n F_n e^{i\theta_n}, \end{aligned} \tag{5.77}$$

keeping in mind that $\theta_n = k_n x - \omega_n t$. As before, these can be substituted into the equations at the next order, ϵ; the method outlined in the KdV derivation shall be used here. Integrating equation (5.22b) with respect to z gives

$$\tilde{p}^{(1)} = \left(\frac{z^2}{2} + z\right) \sum_{n=1}^{3}{}' k_n^2 F_n e^{i\theta_n} + \eta^{(1)}, \tag{5.78}$$

making use of (5.77). The boundary condition on pressure (which is $\tilde{p}^{(1)} = \eta^{(1)}$, from equation (5.6a)) and the dispersion relation (5.19) have been used in this derivation. Expression (5.78) is then substituted into equation (5.22a) along with the expressions for the leading order variables (5.77), to obtain

$$\begin{aligned} \frac{\partial \bar{u}^{(1)}}{\partial t} + \frac{\partial \eta^{(1)}}{\partial x} - \mathrm{Ma}\frac{\partial \bar{B}_x^{(1)}}{\partial x} = &- c\sum_{n=1}^{3}{}' \frac{dF_n}{d\tau} e^{i\theta_n} - i\sum_{n=1}^{3}{}' F_n e^{i\theta_n} \sum_{n=1}^{3}{}' k_n F_n e^{i\theta_n} \\ &+ \frac{1}{3} i \sum_{n=1}^{3}{}' k_n^3 F_n e^{i\theta_n}. \end{aligned} \tag{5.79}$$

This has been depth averaged over the layer as before, removing all explicit occurrences of z. Our next task is to replace all leading order variables in the time evolution equations (5.27a) and (5.22c), using (5.77). Equation (5.27a) becomes

$$\frac{\partial \eta^{(1)}}{\partial t} + \frac{\partial \bar{u}^{(1)}}{\partial x} = -\sum_{n=1}^{3}{}' \frac{dF_n}{d\tau} e^{i\theta_n} - 2ic\sum_{n=1}^{3}{}' F_n e^{i\theta_n} \sum_{n=1}^{3}{}' k_n F_n e^{i\theta_n}, \tag{5.80}$$

and the x-component of the induction equation (5.22c) becomes

$$\frac{\partial \bar{B}_x^{(1)}}{\partial t} - \mathrm{Ma}\frac{\partial \bar{u}^{(1)}}{\partial x} = \mathrm{Ma}\sum_{n=1}^{3}{}' \frac{dF_n}{d\tau} e^{i\theta_n}. \tag{5.81}$$

Note that the z-component of the induction equation (5.22d), and the equation derived from the solenoidal condition on magnetic field and corresponding boundary conditions (5.27b), are both satisfied by (5.77), and so we need not consider them here.

Equations (5.79-5.81) can be combined by differentiating (5.79) with respect to t, and (5.80)-

(5.81) with respect to x, and eliminating in favour of $\bar{u}^{(1)}$ to obtain

$$\begin{aligned}\frac{\partial^2 \bar{u}^{(1)}}{\partial t^2} - c^2\frac{\partial^2 \bar{u}^{(1)}}{\partial x^2} = {} & \underbrace{\frac{1}{3}\sideset{}{'}\sum_{n=1}^{3} k_n^3\omega_n F_n e^{i\theta_n}}_{\text{pressure}} \underbrace{+ic\sideset{}{'}\sum_{n=1}^{3} \omega_n \frac{dF_n}{d\tau}e^{i\theta_n}}_{\text{long time scale}} \\ & \underbrace{-\sideset{}{'}\sum_{n=1}^{3} \omega_n F_n e^{i\theta_n}\sideset{}{'}\sum_{n=1}^{3} k_n F_n e^{i\theta_n} - \sideset{}{'}\sum_{n=1}^{3} F_n e^{i\theta_n}\sideset{}{'}\sum_{n=1}^{3} \omega_n k_n F_n e^{i\theta_n}}_{\text{nonlinear velocity and Lorentz force}} \\ & \underbrace{+i\sideset{}{'}\sum_{n=1}^{3} k_n \frac{dF_n}{d\tau}e^{i\theta_n} - 2c\left(\sideset{}{'}\sum_{n=1}^{3} k_n F_n e^{i\theta_n}\right)^2 - 2c\sideset{}{'}\sum_{n=1}^{3} F_n e^{i\theta_n}\sideset{}{'}\sum_{n=1}^{3} k_n^2 F_n e^{i\theta_n}}_{\text{evolution equation for } \eta} \\ & \underbrace{+i\mathrm{Ma}^2\sideset{}{'}\sum_{n=1}^{3} k_n \frac{dF_n}{d\tau}e^{i\theta_n}}_{\text{induction equation}}. \end{aligned} \tag{5.82}$$

The left hand side of this equation has a complementary function containing $e^{i\theta_n}$, for $n = 1, 2, 3$, since the corresponding homogeneous equation is the same as that satisfied by the leading order variables (5.77). To avoid secular terms in the particular integral, we must ensure that the right hand side of (5.82) does not contain any $e^{i\theta_n}$, because if it did, terms like $\theta_n e^{i\theta_n}$ would be present in the particular integral part of the solution. Such terms grow linearly with time, and so after a time $\sim 1/\epsilon$ the assumed form of the asymptotic solution (5.9) would no longer be valid, as the $\mathcal{O}(\epsilon)$ terms grow to become comparable in size with the leading order terms.

To implement this solvability condition, we set the coefficient of each of the $e^{i\theta_n}$ terms in the right hand side of (5.82) to zero. For the $e^{i\theta_3}$ coefficient, for example, this gives

$$\begin{aligned}&\frac{1}{3}k_3^3\omega_3 F_3 + i\big(c\omega_3 + (\mathrm{Ma}^2+1)k_3\big)\frac{dF_3}{d\tau} \\ &\qquad - (\omega_1 k_2 + \omega_2 k_1 + \omega_1 k_1 + \omega_2 k_2 + 4ck_1k_2 + 2ck_1^2 + 2ck_2^2)F_1^* F_2^* = 0, \end{aligned} \tag{5.83}$$

which simplifies using $k_1 + k_2 + k_3 = 0$ and $\omega_1 + \omega_2 + \omega_3 = 0$ to

$$2c\frac{dF_3}{d\tau} = ik_3\left(\frac{1}{3}k_3^2 F_3 - 3F_1^* F_2^*\right). \tag{5.84}$$

The effect of the magnetic field has again translated into a time rescaling. As before, the factor arising from magnetic field strength is a multiple of $c = \sqrt{\mathrm{Ma}^2 + 1}$, which is a monotonically increasing function of strength Ma for positive Ma. Thus, increasing field strength has the effect of stretching out the time scale, as before. Absorbing the factor $2c$ into the time τ, and performing a similar derivation for the $e^{i\theta_1}$ and $e^{i\theta_2}$, gives the equations for three wave resonance, which are

$$\begin{aligned}\frac{dF_1}{d\tau} &= ik_1\left(\frac{1}{3}k_1^2F_1 - 3F_2^*F_3^*\right),\\ \frac{dF_2}{d\tau} &= ik_2\left(\frac{1}{3}k_2^2F_2 - 3F_1^*F_3^*\right),\\ \frac{dF_3}{d\tau} &= ik_3\left(\frac{1}{3}k_3^2F_3 - 3F_1^*F_2^*\right).\end{aligned} \tag{5.85}$$

The terms in red are those brought about by the non-hydrostatic terms. In the shallow water approximation, these would be neglected.

Equations (5.85) describe the evolution of the amplitudes of the three modes in the triad. They can be simplified, using the integrating factor $\exp(-ik_n^4\tau/12)$ (with $n = 1$ for (5.85a), and so on) to express the first two terms as a perfect derivative. Equation (5.85c) then gives

$$\frac{d}{d\tau}\left(F_3e^{-\frac{1}{12}ik_3^4\tau}\right) = -3ik_3F_1^*F_2^*e^{-\frac{1}{12}ik_3^4\tau}, \tag{5.86}$$

and similarly for the other two equations. At least one of the wavenumbers k_1, k_2, k_3 is negative, in order to uphold the condition $k_1 + k_2 + k_3 = 0$. Let us consider the case with $k_1, k_2 > 0$ and $k_3 < 0$ (other cases can be considered in much the same way). Then we can perform a final scaling of

$$\hat{F}_1 = -3i\sqrt{k_2|k_3|}F_1e^{-\frac{1}{12}ik_1^4\tau}, \quad \hat{F}_2 = 3\sqrt{k_1|k_3|}F_2e^{-\frac{1}{12}ik_2^4\tau}, \quad \hat{F}_3 = 3\sqrt{k_1k_2}F_3e^{-\frac{1}{12}ik_3^4\tau}, \tag{5.87}$$

to yield the simpler equations

$$\begin{aligned}\frac{d\hat{F}_1}{d\tau} &= -\hat{F}_2^*\hat{F}_3^*e^{-\frac{1}{12}i(k_2^4+k_2^4+k_3^4)\tau},\\ \frac{d\hat{F}_2}{d\tau} &= -\hat{F}_1^*\hat{F}_3^*e^{-\frac{1}{12}i(k_2^4+k_2^4+k_3^4)\tau},\\ \frac{d\hat{F}_3}{d\tau} &= \hat{F}_1^*\hat{F}_2^*e^{-\frac{1}{12}i(k_2^4+k_2^4+k_3^4)\tau}.\end{aligned} \tag{5.88}$$

The equations governing triad interactions can therefore be written as

$$\begin{aligned}\frac{d\hat{F}_1}{d\tau} &= -\hat{F}_2^*\hat{F}_3^*e^{iK\tau},\\ \frac{d\hat{F}_2}{d\tau} &= -\hat{F}_1^*\hat{F}_3^*e^{iK\tau},\\ \frac{d\hat{F}_3}{d\tau} &= \hat{F}_1^*\hat{F}_2^*e^{iK\tau},\end{aligned} \tag{5.89}$$

where $K = -(k_1^4 + k_2^4 + k_3^4)/12$. To find the corresponding resonance equations supported by the shallow water equations, one would put $K = 0$ here, keeping in mind that the time scale would be different.

Note that equations (5.85) also satisfy

$$\frac{\partial}{\partial \tau}\left(|F_1|^2 + |F_2|^2 + |F_3|^2\right) = 0, \tag{5.90}$$

as can be seen by taking the derivative with respect to τ.

5.4.2 Solving the three-wave resonance equations

The amplitudes of the three wave modes in the triad can be computed analytically using Jacobi elliptic functions. We do this by writing the scaled complex coefficients $\hat{F}_n$ in polar form so that $\hat{F}_n = b_n e^{i\phi_n}$, where the $b_n(\tau)$ and $\phi_n(\tau)$ are real. Then the amplitudes of the individual waves in the triad are given as the b_j, which change over the long time scale τ. The phases ϕ_n, which will not be solved analytically here, give the phase of the modulations.

Equations (5.89) can then be written as a set of six equations, three of which are the real parts, and describe the amplitude of the modulations, and three the imaginary parts, describing the phases of the modulations. Upon substitution of $\hat{F}_n = b_n e^{i\phi_n}$, equations (5.89) yield

$$\frac{db_1}{d\tau} = -b_2 b_3 \cos\Gamma, \qquad \frac{d\phi_1}{d\tau} = \frac{b_2 b_3}{b_1}\sin\Gamma, \tag{5.91a}$$

$$\frac{db_2}{d\tau} = -b_1 b_3 \cos\Gamma, \qquad \frac{d\phi_2}{d\tau} = \frac{b_1 b_3}{b_2}\sin\Gamma, \tag{5.91b}$$

$$\frac{db_3}{d\tau} = b_1 b_2 \cos\Gamma, \qquad \frac{d\phi_3}{d\tau} = -\frac{b_1 b_2}{b_3}\sin\Gamma, \tag{5.91c}$$

where $\Gamma = \Phi - K\tau$, with $\Phi = \phi_1 + \phi_2 + \phi_3$ denoting the sum of the phases. We can use these equations to find more constants of motion. It is straightforward to verify that

$$W_n = b_1 b_2 b_3 \sin\Gamma - \frac{1}{2}K\mathrm{sgn}(k_n) b_n^2 \tag{5.92}$$

are constants of motion for $n = 1, 2, 3$. This can be shown by differentiating (5.92) with respect to τ, and substituting according to equations (5.91). We can also multiply the amplitude equations (on the left hand side of (5.91)) by the appropriate b_n and integrate, to find three more constants of motion known as the Manley-Rowe equations, which are

$$b_2^2 - b_1^2 = C_3, \qquad b_1^2 + b_3^2 = C_2, \qquad b_2^2 + b_3^2 = C_1, \tag{5.93}$$

for constants C_1, C_2 and C_3. Since the amplitudes of the modulations are linked in such a neat way, it suffices to solve for just one, say b_1, bearing in mind that b_2 and b_3 can be found easily using (5.93). Manipulation of the first of the equations in (5.91) gives

$$\frac{db_1^2}{d\tau} = 2b_1\frac{db_1}{d\tau} = -2b_1b_2b_3\cos\Gamma. \tag{5.94}$$

Squaring both sides of this equation, and defining $y = b_1^2$, gives

$$\left(\frac{dy}{d\tau}\right)^2 = 4b_1^2b_2^2b_3^2(1-\sin^2\Gamma). \tag{5.95}$$

Replacing $\sin^2\Gamma$ according to (5.92), this becomes

$$\left(\frac{dy}{d\tau}\right)^2 = 4b_1^2b_2^2b_3^2 - 4\left(W_1 + \frac{1}{2}Ky\right)^2. \tag{5.96}$$

In (5.96), the constant of motion W_1 has been chosen, but one could just as well have chosen $j = 2$ or $j = 3$ at this stage, and then followed the subsequent steps accordingly: in this sense, generality has not been lost. Using the Manley-Rowe relations (5.93) to eliminate b_2 and b_3 in (5.96) gives the differential equation

$$\left(\frac{dy}{d\tau}\right)^2 = -4\left(y^3 + (C_3 - C_2 + \frac{1}{4}K^2)y^2 + (WK - C_2C_3)y + W^2\right). \tag{5.97}$$

Since the left hand side of equation (5.97) is a square, the cubic on the right hand side must also be positive. There is at least one real root of this cubic, since the coefficients are real; further, the coefficients of y^0 and y^3 in this cubic are negative, and so one of the real roots, y_1 say, is negative. The other two roots, y_2 and y_3, are then either both negative, both positive, or a complex conjugate pair, but since $y = b_1^2$ is itself a square, the cubic on the right hand side must rise above zero for positive y. Then, taking the convention $y_2 < y_3$, the range of values $y_2 \le y \le y_3$ at which this cubic is positive is of particular interest, as these are the values at which (5.97) is valid.

Writing this cubic as a product of its factors, the method of separation of variables can then be applied to equation (5.97), which can be written as

$$2\int_0^\tau d\tau' = \int_{y_0}^y \frac{dy}{\sqrt{-(y-y_1)(y-y_2)(y-y_3)}}. \tag{5.98}$$

We then proceed by making the substitution

$$y = y_3 - (y_3 - y_2)\sin^2\psi, \tag{5.99}$$

yielding

$$\tau = -\int_{\psi_0}^{\psi} \frac{(y_3 - y_2)\sin\psi\cos\psi\, d\psi}{\sqrt{(y_3 - y_1 - (y_3 - y_2)\sin^2\psi)(y_3 - y_2 - (y_3 - y_2)\sin^2\psi)(y_3 - y_2)\sin^2\psi}}. \tag{5.100}$$

The lower limit ψ_0 satisfies equation (5.99) when $y = b_1^2(0)$, so that

$$\sin\psi_0 = \sqrt{\frac{y_3 - b_1^2(0)}{y_3 - y_2}}. \tag{5.101}$$

Simplifying equation (5.100) by cancelling the factor $(y_3 - y_2)\sin\psi\cos\psi$ in the fraction in the integrand, one has

$$\tau = -\frac{1}{\pm\sqrt{y_3 - y_1}} \int_{\psi_0}^{\psi} \frac{d\psi}{\sqrt{1 - m^2\sin^2\psi}}, \tag{5.102}$$

where the parameter m is defined as

$$m = \sqrt{\frac{y_3 - y_2}{y_3 - y_1}}, \tag{5.103}$$

and satisfies $0 \leq m \leq 1$, since $y_1 < y_2 < y_3$. We should take the minus sign in (5.102) to ensure time τ is positive. Rearranging (5.102) gives

$$\sqrt{y_3 - y_1}\tau + \int_0^{\psi_0} \frac{d\psi}{\sqrt{1 - m^2\sin^2\psi}} = \int_0^{\psi} \frac{d\psi}{\sqrt{1 - m^2\sin^2\psi}}. \tag{5.104}$$

The integrals in equation (5.104) are incomplete elliptic integrals of the first kind, with the upper limit understood as the Jacobi amplitude. Consider the right hand integral only for the time being: the sine of the upper limit on the right hand side, ψ, is defined as the ‘sn’ of the left hand side, since the Jacobi elliptic function sn is defined as the inverse of this integral. Hence we have

$$\sin\psi = \operatorname{sn}\left(\sqrt{y_3 - y_1}\tau + \int_0^{\psi_0} \frac{d\psi}{\sqrt{1 - m^2\sin^2\psi}}, m\right). \tag{5.105}$$

Finally, we use this to replace $\sin\psi$ in equation (5.99), giving the analytic solution

$$y = y_3 - (y_3 - y_2)\operatorname{sn}^2\left(\sqrt{y_3 - y_1}\tau + \int_0^{\psi_0} \frac{d\psi}{\sqrt{1 - m^2\sin^2\psi}}, m\right), \tag{5.106}$$

Since the remaining integral is also an incomplete integral of the first kind, and so can be thought of as an inverse ‘sn’ function, (5.106) can be written as

$$y = y_3 - (y_3 - y_2)\operatorname{sn}^2\left(\sqrt{y_3 - y_1}\tau + \operatorname{sn}^{-1}\left(\sqrt{\frac{y_3 - b_1^2(0)}{y_3 - y_2}}, m\right), m\right). \tag{5.107}$$

One can see that if $t = 0$, $y = b_1^2(0)$ as required. The amplitude of the remaining two waves, b_2 and b_3, can then be found using the Manley-Rowe equations (5.93).

The positive square root of y has been plotted in figure 5.4, which depicts the evolution of the amplitudes of the modes in the triad over time τ, for arbitrarily chosen initial conditions.

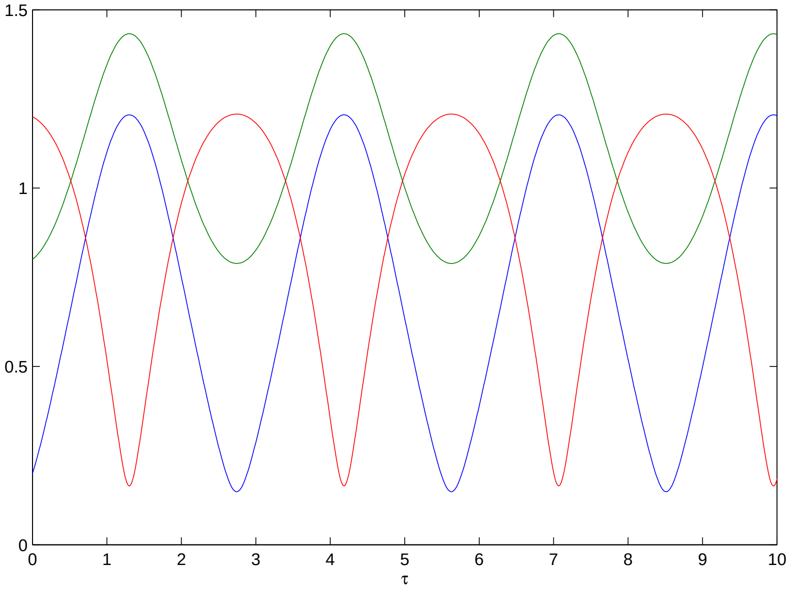

Figure 5.4 – Cnoidal amplitude modulations of the three waves in the triad, over scaled long time τ. The parameters chosen are: $K = 0.2$, with initial values $b_1 = 0.2$, $b_2 = 0.8$, $b_3 = 1.2$, $\phi_1 = 1.2$, $\phi_2 = 0.4$, and $\phi_3 = 0.7$.

5.4.3 Numerical solution of the three-wave resonance equations

Although the amplitudes of the solutions of equations (5.89) can be calculated analytically using (5.107), this is not enough to describe completely the modulations of the amplitudes in real time. This is because the analytical solution gives only the moduli of the complex variables $\hat{F}_n$, but we want to undo the scaling to retrieve the F_n so that we can describe the surface movements according to (5.75). However, to undo this scaling, one would need to know the values of the real and imaginary parts of the $\hat{F}_n$ so that the scaling given in (5.87) could be undone. To do this, we not only need to know the values of b_n, given analytically, but also the ϕ_j, which are as yet unknown.

One way to calculate these would be to use the analytical solutions of the b_n along with the ϕ_n evolution equations in (5.91), to numerically derive the values of the phases. Indeed, this is done in Chapter 6 to initialise a fully nonlinear numerical solver. Another approach would be to solve the primitive equations (5.89) numerically and find the evolution of the complex variables $\hat{F}_n$ themselves. Then the scalings could be easily undone and the amplitudes of the plane waves easily found. This would also enable us to check the validity of the analytical solution.

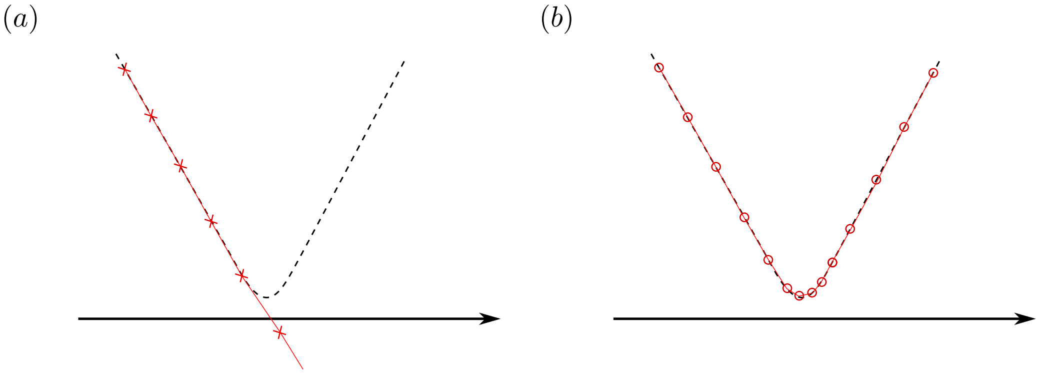

Figure 5.5 – Schematic illustrating the advantages of the adaptive timestepping scheme when a solution curve nears the axis. Figure (a) depicts a fixed timestepping scheme, and one can see that the high curvature of the true solution (dotted line) is missed owing to the relatively large space between samples. However, with adaptive timestepping (b), this spacing is adjusted accordingly.

A fixed timestepping scheme is not valid for all parameter regimes, because the derivatives of the ϕ_n can become extreme when one the the b_n is small. Instead, equations (5.89) were solved using an adaptive timestepping routine in MATLAB. Each timestep consisted of a full step using the RK4 method, and two half-steps, again using the RK4 method. If the discrepancy in the two generated sets of values is smaller than a specified tolerance, the values found using the two half-steps are selected and the next timestep is initiated; otherwise, the data is discarded, the stepsize reduced and the step repeated. If the discrepancy is small enough, the step size is increased to save computation time around parts of the solution curve that have an approximately constant gradient. An adaptive timestepping scheme was favoured over one with a fixed timestep to resolve the behaviour of the curves close to the τ (time) axis: the gradients of the solutions become extreme when initial parameters are chosen so that one of the curves approaches zero. With a fixed timestep, the curve approaches the axis and carries on into the negative values rather than twisting sharply and heading upwards again. An adaptive timestepping scheme such as the one implemented here has the effect of decreasing the step size at these problem areas, so increasing the density of sample points there. Thus, close to the axis, the distance between sample points becomes small enough to capture the curvature, as shown in figure 5.5.

We will now consider some solutions of the resonance equations (5.89) to assess the influence of magnetic field. Figure 5.6 displays the amplitude modulations from the numerical scheme, taking into account all the scalings on the $\hat{F}_n$. One can see that the only effect of introducing a magnetic field is to reduce the period of the modulations. Indeed, this period can be found using

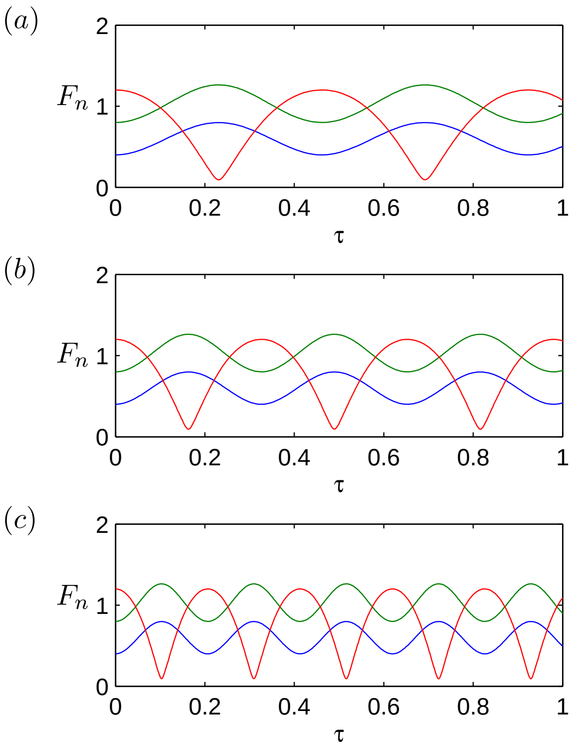

Figure 5.6 – The plane wave amplitude modulations, found using an adaptive timestepping numerical scheme. Initial values of the F_n are the real values $F_1 = 0.4$, $F_2 = 0.8$, and $F_3 = 1.2$. Plot (a) is the hydrodynamic regime, plot (b) the case $\mathrm{Ma} = 1$, and (c) the case $\mathrm{Ma} = 2$. The only change introduced by increasing magnetic field strength is in the period of the modulations.

the complete integral of the first kind, as in the formula

$$T = \frac{2}{\epsilon c\sqrt{y_3 - y_1}} \int_0^{\pi/2} \frac{1}{\sqrt{1 - m^2 \sin^2 \psi}}\, d\psi, \tag{5.108}$$

where T is the period of the modulations. The magnetic dependence is constrained entirely within the factor $c = \sqrt{\mathrm{Ma}^2 + 1}$, and so the reduction in the period is as depicted in figure 5.1. Figure 5.6 illustrates the effect of magnetic field on the modulations. One can see that the period is affected, but not the amplitude or shape. In figure 5.7, snapshots of the surface of the layer are displayed, at equal intervals over one modulation period.

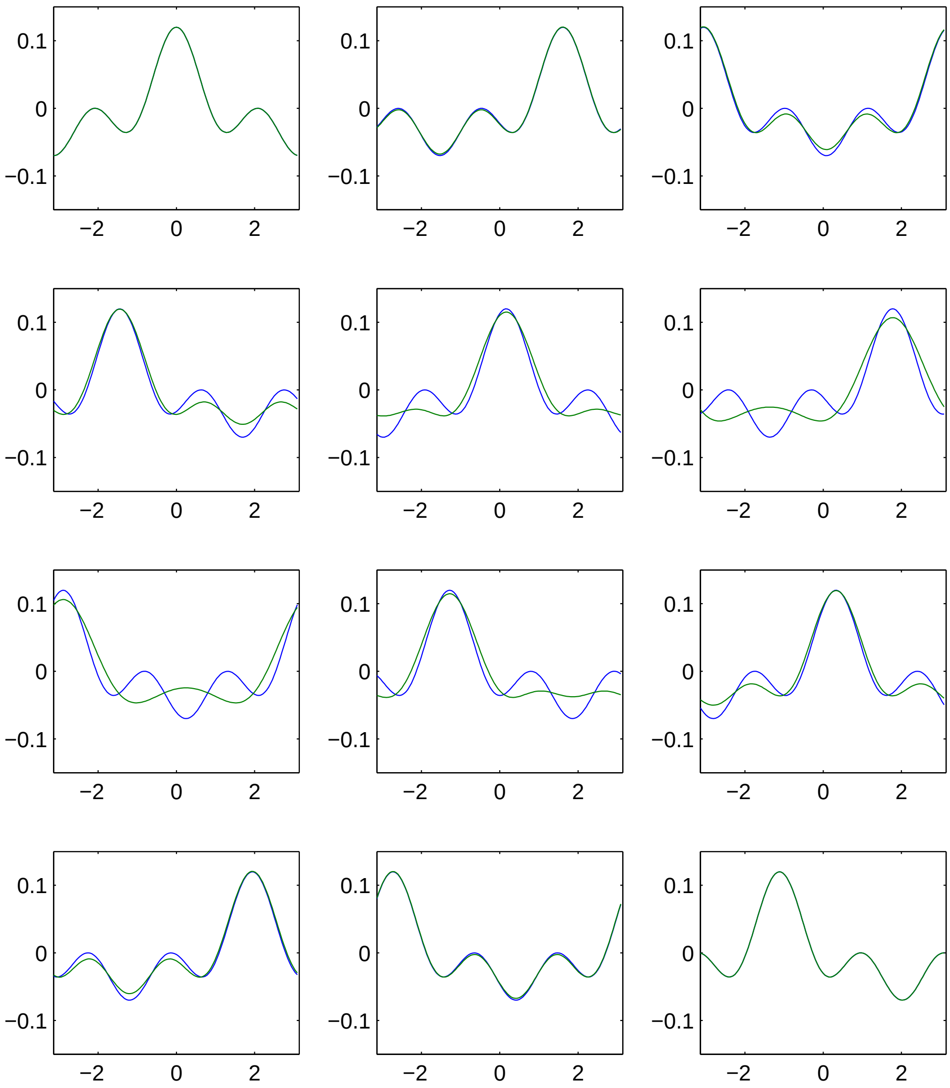

Figure 5.7 – Plots of the surface at regular intervals due to the three-wave resonance phenomenon over one modulation period. The upper left is the initial surface profile, with both linear (blue) and weakly nonlinear (green) curves overlapping. As one scans the images from left to right (like reading a book), the deviation due to weakly nonlinear effects becomes clear. The bottom right plot shows the curves after exactly one modulation period ($T \approx 12.6/$ with $\mathrm{Ma} = 1$ in this case), when they overlap once more; the figures in between are snapshots at equal time intervals. Parameters chosen are those used to produce figure 5.6. The amplitude parameter chosen for the surface plots is $\epsilon = 0.05$.

5.5 Summary and discussion

The aim of this chapter was to investigate the effects of weak nonlinearity on the single layer and 2-layer rigid lid weakly non-hydrostatic models. The nonlinear effects were taken to be small in an asymptotic analysis, so that surface and interface disturbances are small. This improved upon the linear work in earlier chapters, in which perturbed quantities were, infinitesimal, and all nonlinear effects ignored. In this sense, the analysis is slightly more physically applicable.

In section 5.2, we derived a KdV equation for the single layer model. This is an equation that is satisfied when dispersive effects from the non-hydrostatic term in the vertical component of the momentum equation balance the effects of nonlinear steepening. This equation has solutions that propagate without change of shape, including sech^2 and cnoidal profiles. We found that introducing a magnetic field to the single layer model translates to a long-time rescaling, so that slow dynamics occur more quickly with a field present. In the 2-layer rigid lid model, on the other hand, magnetic field dependence is much greater; not only does the long-timescale alter with field strength, but the types of waves supported also depend on ambient magnetic structure. This is manifest mathematically through the different sign combinations of the coefficients in the governing KdV equation.

The phenomenon of three-wave resonance was studied in section 5.4, in which energy is periodically exchanged between three wave modes via the nonlinear terms. We again find that magnetic influence is restricted to redefining the long-time dynamics, which in this case is equivalent to affecting the period of the modulations, or how quickly the modes exchange energy. Any triplet of waves in this system with wavenumbers that sum to zero constitutes a triad, since the linear dispersion relation is relatively simple and dispersive effects arise from the non-hydrostatic term and do not enter into the linear dynamics. In Chapter 6, we consider three-wave resonance in the rotating shallow water system, where dispersion instead comes from rotation.

We should reiterate that although the layers of fluid in this chapter have all been shallow in the sense that horizontal length scales have been much greater than vertical ones, the governing equations used have *not* been the shallow water equations. This is because of the existence of the non-hydrostatic term, which is neglected in the shallow water approximation. One could perform a weakly nonlinear analysis similar to that in section 5.1 without this term (on the shallow water equations), and the result would be Burger's equation; that is, the KdV equation without the dispersive third derivative. Any solutions of this would not travel without change of shape, but would steepen due to nonlinearity, and eventually break. This will be analysed further in Appendix F.

In Chapter 6, we re-introduce rotation and consider hydrostatic flow (i.e. the shallow water equations). After revisiting three-wave resonance, we shall then consider fully nonlinear analytical and numerical solutions, which is a natural extension to the weakly nonlinear work.

Chapter 6

Nonlinear waves with rotation

6.1 Introduction

After a brief departure to weakly non-hydrostatic systems in Chapter 5, we now return to the study of the single layer shallow water MHD system, and re-introduce rotation. Rotation introduces dispersion, so we can anticipate the existence of nonlinear wave solutions that do not break. Our focus is on two problems: three wave resonance, concerning the interaction of several waves at small amplitude; and finite-amplitude travelling waves. Progress with both these problems will be made analytically, but we will now also verify our solutions with the outcome from a nonlinear numerical code. The majority of the work in this chapter will be 1.5D, with y-derivatives set to zero.

Analytical progress can only take us so far. It has its positive points, since it is exact and helps shed light on the fundamental workings of the models, and their physical interpretation. It is an essential part of the understanding of any system, giving a firm foundation upon which to build. It does, however, have its limitations; in order to make progress analytically, one has to make assumptions and simplifications to the governing equations of motion, to reduce their complexity for mathematical manipulation. The main restriction we have faced so far is that the perturbed variables (surface, velocities and magnetic fields) have all been small: infinitesimal in Chapters 2, 3 and 4, and small compared with the layer depth in Chapter 5. In reality, of course, a physical surface may be perturbed by an amount that violates these principles, in which case our models would not be appropriate.

Numerical solution of the equations of SWMHD provides fully nonlinear results that do not necessarily need to be small amplitude. It is the natural extension to the linear and weakly nonlinear analysis of previous chapters, allowing us to verify results. Indeed, in this chapter we will verify weakly nonlinear predictions of three-wave resonance by comparing them against the numerical results. Not only does this help to verify the predictions, but it also allows us to probe the nonlinear dynamics further by considering the deviation from the weakly nonlinear regime.

The downside to solving the governing differential equations by numerical integration is that it is not exact, as in the previous linear work in Chapters 2, 3 and 4. The technique works by approximating the state of the system at discrete time intervals in the future, based on ‘knowledge’ of the system in its present state. The word ‘knowledge’ has quotation marks because, of course, our knowledge of the present state is itself an approximation, based on previous steps (unless the state in question is the initial one). The deviation of the approximating numerical solution from the exact one is the quantity we wish to minimise. This sounds straightforward, except that we do not know what the exact solution should be, or we would not be performing numerical integration at all! However, there are ways in which we can check that our numerical solution is behaving, which are described in detail in Appendix E.

Exact nonlinear solutions are derived analytically in section 6.3. Expanding upon the work of Schecter et al. (2001), we find periodic wave-like disturbances that propagate without change of shape, with the dispersive effects of rotation balancing nonlinear steepening. These waves are neither sinusoidal nor cnoidal, and fall into one of two classifications, determined by their phase speeds and other properties. Such solutions have a wide range of surface profiles: some have periods so large they appear as solitary waves, and some have sharp peaks that appear as cusps. As well as being interesting in their own right, they also provide a useful check that the numerical scheme is working correctly.

Another advantage of numerically solving the shallow water equations is that we can look at wave motion in the 2-dimensional horizontal plane, rather than just the direction of the wavevector. This was touched upon in the linear case when considering phase and group velocities, but we did not discuss the 2-D wave structure. There are exact y-independent solutions of the SWMHD equations on a doubly periodic domain – whether these are stable to perpendicular perturbations is an interesting question, and one that is addressed in section 6.4.2.

$u \sim v \sim \sqrt{\frac{g}{H}}\hat{\eta}$	$t \sim \frac{\sqrt{gH}}{L}$
$B_x \sim B_y \sim \frac{B_0}{H}\hat{\eta}$	

Table 6.1 – The scalings used in the nondimensionalisation of the shallow water equations.

6.2 Three-wave resonance in rotating SWMHD

The aim of this section is to investigate the three-wave resonance phenomenon in the magnetic shallow water system, in the presence of rotation. We consider the (hydrostatic) SWMHD equations, and determine the dynamics of the resonant interactions that the system supports. We are also considering the 1.5D system, so that variables have two horizontal components, but they only vary in the x-direction. Since much of the analysis is similar to that in the Chapter 5, repeated derivations will be shortened or omitted.

The governing equations of shallow water magnetohydrodynamics (2.7), (2.12) and (2.15) can be nondimensionalised about a motionless basic state with a uniform magnetic field to give

$$\frac{\partial u}{\partial t} + \frac{\partial \eta}{\partial x} - \mathrm{Ma}^2\frac{\partial B_x}{\partial x} - \tilde{f}v = \epsilon\left(-\frac{\partial u}{\partial \tau} - u\frac{\partial u}{\partial x} + \mathrm{Ma}^2 B_x\frac{\partial B_x}{\partial x}\right), \tag{6.1a}$$

$$\frac{\partial v}{\partial t} - \mathrm{Ma}^2\frac{\partial B_y}{\partial x} + \tilde{f}u = \epsilon\left(-\frac{\partial v}{\partial \tau} - u\frac{\partial v}{\partial x} + \mathrm{Ma}^2 B_x\frac{\partial B_y}{\partial x}\right), \tag{6.1b}$$

$$\frac{\partial \eta}{\partial t} + \frac{\partial u}{\partial x} = \epsilon\left(-\frac{\partial \eta}{\partial \tau} - \eta\frac{\partial u}{\partial x} - u\frac{\partial \eta}{\partial x}\right), \tag{6.1c}$$

$$\frac{\partial B_x}{\partial t} - \frac{\partial u}{\partial x} = \epsilon\left(-\frac{\partial B_x}{\partial \tau} + B_x\frac{\partial u}{\partial x} - u\frac{\partial B_x}{\partial x}\right), \tag{6.1d}$$

$$\frac{\partial B_y}{\partial t} - \frac{\partial v}{\partial x} = \epsilon\left(-\frac{\partial B_y}{\partial \tau} + B_x\frac{\partial v}{\partial x} - u\frac{\partial B_y}{\partial x}\right). \tag{6.1e}$$

Table 6.1 outlines the scalings used. The nondimensional parameter $\epsilon = \hat{\eta}/H$ is the fractional amplitude of a typical surface perturbation, and so all nonlinear terms are $\mathcal{O}(\epsilon)$ times smaller than the linear terms (on the left hand sides). As in section 5.3, a long-timescale $\tau = \epsilon t$ has been introduced, and in the standard way in 1.5D systems, the y-derivatives have been set to zero. As before, the parameter $\mathrm{Ma} = B_0/\sqrt{gH}$ is a measure of relative field strength. The rotation parameter $\tilde{f} = L/L_D$ is a modified measure of rotation, where $L_D = \sqrt{gH}/f$ is the Rossby radius of deformation. Thus the importance of rotation depends on the assumed length scale of the perturbations; short perturbations (relative to L_D) implies weak rotation. In subsequent work, the $\sim$ shall be dropped from the $\tilde{f}$ for aesthetic reasons.

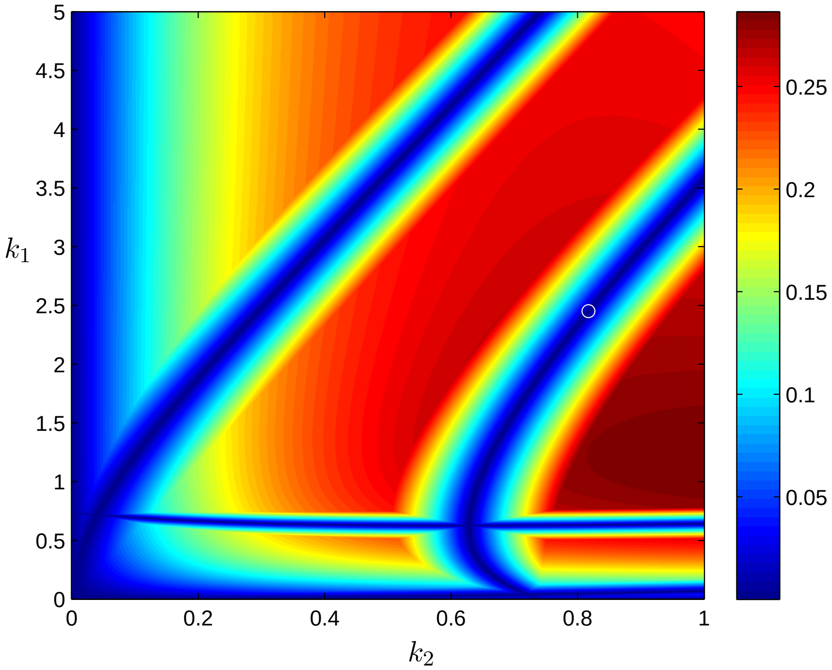

Figure 6.1 – The location of triads in the (k_1, k_2) plane. Values of the wavenumbers k_1 and k_2 define a point on the image, the colour of which represents the least possible absolute value of the sum of the corresponding frequencies. The third wavenumber, $k_3 = -k_1 - k_2$ is dependent on the other wavenumbers and so the system has two degrees of freedom. The dark blue bands are of interest, as they represent wavenumber triplets that also give $\omega_1 + \omega_2 + \omega_3 = 0$. The white circle represents the triad used in the initialisation of the numerical scheme.

Before performing an asymptotic analysis, we should first prove the existence of the triad. The dispersion relation, given later in equation (6.7), is quadratic in ω^2, so that a given value of k gives four possible frequencies, for fixed f and Ma. Given two wavenumbers, k_1 and k_2, one could try to construct a triad by taking $k_3 = -k_1 - k_2$, so that the wavenumbers add to zero, and then determining whether one of the sixty-four possible sums of frequencies is zero. In general, this will not be the case, and different values of k_1 and k_2 will have to be chosen until the properties of a triad are met.

Figure 6.1 is a display of the least possible sum of frequencies for different wavenumber triplets satisfying $k_1+k_2+k_3 = 0$. The colour denotes the value of the least sum of frequencies, with dark blue being optimal (i.e. zero). In the absence of rotation, the display would be completely blue, as any choice of wavenumbers that sum to zero give frequencies that also sum to zero. However, with rotation, the frequency is not a constant multiple of the wavenumber, and so we have to work harder to find triads.

Crucially, three-wave resonance is not supported in the non-magnetic rotating shallow water model (Zeitlin, 2007). The dark blue bands of figure 6.1 clearly indicate their existence in the SWMHD system; magnetic field is required in order for the system to support triad interactions.

It would also be beneficial if the triad consisted of wavenumbers that were multiples of each other. This is not necessary in weakly nonlinear theory, but when it comes to the numerical analysis later, the wave modes have to fit exactly inside a periodic box. In order to facilitate comparisons later, it is prudent to choose a triad with, say, $k_1 = 3k_2$, so that $k_3 = -4k_2$. Plotting the image in figure 6.1 as a surface plot with height given by colour, a cross-section through the surface along the plane $k_1 = 3k_2$ was taken. A numerical Newton-Raphson style iterative approach was then used to find the axis intercept, which is where the frequencies sum to zero. This procedure is equivalent to finding the point of intersection of the line $k_1 = 3k_2$ and the dark blue curve in figure 6.1. The resulting triad found to be

$$\begin{aligned} k_1 &= 2.4518634 \qquad & \omega_1 &= -3.7142402, \\ k_2 &= 0.8172878 \qquad & \omega_2 &= 0.5781486, \\ k_3 &= -3.2691512 \qquad & \omega_3 &= 3.1360906. \end{aligned} \tag{6.2}$$

This triad is represented in figure 6.1 with a white circle. The choice $k_1 = 2k_2$ (so that $k_3 = -3k_1$) is not an option, because in this case the k_2 mode can be fed by the k_1 mode alone. The forthcoming equations for three-wave resonance (6.11) are then not valid, since they do not contain an F_1^{*2} term; they assume that excitation of one mode comes from both other modes in the triad.

6.2.1 Weakly nonlinear analysis

To leading order in ϵ, equations (6.1) are

$$\frac{\partial u^{(0)}}{\partial t} + \frac{\partial \eta^{(0)}}{\partial x} - \mathrm{Ma}^2 \frac{\partial B_x^{(0)}}{\partial x} - f v^{(0)} = 0, \tag{6.3a}$$

$$\frac{\partial v^{(0)}}{\partial t} - \mathrm{Ma}^2 \frac{\partial B_y^{(0)}}{\partial x} + f u^{(0)} = 0, \tag{6.3b}$$

$$\frac{\partial \eta^{(0)}}{\partial t} + \frac{\partial u^{(0)}}{\partial x} = 0, \tag{6.3c}$$

$$\frac{\partial B_x^{(0)}}{\partial t} - \frac{\partial u^{(0)}}{\partial x} = 0, \tag{6.3d}$$

$$\frac{\partial B_y^{(0)}}{\partial t} - \frac{\partial v^{(0)}}{\partial x} = 0. \tag{6.3e}$$

Eliminating $\eta^{(0)}$ and $B_x^{(0)}$ in equations (6.3a,c,d) gives

$$\frac{\partial^2 u^{(0)}}{\partial t^2} - (\mathrm{Ma}^2 + 1) \frac{\partial^2 u^{(0)}}{\partial x^2} - f \frac{\partial v^{(0)}}{\partial t} = 0. \tag{6.4}$$

Similarly, eliminating $B_y^{(0)}$ from equations (6.3b,e) gives

$$\frac{\partial^2 v^{(0)}}{\partial t^2} - \mathrm{Ma}^2 \frac{\partial^2 v^{(0)}}{\partial x^2} + f \frac{\partial u^{(0)}}{\partial t} = 0. \tag{6.5}$$

Equations (6.4) and (6.5) yield

$$\left(\frac{\partial^2}{\partial t^2} - \mathrm{Ma}^2 \frac{\partial^2}{\partial x^2} \right) \left(\frac{\partial^2}{\partial t^2} - (\mathrm{Ma}^2 + 1) \frac{\partial^2}{\partial x^2} \right) u^{(0)} + f^2 \frac{\partial^2 u^{(0)}}{\partial t^2} = 0. \tag{6.6}$$

Given that $u^{(0)}$ is wavelike (i.e. proportional to $e^{i(kx - \omega t)}$), equation (6.6) yields the dispersion relation

$$\omega^4 - \left((2\mathrm{Ma}^2 + 1) k^2 + f^2 \right) \omega^2 + \mathrm{Ma}^2 (\mathrm{Ma}^2 + 1) k^4 = 0. \tag{6.7}$$

This is the reduction of (2.41) when $\delta = 0$, after appropriate scalings.

In a similar manner as in section 5.3, we look for expressions for the leading order variables that satisfy (6.3). One set of possible solutions is given by

$$\eta^{(0)} = \sideset{}{'}\sum_{n=1}^{3} F_n e^{i\theta_n}, \tag{6.8a}$$

$$u^{(0)} = \sideset{}{'}\sum_{n=1}^{3} c_n F_n e^{i\theta_n}, \tag{6.8b}$$

$$v^{(0)} = -if \sideset{}{'}\sum_{n=1}^{3} \frac{c_n \omega_n}{\omega_n^2 - \mathrm{Ma}^2 k_n^2} F_n e^{i\theta_n}, \tag{6.8c}$$

$$B_x^{(0)} = -\sideset{}{'}\sum_{n=1}^{3} F_n e^{i\theta_n}, \tag{6.8d}$$

$$B_y^{(0)} = if \sideset{}{'}\sum_{n=1}^{3} \frac{\omega_n}{\omega_n^2 - \mathrm{Ma}^2 k_n^2} F_n e^{i\theta_n}, \tag{6.8e}$$

where $\theta_n = k_n x - \omega_n t$ and $c_n = \omega_n / k_n$. Note that the phase speeds c_n are no longer equal, and we must treat them with more care than in the non-rotational case, where they would be factorised out of terms and the remaining terms simplified. These solutions represent a superposition of three plane waves, with the complex coefficients F_n as functions of long-time τ, as before.

Order ϵ analysis

At the next order, equations (6.1) are given by

$$\begin{aligned} \frac{\partial u^{(1)}}{\partial t} + \frac{\partial \eta^{(1)}}{\partial x} - \mathrm{Ma}^2 \frac{\partial B_x^{(1)}}{\partial x} - f v^{(1)} &= -\sideset{}{'}\sum_{n=1}^{3} c_n \frac{dF_n}{d\tau} e^{i\theta_n} \\ &\quad - i \sideset{}{'}\sum_{n=1}^{3} c_n F_n e^{i\theta_n} \sideset{}{'}\sum_{n=1}^{3} \omega_n F_n e^{i\theta_n} + i\mathrm{Ma}^2 \sideset{}{'}\sum_{n=1}^{3} F_n e^{i\theta_n} \sideset{}{'}\sum_{n=1}^{3} k_n F_n e^{i\theta_n}, \end{aligned} \tag{6.9a}$$

$$\begin{aligned} \frac{\partial v^{(1)}}{\partial t} - \mathrm{Ma}^2 \frac{\partial B_y^{(1)}}{\partial x} + f u^{(1)} &= if \sideset{}{'}\sum_{n=1}^{3} \frac{c_n \omega_n}{\zeta_n^2} \frac{dF_n}{d\tau} e^{i\theta_n} \\ &\quad - f \sideset{}{'}\sum_{n=1}^{3} c_n F_n e^{i\theta_n} \sideset{}{'}\sum_{n=1}^{3} \frac{\omega_n^2}{\zeta_n^2} F_n e^{i\theta_n} + \mathrm{Ma}^2 f \sideset{}{'}\sum_{n=1}^{3} F_n e^{i\theta_n} \sideset{}{'}\sum_{n=1}^{3} \frac{\omega_n k_n}{\zeta_n^2} F_n e^{i\theta_n}, \end{aligned} \tag{6.9b}$$

$$\begin{aligned} \frac{\partial \eta^{(1)}}{\partial t} + \frac{\partial u^{(1)}}{\partial x} &= -\sideset{}{'}\sum_{n=1}^{3} \frac{dF_n}{d\tau} e^{i\theta_n} \\ &\quad - i \sideset{}{'}\sum_{n=1}^{3} F_n e^{i\theta_n} \sideset{}{'}\sum_{n=1}^{3} \omega_n F_n e^{i\theta_n} - i \sideset{}{'}\sum_{n=1}^{3} c_n F_n e^{i\theta_n} \sideset{}{'}\sum_{n=1}^{3} k_n F_n e^{i\theta_n}, \end{aligned} \tag{6.9c}$$

$$\frac{\partial B_x^{(1)}}{\partial t} - \frac{\partial u^{(1)}}{\partial x} = {\sum_{n=1}^{3}}' \frac{dF_n}{d\tau} e^{i\theta_n}$$
$$- i{\sum_{n=1}^{3}}' F_n e^{i\theta_n} {\sum_{n=1}^{3}}' \omega_n F_n e^{i\theta_n} + i{\sum_{n=1}^{3}}' c_n F_n e^{i\theta_n} {\sum_{n=1}^{3}}' k_n F_n e^{i\theta_n}, \quad (6.9\text{d})$$

$$\frac{\partial B_y^{(1)}}{\partial t} - \frac{\partial v^{(1)}}{\partial x} = -if{\sum_{n=1}^{3}}' \frac{\omega_n}{\zeta_n^2} \frac{dF_n}{d\tau} e^{i\theta_n}$$
$$- f{\sum_{n=1}^{3}}' F_n e^{i\theta_n} {\sum_{n=1}^{3}}' \frac{\omega_n^2}{\zeta_n^2} F_n e^{i\theta_n} + f{\sum_{n=1}^{3}}' c_n F_n e^{i\theta_n} {\sum_{n=1}^{3}}' \frac{\omega_n k_n}{\zeta_n^2} F_n e^{i\theta_n}, \quad (6.9\text{e})$$

where $\zeta_n^2 = \omega_n^2 - \text{Ma}^2 k_n^2$. Equations (6.8) were used to rewrite the right hand sides. Applying the same elimination process as in section 6.2.1 (so that all $\mathcal{O}(\epsilon)$ variables but $u^{(1)}$ are eliminated), we have

$$\left(\frac{\partial^2}{\partial t^2} - \text{Ma}^2 \frac{\partial^2}{\partial x^2}\right)\left(\frac{\partial^2}{\partial t^2} - (\text{Ma}^2+1)\frac{\partial^2}{\partial x^2}\right) u^{(1)} + f^2 \frac{\partial^2 u^{(1)}}{\partial t^2} =$$
$$\frac{\partial^3 r_a}{\partial t^3} - \frac{\partial^3 r_c}{\partial t^2 \partial x} + \text{Ma}^2 \frac{\partial^3 r_d}{\partial t^2 \partial x} - \text{Ma}^2 \frac{\partial^3 r_a}{\partial t \partial x^2} + \text{Ma}^2 \frac{\partial^3 r_c}{\partial x^3} - \text{Ma}^4 \frac{\partial^3 r_d}{\partial x^3} + f\frac{\partial^2 r_b}{\partial t^2} + \text{Ma}^2 f \frac{\partial^2 r_e}{\partial t \partial x}, \quad (6.10)$$

where r_a is the right hand side of (6.9a), r_b is the right hand side of (6.9b), and so on. Since the complementary function of equation (6.10) contains an $e^{i\theta_3}$, say, the particular integral must not contain any multiples of $e^{i\theta_3}$ in order that we avoid secular growth (see section 5.3 for a full explanation). After some heavy algebra, this amounts to the constraint

$$\frac{i}{k_3}\left(-\omega_3^4 - k_3^2\omega_3^2 + (\text{Ma}^2+1)\text{Ma}^2 k_3^4 - \frac{f^2\omega_3^2}{\zeta_3^2}(\omega_3^2 + \text{Ma}^2 k_3^2)\right)\frac{dF_3}{d\tau}$$
$$+\Bigg((c_1c_2 - 2\text{Ma}^2+1)k_3\omega_3\zeta_3^2 - (\text{Ma}^2+1)k_3\zeta_3^2(c_1k_2+c_2k_1) + f^2(c_1c_2-\text{Ma}^2)\omega_3^2\left(\frac{k_1\omega_1}{\zeta_1^2} + \frac{k_2\omega_2}{\zeta_2^2}\right)$$
$$+ \text{Ma}^2 f^2 k_3\omega_3\left(\frac{c_1c_2k_1^2 - \omega_1^2}{\zeta_1^2} + \frac{c_1c_2k_2^2 - \omega_2^2}{\zeta_2^2}\right)\Bigg)F_1^* F_2^* = 0. \quad (6.11)$$

Similar equations can be derived for the time derivatives of F_1 and F_2. These are the equations for three-wave resonance in the rotating SWMHD system. Our aim is to solve these, and use them to predict the outcome of a fully nonlinear numerical solver of the SWMHD equations in section 6.2.3.

In the non-rotating system outlined in section 5.4.1, the shallow water analogue of the three-wave resonance equations could be easily found by removing the non-hydrostatic F_3 term in equation

(5.84), yielding

$$2c\frac{dF_3}{d\tau} = -3ik_3F_1^*F_2^*, \tag{6.12}$$

and similarly for the other two equations. Putting $c_1^2 = c_2^2 = c_3^2 = \mathrm{Ma}^2 + 1$ and $f = 0$ into equation (6.11) gives the reduction to (6.12) that we require.

6.2.2 Results

Now we have derived the three-wave equations, we can examine the kind of behaviour possible. The choice of ϵ enters only into the time-scale of the dynamics, and will not affect other modulation properties. However, the choice of initial amplitudes might; we saw in Chapter 5 that the initial amplitudes can affect the curvature of the modulations, for example, and how cnoidal/sinusoidal the modulations are (i.e. the value of the Jacobi elliptic parameter m).

We will use the triad given in (6.2). For later comparison, we shall plot the total leading order energy, E_n, of each mode, rather than the $|F_n|$. The total energy of the system is calculated as the sum of the squares of the variables The energy E_3 is calculated using

$$E_3 = |\eta_{k_3}^{(0)}|^2 + |u_{k_3}^{(0)}|^2 + |v_{k_3}^{(0)}|^2 + |B_{x_{k_3}}^{(0)}|^2 + |B_{y_{k_3}}^{(0)}|^2 = \left(2 + c_3^2 + (1 + c_3^2)\frac{\omega_3^2}{\zeta_3^4}\right)|F_3|^2, \tag{6.13}$$

making use of (6.8), where the subscript k_3 denotes the k_3-mode component. Similar expressions can be calculated for E_1 (for the k_1-mode) and E_2 (for the k_2-mode).

The three-wave resonance equations (6.11) can be solved using a fourth order Runge-Kutta (RK4) timestepping scheme, to produce the modulations as seen in figure 6.2. The cnoidal appearance of the modulations can be seen by noting the sharp peaks and wider troughs of the red and green curves, and wide troughs and sharper peaks of the blue. Figure 6.3 illustrates the evolution of the $|F_j|$ themselves, and also highlights this cnoidal property.

Visualisations of the surface at regular intervals for one modulation period are displayed in figure 6.4. The green curves represent the surface according to weakly nonlinear theory, and the blue curves linear theory, for comparison. There is a significant deviation from the linear predictions, indicating the importance of nonlinear effects, before the curves match up once more as the time approaches the period of the modulations.

Figures 6.5-6.7 show some predictions for different initial amplitudes. Each of these figures uses $\epsilon = 0.0125$, and the triad given in (6.2). Figure 6.5 shows the modulations when the

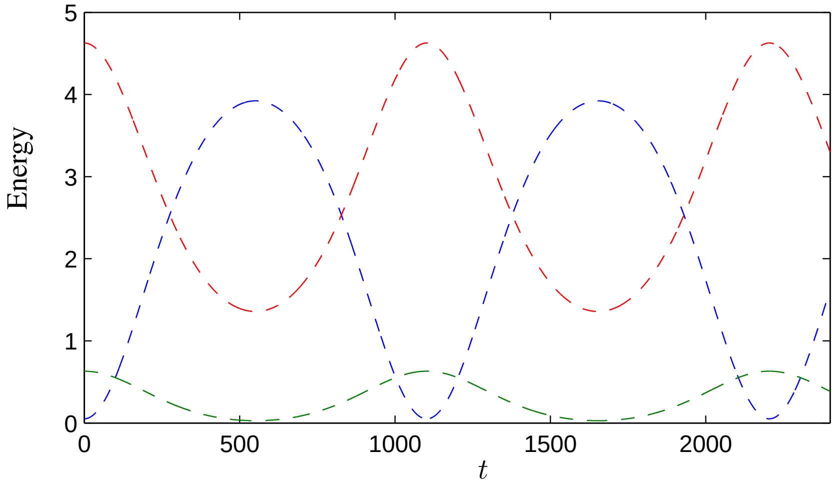

Figure 6.2 – Weakly nonlinear predictions of the exchange of energy of modes in a triad in the rotating SWMHD system. The blue curve represents the k_1-mode (E_1), green the k_2-mode (E_2), and red the k_3-mode (E_3). The triad is given by the values in (6.2), with initial complex amplitudes taking the values $F_1 = 0.1$, $F_2 = 0.3$, and $F_3 = 0.4$. For this figure, $\epsilon = 0.0125$.

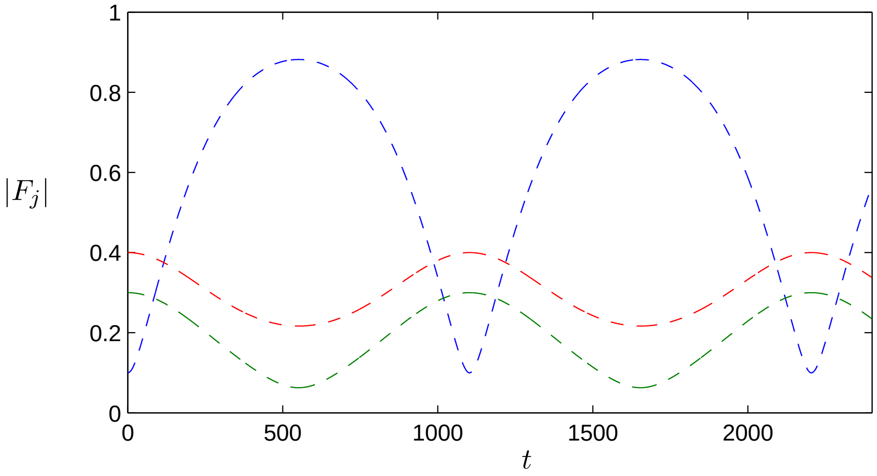

Figure 6.3 – Weakly nonlinear predictions of the mode amplitudes of the waves in the triad. The curves have been found by solving (6.11) numerically using an RK4 scheme. Parameter values are the same as those used in figure 6.2.

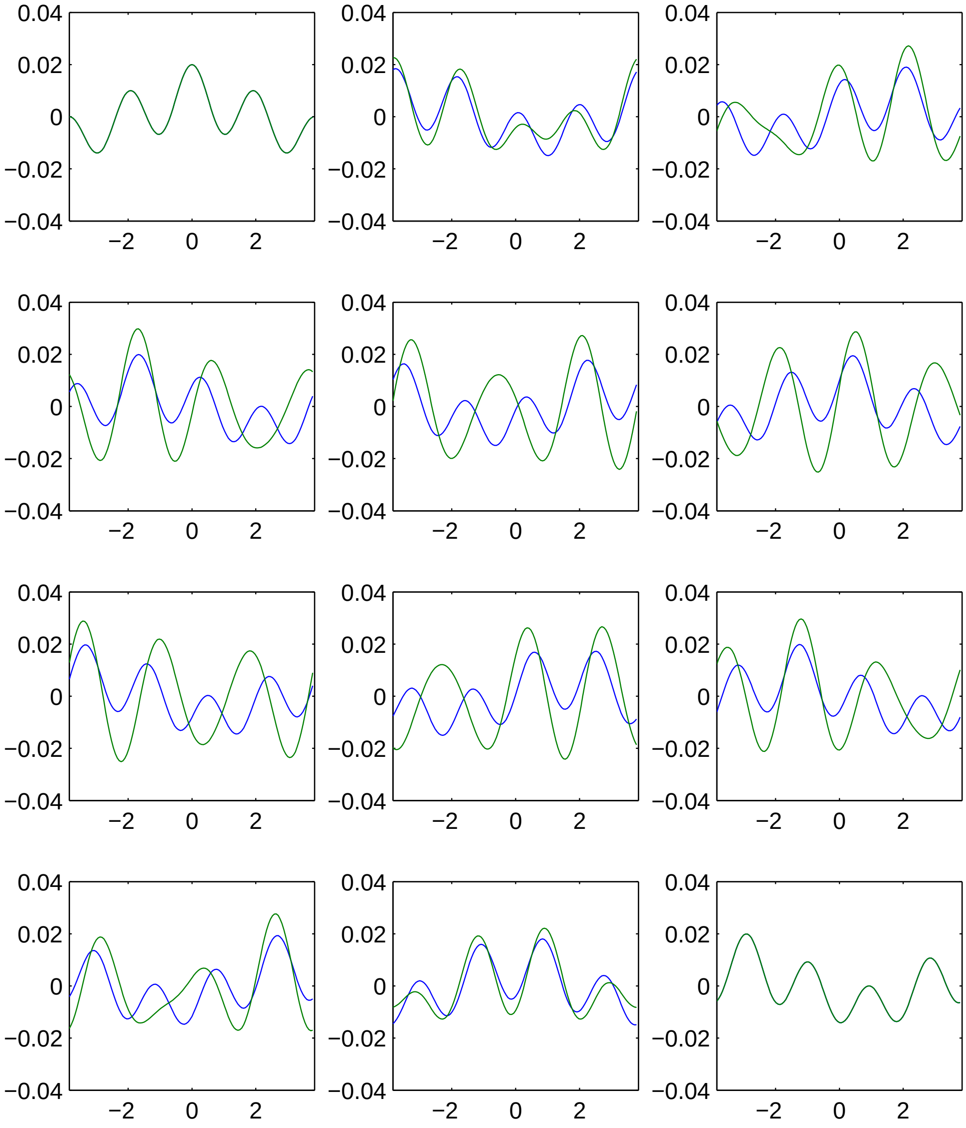

Figure 6.4 – Plots of the surface at regular intervals due to three-wave resonance over a modulation period, in the rotating shallow water case. The blue curves represent the linear regime, in which Fourier coefficients are constant, and the green curves represent the surface profile as predicted in the weakly nonlinear analysis, as in equations (6.11). Unlike figure 5.7, which displays surface profiles in the non-rotating case, the surface in this figure is somewhat choppier, since the three waves comprising the solution are moving at different speeds. Parameter values reflect those in figure 6.2.

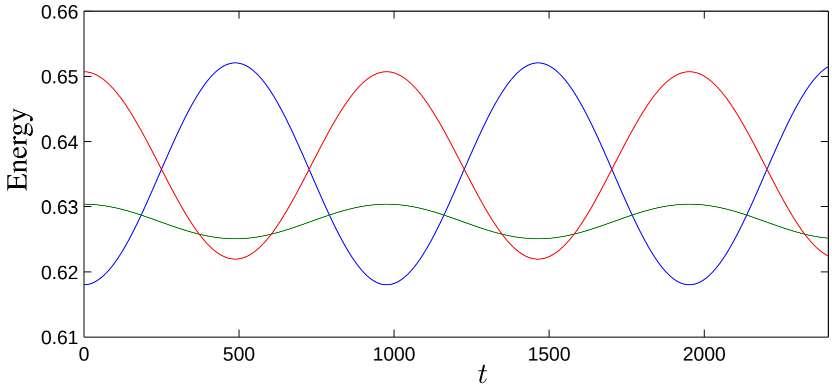

Figure 6.5 – Modulations with initial amplitudes $F_1 = 0.35$, $F_2 = 0.3$, and $F_3 = 0.15$, so that each mode has a similar initial energy. The curves are approximately sinusoidal, with the greatest exchange of energy between the k_1-mode (blue) and the k_3-mode (red).

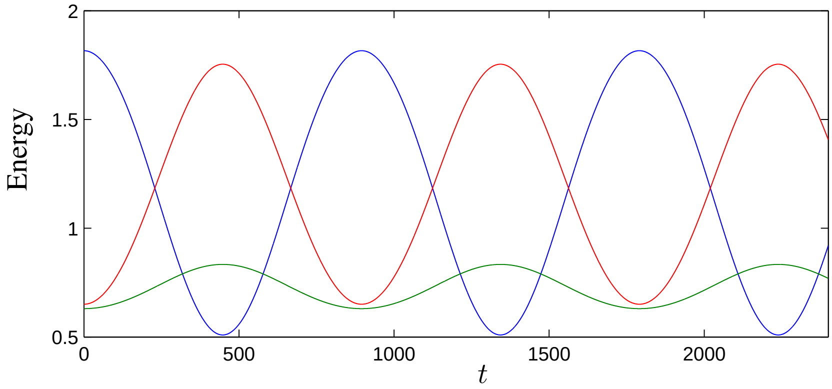

Figure 6.6 – Modulations with initial amplitudes $F_1 = 0.6$, $F_2 = 0.3$, and $F_3 = 0.15$. Again, the k_2-mode component does not change as much as the others, despite having similar initial energy as the k_3-mode.

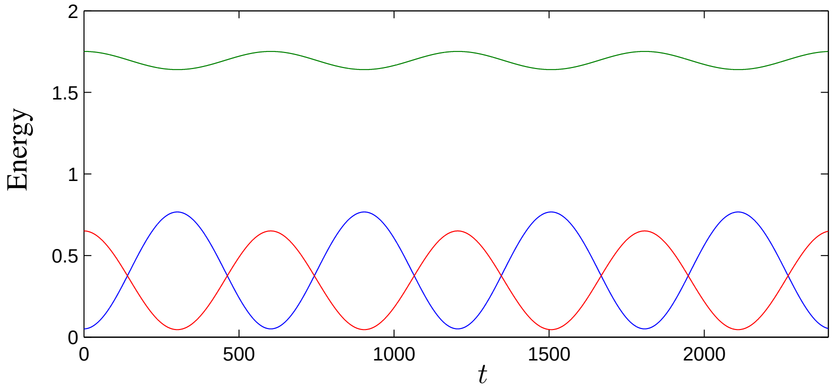

Figure 6.7 – Modulations with initial amplitudes $F_1 = 0.1$, $F_2 = 0.5$, and $F_3 = 0.15$. Even when the k_2-mode has the most energy initially, the amplitude of its modulation is still less than that of the others.

initial amplitudes are chosen so that the initial energy takes a similar value for each mode. The modulations are low, but the k_1- and k_3-modes have the largest fluctuations, as in figure 6.2. In figure 6.6, the energy in the k_2- and k_3-modes is initially similar, but the main exchange of energy is still between the k_1- and k_3-modes. Even when the k_2-mode is injected with more energy than the others, the amplitude of its modulation curve is still smaller than the others. This indicates that the wavenumbers play a large role when determining the modulation amplitudes; $|k_2|$ is lower than $|k_1|$ and $|k_3|$ by at least a factor of 3.

6.2.3 Nonlinear solution with three-wave initialisation

Our aim is now to compare the theoretical predictions of the weakly nonlinear analysis in section 6.2 with numerical solutions of the governing equations. The equations we wish to solve in a numerical scheme are the nondimensional 1.5D SWMHD equations, namely

$$\frac{\partial u}{\partial t} + \frac{\partial \eta}{\partial x} - \mathrm{Ma}^2 \frac{\partial B_x}{\partial x} - \tilde{f} v = -u\frac{\partial u}{\partial x} + \mathrm{Ma}^2 B_x \frac{\partial B_x}{\partial x}, \tag{6.14a}$$

$$\frac{\partial v}{\partial t} - \mathrm{Ma}^2 \frac{\partial B_y}{\partial x} + \tilde{f} u = -u\frac{\partial v}{\partial x} + \mathrm{Ma}^2 B_x \frac{\partial B_y}{\partial x}, \tag{6.14b}$$

$$\frac{\partial \eta}{\partial t} + \frac{\partial u}{\partial x} = -\eta\frac{\partial u}{\partial x} - u\frac{\partial \eta}{\partial x}, \tag{6.14c}$$

$$\frac{\partial B_x}{\partial t} - \frac{\partial u}{\partial x} = B_x\frac{\partial u}{\partial x} - u\frac{\partial B_x}{\partial x}, \tag{6.14d}$$

$$\frac{\partial B_y}{\partial t} - \frac{\partial v}{\partial x} = B_x\frac{\partial v}{\partial x} - u\frac{\partial B_y}{\partial x}, \tag{6.14e}$$

together with the solenoidal constraint on magnetic field:

$$\frac{\partial}{\partial x}(\eta + B_x + \eta B_x) = 0. \tag{6.15}$$

Substitution of $\eta = \epsilon\tilde{\eta}$, and similarly for the other variables, yields (6.1), and so the numerical solver will be initialised with (6.8) multiplied by the factor ϵ. Before considering the results from the numerical code, we shall first outline the scheme used.

For fluency, a brief description of the numerical code is hereby undertaken; see Appendix E for full details. The numerical solver, which was written from scratch for the purpose of solving the SWMHD equations for wave-like dynamics, is designed to solve equations (6.14) on a periodic domain. It calculates spatial derivatives in Fourier space using a spectral method, with a semi-implicit Adams-Bashforth and Crank-Nicolson hybrid timestepping scheme. The code used to produce the figures in this section is also dealiased to limit unwanted numerical artefacts. The numerical scheme is used with 200 spatial grid points.

6.2.4 Numerical results

To compare with the weakly nonlinear predictions shown in figure 6.2, we initialise the code with

$$\eta = \epsilon {\sum_{n=1}^{3}}' F_n e^{i\theta_n}, \tag{6.16}$$

with $\epsilon = 0.0125$ and $F_1 = 0.2$, $F_2 = 0.6$, and $F_3 = 0.8$. Values of the triad are again given in (6.2). The variables u, v and B_y are initialised according to (6.8), but with the factor ϵ in front (as for η in (6.16)), as discussed above. However, we do not use (6.8) to initialise B_x, since then only the linearised solenoidal constraint on magnetic field will be satisfied. Since the scheme solves the fully nonlinear equations, we initialise the x-component of magnetic field with

$$B_x = -\frac{\eta}{1+\eta}, \tag{6.17}$$

so that equation (6.15) is satisfied. Then B_x has a leading (order ϵ) part equal to $-\epsilon{\sum_{n=1}^{3}}' F_n e^{i\theta_n}$, and an order ϵ^2 correction so that $\nabla \cdot (h\mathbf{B})$ is initialised at zero.

Figure 6.8 shows the nonlinear numerical results (solid lines) against the weakly nonlinear predictions (dashed lines) for the Fourier coefficients of each mode; it contains the lines in figure 6.2 for comparison. As expected, the solutions from the dealiased code match the predictions very well for low times, and deviates slightly as time goes on. This deviation can be quantified by calculating the discrepancy between the dashed and solid curves by, for example, finding the area between them for a fixed number of periods; this is easily done numerically.

There are also some barely visible wobbles in the curve generated by the code in figure 6.8. These wobbles are an order ϵ in magnitude less than the amplitude of the modulations, and so are outside the remit of the resonance equations (6.11). They are more marked in plots of $|F_n|$ (rather than energy E_n), as can be seen in figure 6.9.

Quantifying the difference

The discrepancy should decrease as ϵ decreases, because the smaller the perturbation, the more accurate equations (6.11) will be. This discrepancy, Δ, can be defined as the sum of the areas

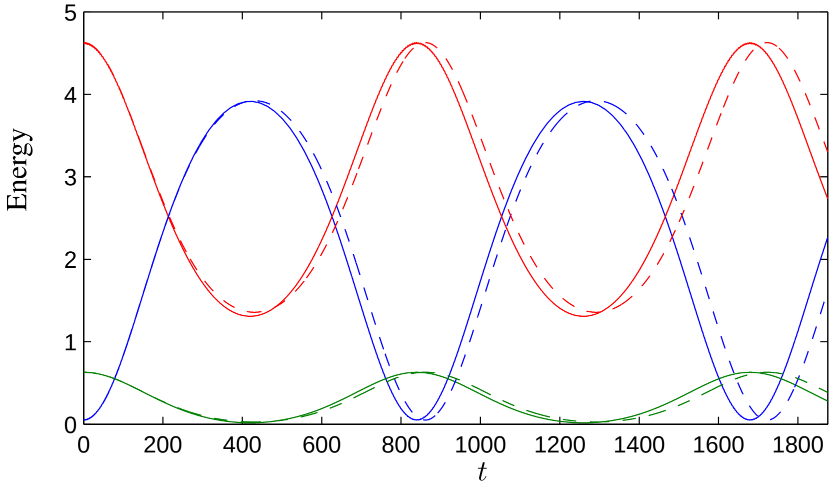

Figure 6.8 – Weakly nonlinear predictions (dashed curves) and nonlinear numerical results (solid curves) of the exchange of energy of modes in a triad in the rotating SWMHD system. The blue curves represent the k_1-mode (E_1), green the k_2-mode (E_2), and red the k_3-mode (E_3). The triad is given by the values in (6.2), with initial complex amplitudes taking the values $F_1 = 0.1$, $F_2 = 0.3$, and $F_3 = 0.4$. For this figure, $\epsilon = 0.016$ and $\delta = 0.005$.

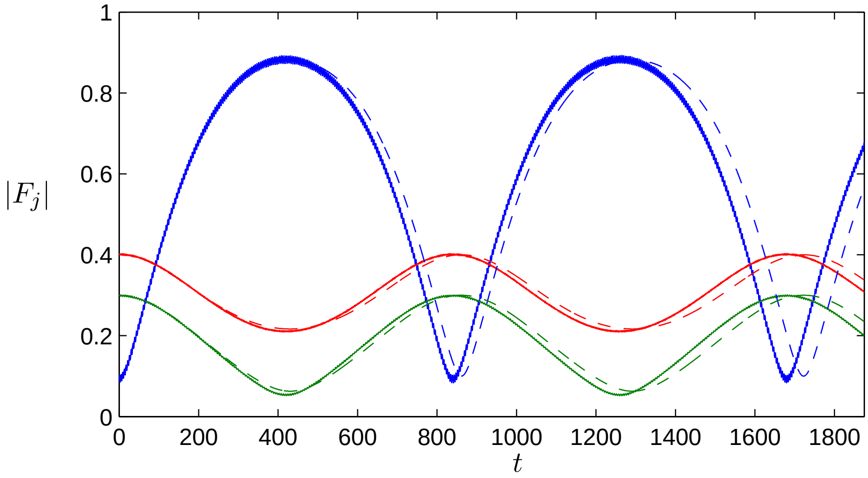

Figure 6.9 – A comparison of the $|F_j|$ predicted by weakly nonlinear analysis (dashed curves) and the numerical scheme (solid curves). The solid curves look thicker owing to the rapid $\mathcal{O}(\epsilon^2)$ wiggles in the numerical solution. The cnoidal nature of the modulations is evident in the blue (k_1 mode) and green (k_2 mode) curves. Parameters used reflect those of figure 6.8.

between the curves, given by the formula

$$\Delta = \sum_{n=1}^{3} \int_0^{\tau_{\text{max}}} |E_{\text{num}_n} - E_{\text{weak}_n}| \, d\tau, \tag{6.18}$$

where τ_{max} is chosen to take the value 30, so that we are comparing at least two modulations worth of curves (as seen in figures 6.8 and 6.9). The time t_{max} at which the code terminates therefore depends on ϵ. The discrepancy given in (6.18) can be estimated by taking the difference of the solution vectors for each mode (one from the numerical scheme, and one from the weakly nonlinear theory), taking the absolute value of each element, taking the sum of all the elements and multiplying by $\epsilon\Delta t$. The three resulting areas, one for each mode, are then added to get an estimate for total area. This definition of discrepancy is used in figure 6.11.

6.2.5 Further results

The results shown so far have been initialised with $F_1 = 0.1$, $F_2 = 0.3$, and $F_3 = 0.4$; these were chosen to give cnoidal modulations as in section 5.4. However, any choice of values for the F_j can be chosen. In this section, we initialise with $F_1 = 0.2$, $F_2 = 0.15$, and $F_3 = 0.4$, in order to consider results with approximately sinusoidal modulations.

Equation (6.18) can be used to calculate the area between the weakly nonlinear predictions and the curves from the numerical scheme, as a measure of the discrepancy between the two. As expected, as ϵ is decreased, the discrepancy decreases, but for small ϵ this discrepancy can rise again. This is because the numerical code is no longer able to resolve the small-amplitude ‘wiggles’ in the curves, the frequency of which decreases with ϵ. This rising discrepancy is therefore reduced by lowering Δt, as can be seen in figure 6.10 (the numerical scheme is second order in Δt). Plots of the discrepancy area against ϵ for different values of Δt shows clearly that the low-ϵ anomaly is greatly reduced by taking a smaller value of Δt. Inspired by this, the value $\Delta t = 0.00125$ is taken (the lowest in figure 6.10), for the subsequent figures in this chapter.

The discrepancy curve for $\Delta t = 0.00125$ in figure 6.10 looks like it approximates a straight line; this is easier to see in figure 6.11. The discrepancy, Δ, is therefore proportional to ϵ.

This is to be expected, because each variable (η, etc.) consists of a leading order part of $\mathcal{O}(\epsilon)$, which is the corresponding variable in the weakly nonlinear analysis, plus an $\mathcal{O}(\epsilon^2)$ correction. Thus the integrand in equation (6.18) is also $\mathcal{O}(\epsilon^2)$. In the numerics, the integral is approximated

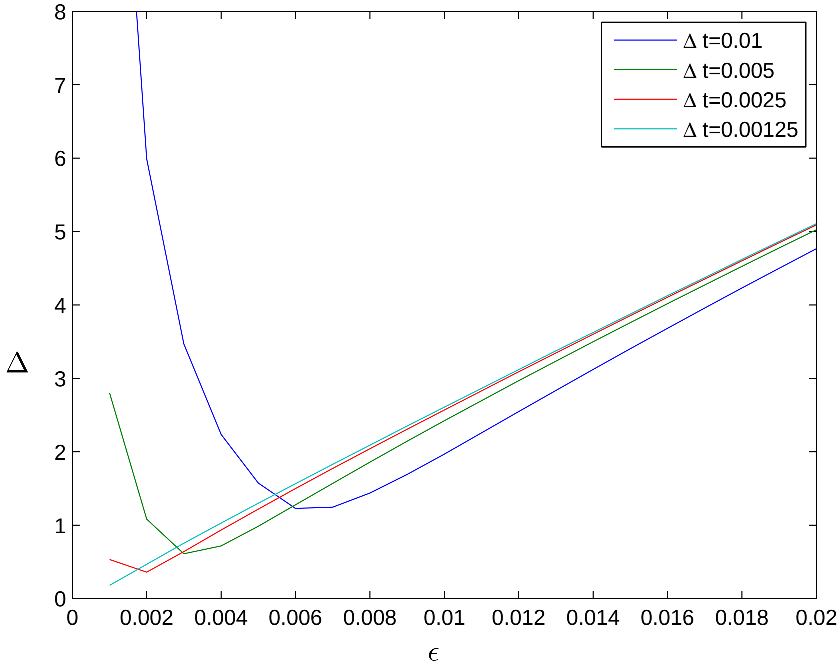

Figure 6.10 – Plots of the discrepancy between weakly nonlinear analysis and numerical results as measured by (6.18), for runs with different values of Δt. One can see that the required convergence is only achieved when Δt is set to be low. For this figure, $F_1 = 0.2$, $F_2 = 0.15$, and $F_3 = 0.4$

as a sum over the $\tau_{\text{max}}/(\epsilon\Delta t)$ elements of each vector, and so we have

$$\int_0^{\tau_{\text{max}}} |E_{\text{num}_n} - E_{\text{weak}_n}|\, d\tau \sim \frac{1}{\epsilon}\epsilon^2, \tag{6.19}$$

and so we expect linear dependence of the area on ϵ, for small ϵ.

Figure 6.12 displays the modulations in energy (plot (a)) and in the $|F_j|$ (plot (b)). The curves are cnoidal, but the Jacobi elliptic parameter m is smaller than in section 6.2.4, and so the curves look more sinusoidal. Note also that due to the slightly lower amplitude surface perturbations than in section 6.2.4 ($0.2 + 0.15 + 0.4 < 0.1 + 0.3 + 0.4$), there are more modulations in the time up to $\tau_{\text{max}} = 30$.

6.2.6 Other measures for the discrepancy

We can, however, do better than simply measuring the discrepancy by taking the distance between points on the curves to find the area. Inspection of figure 6.12 reveals that two contributing factors that make the curves different are modulation period and amplitude. In quantifying the

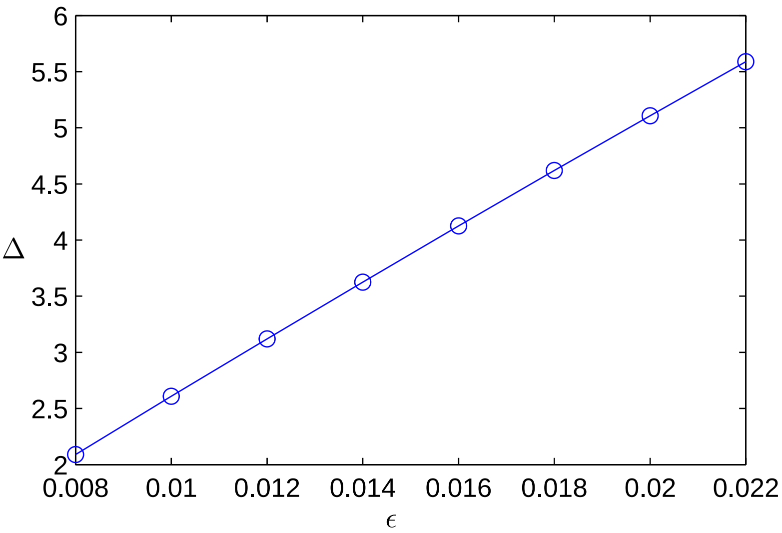

Figure 6.11 – A plot of the discrepancy, Δ, as calculated using equation (6.18), against ϵ, for starting values of $F_1 = 0.2$, $F_2 = 0.15$, and $F_3 = 0.4$. The required convergence for small ϵ is easily seen. In this figure, $\Delta t = 0.00125$

difference between the weakly nonlinear predictions and the results of the numerical scheme, one can investigate these factors separately.

Measuring the discrepancy with period

The period of the modulation curves can be found numerically by advancing in time until the value at a sample point falls within a specified tolerance of the initial value. This method usually has the added complication that in one period, the curves will generally match the initial value twice; however, as we are initialising with real F_j, the solution curves begin at their maximum (or minimum), and so this complication does not affect us.

Since the period of the modulations is the same for each of the three modes both in the weakly nonlinear predictions and the numerical results, we have only one comparison to make in order to quantify discrepancy using period differences. Figure 6.13 shows the relationship between the period and ϵ as predicted by weakly nonlinear theory and the numerics. We know that ϵ is inversely proportional to modulation period, because for a given triad, with a fixed rotation rate and magnetic field strength, the coefficients of the resonance equations (6.11) are constants, and ϵ is confined to the long time-scale τ. Indeed, the blue curve in figure 6.13(b) is a straight line, reflecting the fact that ϵ and T^{-1} are directly proportional, where T is the period of the modulations.

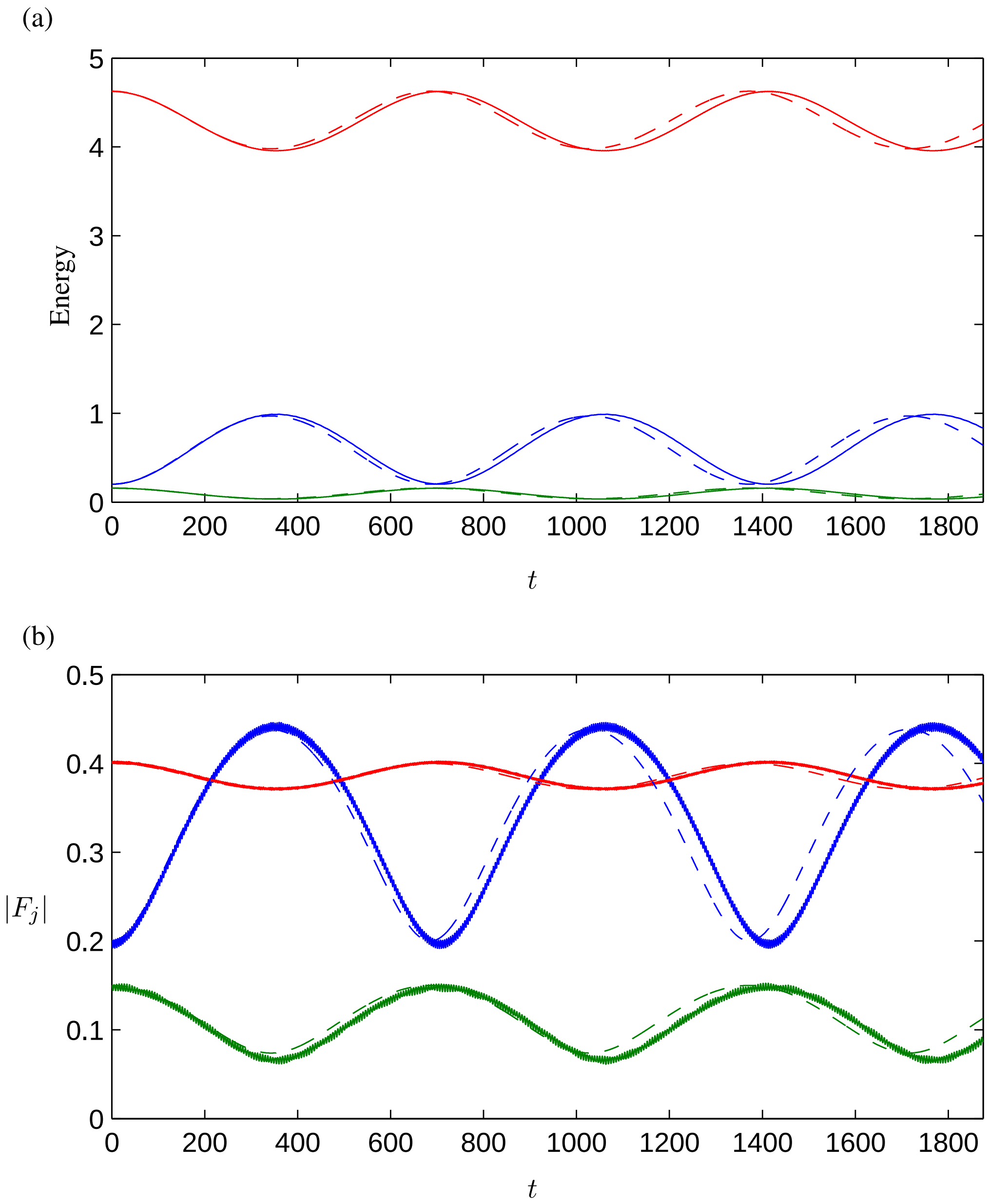

Figure 6.12 – The sinusoid-like modulations of the resonant triad with $F_1 = 0.2$, $F_2 = 0.15$, and $F_3 = 0.4$, and values for the wavenumbers and frequencies given in (6.2). Plot (a) shows the energy E_j for each mode, and (b) the $|F_j|$. In this plot, $\epsilon = 0.016$, $\Delta t = 0.00125$, and the maximum time corresponds to $\tau = 30$, to compare with figures 6.8 and 6.9.

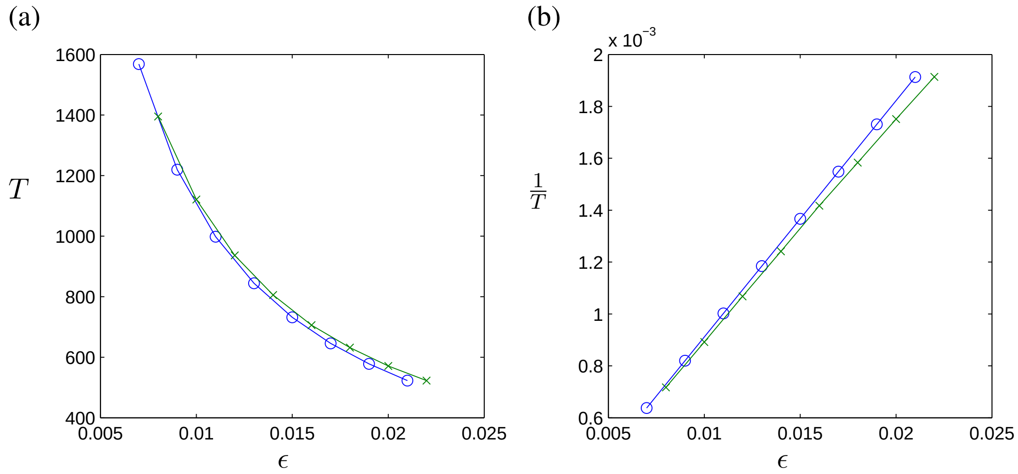

Figure 6.13 – Plots of (a) the period, T, and (b) the reciprocal of the period, against with ϵ. Again, we see that as ϵ decreases, the discrepancy between the theory (blue curves) and the numerics (green curves) also decreases. In this plot, parameters and the numerical scheme match those of figure 6.12, with $\Delta t = 0.00125$.

The green curve in figure 6.13(a) represents the relationship between ϵ and period T according to the numerical results. It is close to the weakly nonlinear prediction (blue curve) for small ϵ, and deviates as ϵ increases. This is because the $\mathcal{O}(\epsilon^2)$ terms in the power series expansions of the variables are getting larger relative to the other terms, and the weakly nonlinear analysis of section 6.2 is less applicable. Figure 6.13(b) displays T^{-1} against ϵ; the blue curve is actually a straight line, as predicted by weakly nonlinear theory. The green curve approaches this line as ϵ decreases.

Measuring the discrepancy with amplitude

The difference in amplitude between the curves in figure 6.12(a) could also be used as a measure of the discrepancy. Since there are three amplitudes (one for each of the modes in the triad), the comparison of amplitudes gives three discrepancies, which can then be combined to give a measure of efficiency. We know that the amplitude of the weakly nonlinear solution curves is independent of ϵ, because the parameter ϵ affects the long-time scale (and therefore the period of the modulations) only. Thus, the discrepancy we wish to measure is the difference between the amplitudes of the modulations of the modes and their corresponding theoretical predictions, marked with a horizontal dashed line in figure 6.14.

We have shown that three-wave resonance is supported in the shallow water system only if a magnetic field is introduced. Weakly nonlinear theory then gives accurate predictions, as verified

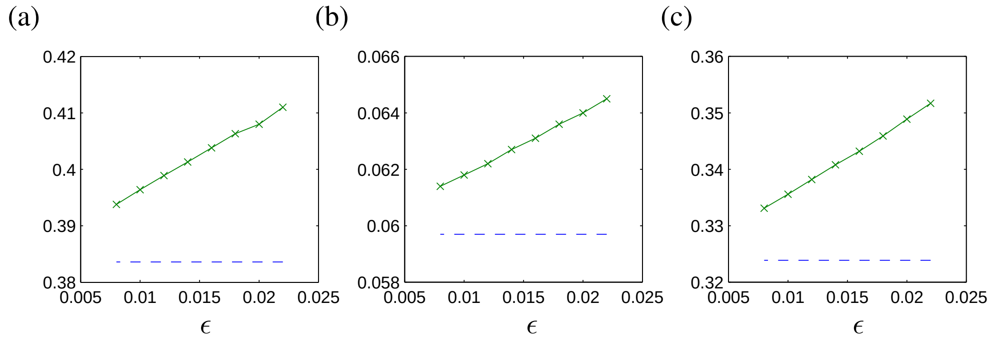

Figure 6.14 – Plots of the amplitudes of the weakly nonlinear prediction (blue dotted line) and the numerics (green curves). Plot (a) shows the k_1-mode, plot (b) the k_2-mode and plot (c) the k_3-mode. One can see that the amplitudes of the individual modes tend towards the weakly nonlinear predictions as ϵ is decreased. In this figure, $\Delta t = 0.00125$.

against the fully nonlinear numerical code. However, there are some numerical issues, such as the small Δt requirement for accurate three-wave resonance results, and the $\mathcal{O}(\epsilon)$ wobbles in the solution curves, which add complications to estimating period and amplitude. It would also be interesting to go to larger values of ϵ, in order to probe the effects of nonlinearity on triad interactions.

6.3 Finite-amplitude travelling wave solutions

Schecter et al. (2001) found 1.5D travelling wave solutions for rotating single layer SWMHD. These waves are periodic and finite amplitude, and exist when the effects of nonlinear steepening balance those of dispersion. These waves were found to fall into one of two types, categorised by their phase speeds. The analysis performed by Schecter is itself an extension to that of Ball (1960), in which the hydrodynamic case was studied, and selected periodic solutions were plotted.

One of the two types of travelling wave solutions has a maximum amplitude, at which the peaks develop into sharp cusp-like points, as first discovered in the hydrodynamic case by Ball (1960). These waves propagate with a greater phase speed than waves in the second branch of finite-amplitude travelling wave solutions, the amplitudes of which are not limited. For both branches, in the hydrodynamic and magnetic cases, infinitesimal amplitude waves are harmonic in form, as we would expect from linear theory.

The aim of this section is to further the work of Ball and Schecter by performing an analysis with a more thorough exploration of parameter space. We shall derive finite-amplitude travelling wave solutions of the SWMHD system, paying particular attention to wave properties such as period and amplitude. We shall also briefly consider stability of these solutions to perpendicular disturbances.

The governing equations are those of nonlinear SWMHD given by (6.14), together with the divergence-free condition on magnetic field, given by

$$\nabla \cdot \big((1+\eta)\mathbf{B}\big). \tag{6.20}$$

Putting y derivatives equal to zero and expanding about a nondimensional uniform basic state $\mathbf{u} = 0 + \mathbf{u}'$, $\mathbf{B} = \hat{\mathbf{x}} + \mathbf{B}'$, we have

$$\begin{aligned}
\frac{\partial \mathbf{u}'}{\partial t} &= -u\frac{\partial \mathbf{u}'}{\partial x} - f\hat{\mathbf{z}} \times \mathbf{u}' - \frac{\partial \eta}{\partial x}\hat{\mathbf{x}} + \mathrm{Ma}^2\frac{\partial \mathbf{B}'}{\partial x} + \mathrm{Ma}^2 B_x\frac{\partial \mathbf{B}'}{\partial x}, && \text{(6.21a)}\\
\frac{\partial \eta}{\partial t} &= -\frac{\partial u}{\partial x} - \frac{\partial}{\partial x}(\eta u), && \text{(6.21b)}\\
\frac{\partial \mathbf{B}'}{\partial t} &= \frac{\partial \mathbf{u}'}{\partial x} + B_x\frac{\partial \mathbf{u}'}{\partial x} - u\frac{\partial \mathbf{B}'}{\partial x}, && \text{(6.21c)}
\end{aligned}$$

where $\mathbf{u}' = (u, v)$ and $\mathbf{B}' = (B_x, B_y)$. Then equation (6.20) gives

$$\frac{\partial}{\partial x}\left(\eta + B_x + \eta B_x\right) = 0. \tag{6.22}$$

[For the interested reader there are some exact nonlinear solutions of multi-layer models in Appendix C.]

We start by seeking a travelling wave solution to equations (6.21). Given that the variables are functions of $\theta = x - ct$, we have

$$\begin{aligned}
0 &= c\frac{\partial \mathbf{u}'}{\partial \theta} - u\frac{\partial \mathbf{u}'}{\partial \theta} - f\hat{\mathbf{z}} \times \mathbf{u}' - \frac{\partial \eta}{\partial \theta}\hat{\mathbf{x}} + \mathrm{Ma}^2\frac{\partial \mathbf{B}'}{\partial \theta} + \mathrm{Ma}^2 B_x\frac{\partial \mathbf{B}'}{\partial \theta}, && \text{(6.23a)}\\
0 &= c\frac{\partial \eta}{\partial \theta} - \frac{\partial u}{\partial \theta} - \frac{\partial}{\partial \theta}(\eta u), && \text{(6.23b)}\\
0 &= c\frac{\partial \mathbf{B}'}{\partial \theta} + \frac{\partial \mathbf{u}'}{\partial \theta} + B_x\frac{\partial \mathbf{u}'}{\partial \theta} - u\frac{\partial \mathbf{B}'}{\partial \theta}. && \text{(6.23c)}
\end{aligned}$$

The wave speed c is unknown, and is to be determined subject to some specified boundary conditions.

These are supplemented by equation (6.22), which can be integrated to give

$$B_x = -\frac{\eta}{1+\eta}, \tag{6.24}$$

where the constant of integration has been put equal to zero. Other values of this constant can be chosen; we choose zero for simplicity, and because this value corresponds to physically relevant settings (i.e. everything decays towards $\pm\infty$. We also have a similar expression for the x-component of velocity from equation (6.23b), which is

$$u = \frac{c\eta}{1+\eta}, \tag{6.25}$$

again making the constant of integration zero. Note that the x-components of velocity and magnetic field satisfy $u = -cB_x$; in fact, the relation $\mathbf{u}' = -c\mathbf{B}'$ satisfies both (6.24) and (6.25) and the induction equation (6.23c). Substituting the relation $\mathbf{u}' = -c\mathbf{B}'$ into (6.23a) gives

$$0 = \frac{\zeta^2}{c^2}(c-u)\frac{du}{d\theta} - \frac{d\eta}{d\theta} + fv, \tag{6.26a}$$

$$0 = \frac{\zeta^2}{c^2}(c-u)\frac{dv}{d\theta} - fu, \tag{6.26b}$$

where $\zeta^2 = c^2 - \mathrm{Ma}^2$. Equations (6.26) can then be combined to eliminate v, giving

$$\frac{d}{d\theta}\left[\left(\frac{\zeta^2}{(1+\eta)^3} - 1\right)\frac{d\eta}{d\theta}\right] + \frac{c^2 f^2}{\zeta^2}\eta = 0. \tag{6.27}$$

This reduces to that of Schecter et al. (2001) with the appropriate scaling of θ.

6.3.1 Numerical generation of nonlinear wave solutions

We now consider waves that are periodic in θ. There are two distinct ways of solving the system given by equation (6.27): given a speed c, find the period of the waves; or, given the period, find c. These are considered in turn, in different sections. In both cases this is done numerically, by introducing ψ to give

$$\frac{d\psi}{d\theta} + \frac{f^2 c^2}{\zeta^2}\eta = 0, \tag{6.28a}$$

$$\psi = \left(\frac{\zeta^2}{(1+\eta)^3} - 1\right)\frac{d\eta}{d\theta}. \tag{6.28b}$$

From equation (6.27), the area under the surface profile, for one period, is given by

$$\oint \eta \, d\theta = 0, \tag{6.29}$$

so that we can set $\eta(0) = 0$ without loss of generality (a plot of the surface profile would pass through zero at some value of x; we transform to a frame of reference in which this value of x is zero). Our first focus is on the ‘finding the period, given c’ problem.

Equations (6.28) can be solved with a fourth order Runge-Kutta scheme. Since $\eta(0) = 0$, we have only two parameters to choose for our initialisation: ψ (initially ψ_0) and c. Having chosen ψ_0, we have

$$\psi_0 = \left(c^2 - (\mathrm{Ma}^2 + 1)\right) \left.\frac{d\eta}{d\theta}\right|_{\theta=0}, \tag{6.30}$$

so that, for fixed c, the smaller this value, the lower amplitude the waves will be. It turns out that there is a limit to how large we can choose ψ_0, which will be discussed later.

Once the initial parameters have been chosen, we advance some small distance $\Delta\theta$ to a further point in θ-space. This is repeated until η crosses the x-axis again, which is found by checking the sign of the product of two consecutive values of η. For a periodic solution, this will happen twice in one wavelength, and it is the second time which will signify one period of the wave. At the points where η changes sign, a further check that ψ has reached its initial value ψ_0 is required. Indeed, one can see by integrating (6.27) and using the definition of ψ given in (6.28b), that ψ is periodic (and has the same period) as η.

For initial values ψ_0 and c, the numerical scheme then produces the surface profile for one wavelength of the wave, along with the period, for periodic waves. Figure 6.15 is a plot in (ψ_0, c) parameter space ($\mathrm{Ma} = f = 1$) with colour representing period. There are two distinct areas in the image that contain periodic solutions: one with $c < 1$ and one with $c > \sqrt{2}$, as noted by Schecter et al. (2001). We shall discuss each of these in turn.

The $c^2 < v_A^2$ branch

The points in the area in figure 6.15 above the line $c = 1$ correspond to solutions for which $c^2 < v_A^2$ (so that $\zeta^2 < 0$), since $\mathrm{Ma} = 1$ in the plot. There are solutions for all values of ψ_0, and all c such that $c^2 < v_A^2$. As c gets smaller, the wavelength of the solutions increases, as illustrated in figure 6.16.

The $c^2 > v_A^2$ branch

The second shaded area of figure 6.15 corresponds to the region where $\zeta^2 > 1$. In this regime, not every possible pair of (ψ_0, c) gives a periodic solution. This is because there is a limit on how large we can make ψ_0, which determines the slope of the surface as it crosses the x-axis. After

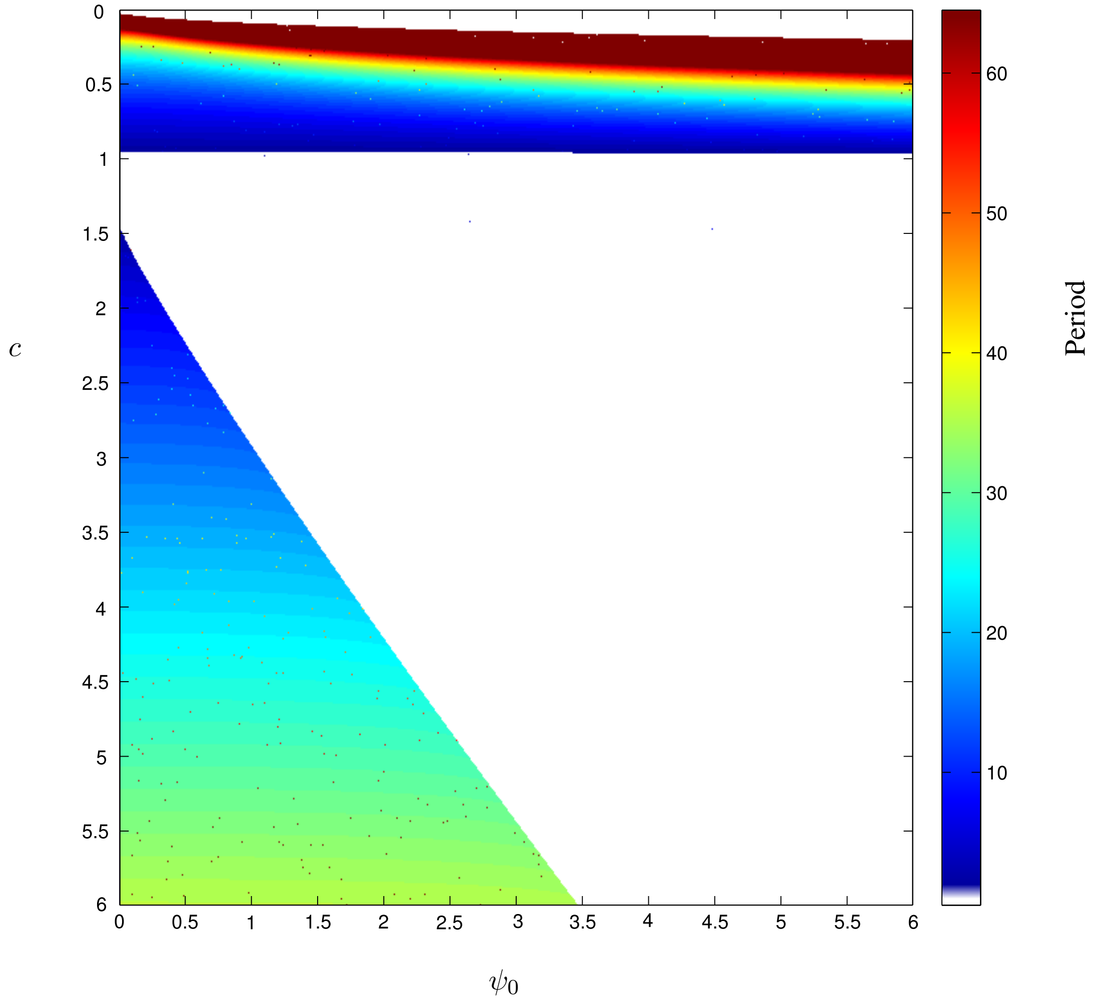

Figure 6.15 – The period of nonlinear periodic solutions of equations (6.28), with colour representing period, in (ψ_0, c) parameter space. In the white areas, no periodic solutions exist. Barely visible are tiny specks that do not appear to match the colour of their immediate surroundings. These are numerical artefacts, arising from the slight mismatch of the selected ψ and ψ_0 at the change of sign of η, making the numerical scheme continue on one wavelength. The white strip at the top of the image is due to numerical limitations; the scheme can only advance spatially so far. The period of the waves increases as c is decreased. In this figure $f = \text{Ma} = 1$.

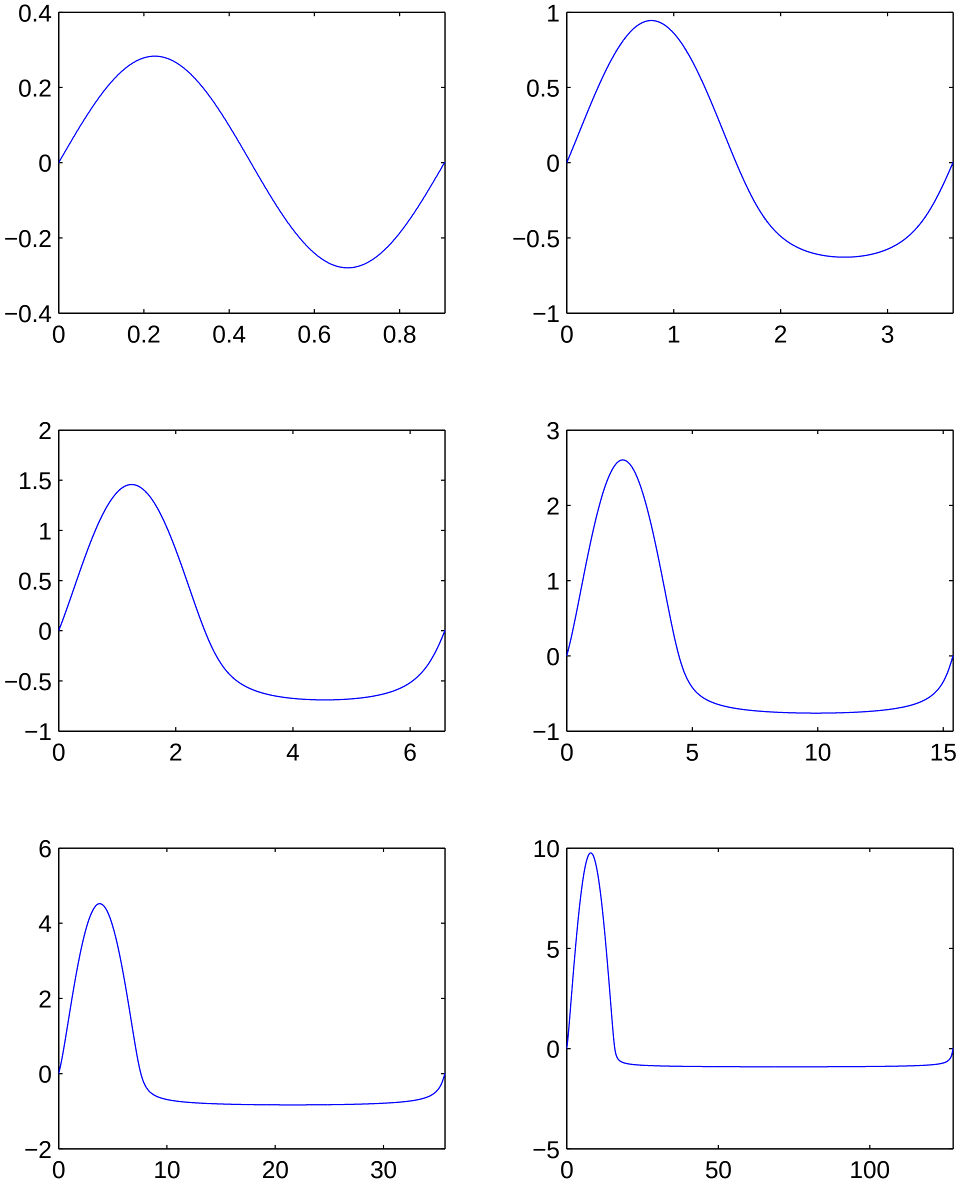

Figure 6.16 – A set of nonlinear solutions of equations (6.28), for a fixed value of $\psi_0 = 2$, for the Alfvén branch. The top right plot shows the almost sinusoidal small-amplitude surface profile for a value of c close to 1. As one reads from left to right, the value of c decreases; the values for the individual plots are $c = 0.99$, $c = 0.9$, $c = 0.8$, $c = 0.6$, $c = 0.4$, and $c = 0.2$. One can see that the lower the value of c, the higher the amplitude and the longer the wavelength of the waves. In this figure $f = \mathrm{Ma} = 1$.

multiplying equation (6.28a) by ψ and integrating, one gets

$$\psi^2 = -\frac{2f^2c^2}{\zeta^2}\int \eta\left(\frac{\zeta^2}{(1+\eta)^2}-1\right)d\eta, \tag{6.31}$$

which can be integrated by substitution, setting $\psi = \psi_0$ when $\eta = 0$, giving

$$\psi^2 - \psi_0^2 = f^2c^2\left(\frac{1}{\zeta^2}-\frac{1}{(1+\eta)^2}\right)\eta^2. \tag{6.32}$$

We now turn our attention briefly to the maximum of the surface perturbation. This occurs when $\psi = 0$, since ψ is a multiple of $\frac{d\eta}{d\theta}$ – see equation (6.28b). We thus have

$$\psi_0^2 + f^2c^2\left(\frac{1}{\zeta^2}-\frac{1}{(1+\eta_{max})^2}\right)\eta_{max}^2 = 0, \tag{6.33}$$

where η_{max} is the maximum height of the surface, which will depend on the initial value ψ_0. As the waves get higher amplitude, the peaks get sharper, so that the second derivative of η gets very large, as can be seen in figure 6.18. Thus the coefficient of $d^2\eta/d\theta^2$ in the expansion of equation (6.27) must get very small, so that the product balances the other terms. This occurs when $\eta_{max} = \zeta^{2/3} - 1$, by making the nested bracket in (6.27) equal to zero. Upon substitution into (6.33), this gives

$$\psi_0 = fc\left(\zeta^{-\frac{4}{3}} - \zeta^{-2}\right)^{\frac{1}{2}}(\zeta^{\frac{2}{3}} - 1), \tag{6.34}$$

which can be used to find the wave speed c at which the surface has a maximum height. Equation (6.34) is plotted in figure 6.17; it shows the boundary of the $\zeta^2 > 1$ region of figure 6.15 (but upside-down). Schecter et al. (2001) found an expression for the maximum height, but equation (6.34) is, we believe, new.

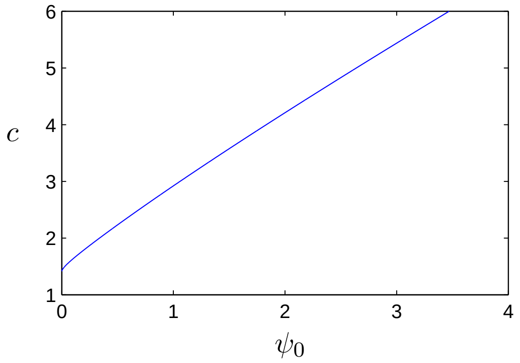

Figure 6.17 – A plot of the relationship between ψ_0 and c (given by equation (6.34)) at which wave crests become cusp-like, and the modes reach their maximum amplitude. As before, Ma $= f = 1$ in this figure.

A surface profile of a solution with (almost) maximum amplitude can be seen in the bottom right plot of figure 6.18, which shows surface plots for fixed ψ_0. Setting $\psi_0 = 2$, as before, there are periodic solutions of (6.27) for $c > 4.2$, using equation (6.34).

It should be noted, however, that close to this maximum amplitude, we have to be careful when using the shallow water model in this regime. The shallow water equations break down when the horizontal length scales become comparable to the vertical ones, and so we cannot use SWMHD to draw conclusions about the waves in this cusp-like limit. This does not mean that waves with cusp-like peaks do not exist: only that we cannot infer them with a shallow water analysis.

6.3.2 Numerical wave solutions – the shooting algorithm

One focus of the previous section was to find the period of travelling wave solutions to (6.27), given c. We now consider the complementary approach of fixing the domain (equivalent to fixing the period) and seeking possible values of c. This is achieved using a shooting algorithm.

The algorithm works by prescribing $\eta(0) = 0$, as before, and guessing values of ψ_0 and c. The system is then integrated forward to 2π, using equations (6.28); the aim is to find a periodic solution. This shooting methodology is standard procedure (see, for example, Press, 2002).

Numerical integration is realised using a fourth order Runge Kutta scheme as before. However, this time η is only advanced until 2π, at which a discrepancy vector is calculated using $(\eta(2\pi) - 0, \psi(2\pi) - \psi_0)$. If this vector is within a small tolerance of 0, then the solution is accepted, and the initial values ψ_0 and c give a 2π-periodic solution of (6.27).

If, more likely, the discrepancy vector is not close enough to zero, then ψ_0 and c need to be altered so that the resulting surface profile has the required wavelength. This is achieved by advancing ψ_0 fractionally (say 1%) and applying the above procedure (a 'shot'). Another shot is then executed with the original ψ_0, but a similarly modified c, the discrepancy vectors calculated in each case. These are then used to estimate derivatives of the discrepancy vector with respect to ψ_0 and c, which are then used to populate a Jacobian. The final part of this step involves solving a system of two equations with elements of the Jacobian as coefficients, which are equivalent to two incarnations of the extended chain rule. This gives new values of ψ_0 and c, with which we apply the whole process again. This stops when the discrepancy vector is smaller than the specified tolerance.

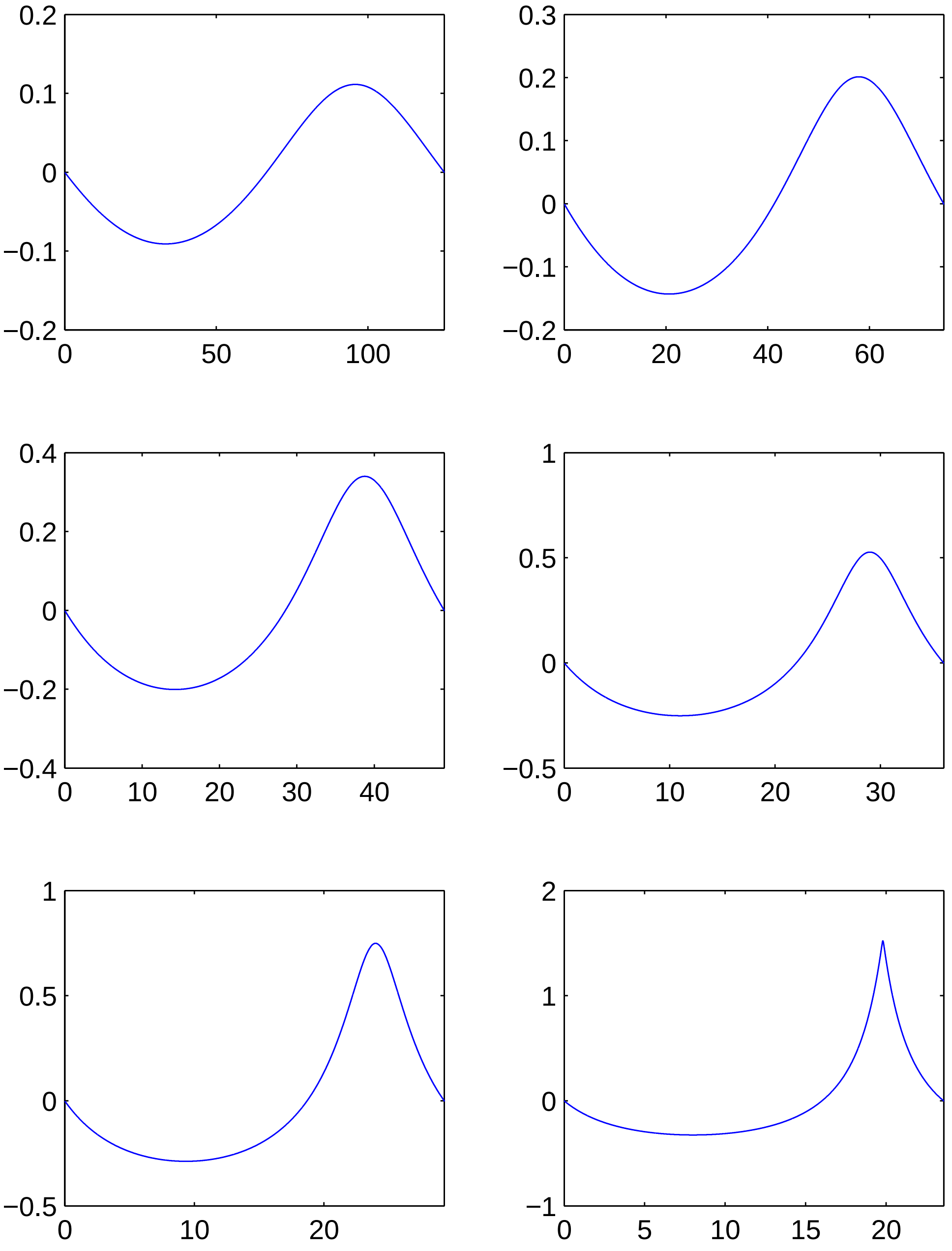

Figure 6.18 – A set of nonlinear solutions of equations (6.28), for a fixed value of $\psi_0 = 2$, for the $\zeta^2 > 1$ branch. The top right plot shows the almost sinusoidal shape of a low amplitude fast moving wave. As one reads from left to right, the value of c decreases; the values for the individual plots are $c = 20$, $c = 12$, $c = 8$, $c = 6$, $c = 5$, and $c = 4.21$. One can see that the lower the value of c, the higher the amplitude and the sharper the maximum. The period also decreases as c is increased, which is verified by figure 6.15. Here, $\mathrm{Ma} = f = 1$.

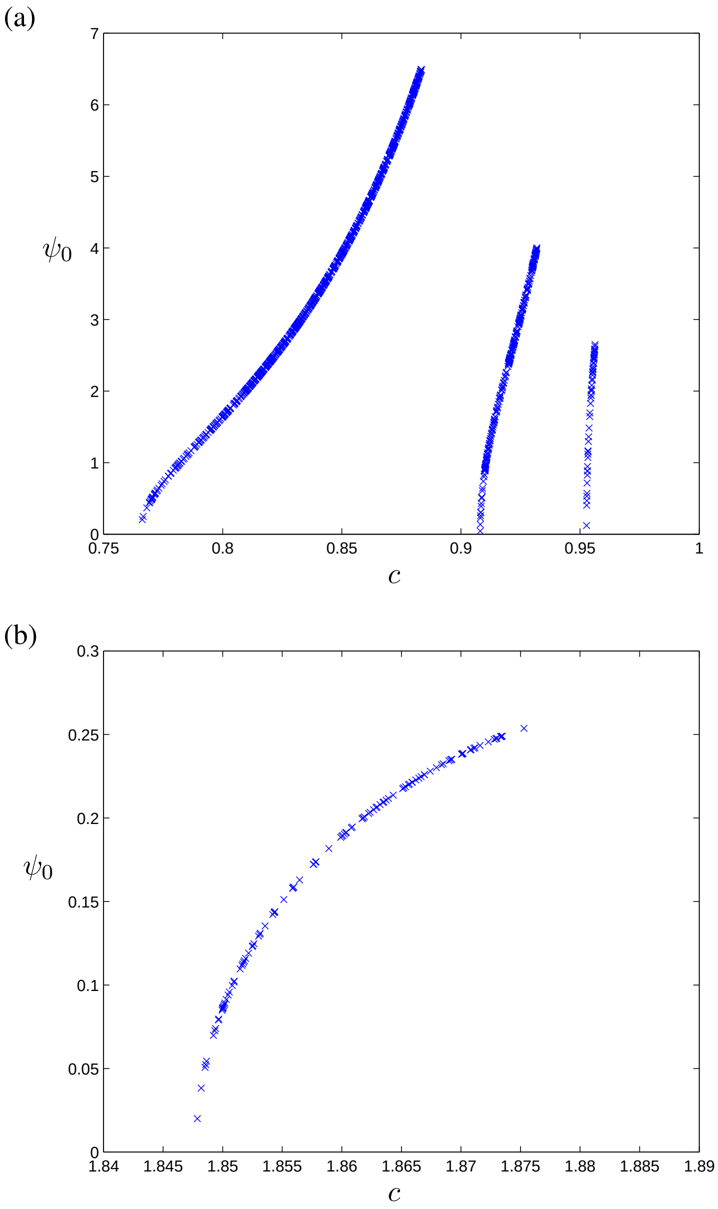

Figure 6.19 – Values of (ψ_0, c) with 2π periodic solutions, found using a shooting algorithm. For aesthetic reasons the graph has been split into two: (a) points corresponding to the $\zeta^2 < 0$ branch and (b) the $\zeta^2 > 1$ branch. The axes have been swapped for easier reconciliation with figure 6.15; rotating these figures 90^o clockwise (or one's head anticlockwise!), the curves these points trace overlap the deep blue (2π) of the image. The exceptions to this are an extra two sets of points in plot (a): the left hand set of points represent 2π-periodic solutions, whereas the middle and far right sets represent those with period π and $\pi/2$ respectively. These extra points were picked up by the shooting algorithm because they produce surface profiles that obey the rules of the scheme, which had no way of distinguishing harmonics. In this figure, $\mathrm{Ma} = f = 1$ as before.

This algorithm has been used to produce figure 6.19, which shows the (ψ_0, c) pairs that produce 2π-periodic solutions, for Ma $= f = 1$. The code was initiated with values of ψ_0 ranging from -7 to 7 in increments of 0.05, and similarly for c. Most of these starting pairs of points would not have converged at all, while some would have converged to points in (ψ, c) space far from where they started. The results of this shooting method are plotted as points in figure 6.19; this image is reflected both in the c-axis, so that 'upside-down' solutions exist, and in the ψ-axis, so that waves propagating to the left also exist. Leftward moving and upside down waves were not considered in the previous section, although they are supported.

The many crosses in figure 6.19 appear as if they are tracing out curves in (ψ_0, c)-space, so that there is a continuous spectrum of values for c. The left hand set of points in figure 6.19a represent the 'fundamental' waves, which have a period of 2π, and the other sets of points represent 'higher harmonics', which we shall not discuss here. The points tracing out the fundamental curve correspond to the dark blue points in the upper section ($c < 1$) of figure 6.15, the colour of which represent the value 2π. Similarly, the curve traced in figure 6.19b match the corresponding points in the $c > \sqrt{2}$ section of figure 6.15.

There would be no bound to the curve traced out in figure 6.19a, since the amplitude of these waves is not limited. However, the curve implied by 6.19b would have an end (the upper right of the curve), at which the sharp-crested waveforms occur. Indeed, the point with the highest value of c, close to the end of the curve, represents a wave with $c \approx 1.875$ and $\psi_0 \approx 0.255$, and these values satisfy the condition (6.34) found in the previous section.

6.3.3 Initialising the numerical solver with an exact nonlinear solution

At the beginning of this chapter, the dispersive influence of rotation was introduced to counter the steepening effects of nonlinearity. In section 6.3.1, exact nonlinear solutions were found that balance these two effects perfectly, and propagate without change of shape (Schecter et al., 2001). Whilst being interesting in their own right, such solutions are also useful to test the nonlinear code. The code has been used to check the evolution for $0 < t < 10$ for waves corresponding to several of the points shown in figure 6.19, including waves from both categories. We find that the numerical results have very little error for this range of times.

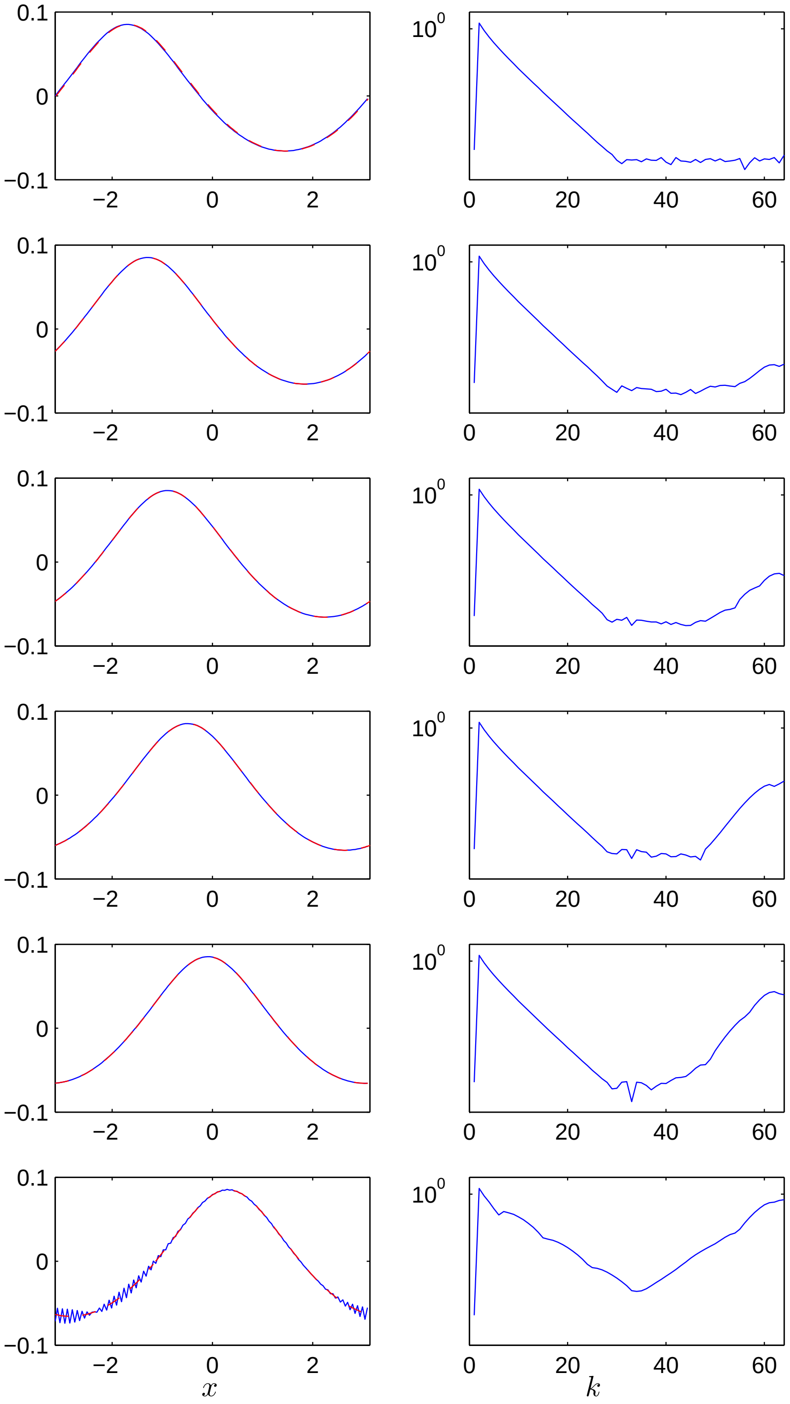

Figure 6.20 – Numerical results from the 1D code without dealiasing, initialised with a travelling wave solution with $c = 1.85$, and $\psi_0 = 0.08$ (Ma $= f = 1$ as before). On the left are snapshots of the surface profile, with red dotted curves representing the 'true' solution (solved analytically in section 6.3), and the blue representing the numerical results. The plots on the right show the spectrum, which in an ideal world would not change over time. The top row of plots is at time 0, and each subsequent row is 10.4 time units after the previous. The solution curve develops grid scale features after some time, as seen on the bottom left plot. The y-axis is logarithmic, so that the spectrum for large k (small scales) grows to become $\mathcal{O}(1)$.

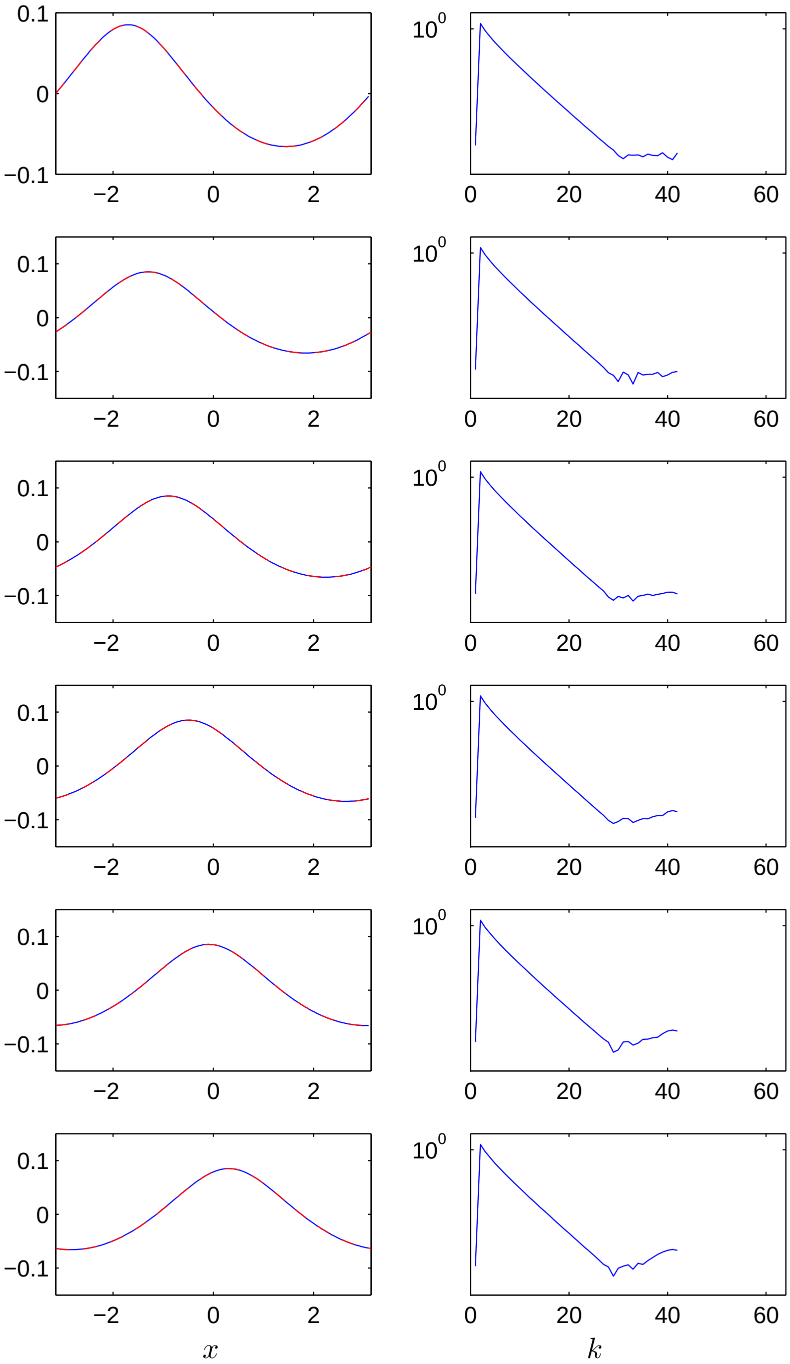

Figure 6.21 – Numerical results from the 1.5D code *with* dealiasing, initialised with the same fully nonlinear solution. The surface does not grow grid scale features when dealiasing is employed, and the height spectra (right plots) remain similar as time is increased. This plot can be compared directly with figure 6.20, in which dealiasing is turned off.

However, eventually we run into another problem: if left long enough the code breaks (see figure 6.20). We find that the small scales are gaining energy somehow, even though the surface spectrum should be the same for all times for a mode that does not change shape as it propagates. The right hand plots of figure 6.20 display the surface spectrum, corresponding to the surface plots (on the left hand side). Initially, the modes with the highest wavenumbers have coefficients which hover around zero (although not exactly – they take values around 10^{-16}, which is machine precision for our numerical code). Over time, the smallest scales gain energy, although this is *not* through nonlinear steepening, as one can see on the left hand plots.

This phenomenon is known as aliasing, and arises because the spectral code samples at discrete data points, and has no way of discriminating between a high frequency and a low frequency interpolator. For example, consider the (x, y) data points $(0, 0)$, $(\pi/4, 1/\sqrt{2})$, $(3\pi/4, 1/\sqrt{2})$, and $(5\pi/4, -1/\sqrt{2})$. These can be interpolated by $y = \sin x$, which is a low-wavenumber solution that one may expect. However, they can also be interpolated by $y = \sin 3x$, a higher wavenumber interpolator.

This problem is overcome by zeroing the spectra of η, u, v, B_x and B_y for the highest third of the wavenumbers (see Orszag 1971). For example, the results of the code pictured are resolved at $N = 128$ gridpoints. This means that the code can handle modes with wavenumbers up to $N/2 = 64$, of which the highest third are $44, 45, 46, \cdots 64$. To counter aliasing, we zero the spectral components of u, v, η, B_x and B_y corresponding to these wavenumbers. Figure 6.21 shows the effect of dealiasing, can be compared directly to figure 6.20, which had none.

6.4 Fully two-dimensional simulations

The real world is not one-dimensional, and physical thin fluid layers are described more accurately by considering a 2D shallow water model. The previous 1.5D analysis is limited because it cannot model flows with nonzero y-dependence. There are interesting dynamics that occur in 2D but not in 1D; for example, where a solution (e.g. a travelling wave) is unstable in 2D, but not in 1D. This is one case we will consider in this section. It would be interesting to understand the dynamics when d/dy is nonzero, and for this we require a 2D numerical solver.

Until now, the results shown have been from the 1.5D code, in which all y-derivatives are set to zero, but the equations still contain y-components of velocity and magnetic field so that rotation

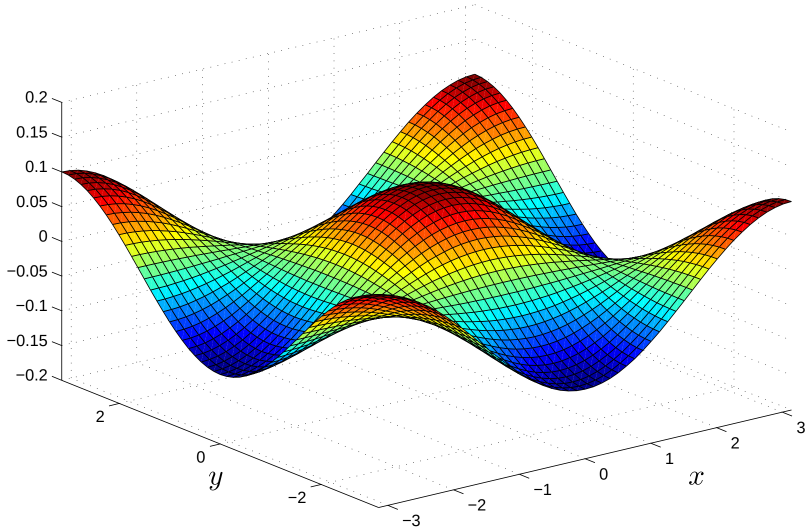

Figure 6.22 – A possible linear initialisation for the 2-D code. The surface is $\eta = 0.1\cos(x)\cos(y)$, which we can advance in time exactly for comparison with the code.

can be taken into account. In this section, we allow all variables to depend on y as well as x and t. The variables are then represented in the numerics as matrices, with element (i, j) giving the value at that point on the mesh. They are then best visualised using a surface plot, as in figure 6.22. The 2D numerical code has some small differences to the 1.5D code. It includes two wavenumber matrices that differentiate in spectral space (one for x and one for y), rather than the single vector in the 1.5D analysis, and the data saving methods in each timestep are slightly different, but otherwise it is very similar to the 1.5D code.

6.4.1 Code verification

In the linear regime, with all nonlinear terms set to zero, we can examine the numerical results. One exact linear solution which is doubly periodic in our domain $(-\pi, \pi)$ is

$$\eta = A\cos(x)\cos(y)\cos(t), u = \frac{1}{2}A\sin(x)\cos(y)\sin(t), v = \frac{1}{2}A\cos(x)\sin(y)\sin(t),$$
$$B_x = -\frac{1}{2}A\cos(x)\cos(y)\cos(t), B_y = \frac{1}{2}A\sin(x)\sin(y)\cos(t). \quad (6.35)$$

The initial surface (i.e. with $t = 0$) is plotted in figure 6.22. In a similar manner as in the 1.5D case, we can initialise the code with (6.35), and check that the linear part of the scheme is working. To check the efficacy of the nonlinear components of the code, we can initialise with an exact nonlinear solution in a similar manner as in the 1D case.

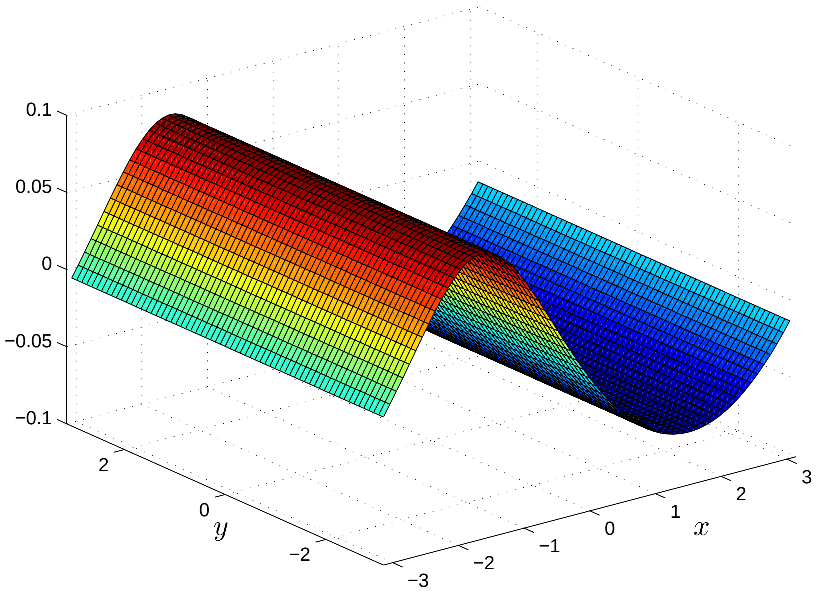

Figure 6.23 – A possible nonlinear initialisation for the 2-D code. The surface is wave-like in the x-direction, with an exact nonlinear solution found earlier in the chapter as the profile, and independent of y.

Nonlinear checks

For nonlinear runs, the code is dealiased by default in order to stop the high wavenumbers gaining energy erroneously. By inputting initial conditions that are independent of y and have an exact nonlinear solution profile in the x-direction, we can test the nonlinear parts of the 2D code. We do this by choosing an exact 2π-periodic solution as before, and generating a surface that is wave-like in the x-direction and constant in the y-direction, as in figure 6.23. The y-independence remains over time, and the wave propagates without change of shape and at a constant speed. A similar initialisation that is wave-like in y and independent of x has also been initialised, with the same results. In this case, however, the ambient magnetic field has to be altered so that it points in the direction of the wavevector.

6.4.2 Perturbations to an exact nonlinear solution

The propagation of the y-independent nonlinear wave has helped check that the 2D numerical scheme is doing what we want it to. This y-independence is conserved as time progresses, as expected. An interesting question is whether perturbations that can depend on y of this wave would grow or decay over time. To answer this question, we initialise with the exact nonlinear solution, with an added small sinusoidal perturbation.

We now consider how to choose an initial condition that is a weak perturbation of an exact nonlinear travelling wave solution. Denoting the exact solution variables with a subscript e, and the added perturbations with a tilde ($\sim$), gives

$$\eta = \eta_e(x,t) + \tilde{\eta}(x,y,t), \tag{6.36}$$

and similarly for the other variables. They, of course, have to satisfy conservation of mass and the condition on magnetic field. The former of these is given by

$$\frac{\partial \eta}{\partial t} + \frac{\partial}{\partial x}\big((1+\eta)u\big) + \frac{\partial}{\partial y}\big((1+\eta)v\big) = 0. \tag{6.37}$$

Now, we know that (6.37) holds for the exact nonlinear solution (i.e. the equation holds when all variables have a subscript e), because we have verified this as part of our code checks. We then substitute (6.36), along with similar expressions for the other variables, into equation (6.37) and cancel off the appropriate terms to give

$$\frac{\partial \tilde{\eta}}{\partial t} + \frac{\partial}{\partial x}\big(\tilde{u} + \eta_e\tilde{u} + \tilde{\eta}u_e + \tilde{\eta}\tilde{u}\big) + \frac{\partial}{\partial y}\big(\tilde{v} + \eta_e\tilde{v} + \tilde{\eta}v_e + \tilde{\eta}\tilde{v}\big) = 0. \tag{6.38}$$

Given $\tilde{\eta}$, we have a choice of expressions for $\tilde{u}$ and $\tilde{v}$, since these are the two unknowns in equation (6.38). We choose to set $\tilde{u} = 0$; this not only simplifies proceedings, but is also sensible, since the perturbation is in the y-direction. If we further stipulate that the perturbation of the surface is given by

$$\tilde{\eta} = a\sin\big(k(y-\chi t)\big), \tag{6.39}$$

where a is a constant amplitude and k is the wavenumber of the disturbance, then equation (6.38) becomes

$$-ak\chi\cos\big(k(y-\chi t)\big) + a\sin\big(k(y-\chi t)\big)\frac{\partial u_e}{\partial x} + \frac{\partial}{\partial y}\big((1+\eta_e+\tilde{\eta})\tilde{v} + \tilde{\eta}v_e\big) = 0. \tag{6.40}$$

Upon integration with respect to y, we obtain

$$\tilde{v} = \frac{a(\chi - v_e)\sin\big(k(y-\chi t)\big) + \frac{a}{k}\frac{\partial u_e}{\partial x}\cos\big(k(y-\chi t)\big)}{1+\eta_e + a\sin\big(k(y-\chi t)\big)}. \tag{6.41}$$

[Note that one need not consider time dependence in the initial conditions. Simply setting $\tilde{\eta} = a\sin ky$ and putting $\tilde{u} = \tilde{v} = 0$ would also be a valid choice of velocity for initialisation.] The magnetic perturbations have to satisfy

$$\frac{\partial}{\partial x}\big((1+\eta_e+\tilde{\eta})(1+B_{xe}+\tilde{B}_x)\big) + \frac{\partial}{\partial y}\big((1+\eta_e+\tilde{\eta})(B_{y_e}+\tilde{B}_y)\big) = 0. \tag{6.42}$$

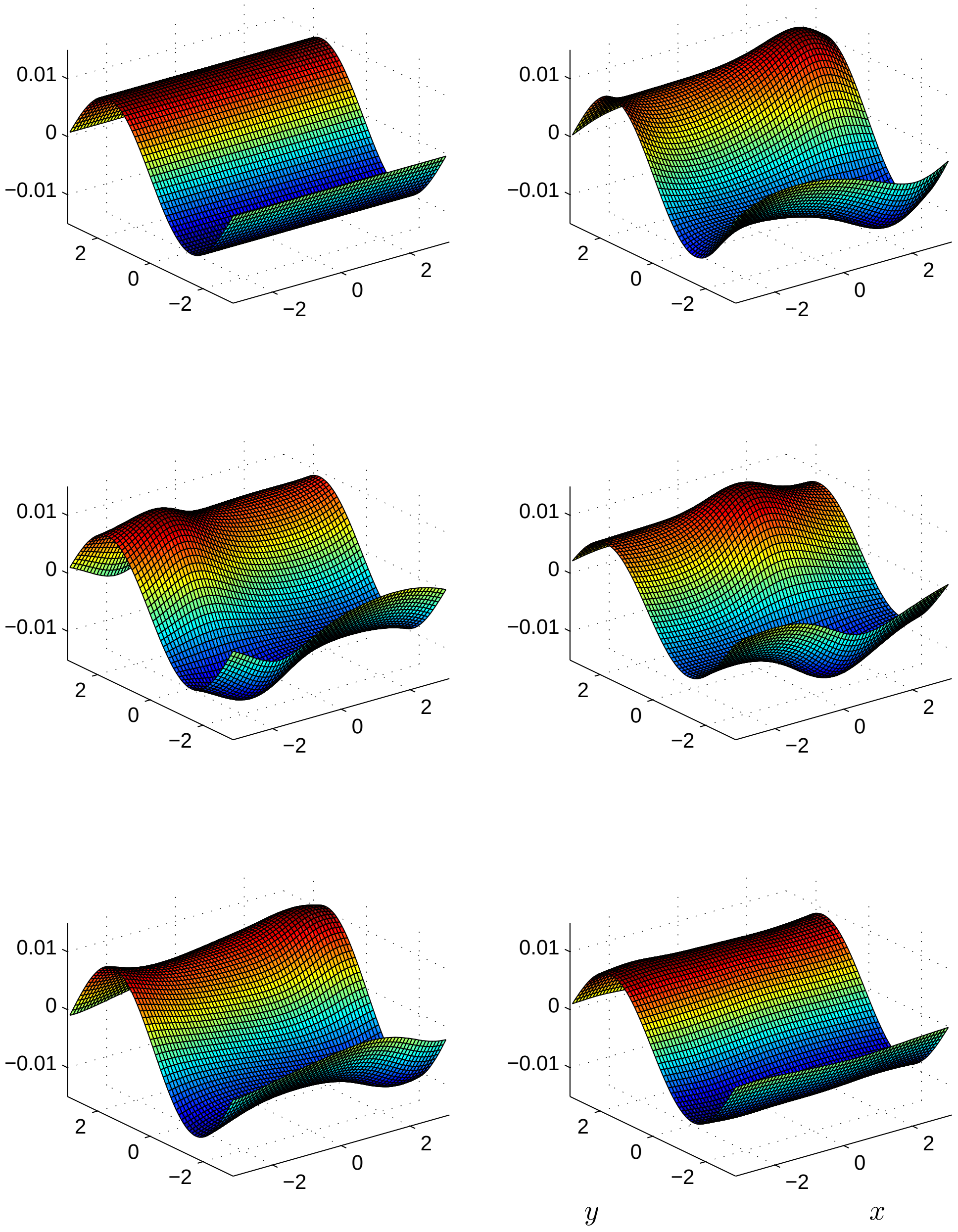

Figure 6.24 – Snapshots of the difference in surface heights between the perturbed and non-perturbed exact nonlinear solution, for the case $k = 1$. Initially (top left), the difference is simply $0.01\sin(y)$. At time $t = 4.5$ (top right plot) a dependence on x has developed. Each subsequent plot is taken at intervals of 4.5. The dependence on x eventually reduces to approximately zero again, as seen in the bottom right plot in which $t = 22.5$. For these figures, $\chi = 1$, with $\mathrm{Ma} = f = 1$.

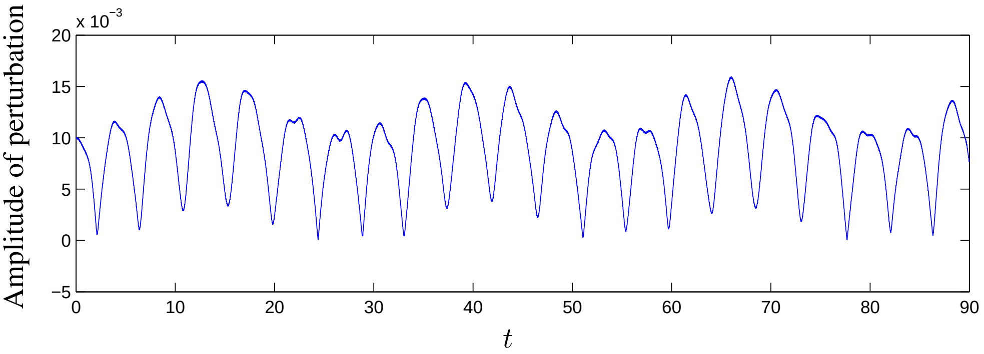

Figure 6.25 – A plot of the maximum amplitude of the perturbation of the travelling nonlinear solution displayed in figure 6.23. The oscillatory behaviour of the amplitude of the disturbance is clearly visible; moreover, the modulations themselves modulate over a greater time. For this plot, parameters reflect those of figure 6.24.

By choosing $\tilde{B}_x = 0$, this gives

$$\tilde{B}_y = \frac{\frac{a}{k}\frac{\partial B_{xe}}{\partial x}\cos\big(k(y-\chi t)\big) - aB_{y_e}\sin\big(k(y-\chi t)\big)}{1+\eta_e + a\sin\big(k(y-\chi t)\big)}. \tag{6.43}$$

The numerical results for this initialisation for the wavenumber $k = 1$ can be inferred from figure 6.24, which displays the difference between the evolution of the perturbed surface and that of the non-perturbed exact nonlinear solution, i.e. the evolution of $\tilde{\eta}$. The perturbations do not appear to grow nor decay over time; rather, they oscillate in a complicated manner. An x-dependence also grows and decays in a finite time, so that the perturbed quantities develop a ‘wobble’ in the x-direction which decays away again. However, the wobble does not necessarily decay to its initial amplitude of zero before rising again; it may take more than one modulation to complete a cycle, as displayed in figure 6.25. This perturbation seems to be stable, but it may be necessary to run for a longer period of time.

Of course, there may be wavenumbers other than $k = 1$ that are unstable; however, none have been found. One can also vary χ, the speed of the perturbation, if the initialisation is chosen as in this section. Although different values of k and χ give differing modulation patterns, no long-term growth has yet been detected. However, one restriction we encounter with the numerics is that the higher the value of k, the higher the gradient of the surface, owing to the fact that more waves have to be fit into the grid. Nonlinear steepening then overtakes the dispersive effects of rotation. Similarly, when χ is set too high, the perturbations develop steep fronts to much the same effect.

It appears that the exact nonlinear solution tested here is stable to perpendicular perturbations, but this is not confirmed in this work. It could be the focus of further studies to prove or disprove this, by testing more values of k, χ, or by perturbing another exact solution, perhaps one in which wave crests are very sharp as in figure 6.18.

6.5 Summary and Discussion

In this chapter we considered waves in rotating SWMHD, with a focus on two main calculations: three-wave resonance in shallow water, and nonlinear travelling waves.

One new result from section 6.2 is that three-wave resonance is supported in the rotating single layer shallow water model *only* in the presence of magnetic field. Triads in the SWMHD system travel at different speeds (with one travelling in the opposite direction to the other two). The period of the modulations of energy exchange is affected by magnetic field strength. Unlike the analysis in section 5.4, in which the system was weakly non-hydrostatic and non-rotating, the work in this chapter is on the shallow water model, and so we are able to compare the weakly nonlinear predictions with nonlinear results from a numerical code. The comparison shows a good agreement between the theory and numerics, especially for low amplitude waves.

The triad used in sections 6.2 and 6.2.3 is found with the values $\mathrm{Ma} = 1$ and $f = 1$. Appealing to table 1.1, we estimate that $\mathrm{Ma} = 1$ is a sensible figure for the tachocline, but we have not yet discussed the choice of rotation parameter. The measure of rotation f is actually a scaled vertical rotation rate of the Sun in this work, and so it is zero on the equator. In scaling the rotation parameter, we multiply by $L/\sqrt{gH}$, and so close to the poles, in which the rotation rate is around $400\,\mathrm{nHz}$ (see, for example, Hughes et al. 2007), giving a scaled rotation rate of around $f \approx 3000$. We then have a range of $0 \leq f \leq 3000$ for the tachocline; our choice of $f = 1$ falls well within these limits. If the typical horizontal length scale of a wave exceeds the Rossby deformation radius ($L_D = \sqrt{gH}/f = 354/f$, rotation plays a role in the evolution of the wave.

The manner in which energy is transferred between the waves in the triad depends on the initial energy of each mode, as well as the wavenumbers of the modes. For the mode with the lowest wavenumber, the modulations are smaller than the others, with the main exchange of energy between the modes with the higher wavenumbers. As the disturbance amplitude is increased, the numerical modulations deviate from the predictions in amplitude and period. The manner in which they deviate depends on the initial energy of each mode; some (as in the first example in section 6.2.3) decrease in amplitude and period as ϵ is increased, whereas others (such as the second example) increase in both amplitude and period. We find that for small amplitude perturbations, the timestep has to be small.

Although we chose one set of wavenumbers and frequencies assigned to waves in a triad, there are many other such triads in the rotating SWMHD system, even if (as we are in this thesis) one is restricted to choosing wavenumbers that are multiples, but not doubles, of each other. This restriction arises from the need to fit integer numbers of waves exactly inside a periodic box. In the tachocline, of course, no such restriction is needed, and wave triplets with any of the wavenumber combinations in the dark blue regions of figure 6.1 could resonate.

There are two families of exact nonlinear travelling solutions of the 1.5D SWMHD equations. Expanding on the work of Schecter et al. (2001), we found that one of the branches supports waves with (almost) flat troughs taking up such a large proportion of the wavelength that they appear to be solitary modes (see figure 6.16). They propagate without change of shape, slower than the Alfvén speed, and there is no limit to their amplitude or period. They do, however, have a slightly different shape than the sech^2 solution of the KdV equation, although in practice one would tell them apart by their amplitudes; solitary waves arise from weakly nonlinear analysis and so would be of small amplitude, whereas the exact nonlinear solutions that are of a similar form are necessarily high amplitude.

The second branch of exact nonlinear solutions consist of waves that travel faster than the Alfvén speed. There is no limit to how fast they can go, or how long their periods can be. There is, however, a limit on their amplitudes; one can quantify this for a given phase speed. At this maximum amplitude, the waves develop cusp-like crests. Although viscosity is low in the tachocline (it is around $\nu \approx 27\text{cm}^2\text{s}^{-1}$ – figure taken from Hughes et al. (2007), giving a Reynolds number of around Re=10^{10} for fluid moving at $1\text{m}\,\text{s}^{-1}$), it would work to smooth out any sharp changes in gradient. However, this analysis describes planetary scale waves, and so to an observer, there may well be cusp-like features. There would also be the turbulent motions of the surrounding fluid acting on the wave, and such a fragile form would be deformed quickly, even if the wave mode is stable to most perturbations. The travelling wave analysis can be generalised and applied to the n-layer system: see Appendix C for details. Fully nonlinear internal waves in the hydrodynamic 2-layer model were also considered by Choi and Camassa (1999).

Extending the work on 1.5D dynamics, a 2D numerical scheme was used in conjunction with the travelling wave solutions to examine some effects of y-dependence. It appears (although this has not been proven) that this solution is stable to perturbations in the perpendicular direction to the wavevector. There are, however, modulations in the amplitude of the disturbance that depend on the speed and the wavenumber of the travelling disturbance, although for no combination found do these grow over time. This may indicate that such exact travelling forms are stable, and any that exist in the tachocline may be robust to at least some of the constant nudges and machinations of the surrounding turbulent fluid.

Chapter 7

Conclusion

7.1 Overview

The SWMHD framework has been used in recent years to study waves and instabilities in astrophysical fluid dynamics (see, for example, Gilman 2000, Dikpati and Gilman 2001, Zaqarashvili et al. 2008, Mak 2013). There has been a lot of work on instabilities (see Dikpati and Gilman 2001, Mak 2013). Most studies involve the single layer system, but there are some that utilise the multi-layer set-up; Zeitlin (2013) briefly considered the n-layer SWMHD model and proposed the equations for the 2-layer system (at the same time, incidentally, as the n-layer system was being developed for this thesis). Some work has been on waves (see, for example, planetary waves in Zaqarashvili et al. 2009, Rossby waves in Zaqarashvili et al. 2008, linear waves in Heng and Spitkovsky 2009, and nonlinear waves in Schecter et al. 2001 and London 2014).

This thesis provides a more detailed and comprehensive study of SWMHD waves in closely related systems. The main simplifying assumption in this work is the Cartesian geometry on which it is based, but with a large range of topics including: a careful analysis of the types of waves in multi-layer systems (in particular the 1-, 2- and 3- layer models); weakly nonlinear and weakly non-hydrostatic extensions, which is completely new; and numerical solutions of the rotating SWMHD equations.

As we have discussed, an obvious application of this work is to the solar tachocline. Here, the magnetic field is strong relative to that of the surrounding convection and radiative zones, and there is stable stratification; the gravity wave speed is of the same order as the Alfvén speed, justifying the study of completely coupled SWMHD. In reality, waves propagating in the tachocline would be influenced by many factors, including shear flows, curvature, density stratification, rotation and magnetic fields. In this work, we focus on the latter three of these, and exploit the small aspect ratio of vertical to horizontal length scales in the tachocline to simplify the fluid equations of motion.

System formulation and linear results

There are two main themes in Chapters 2, 3, and 4. The first is the formulation of the SWMHD model. Multi-layer equations are derived (this was achieved at the same time as Zeitlin 2013), and the first qualitative comparison of the SWMHD and 2D compressible MHD systems was undertaken, including a discussion of the breaking of the analogy between the two systems with the introduction of magnetic field.

The second theme concerns the dynamics of linear perturbations to a state of rest. One naturally arising question is, is this stable? The answer to this is yes, even in the multi-layered model with a structured magnetic field. Another pertinent question involves the energy of the system, and what form the energy flux takes. This has been derived, and with it a newly discovered shallow water Poynting flux, which differs from the traditional 3D MHD Poynting flux, and describes how magnetic energy is transported in the SWMHD system.

An overarching question in Chapters 2, 3, and 4, is how stratification and magnetic field compete. Stratification effects lead to gravity waves, and magnetic effects to Alfvén waves, and much of this work focuses on hybrids of the two. These magneto-gravity waves have interesting limits and properties, particularly in the multi-layer models: strong field in one layer can imbue hydrodynamic properties in a mode; the thinner a magnetised layer the more of an effect the magnetic field has in the rigid lid model; and modes can propagate with interfaces and surfaces locked in a flat horizontal state, to name but a few.

The triumph of the multi-layer system is that it enables a more complicated basic state magnetic field, and so is much more applicable to the tachocline, through which permeates a horizontal field with unknown vertical dependence.

Weakly nonlinear non-hydrostatic results

A limitation of SWMHD is that it assumes perfect hydrostatic balance in the vertical, owing to the small aspect ratio of vertical to horizontal length scales. However, this is not exactly the case, and in hydrodynamic shallow water it is well-known that weakly non-hydrostatic effects can lead to other important dynamics. In particular, waves become weakly dispersive, and when this dispersion balances the steepening effects of nonlinearity there is the possibility of isolated travelling waves (solitons).

The influence of magnetic field is restricted to a rescaling of the long-timescale in which these weakly nonlinear dynamics occur, in the single layer case. In the 2-layer rigid lid case, however, magnetic field structure affects more than this long timescale; it also affects the types of solution one gets. In the tachocline, where magnetic field is most likely dependent on vertical coordinate z, the 2-layer rigid lid model would be most relevant. For boundary conditions that correspond to perturbations that are zero at infinity, which may be most apt for the tachocline, the soliton solutions have width, amplitude, and speed that all vary with magnetic field geometry. Such travelling solitary waves may exist at a fluid-fluid boundary within the tachocline, as in the model, but they are more likely to be internally propagating in a continuously stratified medium.

Cnoidal waves, too, are supported by the 2-layer rigid lid model, and most likely exist in the tachocline. The cnoidal parameter, which describes how ‘sinusoidal’ the waves are, depends on the magnetic field strength and structure; it is unlikely that waves propagating in the tachocline are perfect sine curves for these reasons.

The phenomenon of three-wave resonance is also supported in the single layer non-hydrostatic model, whereby three wave modes exchange energy periodically. The timescale on which this periodic exchange occurs is dependent on magnetic field strength. In the tachocline, such dynamics would be manifest as a sum of the three waves in the triad perturbing, say, an internal interface. Over time, this would change as the waves propagate and eventually return to its original form. It is unlikely that this would be the only factor perturbing the interface; there would surely be other waves (and possibly other triads) disturbing the fluid alongside.

Rotating shallow water and nonlinear results

Rotation often plays an important role in astrophysical bodies. The introduction of rotation into the SWMHD model would allow for more complex inertia-magneto-gravity waves (Schecter et al. 2001; Dellar 2002a; Zeitlin 2013). The key point is that in the presence of rotation, waves are dispersive, allowing for interesting nonlinear/dispersive balances.

It is known (see, for example, Zeitlin 2007) that three-wave resonance is not possible in rotating hydrodynamic shallow water systems. However, here we show that three-wave resonance is possible in SWMHD; we analyse this new effect. The set of possible triads is much more limited than in the weakly non-hydrostatic non-rotating case. This limitation is actually a blessing, as in the non-hydrostatic case, each member of a triad was itself a member of infinitely many more triads, some containing modes which had wavenumbers that were double those of other modes in the same triad. This is not described by the equations of three-wave resonance, and so cannot be accounted for. In reality, rotation is present in the tachocline, and so the modes comprising the triad do not have the same propagation speed and direction, as they do in the non-hydrostatic case; they have different phase speeds, with one travelling in the opposite direction to the other two.

The predicted modulations from weakly nonlinear theory match those produced by a numerical solver for small perturbations, keeping in mind that the timestep in the scheme has to be small in this regime for accurate results. How the modulations deviate from the weak predictions depends on the initialisation parameters; for one choice, the amplitude and period increases, and for another it decreases, as the perturbation amplitude is increased.

There also exists exact nonlinear travelling-wave solutions in SWMHD, as first derived by Schecter et al. (2001), that are neither sinusoidal nor cnoidal. This work extends that of Schecter's by providing a detailed analysis of the types of supported modes, and their use in numerical simulations; also considered is their stability to transverse perturbations in section 6.4.2. There are two types of exact solution: the first can take on the appearance of solitons, travel at sub-Alfvén speeds, and can take any period or amplitude (although in reality, amplitude would be limited in order that the shallow water approximations remain accurate); the second type propagate faster than the Alfvén speed and can have sharp wave crests.

Both the three-wave resonance and the exact solutions are robust, in that they will be maintained for extended periods of time; either one of these nonlinear solutions may thus be expected to occur in astrophysical bodies. Random perturbations, from overshooting plumes from the convection zone into the tachocline, for example, may produce such ordered behaviour. If, as preliminary investigation in Chapter 6 shows, exact travelling forms are stable to some disturbances, they may be more prevalent than originally thought.

7.2 Further work

To further the work in this thesis, one could implement a more accurate rotation set-up. The tachocline is approximately spherical, and so the rotation rate changes with latitude. In this thesis, we used the f-plane approximation, which is constant f, and is equivalent to working with a flat layer of fluid that is tangential to the sphere. By using the β-plane approximation, where rotation rate is a linear function of latitude, this is more accurately represented (see Zeitlin 2013).

One could also work with spherical coordinates, extending the work of Zaqarashvili et al. (2009) and Heng and Spitkovsky (2009). This would not only capture the full effects of rotation, but would also incorporate the curvature of the tachocline, too. This may have some significant effects, especially since the waves in shallow water flow have wavelengths much longer than the height of the layer, and so would be a significant fraction of the radius of the Sun.

Rotation could also be added to the multi-layer model, in a similar manner to Dellar (2002a). The combined effect of rotation and magnetic field in the 2-layer rigid lid model would be an intriguing avenue of interest. For example, differing basic state magnetic field structures in a 2-layer model may have more effects on the triad interactions than a long-time rescaling.

We have considered multi-layer models with ambient magnetic fields that vary with depth, but we have not considered moving basic states, with horizontal velocity that depends on depth. This could be used to represent the velocity shear in the tachocline, in which horizontal flow depends on depth, as well as latitude (see, for example, Hughes et al. 2007). One could include the effects of velocity shear in a 2-layer model, for example, by perturbing a basic state which is not motionless in one of the layers (equivalent to having basic state fluid motion in both layers, and then applying a Galilean transformation). Of course, waves may not be the only dynamics in such a system; Kelvin-Helmholtz type instabilities may occur. One could also investigate the stabilisation by magnetic field (see, for example, Miura 1996).

One could also include a variable bottom topology in the single (or indeed n-layer) models. This is common practice in hydrodynamic shallow water models of the Earth's oceans (see, for example, Dellar and Salmon 2005), especially near the coast; tsunamis, for example, are known to increase in amplitude and decrease in wavelength as the sea gets shallower. The advantage of including bottom topography in a SWMHD model is that one could then model the change in depth of the tachocline, which is known to be thicker at the poles than at the equator. Such a model may be useful to describe the north-south propagation of waves in the tachocline.

It would also be interesting to further the study of 2D waves in the SWMHD system. In this work, the phase and group velocities of the multi-layer models in the linear regime are scrutinised, and it may be of interest to extend the weakly nonlinear analysis to include both horizontal directions. Nontrivial resonant triad interactions are supported in the hydrodynamic shallow water system (see Lynch 2003 for a consideration of 2D Rossby wave triads).

A remaining challenge, that of observation, lies with the astronomers. Perhaps one day it will be possible to probe the depths of the Sun accurately, allowing us to look for the wave dynamics predicted in this work, such as three-wave resonance, solitons and other travelling wave solutions. If it remains unrealistic to detect these waves in the solar interior, maybe they will be manifest in other astrophysical bodies, such as the giant planets of our solar system.

Appendices

A The magnetic constraint and spurious modes

During the derivation of equation (3.45) in chapter 3, we alluded to the fact that the divergence free condition on magnetic field was not used, except to rule out a zero-frequency mode in a rather hand-wavy manner. The aim of this appendix is to explain this with more mathematical vigour, outside the derivation in chapter 3 in order to maintain the mathematical continuity in the text.

In order to get equation (3.43), we eliminated the variable $\tilde{\mathbf{u}}_j$ (and $\tilde{\mathbf{B}}_j$, but we'll leave this in for now). To do this we made use of equation (3.41b), which can be written as

$$\omega(\tilde{\eta}_j - \tilde{\eta}_{j-1}) = H_j \mathbf{k} \cdot \tilde{\mathbf{u}}_j. \tag{A.1}$$

We took dot products with $H_j\mathbf{k}$ and eliminated any $H_j\mathbf{k} \cdot \tilde{\mathbf{u}}_j$ according to this equation. If we do the same thing here, before eliminating the $\tilde{\mathbf{B}}_j$, the induction equation (3.41c) becomes

$$H_j \mathbf{k} \cdot \tilde{\mathbf{B}}_j = -\big(\mathbf{B}_{0j} \cdot \mathbf{k}\big)\,(\tilde{\eta}_j - \tilde{\eta}_{j-1}). \tag{A.2}$$

One could then proceed by eliminating $\tilde{\mathbf{B}}_j$ in the momentum equation, which is what we did in the text. However, one could use the magnetic divergence condition instead of the induction equation in the following way. Seeking solutions of the form (2.35), equation (3.44) becomes

$$H_j \mathbf{k} \cdot \tilde{\mathbf{B}}_j + \big(\mathbf{B}_{0j} \cdot \mathbf{k}\big)\,(\tilde{\eta}_{j-1} - \tilde{\eta}_j) = 0, \tag{A.3}$$

but this is equivalent to (A.2) above! In the derivation of (3.45), then, one can use either the induction equation or the divergence condition.

Analysis with $\partial_t \equiv 0$

Perhaps a more thorough way to discount the zero frequency mode is to put all time derivatives identically zero and follow through with the analysis of linear waves, since a zero frequency mode would be unchanging over time. Then the linearised n-layer equations (3.35) become

$$0 = -\frac{1}{\rho_j}\sum_{i=1}^{j} g^r_{i-1}\rho_i\nabla\eta_{i-1} - \frac{1}{\rho_j}\nabla P + \mathbf{B}_{0j}\cdot\nabla\mathbf{B}'_j \tag{A.4a}$$

$$0 = H_j\nabla\cdot\mathbf{u}'_j \tag{A.4b}$$

$$0 = \mathbf{B}_{0j}\cdot\nabla\mathbf{u}'_j, \tag{A.4c}$$

together with the magnetic condition (3.44), which can be written as

$$\mathbf{B}_{0j}\cdot\nabla(\eta_{j-1}-\eta_j) + H_j\nabla\cdot\mathbf{B}'_j = 0. \tag{A.5}$$

Equations (A.4) appear to admit a zero frequency mode, at least mathematically. Such a mode would have magnetic tension balancing the surface height terms (since the pressure from a lid, if there was one, is in response to the fluid motions immediately below it). This physically corresponds to a scenario where interfaces are held in place, motionless, by a magnetic field, which seems non-physical. We should check to see if (A.5) is violated (knowing it should be).

In the first part of this appendix, we showed that one could have used the magnetic condition instead of the induction equation to derive (3.45), and so any dispersion relations. This means that we can 'throw away' equation (A.4c) and continue with equation (A.5) instead. This derivation is made easier since there is no need to eliminate $\mathbf{u}'_j$ using (A.4b), as the fluid is motionless, but the outcome is the same: equation (3.45) with $c = 0$. [One can easily check this by taking the divergence of (A.4a) and substituting according to (A.5).] This would in turn yield an n-layer dispersion relation with $c = 0$.

The significance of this is that all terms left in such a 'relation' are positive-definite (or negative-definite if n is odd). This is perhaps more easily seen by observing the matrix of coefficients of $\tilde{\eta}_j$ (for $j = 1 \ldots n$) given by equation (3.45), which is outlined in the appendix B in (B.3). One can see that the upper left element is negative if $c = 0$, so that the leading principle minor of the $n = 2$ matrix is negative. This statement is equivalent to saying that the $n = 2$ matrix is a negative-definite one; that is, it has a negative determinant. Then all the leading principle minor matrices of the $n = 3$ matrix have negative determinants, so the $n = 3$ matrix has also, and so-on. In general, if the determinant of the matrix for the n-layer system is not zero, the dispersion relation with $c = 0$ cannot hold, and we have our contradiction.

B The n-layer inductively defined dispersion relation

The dispersion relation for the n layer system was found in chapter 4 for the special cases $n = 2$ and $n = 3$, by eliminating the $\tilde{\eta}_j$ (and possibly $\hat{P}$) in equations (3.45). They were found by writing the set of equations given by (3.45) in matrix form, and setting the determinant of the matrix of coefficients to be zero, for non-trivial solutions. In this appendix, another method of finding the n-layer dispersion relation will be proposed and its relative efficiency discussed. This new method involves finding all the previous dispersion relations (that is, for $1, 2, \ldots, n-1$); although at first this seems like a more laborious route, we shall argue that for large n it is more efficient.

Consider the free surface case, $P = 0$. For $n = 1$, the single layer model, we have $\tilde{\eta}_1 = 0$ (at the floor) and equation (3.45) gives us non-trivial solutions satisfying

$$\zeta_1^2 - gH_1 = 0, \tag{B.1}$$

where $\zeta_j = c^2 - v_{A_j}^2$, as we expect. For the 2-layer free surface case, we have

$$\begin{pmatrix} \zeta_1^2 - gH_1 & -\zeta_1^2 \\ -(1-\alpha_{1,2})gH_2 & \zeta_2^2 - \alpha_{1,2}gH_2 \end{pmatrix} \begin{pmatrix} \tilde{\eta}_1 \\ \tilde{\eta}_2 \end{pmatrix} = 0, \tag{B.2}$$

where $\alpha_{i,j}$ is the non-dimensional reduced gravity, defined in equation (3.50). One may notice that the upper left entry in the matrix in the equation above is the left hand side of equation (B.1), the single layer dispersion relation. Indeed, in general, the matrix of coefficients of the $\tilde{\eta}_j$ for the n-layer system is

$$\begin{pmatrix} \zeta_1^2 - gH_1 & -\zeta_1^2 & 0 & 0 & \cdots & \\ -(1-\alpha_{1,2})gH_2 & \zeta_2^2 - \alpha_{1,2}gH_2 & -\zeta_2^2 & 0 & 0 & \cdots \\ -(1-\alpha_{1,3})gH_3 & -(1-\alpha_{2,3})\alpha_{1,2}gH_3 & \zeta_3^2 - \alpha_{2,3}gH_3 & -\zeta_3^2 & 0 & \cdots \\ \vdots & \vdots & & & & \end{pmatrix}. \tag{B.3}$$

The entry in red is the single layer coefficient, and the entries in blue and red show the coefficients in the 2-layer case. Green denotes the additions required for the 3-layer model, and so on. Note that in order to derive the dispersion for the 3-layer system, for example, one would need to compute all the calculations required for the 2-layer derivation, plus some extras. Thus, if one had a *simplified* 2-layer dispersion relation in advance, its use could save some work in calculating the 3-layer one.

Indeed, dispersion relations can be simplified by combining terms in the coefficients of products of ζ_j^2. For example, the 3-layer case contains 1 $\zeta_1^2\zeta_2^2\zeta_3^2$ term, 3 $\zeta_j^2\zeta_l^2$ terms (for $j \neq l$), 3 ζ_j^2 terms ($j = 1, 2, 3$) and 1 purely hydrodynamic term. These numbers of terms are simply the entries in the third row of Pascal's triangle, and so the total number of terms in the *simplified* dispersion relation is the sum of these. In general then, the number of terms in the simplified n-layer dispersion relation, $N_{\text{simp}}(n)$, is given by

$$N_{\text{simp}}(n) = 2^n. \tag{B.4}$$

Contrast this with the number of terms one gets when using equation (B.3) above, before any simplifying. To find the determinant of the matrix of coefficients, one could start with the lower right entry (containing 2 terms) and multiply by the previous (unsimplified) determinant, and so on. This results in a recurrence relation containing all the previous matrices of coefficients:

$$N_{\text{unsimp}}(n) = 2N_{\text{unsimp}}(n-1) + N_{\text{unsimp}}(n-2) + \cdots + N_{\text{unsimp}}(1) + 1. \tag{B.5}$$

Then the number of terms in the unsimplified dispersion relation is an odd Fibonacci number, and so satisfies

$$N_{\text{unsimp}}(n) = \frac{\Phi^{2n+1} - (-\Phi)^{-2n-1}}{\sqrt{5}}, \tag{B.6}$$

where $\Phi = (1+\sqrt{5})/2$ is the golden ratio. The number of calculations required to simplify the n-layer relation is then the difference between (B.6) and (B.4).

However, suppose that one has simplified versions of the previous $n-1$ relations for use when calculating the n^{th}. Then we could use (B.5) with the *simplified* numbers of terms, and from this we could find the number of calculations needed to fully simplify the relation in this case; using formula (B.4), this is $2^{n-1}-1$. However, we would have had to simplify all the previous dispersion relations too, and so we should add these in a cumulative total. This gives $2^n - n + 1$ simplifying calculations in total when using this cumulative method.

We can now write down the number of calculations saved:

$$\begin{aligned}\text{calculations saved} &= N_{\text{unsimp}}(n) - N_{\text{simp}}(n) - (2^n - n - 1)\\ &= N_{\text{unsimp}}(n) - 2^{n+1} + n + 1. \end{aligned} \tag{B.7}$$

This is the saving we would have in calculating the n-layer dispersion relation if we found the previous $n-1$ relations first, simplifying as we go. This is not a great saving when n is small; for example, when $n = 2$ there are no savings at all, and when $n = 3$ the saving is only 1 calculation.

However, due to the exponential nature of (B.7), this rises dramatically when n is large. For the 8-layer system, for example, 1094 calculations can be saved using this cumulative method.

Let us denote the determinant of the matrix of coefficients for the n-layer system by $D(n)$, so that the dispersion relation is $D(n) = 0$. Then equation (B.3) gives us

$$\begin{aligned} D(n) &= (\zeta_n^2 - \alpha_{n-1,n} g H_n) D(n-1) \\ &\qquad + \zeta_{n-1}^2 \Big(-(1-\alpha_{n-1,n})\alpha_{n-2,n-1} g H_n D(n-2) + \cdots \Big). \end{aligned} \tag{B.8}$$

Using summation convention, this can be written

$$\begin{aligned} D(n) &= (\zeta_n^2 - \alpha_{n-1,n} g H_n) D(n-1) \\ &\qquad + g H_n \sum_{j=1}^{n-1} (-1)^{j+n} (1-\alpha_{j,n})\alpha_{j-1,j} \left(\prod_{i=j}^{n-1} \zeta_i^2 \right) D(j-1), \end{aligned} \tag{B.9}$$

where $D(0) = 1$.

C Fully nonlinear solutions of the n-layer system

We can find exact nonlinear solutions of the n-layer model by considering fixed-shape travelling solutions in a similar manner to that of Schecter et al. (2001). However, to counter nonlinear steepening we must include the dispersive effects of rotation. In the solutions we shall find, these two effects balance and the wave propagates without changing shape (see, for example Choi and Camassa, 1999).

The momentum equation for the jth layer in the rotating n-layer shallow water system (3.10) can be written as

$$\frac{\partial \mathbf{u}_j}{\partial t} + \mathbf{u}_j \cdot \nabla \mathbf{u}_j + f\hat{\mathbf{z}} \times \mathbf{u}_j = -\frac{1}{\rho_j}\sum_{i=1}^{j} g^r_{i-1}\rho_i \nabla \eta_{i-1} - \frac{1}{\rho_j}\nabla P + \mathbf{B}_j \cdot \nabla \mathbf{B}_j, \tag{C.1}$$

when rotation (third term on the left hand side) is included, for $j = 1, \ldots n$. Aligning the x-axis with the wavevector (direction of travelling solution) so that y derivatives are zero, this is

$$\frac{\partial \mathbf{u}_j}{\partial t} + u_j\frac{\partial \mathbf{u}_j}{\partial x} + f\hat{\mathbf{z}} \times \mathbf{u}_j = -\frac{1}{\rho_j}\sum_{i=1}^{j} g^r_{i-1}\rho_i \frac{\partial \eta_{i-1}}{\partial x}\hat{\mathbf{x}} - \frac{1}{\rho_j}\frac{\partial P}{\partial x}\hat{\mathbf{x}} + (B_{0j} + B_{xj})\frac{\partial \mathbf{B}_j}{\partial x}, \tag{C.2}$$

where u_j is the x component of $\mathbf{u}_j$, and the magnetic field has been separated into its basic state and fluctuating parts. We now seek solutions that are functions of $\theta = x - ct$. This temporal and spatial variables now have been absorbed into θ, which is equivalent to transforming to a frame of reference moving to the right with speed c. We then have

$$-c\frac{\partial \mathbf{u}_j}{\partial \theta} + u_j\frac{\partial \mathbf{u}_j}{\partial \theta} + f\hat{\mathbf{z}} \times \mathbf{u}_j = -\frac{1}{\rho_j}\sum_{i=1}^{j} g^r_{i-1}\rho_i \frac{\partial \eta_{i-1}}{\partial \theta}\hat{\mathbf{x}} - \frac{1}{\rho_j}\frac{\partial P}{\partial \theta}\hat{\mathbf{x}} + (B_{0j} + B_{xj})\frac{\partial \mathbf{B}_j}{\partial \theta}. \tag{C.3}$$

We can do the same thing to the height and induction equations, and continue by combining the resulting equations to eliminate variables. However, as has previously been the case, we can use the divergence-free condition on magnetic field instead of the induction equation to make the analysis simpler. The induction equation will be satisfied by our solutions, as we shall verify. The height equation (3.14) and divergence free condition (3.20) on magnetic field for layer j are

$$\frac{\partial}{\partial t}(\eta_{j-1} - \eta_j) + \frac{\partial}{\partial x}((H_j + \eta_{j-1} - \eta_j)u_j) = 0 \tag{C.4}$$

$$\frac{\partial}{\partial x}\left((H_j + \eta_{j-1} - \eta_j)B_{x_j}\right) = 0. \tag{C.5}$$

Seeking solutions that are functions of $\theta = x - ct$, these become

$$-c(\eta_{j-1} - \eta_j) + (H_j + \eta_{j-1} - \eta_j)u_j = const \tag{C.6}$$

$$(\eta_{j-1} - \eta_j)B_{0_j} + (H_j + \eta_{j-1} - \eta_j)B_{x_j} = const. \tag{C.7}$$

Ensuring that disturbances vanish at infinity implies these constants on the right hand sides are zero. Nondimensionalising u_j with c, η_j with H, and B_{x_j} with B_{0_j} (and P with $\rho_1 gH$), these yield

$$u_j = -B_{x_j}, \text{with } u_j = \frac{\eta_{j-1}-\eta_j}{\beta_j+\eta_{j-1}-\eta_j}. \tag{C.8}$$

The momentum equation then becomes

$$-c^2(1-u_j)\frac{\partial \mathbf{u}_j}{\partial\theta} + cf\hat{\mathbf{z}}\times\mathbf{u}_j = -\frac{1}{\rho_j}\sum_{i=1}^{j} g^r_{i-1}H\rho_i\frac{\partial\eta_{i-1}}{\partial\theta}\hat{\mathbf{x}} - \frac{\rho_1}{\rho_j}gH\frac{\partial P}{\partial\theta}\hat{\mathbf{x}}$$
$$+\frac{B_{0_j}^2}{\mu_0\rho_j}(1+B_{x_j})\frac{\partial\mathbf{B}_j}{\partial\theta}. \tag{C.9}$$

Writing $\mathbf{B}_j = -\mathbf{u}_j$, so that (C.8) and the induction equation is satisfied, this can be written

$$-(c^2-v_{A_j}^2)(1-u_j)\frac{\partial\mathbf{u}_j}{\partial\theta} + cf\hat{\mathbf{z}}\times\mathbf{u}_j = -\frac{1}{\rho_j}\sum_{i=1}^{j} g^r_{i-1}H\rho_i\frac{\partial\eta_{i-1}}{\partial\theta}\hat{\mathbf{x}} - \frac{\rho_1}{\rho_j}gH\frac{\partial P}{\partial\theta}\hat{\mathbf{x}}, \tag{C.10}$$

where $v_{A_j} = B_{0_j}/\sqrt{\mu_0\rho_j}$. Now, introducing the variable $X = \frac{cf}{gH}\theta$, this becomes

$$-\zeta_j^2(1-u_j)\frac{d\mathbf{u}_j}{dX} + \hat{\mathbf{z}}\times\mathbf{u}_j = -\frac{1}{\rho_j}\sum_{i=1}^{j}\alpha_{i-1,i}\rho_i\frac{d\eta_{i-1}}{dX}\hat{\mathbf{x}} - (1-\alpha_{1,j})\frac{dP}{dX}\hat{\mathbf{x}}, \tag{C.11}$$

where $\zeta_j^2 = (c^2 - v_{A_j}^2)/gH$. This can be split into its constituent parts:

$$\zeta_j^2(1-u_j)\frac{du_j}{dX} + v_j = \frac{1}{\rho_j}\sum_{i=1}^{j}\alpha_{i-1,i}\rho_i\frac{d\eta_{i-1}}{dX} + (1-\alpha_{1,j})\frac{dP}{dX} \tag{C.12}$$

$$\zeta_j^2(1-u_j)\frac{dv_j}{dX} = u_j. \tag{C.13}$$

Eliminating v_j, we have

$$\zeta_j^2(1-u_j)\frac{d}{dX}\left(\zeta_j^2(1-u_j)\frac{du_j}{dX} - \frac{1}{\rho_j}\sum_{i=1}^{j}\alpha_{i-1,i}\rho_i\frac{d\eta_{i-1}}{dX} - (1-\alpha_{1,j})\frac{dP}{dX}\right) + u_j = 0. \tag{C.14}$$

Since u_j is known in terms of the interface displacements, this is a series of n equations with n unknowns (eliminate P or η_0 as required). They can (in theory) be solved for wave structure (and hence velocity and field fluctuations). The equation above can be written solely in terms of interface displacements as

$$\beta_j\zeta_j^2\frac{d}{dX}\left(\frac{\beta_j^2\zeta_j^2}{(\beta_j+\eta_{j-1}-\eta_j)^3}\frac{d}{dX}(\eta_{j-1}-\eta_j) - \frac{1}{\rho_j}\sum_{i=1}^{j}\alpha_{i-1,i}\rho_i\frac{d\eta_{i-1}}{dX} - \frac{\rho_1}{\rho_j}\frac{dP}{dX}\right)$$
$$+\eta_{j-1}-\eta_j = 0. \tag{C.15}$$

For example, for the 2-layer rigid lid model (the simplest multi- layer model), we have

$$\beta_1\zeta_1^2\frac{d}{dX}\left(\frac{\beta_1^2\zeta_1^2}{(\beta_1-\eta_1)^3}\frac{d\eta_1}{dX}+\frac{dP}{dX}\right)+\eta_1=0 \tag{C.16}$$

$$\beta_2\zeta_2^2\frac{d}{dX}\left(\frac{\beta_2^2\zeta_2^2}{(\beta_2+\eta_1)^3}\frac{d\eta_1}{dX}-\alpha\frac{d\eta_1}{dX}-(1-\alpha)\frac{dP}{dX}\right)+\eta_1=0 \tag{C.17}$$

Eliminating P one gets

$$\beta_1\beta_2\zeta_1^2\zeta_2^2\frac{d}{dX}\left(\left(\frac{(1-\alpha)\beta_1^2\zeta_1^2}{(\beta_2-\eta_1)^3}+\frac{\beta_2^2\zeta_2^2}{(\beta_2+\eta_1)^3}-\alpha\right)\frac{d\eta_1}{dX}\right)+\big((1-\alpha)\beta_2\zeta_1^2+\beta_1\zeta_2^2\big)\eta_1=0. \tag{C.18}$$

Putting $\alpha=1$ and $\beta_2=1$ returns Schecter's result.

D The $(n-1)+\frac{1}{2}$-layer models

In some layered shallow water systems, one layer is much deeper than the others. For example, the ocean can be modelled with a shallow layer of water of slightly lower density (above the thermocline) overlaying a much deeper, but still shallow in the shallow water sense, quiescent body of water. Another example would be Jupiter's atmosphere, in which shallow water models with one deep quiescent layer have been utilised (see, for example, Warneford and Dellar, 2014).

The set-up would be very similar to that displayed in figure 3.1, but one (or more, as we will explore) of the layers is much deeper than the others. This deep layer would have an undisturbed height which was much greater than that of the other layers, but would still be much less than the wavelength of the modes in the system, so that we can apply the shallow water approximation. This latter constraint is not always imposed, but without it one can only go so far in the analysis, as we shall see.

Given the motion of the interfaces bounding a layer, the horizontal flux of fluid in a layer through a vertical plane would be the same regardless of the layer's depth. This means that for deeper layers, the fluid does not have to move horizontally as far to reach this quota, because there is more of it. To quantify this, the fluid in a deep layer (layer j, say) would have a velocity around H_i/H_j times less than the fluid in a shallower layer, i say. The deep layers under scrutiny in this appendix are so deep that the horizontal motion of fluid is negligible, and the layer is modelled as quiescent. The balance of terms in the momentum equation for this deep layer is then between magnetic tension and the interface motions (and the lid, if one is present). The removal of the time derivative (of velocity) in this equation then leads to the loss of a wave mode in the system, since there would be one less c^2 in the matrix of coefficients for the system.

D.1 The $1\frac{1}{2}$-layer model

For the 2-layer model with a quiescent lower layer, the governing equations are

$$\frac{D\mathbf{u}_1}{Dt} = \frac{\rho_2}{\rho_1} g_1^r \nabla \eta_1 - \frac{\rho_2}{\rho_1} \mathbf{B}_2 \cdot \nabla \mathbf{B}_2 + \mathbf{B}_1 \cdot \nabla \mathbf{B}_1, \tag{D.1a}$$

$$\frac{\partial h_1}{\partial t} = -\nabla \cdot \left(h_1 \mathbf{u}_1 \right), \tag{D.1b}$$

$$\frac{D\mathbf{B}_1}{Dt} = \mathbf{B}_{0_1} \cdot \nabla \mathbf{u}_1, \tag{D.1c}$$

with $\frac{\rho_1}{\rho_2}\nabla(\eta_0+P)+g_1^r\nabla\eta_1-\mathbf{B}_2\cdot\nabla\mathbf{B}_2=0$, in dimensional form, making use of equations (4.3-4.4). The height h is given by $h=H_1+\eta_0-\eta_1$ if the surface is free, or by $h=H_1-\eta_1$ if there is a rigid lid present. Note the analogy between the $1\frac{1}{2}$-layer free surface model given by equations (D.1) and the single layer model given by equations (2.31a-c), in the absence of rotation and magnetic field. Equation (D.1b) becomes

$$\frac{\partial\eta_1}{\partial t}=\nabla\cdot\left((\frac{\rho_1}{\rho_2}H-\eta_1)\mathbf{u}_1\right), \tag{D.2}$$

and the two systems are equivalent with $\eta\rightarrow(1-\rho_2/\rho_1)\eta_1$ and $H\rightarrow(1-\frac{\rho_1}{\rho_2})H_1$.

The analysis in section 3.4, that led to the derivation of the generating equation (3.45) could then be repeated but with the $\frac{\partial\mathbf{u}_j}{\partial t}$ term (if layer j is deep) omitted. One could then find a dispersion relation for such a system, which could also be found by putting $\zeta_j^2=-{v_A}_j^2$ into the n-layer dispersion relation. Using equation (4.9), we find that the dispersion relation for the $1\frac{1}{2}$-layer model with a quiescent lower layer is given by

$$(\beta_2+{v_A}_2^2)\zeta_1^2=\beta_1(\alpha_{1,2}\beta_2+{v_A}_2^2), \tag{D.3}$$

Note that this requires that the lower deeper layer is still ‘shallow’ in the shallow water sense; that is, typical horizontal length scales are much greater than vertical ones. Equation (D.3) reduces to the well-known hydrodynamic $1\frac{1}{2}$-layer dispersion relation

$$c^2=\alpha_{1,2}\beta_1. \tag{D.4}$$

Note how easy it was to derive the $1\frac{1}{2}$-layer dispersion relation from the full 2-layer relation (4.9); all we had to do was replace ζ_2 with v_{A2}. The inclusion of a magnetic field in the system has made things easier for us, because the c we had to delete was ‘tagged’ with an Alfvén speed. In the hydrodynamic case, in order to derive the $1\frac{1}{2}$-layer dispersion relation one could not use the hydrodynamic relation, as there would be no way to tell ‘which’ c^2 to remove. One would have to re-derive the relation, at least from the matrix of coefficients.

This analysis assumes that the magnetic field in the quiescent layer is of the same order as that in the shallower layer. If this were not the case, and the magnetic field strength was inversely proportional to the layer depth (or less), we omit the corresponding Alfvén speed by writing ${v_A}_j=0$ in addition to the deletion of the c^2. This is equivalent to putting $\zeta_j=0$ into the dispersion relation. For the 2-layer free surface model, this gives

$$c^2=\alpha_{1,2}\beta_1+{v_A}_1^2. \tag{D.5}$$

If we compare this to the single layer dispersion relation ($c^2 = \beta_1 + v_{A1}^2$), we can see that the only difference is the hydrodynamic term, which corresponds to $g^r H_1$ before scaling. The $1\frac{1}{2}$-layer model phase speed is then the same as that of the single layer, but with the effective gravity now g^r instead of g. The interface provides the hydrodynamic driving force of the modes when the lower layer is deep and quiescent, as opposed to the surface.

D.2 Generalisations

The analysis above can be generalised to systems with more than two layers, with possibly more than one deeper layer. For example, the waves supported by a model in which one shallow electrically conducting layer is sandwiched between two deeper hydrodynamic layers have phase speeds

$$c^2 = v_{A2}^2 + \frac{\alpha_{1,2}\alpha_{2,3}}{\alpha_{1,3}}\beta_2, \tag{D.6}$$

making use of equation (4.61). In the modelling of Jupiter's atmosphere, it may be useful to put $v_{A1} = 0$ and $\zeta_n^2 = v_{An}^2$ into the n-layer model, in order to simulate a shallow hydrodynamic upper weather layer and a deeper lower electrically conducting layer, perhaps with varying magnetic field strengths in the layer in between.

In general, we can write the momentum equations for the n-layer system as

$$\frac{D\mathbf{u}_j}{Dt} = \frac{1}{\rho_j}\nabla Y_j + \mathbf{B}_j \cdot \nabla \mathbf{B}_j, \tag{D.7}$$

where the Y_j are given by

$$Y_j = \begin{cases} -\sum_{i=1}^{j} g_{i-1}^r \rho_i \eta_{i-1} & n\text{-layer free surface} \\ -\sum_{i=2}^{j} g_{i-1}^r \rho_i \eta_{i-1} & \text{top quiescent} \\ \sum_{i=j+1}^{n} g_{i-1}^r \rho_i \eta_{i-1} & \text{bottom quiescent} \\ \sum_{i=j}^{n} g_{i-1}^r \rho_i \eta_{i-1} & \text{both top and bottom quiescent} \end{cases}. \tag{D.8}$$

The equations for evolution of interface heights and magnetic field remain the same as in the n-layer case. One can show, in a similar manner as in section 2.3, that the n-layer system with a quiescent upper layer conserves energy, since the governing equations satisfy the conservation law

$$\frac{\partial}{\partial t}\left(\frac{1}{2}\rho_j h_j|\mathbf{u}_j|^2+\frac{1}{2\mu_0}h_j|\mathbf{B}_j|^2+\frac{1}{2}g^r_{j-1}\rho_j\eta^2_{j-1}\right)$$
$$+\nabla\cdot\left(\frac{1}{2}\rho_j|\mathbf{u}_j|^2\mathbf{u}_j+\frac{1}{2\mu_0}h_j|\mathbf{B}_j|^2\mathbf{u}_j-\frac{1}{\mu_0}h_j(\mathbf{u}_j\cdot\mathbf{B}_j)\mathbf{B}_j+h_j\mathbf{u}_j\sum_{i=2}^{j}g^r_{i-1}\rho_i\eta^2_{i-1}\right)=0. \tag{D.9}$$

E The numerical method used in Chapter 6

Our aim is to solve the rotating single-layer nondimensional shallow water equations given by (6.14). These equations are the same as those used in Chapter 2; fluid is inviscid and perfectly conducting, as before. We solve these on a periodic domain, with a flat bottom as in previous work. This is equivalent to having infinitely many such domains placed in a line, with fluid flow matching at the boundaries. This horizontally infinite expanse matches our previous work, and eliminates the need for boundary conditions at walls. The conditions on the floor and at the surface are the same as in the single layer set-up in Chapter 2 (impermeable and perfectly conducting).

Our first task is to discretise space and time. Samples points will be spaced at regular intervals in the domain, and there will be N such points altogether. Then the perturbation variables η, u, v, B_x and B_y can be written as vectors of length N, and the numerical solution will be expressed as an interpolation of these vectors. Obviously, the higher the value of N, the more accurately the discrete points can capture a continuous curve, but at a cost of longer computation time. Time is similarly discretised into sample times separated by Δt, so the numerical scheme will advance all spatial points (sampled at time t) to those same points in space at time $t + \Delta t$, via some kind of finite difference scheme.

Our task will be to numerically calculate the right hand sides of equations (6.14), in order to advance them in time. This would be simple if there were no derivatives, since the calculation would be a trivial manipulation of vectors; one of the problems facing us as numerical modellers is the spatial differentiation of vectors. There are 3 approaches to this:

- **The finite difference** approach (see Smith, 1965; Press, 2002). This involves generating a differentiation matrix that, when left multiplies a vector, estimates its derivative vector. It does this by applying a stencil of coefficients to the elements of the vector surrounding a desired point to approximate the derivative, for all such points. The larger the stencil, the more accurate is the derivative.

- **The pseudospectral** approach (see Fornberg, 1996). Here, we make the stencil of the differentiation matrix so large that it contains *all* other points in the vector. Further, it contains all points in the infinity of surrounding boxes, giving a differentiation matrix that computes derivatives with spectral accuracy.

- **The spectral** approach (see Trefethen, 2000). This method is as accurate as the pseudospectral one, but is applied differently. This is the one we shall be using in this thesis, and will be expanded upon in the following section.

E.1 Description of the numerical scheme

Fourier decomposition

We start by writing all variables as a decomposition of Fourier modes; that is, we approximate the surface height profile (and other variables) as a sum of sinusoids of varying amplitudes. When written in complex exponential form, terms can then be differentiated trivially by multiplication of a wavevector. The coefficients of the complex exponentials are known as Fourier coefficients, and are calculated using the following definition:

$$\hat{f}(k) = \sum_{x=0}^{N-1} f(x) e^{-2\pi i(k-1)(x-1)/N}. \tag{E.1}$$

For example, given the vector $f = (2, 3, 1, 4)$, the above transform gives the vector of Fourier coefficients $\hat{f} = (10, 1+i, -4, 1-i)$. It is in this 'Fourier space' that differentiation can take place easily, before applying the inverse Fourier transform

$$f(x) = \frac{1}{N} \sum_{k=0}^{N-1} \hat{f}(k) e^{-2\pi i(k-1)(x-1)/N}. \tag{E.2}$$

One can check that, with the input $\hat{f} = (10, 1+i, -4, 1-i)$, one recovers our original vector f. The calculation of these Fourier coefficients is the most computationally costly bit of the numerical scheme.

Toy example explained

For our small example, we have

$$4f(x+1) = 10 + (1+i)e^{i\pi x/2} - 4e^{i\pi x} + (1-i)e^{3i\pi x/2}, \tag{E.3}$$

the real part of which can be written as $10 + \cos(\pi x/2) - \sin(\pi x/2) - 4\cos(\pi x) + \cos(3\pi x/2) + \sin(3\pi x/2)$. This real part can be further expressed as

$$4\Re f(x+1) = 10 - 4\cos(\pi x) + \sqrt{2}\left(\cos\left(\frac{\pi}{2}x + \frac{\pi}{4}\right) + \cos\left(\frac{3\pi}{2}x - \frac{\pi}{4}\right)\right). \tag{E.4}$$

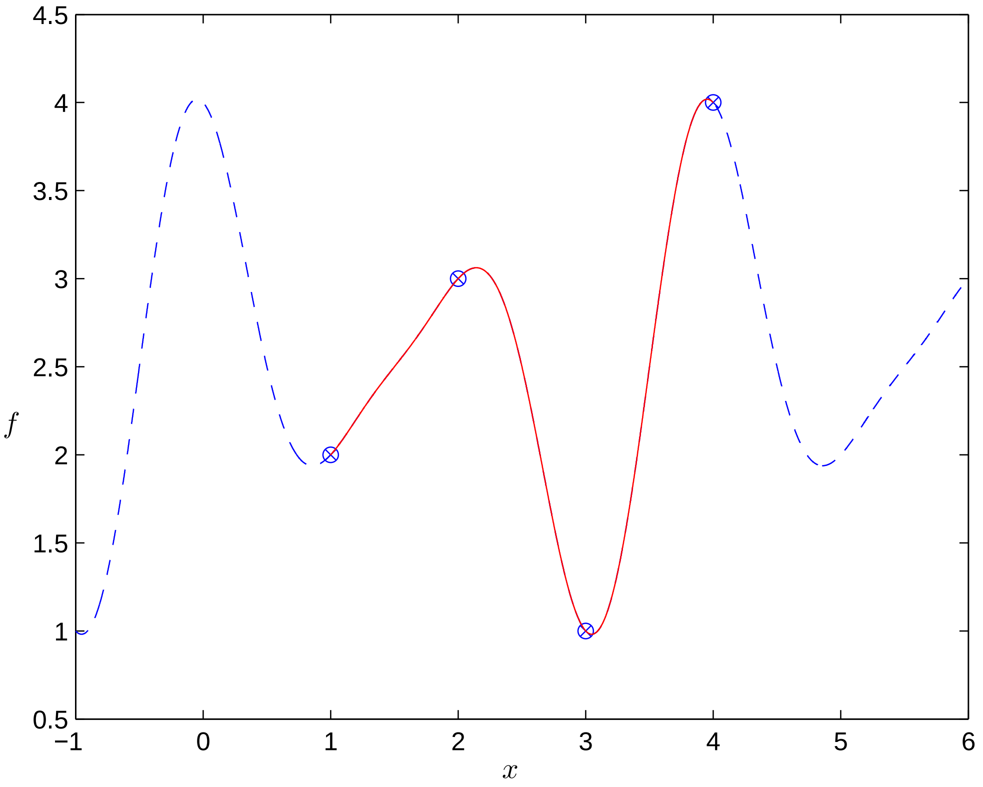

Figure E.1 – Graph illustrating the interpolation of data points with a sum of sinusoids, as in our toy example. The original values in the vector f are represented by the circled crosses. The curve described in (E.4) is plotted in red, with the dashed curve displaying the cyclic behaviour outside the domain.

This is plotted in figure E.1, where one can see the curve passing through the data points. At these points, the imaginary part of (E.3) is zero, although a computer may bring an error in by introducing a small imaginary part at machine precision. This can be countered by zeroing any imaginary parts of variables that should be real, but this is computationally costly and is not needed for our purposes.

Equation (E.4) is a sum of waves with wavenumbers 0 (from the constant term), $\pi/2$, π, and $3\pi/2$. The principle of differentiating in Fourier (spectral) space is that we differentiate (E.4), which is easy, and sample at the required points. In practice, this is done using (E.3), whence differentiation with respect to x is simply a matter of multiplying the terms by the appropriate constants. These constants are the wavenumbers – almost. The argument of the exponential in the final term in equation (E.3) can be written as $-i\pi x/2$ (an Argand diagram can shed light on this). Thus, for our toy example, in order to differentiate f we would multiply our Fourier coefficients by i and the modified wavenumber vector $k = (0, 1, 2, -1)$, before transforming back into real space using (E.2).

Explicit schemes

In general, the vector of wavenumbers would be

$$k = (0, 1, 2, \ldots, N/2, -N/2 + 1, -N/2 + 2, \cdots - 1). \tag{E.5}$$

This is equivalent to saying that a spatial discretisation into N points can only support wavenumbers up to $N/2$ (N has to be even here). Dynamics on a shorter scale than the space between samples cannot be resolved using this method; the 'most wavy' a surface, for example, could be is when the data points are in a zig-zag pattern, which could be interpolated by a sum of waves with wavenumbers up to $N/2$.

To summarise, we calculate the derivative of a vector f of length N by applying the Fourier transform given by equation (E.1), multiplying by ik, and applying the inverse Fourier transform to return to real space. This can be written as

$$\frac{\partial f}{\partial x} \approx \mathcal{F}^{-1}\left(ik\mathcal{F}(f)\right), \tag{E.6}$$

where the operator $\mathcal{F}$ takes the Fourier transform. Any multiplication of vectors here is an element-by-element multiplication, and not a vector product.

Now we have solved the problem of how to differentiate vectors, we are in a position to calculate the right hand sides of the equations we wish to solve (6.14). There are 2 ways to proceed: the first is to work in real space, and only converting a variable to its Fourier counterpart in order to differentiate it; the second is to work entirely in spectral space, which is the method adopted here. Then the Fourier transformations are all contained in the nonlinear terms, which are a product of a vector and a 'derivative' of a vector. They contain 3 transformations: the first so that we can differentiate, the second to change back into real space so that we can multiply element-by-element, and the third to convert the resulting product back into spectral space again.

We can now calculate the time derivatives of surface height, velocity and magnetic field at any fixed point in time. The idea is to use these to project the known current values forward in time by

Δt, which can be done using the Euler method. However, the Euler method can be unstable if Δt is not small enough, and it is first order accurate only, meaning error is proportional to Δt. The fourth order Runge Kutta method (a variant of that used to solve the 3-wave resonance equations in chapter 5) would provide more accurate results for a given step size. Alternatively, one could make use of the values from previous steps, as well as the current one. These Adams-Bashforth schemes lead to increased stability as well as accuracy, and is a technique we will incorporate into our scheme.

Of course, requiring the values from previous times is problematic for the first timesteps, where there are little or no previous data. To work around this, a different timestepping scheme will have to be implemented at the start, to advance by enough steps so that use can be made of the generated data.

Semi-implicit schemes

Another way to improve stability in a timestepping scheme is to use the (unknown) future values. The Crank-Nicolson scheme involves finding the derivatives of a vector at the current step and the vector we are trying to find at the next step, and taking an average of the two. This introduces all the future variables into every equation, leading to a system of equations that we need to solve simultaneously. Such simultaneous solving is also computationally heavy, but is more than worth it for the saving gained from not having to stipulate too low a value for Δt.

The Crank-Nicolson scheme cannot be used on the nonlinear terms, however, because that would involve products of future variables; it can only be used on the linear terms. We will make it our aim, then, to isolate all possible linear terms in the equations we wish to solve, so that a stable semi-implicit scheme can be used on these, and an explicit multistep Adams-Bashforth technique can be used on the nonlinear terms. We are now in a position to derive our timestepping scheme.

E.2 Outline of 1D numerical scheme

The derivation of the one-dimensional scheme shall be outlined here (a two-dimensional scheme can be derived in a very similar manner, that uses the same spectral differentiation and timestepping methods, but with the added complication is that the ‘vectors’ are matrices, and y-derivatives are not nonzero). First, we write the variables as a sum of the basic state and perturbed quantities as before, so that $\mathbf{u} = \mathbf{u}'$, $\mathbf{B} = \hat{\mathbf{x}} + \mathbf{B}'$, where the ambient magnetic field has been aligned with the x-axis.

The equations that the numerical scheme intends to solve are the 1.5-D rotating shallow water equations given by (6.21). Separating the components of these equations, and using the notation u_n for the x-component of velocity at the n^{th} step (and so on), we have

$$\begin{aligned}\frac{u_{n+1}-u_n}{\Delta t} =& \frac{1}{2}\left(f(v_{n+1}+v_n) - \frac{\partial}{\partial x}(\eta_{n+1}+\eta_n) + \text{Ma}^2\frac{\partial}{\partial x}(B_{xn+1}+B_{xn})\right)\\ &+\frac{23}{12}\left(-u_n\frac{\partial u_n}{\partial x}+\text{Ma}^2 B_{xn}\frac{\partial B_{xn}}{\partial x}\right)\\ &-\frac{4}{3}\left(-u_{n-1}\frac{\partial u_{n-1}}{\partial x}+\text{Ma}^2 B_{xn-1}\frac{\partial B_{xn-1}}{\partial x}\right)\\ &+\frac{5}{12}\left(-u_{n-2}\frac{\partial u_{n-2}}{\partial x}+\text{Ma}^2 B_{xn-2}\frac{\partial B_{xn-2}}{\partial x}\right),\end{aligned}\tag{E.7a}$$

$$\begin{aligned}\frac{v_{n+1}-v_n}{\Delta t} =& \frac{1}{2}\left(-f(u_{n+1}+u_n) + \text{Ma}^2\frac{\partial}{\partial x}(B_{y_{n+1}}+B_{y_n})\right)\\ &+\frac{23}{12}\left(-u_n\frac{\partial v_n}{\partial x}+\text{Ma}^2 B_{xn}\frac{\partial B_{y_n}}{\partial x}\right)\\ &-\frac{4}{3}\left(-u_{n-1}\frac{\partial v_{n-1}}{\partial x}+\text{Ma}^2 B_{xn-1}\frac{\partial B_{y_{n-1}}}{\partial x}\right)\\ &+\frac{5}{12}\left(-u_{n-2}\frac{\partial v_{n-2}}{\partial x}+\text{Ma}^2 B_{xn-2}\frac{\partial B_{y_{n-2}}}{\partial x}\right),\end{aligned}\tag{E.7b}$$

$$\begin{aligned}\frac{\eta_{n+1}-\eta_n}{\Delta t} =& -\frac{1}{2}\frac{\partial}{\partial x}(u_{n+1}+u_n)\\ &-\frac{23}{12}\frac{\partial}{\partial x}(\eta_n u_n)+\frac{4}{3}\frac{\partial}{\partial x}(\eta_{n-1}u_{n-1})-\frac{5}{12}\frac{\partial}{\partial x}(\eta_{n-2}u_{n-2}),\end{aligned}\tag{E.7c}$$

$$\begin{aligned}\frac{B_{xn+1}-B_{xn}}{\Delta t} =& \frac{1}{2}\frac{\partial}{\partial x}(u_{n+1}+u_n)+\frac{23}{12}\left(B_{xn}\frac{\partial u_n}{\partial x}-u_n\frac{\partial B_{xn}}{\partial x}\right)\\ &-\frac{4}{3}\left(B_{xn-1}\frac{\partial u_{n-1}}{\partial x}-u_{n-1}\frac{\partial B_{xn-1}}{\partial x}\right)\\ &+\frac{5}{12}\left(B_{xn-2}\frac{\partial u_{n-2}}{\partial x}-u_{n-2}\frac{\partial B_{xn-2}}{\partial x}\right),\end{aligned}\tag{E.7d}$$

$$\begin{aligned}\frac{B_{y_{n+1}}-B_{y_n}}{\Delta t} =& \frac{1}{2}\frac{\partial}{\partial x}(v_{n+1}+v_n)+\frac{23}{12}\left(B_{xn}\frac{\partial v_n}{\partial x}-u_n\frac{\partial B_{y_n}}{\partial x}\right)\\ &-\frac{4}{3}\left(B_{xn-1}\frac{\partial v_{n-1}}{\partial x}-u_{n-1}\frac{\partial B_{y_{n-1}}}{\partial x}\right)\\ &+\frac{5}{12}\left(B_{xn-2}\frac{\partial v_{n-2}}{\partial x}-u_{n-2}\frac{\partial B_{y_{n-2}}}{\partial x}\right).\end{aligned}\tag{E.7e}$$

The terms with the factor of 1/2 in front of them are the Crank-Nicolson terms, which involve future variables. The others are third order Adams-Bashforth multistep terms, that involve previous data. The aim is to solve these equations for the unknown (subscript $n + 1$) variables.

Taking the Fourier transform, these equations can be written as

$$\begin{aligned}
\frac{\hat{u}_{n+1}-\hat{u}_n}{\Delta t} =&\frac{1}{2}\left(f(\hat{v}_{n+1}+\hat{v}_n)-ik(\hat{\eta}_{n+1}+\hat{\eta}_n)+\mathrm{Ma}^2 ik(\hat{B}_{xn+1}+\hat{B}_{xn})\right)\\
&-\mathcal{A}(\hat{u},ik\hat{u})+\mathrm{Ma}^2\mathcal{A}(\hat{B}_x,ik\hat{B}_x), \qquad \text{(E.8a)}\\
\frac{\hat{v}_{n+1}-\hat{v}_n}{\Delta t} =&\frac{1}{2}\left(-f(\hat{u}_{n+1}+\hat{u}_n)+\mathrm{Ma}^2 ik(\hat{B}_{yn+1}+\hat{B}_{yn})\right)\\
&-\mathcal{A}(\hat{u},ik\hat{v})+\mathrm{Ma}^2\mathcal{A}(\hat{B}_x,ik\hat{B}_y), \qquad \text{(E.8b)}\\
\frac{\hat{\eta}_{n+1}-\hat{\eta}_n}{\Delta t} =&-\frac{1}{2}ik(\hat{u}_{n+1}+\hat{u}_n)-ik\mathcal{A}(\hat{\eta},\hat{u}), \qquad \text{(E.8c)}\\
\frac{\hat{B}_{xn+1}-\hat{B}_{xn}}{\Delta t} =&\frac{1}{2}ik(\hat{u}_{n+1}+\hat{u}_n)+\mathcal{A}(\hat{B}_x,ik\hat{u})-\mathcal{A}(\hat{u},ik\hat{B}_x), \qquad \text{(E.8d)}\\
\frac{\hat{B}_{yn+1}-\hat{B}_{yn}}{\Delta t} =&\frac{1}{2}ik(\hat{v}_{n+1}+\hat{v}_n)+\mathcal{A}(\hat{B}_x,ik\hat{v})-\mathcal{A}(\hat{u},ik\hat{B}_y), \qquad \text{(E.8e)}
\end{aligned}$$

where the operator $\mathcal{A}$ is defined by

$$\mathcal{A}(\hat{u},\hat{\eta})=\sum_{j=n-2}^{n} a_j\mathcal{F}\left(\mathcal{F}^{-1}(\hat{u}_j)\mathcal{F}^{-1}(\hat{\eta}_j)\right), \qquad \text{(E.9)}$$

where $a_{n-2}=5/12$, $a_{n-1}=-4/3$ and $a_n=23/12$. After some algebraic manipulation, the equations above can be written as

$$\begin{aligned}
\hat{u}_{n+1}+\frac{\Delta t}{2}\left(-f\hat{v}_{n+1}+ik\hat{\eta}_{n+1}-\mathrm{Ma}^2 ik\hat{B}_{xn+1}\right)&=(xmom), \qquad \text{(E.10a)}\\
\hat{v}_{n+1}+\frac{\Delta t}{2}\left(f\hat{u}_{n+1}-\mathrm{Ma}^2 ik\hat{B}_{yn+1}\right)&=(ymom), \qquad \text{(E.10b)}\\
\hat{\eta}_{n+1}+\frac{\Delta t}{2}ik\hat{u}_{n+1}&=(height), \qquad \text{(E.10c)}\\
\hat{B}_{xn+1}-\frac{\Delta t}{2}ik\hat{u}_{n+1}&=(xind), \qquad \text{(E.10d)}\\
\hat{B}_{yn+1}-\frac{\Delta t}{2}ik\hat{v}_{n+1}&=(yind), \qquad \text{(E.10e)}
\end{aligned}$$

where the right hand sides of the equations are in terms of current known values. These can be solved simultaneously in a numerical scheme. However, in order to make the scheme as efficient as possible, we should endeavour to perform as many analytical calculations beforehand as possible, so that the code does not have to repeat unnecessary work. With this in mind, we analytically solve the equations above to give the $t+\Delta t$ variables in terms of the known, current time ones, by systematically eliminating in favour of $\hat{u}_{n+1}$ and then substituting.

E.3 Practicalities and extra parts

The outline above explains the main timestepping scheme, which is third order Adams-Bashforth for the nonlinear terms and Crank-Nicolson on the linear terms. This combination gives accuracy and stability for relatively large timesteps, compared to simpler schemes such as that of Euler. It also requires data from the previous two timesteps, as well as the current data. To account for this, the first two timesteps will consist of ten single-step explicit fourth order Runge Kutta sub-steps of size $\Delta t/10$, each of which require data from the current sub-step only. From time $2\Delta t$ onwards, the Adams-Bashforth/Crank-Nicolson scheme described above, which is much more efficient, will take over. This scheme is illustrated in figure E.2. After each subsequent timestep, only the data required for the Adams-Bashforth terms will be saved, with the earliest values (from three steps ago) will be deleted. This will keep the required memory low, which would otherwise build up very quickly, especially in the 2D case. If any data needs to be saved, for later observations or further analysis, this will be done separately; for example, the surface profile can be saved every one hundred timesteps to a seperate vector or file using an IF statement.

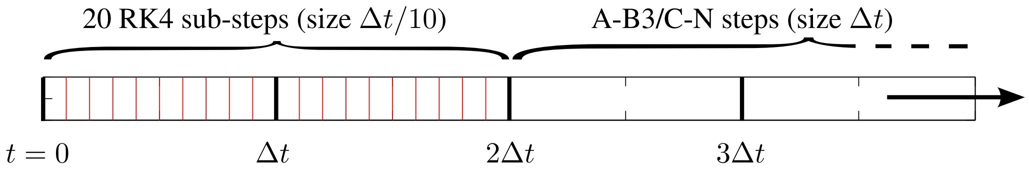

Figure E.2 – Schematic illustrating the timestepping procedure. Given initial conditions, which are saved, there follows 20 sub-steps using the Runge-Kutta fourth order method, with data saved at times Δt and $2\Delta t$. After this, there is enough data for the multistep hybrid Adams-Bashforth/Crank-Nicolson scheme to kick in. Each of these timesteps deletes all data that is not needed for subsequent steps, to reduce memory cost.

The timesteps themselves are written as subroutines, each containing more subroutines (such as the Adams-Bashforth calculations using equation (E.9)). These are then placed in the main body of the code inside a loop, which inductively repeats the timesteps. Inside this loop are options for generating figures and saving data, as well as system checks, which we shall discuss momentarily.

System checks

One of the challenges in numerical schemes is ensuring that the code does what it is supposed to, since most of the time we will not have an exact solution to compare with. However, there are still checks we can make. The shallow water equations satisfy the condition $\nabla \cdot ((1 + \eta)\mathbf{B}) = 0$, and so calculating the left hand side of this constraint every fifty timesteps or so to see how much it is deviating from 0 would shed some light on how well the scheme is doing. Another similar check would be to calculate the total energy of the system, using the definition of single-layer energy in equation (2.27). This should remain constant as time progresses, and so any deviation from this constant value will give us an idea of the cumulative error.

Seperate codes have also been written that solve the momentum and height equations (as shown above), but with an equation for evolution of the quantity $h\mathbf{B}$ instead of the induction equation as written. This extra equation is derived from the height and induction equations using the product rule, and for the 1D case this is

$$\frac{\partial}{\partial t}\left(hB_x\right) = 0, \tag{E.11a}$$

$$\frac{\partial}{\partial t}\left(hB_y\right) = \frac{\partial}{\partial x}(hvB_x - huB_y). \tag{E.11b}$$

From these directly follows that the rate of change of the x-derivative of hB_x is zero, so that if the divergence-free constraint is satisfied initially, it is satisfied for all times. This code calculates the data for the next step differently, in that $\nabla \cdot (h\mathbf{B})$ is kept lower (at around machine precision), but is slightly less stable as there is not quite the same freedom to separate the linear terms on which to use the implicit Crank-Nicolson method. It does provide outputs, however, that coincide remarkably well with those of the other numerical scheme described so far in this appendix, and thus presents more evidence that each is working correctly.

We can also build a linear/nonlinear switch into the code, so that when the switch is off all the nonlinear terms are set to zero. As well as making the code run faster, since the Fourier transforms will no longer be needed, it will enable us to compare the output with our exact linear predictions. If these match, it will at least indicate that the linear part of the code is working correctly. We can also turn the nonlinear terms back on and initialise with a small-amplitude perturbation; this should approximately follow the linear solutions, at least for low times.

One way we can check to find out if the nonlinear part of the code is correct is to initialise with an exact nonlinear solution. Given such a solution, we would have something to compare the output of the code against, and thus infer the efficiency and integrity of the code. In order to achieve this, we can initialise with the exact nonlinear solution found in section 6.3: that is, our numerical solution of (6.27). The unchanging spectrum as the code cycles through timesteps, found using the Fourier transform of the surface vector, gives sufficient evidence that the numerical scheme was working correctly, and allows us to initialise the code with more exotic conditions in our search for new dynamics.

F Results from the numerical shallow water scheme

We are now in a position to consider the results from the numerical schemes outlined earlier in this Appendix. We shall begin by initialising the codes with a linear solution (the exact evolution of which is known), and analysing the numerical error.

F.1 Linear tests and error analysis

One of the easiest ways to check that the code may be working is to plot the surface profile in every timestep, so that as the code runs the picture constantly refreshes, appearing like a movie. At a glance, one can see if the surface is behaving as expected, in some cases. For example, initialising the linear code with a travelling wave with linear phase speed $\sqrt{\mathrm{Ma}^2 + 1}$ (without rotation, and with the linear switch on), this movie would show a sinusoidal wave travelling at a constant speed without change of shape. We can also find the numerical error by comparing to the exact solution, testing the code further. The error could be measured as the maximum of the elements of the discrepancy vector, which we define as the difference of the surface profile from the code output and the exact travelling wave solution.

The initial conditions

$$\eta = 0.1\cos(x), \qquad u = c\eta, \qquad v = 0, \qquad B_x = -\eta, \qquad B_y = 0, \tag{F.12}$$

produce a mode travelling to the right with phase speed $c = \sqrt{\mathrm{Ma}^2 + 1}$, wavenumber 1. The expressions for u and B have been chosen so that the linearised equations (6.14b) and (6.20) are satisfied. The analytical solution for η is $\eta = 0.1\cos(x - ct)$, and this is our exact solution for comparison. We find that the error brought about by the code grows linearly with time, approaching 1.5×10^{-4} after six thousand timesteps, each of length $\Delta t = 10^{-2}$. If one increases Δt and runs the code again, the error increases with time as before, but with a faster rate. In fact, doubling Δt quadruples the error, indicating that the scheme is second-order. This is due to the application of the second-order Crank-Nicolson on the linear terms in the code. Of course it is possible to use a higher order scheme like the fourth order Runge Kutta method, which will produce a much lower error; however, this is much less stable and requires smaller timesteps. The efficiency trade-off with the semi-implicit Crank-Nicolson scheme is worth it for the stability it provides.

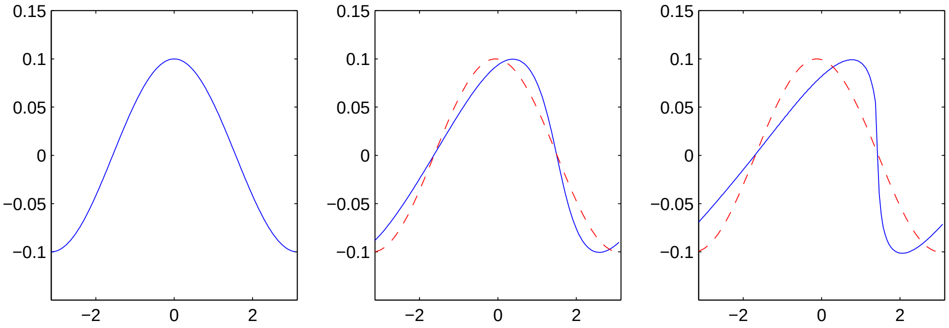

Figure F.3 – Evolution of the surface profile in the absence of rotation, according to the 1D code. The left hand plot shows the initial sinusoid, and the plots to the right show the surface profile after 1 and 2 periods. The wave travels to the right, and the gradient of the leading fluid surface steepens due to nonlinearity.

F.2 Nonlinear initialisation

Turning the linear switch off (so that nonlinear terms play a role) allows us to investigate nonlinear effects more thoroughly. Initialising the code with a travelling wave similar to the one in the linear case above, we have

$$\eta = 0.1\cos(x), \qquad u = \frac{c\eta}{1+\eta}, \qquad v = 0, \qquad B_x = -\frac{\eta}{1+\eta}, \qquad B_y = 0, \qquad \text{(F.13)}$$

where the expressions for u and B have been calculated so that the fully nonlinear conservation of mass (6.14b) and magnetic field condition (6.20) are satisfied. In this case, the mode changes shape as it propagates, the leading slope of the wave steepening over time.

This is known as nonlinear steepening, since it works by wave modes passing energy down to the smaller scales (larger wavenumbers) through the nonlinear terms – see figure F.3. Eventually, the code will ‘break’, since it cannot resolve wavenumbers higher than $N/2$ (where N is the number of gridpoints) so the small scales are not accounted for; in the example above, this occurs shortly before the third period. Figure F.3 illustrates this steepening behaviour.

Intriguingly, without adding any dispersion to the system (without rotation the dispersion relation is of the form $\omega = ck$, and so $\omega_{kk} = 0$), we can delay this break in the code. By initialising with

$$\eta = 0.1\cos(x), \qquad u = 0, \qquad v = 0, \qquad B_x = -\frac{\eta}{1+\eta}, \qquad B_y = 0, \qquad \text{(F.14)}$$

where the only difference is with the expression for u, the time it takes for the code to break is around $t = 30$, whereas for the earlier initialisation it was around $t = 11$. These new initial

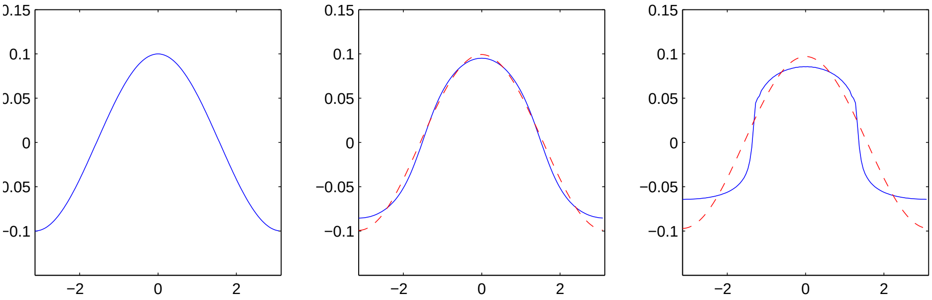

Figure F.4 – As in figure F.3, but with the initialisation given in (F.14). This time, the middle and right plots are after 2 and 4 periods respectively, to illustrate the longevity of the code under these initial conditions.

conditions is equivalent to initialising with two waves, each propagating in the opposite direction. The extra time taken for the code to break is due to the fact that travelling sections of the surface do not face the same way as the surface evolves, because another surge from the opposite direction changes the sign of the gradient; wave fronts are not left to steepen unhindered.

A final note

In the tachocline, the effects of weak nonlinearity and rotation may balance this nonlinear steepening, leading to waves with greater longevity. However, it is still possible that some larger disturbances form internal waves that break, which has implications in mixing processes. This could be part of a mechanism that brings lithium down from the convection zone through the stably stratified tachocline, which may explain the paucity of the element at the surface of the Sun.

Bibliography

Acheson, D. J. (1990). *Elementary fluid dynamics*. Oxford University Press.

Alfvén, H. (1942). Existence of electromagnetic-hydrodynamic waves. *Nature*, 150:405–406.

Alfvén, H. (1947). Granulation, magneto-hydrodynamic waves, and the heating of the solar corona. *Royal Astronomical Soc.*, 107:211–219.

Apel, J. R., Byrne, H. M., Proni, J. R., and Charnell, R. L. (1975). Observations of oceanic internal and surface waves from the Earth Resources Technology Satellite. *J. Geophys. Res.*, 80:865–881.

Balbus, S. A. and Hawley, J. F. (1998). Instability, turbulence, and enhanced transport in accretion disks. *Rev. Mod. Phys.*, 70:1.

Ball, F. K. (1960). Finite tidal waves propagated without change of shape. *J. Fluid. Mech.*, 9:506–512.

Benjamin, T. B. (1966). Internal waves of finite amplitude and permanent form. *J. Fluid Mech.*, 25:241–270.

Blaes, O. M. (2003). *Accretion discs, jets and high energy phenomena in astrophysics*. Springer.

Burden, R. L. and Faires, J. D. (1993). *Numerical analysis (5th ed.)*. Brooks Cole, Boston, Ma.

Charbonneau, P., Christensen-Dalsgaard, J., Henning, R., Larsen, R. M., Schou, J., Thompson, M. J., and Tomczyk, S. (1999). Helioseismic constraints on the structure of the solar tachocline. *Astrophys. J*, 527:445–460.

Choi, W. and Camassa, R. (1999). Fully nonlinear internal waves in a two-fluid system. *J. Fluid Mech.*, 396:1–36.

Christensen-Dalsgaard, J. et al. (1996). The current state of solar modeling. Technical Report 5266, JSTOR.

Clarke, R. H. (1971). The morning glory: an atmospheric hydraulic jump. *J. Appl. Meteorol.*, 11:304–311.

Craik, A. D. D. (1985). *Wave interactions and fluid flows*. Cambridge University Press.

De Sterck, H. (2001). Hyperbolic theory of the ”shallow water” magnetohydrodynamics equations. *Phys. Plasmas*, 8:3293–3304.

Dellar, P. J. (2002a). Dispersive shallow water magnetohydrodynamics. *Phys. Plasmas*, 10:581–590.

Dellar, P. J. (2002b). Hamiltonian and symmetric hyperbolic structures of shallow water magnetohydrodynamics. *Phys. Plasmas*, 9:1130–1136.

Dellar, P. J. and Salmon, R. (2005). Shallow water equations with a complete Coriolis force and topography. *Phys. fluids*, 10:106601.

Dikpati, M. and Gilman, P. A. (2001). Prolateness of the solar tachocline inferred from latitudinal force balance in a magnetohydrodynamic shallow-water model. *Astrophys. J*, 552:348–353.

Dowling, T. E. and Ingersoll, A. P. (1989). Jupiter’s great red spot as a shallow water system. *J. Atmos. Sci.*, 46:3256–3278.

Drazin, P. G. and Johnson, R. S. (1989). *Solitons: an introduction*. Cambridge University Press.

Dungey, J. W. (1954). The attenuation of Alfvén waves. *J. geophys. res.*, 59:323–328.

Erdélyi, R. and Mendoza-Briceno, C. A. (2008). *Waves and oscillations in the solar atmosphere*. Cambridge University Press.

Forgacs-Dajka, E. and Petrovay, K. (2001). Tachocline confinement by an oscillatory magnetic field. *Sol. Phys.*, 203:195–210.

Fornberg, B. (1996). *A practical guide to pseudospectral methods*. Cambridge University Press.

Garrett, C. and Munk, W. (1972). Oceanic mixing by breaking internal waves. *Deep Sea Res.*, 3:823–832.

Gill, A. E. (1982). *Atmosphere–Ocean Dynamics*. Academic Press.

Gilman, P. A. (1967a). Stability of baroclinic flows in a zonal magnetic field: part i. *J. Atmos. Sci.*, 24:101–118.

Gilman, P. A. (1967b). Stability of baroclinic flows in a zonal magnetic field: part ii. *J. Atmos. Sci.*, 24:119–129.

Gilman, P. A. (1967c). Stability of baroclinic flows in a zonal magnetic field: part iii. *J. Atmos. Sci.*, 24:130–143.

Gilman, P. A. (2000). Magnetohydrodynamic ‘shallow water’ equations for the solar tachocline. *Astrophys. J*, 544:79–82.

Goedbloed, H. and Poedts, S. (2004). *Principles of magnetohydrodynamics: with applications to laboratory and astrophysical plasmas*. Cambridge University Press.

Goldston, R. J. and Rutherford, P. H. (1995). *Introduction to Plasma Physics*. IoP.

Gough, D. O. (2007). An introduction to the solar tachocline. In *The solar tachocline*. Springer.

Grimshaw, R. (2005). *Nonlinear waves in fluids: recent advances and modern applications*. Springer.

Heng, K. and Spitkovsky, A. (2009). Magnetohydrodynamic shallow water waves: linear analysis. *Astrophys. J*, 703:1819–1831.

Hocke, K. and Schlegel, K. (1996). A review of atmospheric gravity waves and travelling ionospheric disturbances:1982-1995. *Ann. Geophysicae*, 14:917–940.

Hughes, D. W., Rosner, R., and Weiss, N. O. (2007). *The Solar Tachocline*. Springer.

Jones, C. A., Thompson, M. J., and Tobias, S. M. (2010). The solar dynamo. *Space Sci. Rev.*, 152:591–616.

Korteweg, D. J. and de Vries, G. (1895). On the change of form of long waves advancing in a rectangular canal, and on a new type of long stationary waves. *Philos. mag.*, 39:422–443.

Lamb, H. (1932). *Hydrodynamics*. Cambridge University Press.

Lehnert, B. (1955). Magnetohydrodynamic waves under the action of the Coriolis force. *Astrophys. J*, 121:481–490.

Lighthill, J. (1978). *Waves in Fluids*. Cambridge University Press.

Lillo, R., Mininni, P. D., and Gómez, D. O. (2005). Toward a dynamo model for the solar tachocline. *Physica A*, 349:667–674.

Liu, P. L.-F. and Wang, X. (2012). A multi-layer model for nonlinear internal wave propagation in shallow water. *J. Fluid Mech.*, 695:341–365.

London, S. D. (2014). Weakly nonlinear shallow water magnetohydrodynamic waves. *Geophys. Astrophys. Fluid.*, 108.

Lynch, P. (2003). Resonant Rossby wave triads and the swinging spring. *Amer. Meteor. Soc.*, 84:605–616.

MacKenzie, K. V. (1981). Discussion of sea water sound-speed determinations. *Acoust. Soc. Am.*, 70:801–806.

Mak, J. (2013). *Shear flow instabilities in shallow-water magnetohydrodynamics*. PhD thesis, University of Leeds.

Maxwell, J. C. (1861). *On physical lines of force*. Philosophical Magazine.

McLellan, A. and Winterberg, F. (1968). Magneto-gravity waves and the heating of the solar corona. *Solar Phys.*, 4:401–408.

Melendez, J. et al. (1968). The solar, exoplanet and cosmological lithium problems. *Sol. Phys.*, 4:401–408.

Miura, A. (1996). Stabilisation of the Kelvin-Helmholtz instability by the transverse magnetic field in the magnetosphere-ionosphere coupling system. *Geophys. res. letters*, 23:761–764.

Narayanan, A. S. (2012). *An introduction to waves and oscillations in the Sun*. Springer.

Orszag, S. A. (1971). On the elimination of aliasing in finite-difference schemes by filtering high-wavenumber components. *J. Atmos. Sci.*, 28:1074–1074.

Ovsyannikov, L. V. (1979). Two-layer ”shallow water” model. *Applied mech. and tech. phys.*, 20.

Parker, E. N. (1955). Hydromagnetic waves and the acceleration of cosmic rays. *Phys. Rev.*, 99:241–253.

Pedlosky, J. (1987). *Geophysical fluid dynamics*. Springer.

Poynting, J. (1884). On the transfer of energy in the electromagnetic field. *J Phil. Trans. of the Royal Soc. of London*, pages 343–361.

Press, W. H. (2002). *Numerical recipes: the art of scientific computing*. Cambridge University Press.

Priest, E. R. (1982). *Solar magnetohydrodynamics*. Reidel, Dordrecht, Holland.

Rayleigh, J. W. S. (1876). On waves. *Philos. Mag. Ser.*, pages 257–279.

Rayleigh, J. W. S. (1877). *The theory of sound*. London, Macmillian and co.

Ripa, P. (1993). Conservation laws for primitive equations models with inhomogeneous layers. *Geophys. Astro. Fluid.*, 70.

Schecter, D. A., Boyd, J. F., and Gilman, P. A. (2001). 'shallow water' magnetohydrodynamic waves in the solar tachocline. *Astrophys. J*, 551:185–188.

Schou, J. et al. (1997). Structure and rotation of the solar interior: initial results from the MDI medium-L program. *Sol. Phys.*, 170:43–61.

Showman, A. P. (2007). Numerical simulations of forced shallow-water turbulence: effects of moist convection on the large-scale circulation of Jupiter and Saturn. *J. Atmos. Sci.*, 64:3132–3157.

Smith, G. D. (1965). *Numerical solution of partial differential equations*. Oxford University Press.

Spiegel, E. and Zahn, J.-P. (1992). The solar tachocline. *Astron. Astrophys.*, 265:106–114.

Stewart, A. and Dellar, P. J. (2010). Multilayer shallow water equations with complete Coriolis force. part i: Derivation on a non-traditional beta-plane. *J. Fluid Mech.*, 651:387–413.

Stix, T. H. (1992). *Waves in plasmas*. Springer.

Stokes, G. G. (1849). On the theory of oscillating waves. *Trans. Cambridge Philos. Soc.*, 1:314.

Trefethen, L. N. (2000). *Spectral methods in MATLAB*. SIAM.

Turner, J. S. (1973). *Buoyancy effects in fluids*. Cambridge University Press.

Umurhan, O. M. (2008). A shallow-water theory for annular sections of Keplerian disks. *Astron. Astrophys.*, 489:953–962.

Umurhan, O. M. (2013). The equations of magnetoquasigeostrophy. *Astron. Astrophys. (under consideration)*, page 13.

Vallis, G. K. (2006). *Atmospheric and Oceanic Fluid Dynamics*. Cambridge University Press, Cambridge, U.K.

Vreugdenhil, C. B. (1994). *Numerical methods for shallow-water flow*. Kluwer Academic Publishers.

Warneford, E. S. and Dellar, P. J. (2013). The quasi-geostrophic theory of the thermal shallow water equations. *J. Fluid Mech.*, 723:374–403.

Warneford, E. S. and Dellar, P. J. (2014). Thermal shallow water models of geostrophic turbulence in Jovian atmospheres. *Phys. Fluids*, 26.

Weizsacker, C. F. V. (1948). Die rotation kosmischer gasmassen. *Zeitschrift Naturforschung*, 3:524.

Whitham, G. B. (1974). *Linear and nonlinear waves*. Wiley.

Wu, T. Y. (1981). Long waves in ocean and coastal waters. *J. Eng. Mech. Div. (Amer. Soc. Civil Eng.)*, 102:501–522.

Zaqarashvili, T. V., Oliver, R., and Ballester, J. L. (2009). Global shallow water magnetohydrodynamic waves in the solar tachocline. *Astrophys. J*, 691:41–44.

Zaqarashvili, T. V., Oliver, R., Ballester, J. L., and Shergelashvili, B. M. (2008). Rossby waves in ‘shallow water’ magnetohydrodynamics. *Astro. Astrophys.*, 470:815–820.

Zeitlin, V. (2007). *Nonlinear dynamics of rotating shallow water: methods and advances*. Elsevier.

Zeitlin, V. (2013). Remarks on rotating shallow-water magnetohydrodynamics. *Nonlinear Proc. Geophys.*, 20:893–898.